THE UNIVERSITY OF QUEENSLAND

AUSTRALIA

Novel Techniques in Ore Characterisation and Sorting

Geoffrey Leonard Genn

B.Sc (Hons)

A thesis submitted for the degree of Doctor of Philosophy at

The University of Queensland in 2013

The Sustainable Minerals Institute

Abstract

Ore sorting is becoming increasingly important to the minerals industry but is a difficult technology to apply effectively to many ore types. Microwave excitation and infrared detection (MW/IR) is a potential new sensor technology for sorting copper sulphide ores. This technology utilises the high dielectric permittivity of copper sulphide minerals and relatively low dielectric properties of gangue minerals to selectively heat copper rich particles and thereby gauge particle grade from temperature. To date, the dielectric properties of minerals and the role of mineral structures within particles are not fully understood and can vary significantly from deposit to deposit due to differences in geochemistry and genesis. These variations in mineralogy and dielectric properties can mean that some ores are unsuitable for sorting. The aim of this thesis is to develop a characterisation methodology to assess the suitability of ores for MW/IR based sorting from small sets of particles.

The microwave heating of six different ores, chosen to represent a range of minerals and mineral textures, was characterised using randomly split particles, a domestic microwave oven and thermal imaging. The dielectric properties of core and powder subsamples of particles from four ores were then measured using a resonant cavity perturbation experiments at The University of Nottingham. Three effects were identified that may influence the observed relationship between microwave heating and dielectric properties: strong interaction with the magnetic field, mineral structures and sulphide heterogeneity in samples. These effects were investigated using radiofrequency magnetic permeability measurements, rotation of rock cylinders in a rectangular waveguide resonant cavity and automated scanning electron microscopy (MLA). The modal mineralogy of ore samples was measured using MLA while geochemistry was investigated using electron probe microscopy. The dielectric properties of mineral groups were then calculated using systems of linear equations based on the Landau-Lifschitz-Looyenga mixture equation as well as modal mineralogy and dielectric property data. Finally, numerical simulations of microwave heating were performed using data on mineralogy, mineral dielectric properties and variability in particle heating to determine to assess the potential of rocks types for sorting.

MW/IR characterisation showed that quartzite, monzonite and skarn ores have distinct particle temperature distributions and that variation in the pixel temperatures of individual particle surfaces might be useful in distinguishing particle petrology. A power law was found to describe the relationship between microwave heating and dielectric loss tangent (R^2 = 79%) although a good fit could be achieved with a linear relationship (R^2 = 89%) when specific, termed anomalous, particles were excluded. Magnetic permeability measurements indicated that there was no significant difference in permeability between normal and anomalously heating particles. Changes in cavity perturbation were observed with core rotation and were consistent with bulk dielectric anisotropy resulting from mineral structures. MLA imaging of the solid sections of skarn samples demonstrated a high degree of sulphide heterogeneity. Calculation of dielectric constant using least squares regression of overdetermined systems of linear equations produced statistically significant results that compared well with values reported in literature but had large standard errors (> 10%). Dielectric loss factors calculated in this manner were not reliable as regressions only produced statistically significant data for some minerals and standard errors were much higher. Grade recovery curves produced by simulation of microwave heating indicated that quartzite ore is likely to be a suitable candidate for MW/IR sorting, however, some monzonite type ores may be unsuitable.

Future work on this topic may include:

- development of particle surface temperature variation as a metric for petrology
- MW/IR characterisation at 915 MHz
- Measurements of permeability at microwave frequencies
- Development of the resonant cavity texture measurement technique
- Development of the regression method for dielectric mixture calculation and validation of the numerical simulation of MW/IR detection.

Declaration by author

This thesis ***is composed of my original work, and contains*** no material previously published or written by another person except where due reference has been made in the text. I have clearly stated the contribution by others to jointly-authored works that I have included in my thesis.

I have clearly stated the contribution of others to my thesis as a whole, including statistical assistance, survey design, data analysis, significant technical procedures, professional editorial advice, and any other original research work used or reported in my thesis. The content of my thesis is the result of work I have carried out since the commencement of my research higher degree candidature and does not include a substantial part of work that has been submitted ***to qualify for the award of any*** other degree or diploma in any university or other tertiary institution. I have clearly stated which parts of my thesis, if any, have been submitted to qualify for another award.

I acknowledge that an electronic copy of my thesis must be lodged with the University Library and, subject to the General Award Rules of The University of Queensland, immediately made available for research and study in accordance with the *Copyright Act 1968*.

I acknowledge that copyright of all material contained in my thesis resides with the copyright holder(s) of that material. Where appropriate I have obtained copyright permission from the copyright holder to reproduce material in this thesis.

Publications during candidature

No publications

Publications included in this thesis

No publications included

Contributions by others to the thesis

No contribution by others

Statement of parts of the thesis submitted to qualify for the award of another degree

None

Acknowledgements

I sincerely thank my advisors: Dr Rob Morrison & Dr Nenad Djordjevic of The Julius Kruttschnitt Mineral Research Centre (JKMRC) at The University of Queensland (UQ) and Prof Sam Kingman of The National Centre for Industrial Microwave Processing (NCIMP) at The University of Nottingham (UoN) for their guidance, advice, and support. I'd like to extend my gratitude to Rio Tinto Technology & Innovation for sponsoring this project and particularly Dr Grant Wellwood for his encouragement and support.

Particular thanks go to Prof Ben Adair who provided mineral specimens from his private collection; Prof Tim Napier-Munn for his advice and assistance in creating factorial experiment to characterise error in dielectric measurements and Dr Georgios Dimitrakis for instructing me how to perform dielectric measurements using the C1 cavity at The NCIMP, insightful discussions, and proofreading chapters of this thesis. Thanks also go to Dr David Steele of JKTech for teaching me to use the microprobe, assistance in analysing microprobe data, and providing elemental detection limit data; and Dr Elaine Wightman and the staff of the JKMRC MLA facility for running the XMOD and GXMAP analyses as well as mounting samples in resin for microprobe measurements.

Thanks are due to all the staff and students of JKMRC and NCIMP, both past and present, that I have had the pleasure of interacting with although my fellow students, and colleagues, Dr Vladimir Jokovic and Dr Vladimir Rizmanoski deserve singling out. Finally, thank-you to my family and my partner, Claire: I feel that without your encouragement, patience and love I would never have reached the end.

Keywords

minerals, dielectric properties, microwave heating, mineral texture, sorting

Australian and New Zealand Standard Research Classifications (ANZSRC)

ANZSRC code: 091404, Mineral Processing/Beneficiation, 100%

Fields of Research (FoR) Classification

FoR code: 0914, Resources Engineering and Extractive Metallurgy, 100%

Statement of originality

I hereby declare that the contents of this thesis have not been included in any other work submitted by the author for another degree. The subject matters that comprise original contributions to this field of knowledge are outlined briefly below.

1. Measurement Technique

   The combination of mineralogical measurement techniques, such as electron micro-probes, with dielectric property, and microwave heating measurements to characterise the sorting potential of ores.

2. Dielectric Property Data

   New microwave frequency dielectric property data of ores which supports existing measurements.

3. Mineral Dielectric Properties from Ore

   The calculation of mineral dielectric properties from complex ore mixtures by way of a system of mixture equations which contain modal mineralogy and dielectric property data.

4. Characterisation Methodology simulation

   A methodology for evaluating the potential of ores for microwave sorting based primarily on the dielectric properties of minerals which involves Monte Carlo simulations of ores and microwave heating using the dielectric property data of minerals along with empirical models of heating variability of determine the heating behaviour of particles in an ore with respect to their mineral grade.

5. Particle Temperature Variation

   The use of the relative standard deviation in the temperature of individual particle surfaces in Microwave-IR analysis as a means of assessing their petrology.

Table of Contents

List of Figures

List of Tables

1 Introduction

It is common in minerals processing practice to grind all ore deemed to be above the cut-off grade to the size optimal for flotation, this is a very energy intensive process. As potential ore deposits decline in grade and increase in complexity there will be significant increases in the energy required for comminution to produce a unit of metal (Ayres, Ayres & Råde 2003; Mudd 2010). Ore sorting has the potential to ameliorate this problem by improving the grade of mined material and allowing barren particles to be ejected from the processing stream before grinding (Sivamohan & Forssberg 1991). It also has the potential to recover additional metal in a deposit by processing mineralised waste which is below conventional cut-off grades. Sorting is currently used commercially in niche applications but may have significant implications for the sustainability of mining and minerals processing should a more broadly applicable detection process be identified.

For sorting to be applied to an ore, a method for gauging the quantity of valuable minerals on a particle-by-particle basis is required. With this knowledge, decisions can be made regarding the value of processing each particle and every particle in a processing stream. If a particle does not warrant further processing it can be immediately ejected from the processing stream. Sorting thereby offers the opportunity to simultaneously increase the ore grade and reduce the volume of the material entering the comminution process; consequently reducing the processing energy requirements per ton of ore mined (Sivamohan & Forssberg 1991).

There are several ways to integrate sorting into minerals processing. In one mode a sorting plant may operate as a pre-concentrator; and remove the leanest particles from the processing stream. As a result of rejecting the lean fraction, the feed rate and energy requirements of comminution plants are reduced, while the grade of material passing through the plant is increased. This has the advantage of reducing effective cut-off grades, extending mine lifetimes and increasing ore reserves as well as reducing the energy use per unit of metal produced. Alternatively, sorting plants could be used to process waste rock which as a whole

does not contain enough valuable minerals to be processed economically. This involves selecting the particles rich in valuable minerals from the waste material and diverting them to the minerals processing plant. This mode both finds value in otherwise unprocessed material and reduces the quantity of hazardous minerals, such as metal sulphides, in waste piles is reduced which consequently leads to lower rates of acid mine drainage.

Separation systems based on static or low frequency electromagnetic fields, such as electrostatic or magnetic roll separators, already exist in minerals processing. However, these techniques are used to separate particles after energy-intensive comminution. The use of microwave frequency fields for bulk heating has been of interest since the 1980's and has inspired research into the dielectric properties of numerous materials, including pure minerals. Investigation into the microwave properties of minerals began with Chen, TT et al. (1984) who found that valuable minerals, particularly sulphides, were markedly more responsive to microwave heating than the gangue minerals with which they are commonly found.

Selective heating of minerals led to research into a number of different applications of microwave heating to minerals processing including comminution, liberation and leaching (KingmanJacksonBradshaw, et al. 2004; Kruesi & Frahm 1980; Sahyoun, Kingman & Rowson 2003; Walkiewicz, Clark & McGill 1991). Most of these lines of investigation focussed on using selective heating to create differential thermal stresses in rock matrix. The hypothesis is that thermal stresses will induce cracking and consequently weaken rock matrices which will require less energy to crush or mill, or weakened grain interfaces from which a higher degree of liberation can be achieved. Research into these techniques has found that best results are most often achieved with very high power, short duration microwave exposures (Bradshaw et al. 2007; Salsman et al. 1996).

The combination of sorting and microwaves has also been investigated in at least three different incarnations. The first approach was first investigated by Mercer et al. (1988) who

used microwave absorption detection to sort gabbro from kimberlite. Investigations by Cutmore, N.G., Liu and Middleton (1997) found microwave frequency dielectric properties could be a metric for the quantity of valuable minerals in iron ore samples but noted a new approach to sensing was required. More recently, an indirect method for measuring the dielectric properties of particles has emerged and has been investigated by groups at RWTH Aachen University, Aachen, Germany; ORETOME Ltd., Toronto, Canada; and the University of Queensland, Brisbane, Australia (Djordjevic 2009; van Weert & Kondos 2007; Wotruba & Riedel 2006). This technique, termed microwave/infrared (MW/IR) sorting, is based on thermal measurements of particles after they have been exposed to microwave fields.

The degree to which each particle heats in the microwave field is nominally due to the bulk dielectric properties of particles. For metal ores this assumes that the temperature increase is a function of the grade, since valuable minerals heat much more than gangue minerals. However, this is a simplified approach and there are a number of complicating factors in microwave heating including: widely varying mineral dielectric properties; particle shape; mineral structuring; or even the homogeneity of the applied field. The combination of these factors mean that some ores may be more, or less, suitable for electromagnetic sorting applications than others. Furthermore, this approach is largely limited to metal ores as industrial minerals, along with precious and semi-precious stones tend to heat similarly to their gangue matrix in a microwave field. To date there is no method for examining an ores potential for MW/IR sorting beyond a feasibility study which involves repeated microwave heating and thermal analysis of a large number of particles followed by individual assay of each particle to determine the valuable mineral content.

This thesis focuses on developing a methodology for characterising the MW/IR performance of copper ores using a small number of samples and dielectric property measurements. In the development of this methodology several questions need to be addressed:

- Do the dielectric properties of powdered samples correlate with the MW/IR heating of particles?

- Can particles be considered purely as lossy dielectrics?
- Do mineral structures within particles affect microwave heating?
- Can the dielectric properties of mineral species be calculated from the dielectric properties of mixtures and modal mineralogy data?
- And finally, can simulations of microwave heating predict different sorting outcomes for different gangue matrices?

Firstly, scholarly literature on sorting and microwave processing is reviewed (Chapter 2) with a focus on minerals processing along with dielectric measurement techniques for microwave frequencies, the measured microwave frequency dielectric properties of minerals and the various dielectric mixing equations. The literature review is followed by microwave heating and infrared thermography of particles from six different ores (Chapter 3) – a quartzite ore, a skarn ore, and four monzonite ores – from different regions in a single deposit. Powdered samples and core subsections were then extracted from particles in four of the six ores. The dielectric properties of these samples were then measured using a resonant cavity perturbation technique at the University of Nottingham. These measurements allow the microwave heating to be related to the dielectric properties. Magnetic permeability, mineral structuring, and sulphide heterogeneity are then investigated as potential complicating factors in the relationship between microwave heating-dielectric properties. Radiofrequency measurements of magnetic permeability are performed on the powdered samples using a Magnasat, while internal mineral structuring is investigated using rock cores and a custom rectangular waveguide cavity with a TE_{101} resonance at 2.29 GHz.

In the final experimental chapter, the modal mineralogy of samples is measured using automated scanning electron microscopy (MLA). The MLA modal mineralogy data is then complimented by electron microprobe measurements of mineral chemistry from which end-member compositions are determined. The modal mineralogy data is then coupled with the dielectric properties measured in Chapter 3 to form a system of linear equations based on a dielectric mixing equation. Solving this system of equations produces estimate of the dielectric properties of the major mineral groups.

Finally, Monte Carlo simulations are used to predict the performance of MI/IR sorting of gangue matrices at industrial scales. Several intermediate steps are required in these simulations including: mixing the properties of gangue mixtures with particle-by-particle distributions of copper grade; modelling microwave heating of mixtures; and finally modelling heating uncertainty. The simulated mixtures are then sorted by temperature to arrive at plots comparing cumulative metal grade with cumulative mass from which conclusions regarding the suitability of that ore for sorting. Conclusions and suggestions for future work are provided in Chapter 6.

2 Literature Review

2.1 Sorting

2.1.1 A History of Sorting in the Minerals Industry

Sorting is potentially the oldest minerals processing technique dating back to Palaeolithic peoples who carefully selected, by hand, which shards of flint would be knapped into stone tools and weapons. Hand sorting is an effective processing technique and persisted into the twentieth century (Salter & Wyatt 1991). Decreasing ore grades and liberation sizes, as well as increasing ore complexities and throughput demands have precluded hand sorting in modern operations and it was almost completely abandoned by the early 1970's (Salter & Wyatt 1991). Madame Curie is apocryphally credited as the designer of the first sorting machine which used x-ray attenuation to differentiate between lumps of dirt and dirt-covered potatoes although this design was not realized in a fully automated form until the 1960's (Slight 1966). This same design was later adapted to separate waste from coal (Jenkinson et al. 1974).

The food industry has long held the belief that automated processing is crucial to maintaining the profitability of modern operations as they see traditional methods as expensive, inefficient and labour-intensive and it for these reasons that they developed the first true commercial automated sorting systems in the 1930's (Salter & Wyatt 1991). To date the application of sorting techniques in the minerals industry has always followed the development of new laboratory analysis methods and the implementation of those methods to sorting in the food industry (Salter & Wyatt 1991). It has been suggested the minerals industry lags behind in this field because different economic drivers acting on the them and has made sorting less critical to maintaining profitability (Salter & Wyatt 1991). Another consideration is that, with certain exceptions, economic sorting of minerals is much more complex and difficult than in the food industry because the feed properties of run-of-mine particles are highly variable and not visible on particle surfaces (Wotruba & Riedel 2006).

According to Salter & Wyatt (1991) one of the pinnacles of ore sorting was in the early 1980's and coincided with the development of the Model 17 ore sorter by RTZ Ore Sorters Ltd. In the period 1960 to 2000 Cutmore & Eberhardt (2002) found more than 1300 scholarly articles on minerals sorting of which photometric and radiometric sorting were the two most widely used technologies. Cutmore and Eberhardt (2002) believe that, starting in the late 1980's, a strong decline in the publication of scholarly articles per year corresponded to an earlier decline in the usage of sorting systems. This matches with the views of Salter and Wyatt (1991) who believe the decline of sorting operations began early in the 1980's and identified three major factors responsible for the decline: a depressed uranium market; changes in mine process philosophy; and, for a variety of reasons, a poor reputation. Additionally, ore sorting also faces the steadily increasing challenge of declining ore grades (Ayres, Ayres & Råde 2003; Mudd 2010).

In 2002 Cutmore & Eberhardt found no increase in the publication rate of scholarly articles on mineral sorting but in 2006 Wotruba & Riedel's review of sensor technologies for sorting metalliferous ores noted a resurging interest in the field. The renewed interest may be attributed to economic pressures as ore reserves, declining in grade and increasing in complexity, become difficult process efficiently with conventional methods and additional burdens of sustainability and taxes on carbon emissions are applied (Cutmore, N. G. & Eberhardt 2002; Wotruba & Riedel 2006).

Cutmore & Eberhardt (2002) list many potential sensor technologies (see Table 2-1) but Wotruba & Riedel (2006) focus on the six they believe are the most promising:

- Optical sensors
- Microwave assisted infrared sensors
- X-ray absorption/transmission
- Metal detectors
- Laser Induced Fluorescence (LIF), and Laser Induced Breakdown Spectrometry (LIBS)

Table 2-1 – Potential ore analysis techniques – after Cutmore, N. G. and Eberhardt (2002))

Nuclear	Activation, Natural, Alpha, Gamma, Beta, X-ray, Neutron
Optical	Reflectance, Fluorescence, Luminescence, LIBS, LIF, Raman, Scattering, Image Analysis (Spots & Striations), Refractive Index
Electrical	Conductivity, Permittivity, Microwave Attenuation, Triboelectric Effect
Magnetic	Induction, ESR, NQR, Permeability, NMR
Acoustic	Transmission, Ring-down, Optoacoustic
Thermal	Conductance, Diffusivity, Emissivity, Microwave Loss
Surface Modification	Fluorescent dip, Hydrophobic/Hydrophilic, Melting, Scratch & Hardness, Streak
Gravitational	Density, Weight
Other	Shape, Aspect Ratio, Smell, Friction, Texture

Optical sensors in sorting are in widespread use in the food industry. Detectors are fast, and can have very good resolution (<0.1mm). According to Wotruba & Riedel (2006), optical sorting is an excellent choice when the valuable and gangue minerals have sharply defined differences in colour, brightness, reflection or transparency. Unfortunately this is rarely the case in ores. An additional issue with optical sensors is that only the particle surface can be measured.

Infrared imaging can be used to measure the temperature of particles with commercially available cameras accurate to 0.1K. When thermal imaging is coupled with a process capable of selective heating, such as microwaves, there is potential for sorting. A number of groups are researching this technology including: RWTH Aachen University (Wotruba & Riedel 2006), Process Research ORTECH in Ontario (van Weert, Kondos & Gluck 2009), and the Rio Tinto Centre for Advanced Mineral Sorting (RT CAMS) at the University of Queensland (Djordjevic 2009; Djordjevic & Adair 2010; Morrison 2010). While infrared imaging has a lower resolution than optical imaging and both are surface measurements, the thermal bloom of microwave absorbent minerals may allow insights on the sub-surface composition of particles.

X-ray sensors and metal detectors are both capable of obtaining information about the interior of particles. Many valuable minerals (such as diamond and sulphides) have high x-ray attenuation coefficients relative to gangue minerals (Ketcham & Carlson 2001). When x-rays pass through a particle it is possible to estimate the amount of valuable minerals present from the imaged silhouette. Metal detectors can be used to find samples containing valuable minerals, such as native metals or sulphides (Bamber 2008). In this technique, eddy currents are induced in conductive grains and form a magnetic field in response to an applied oscillating magnetic field. However, this technique can perform poorly in ores with low mineral grades and finely disseminated conductive minerals due to a high sensitivity to both particle and grain sizes (Sivamohan & Forssberg 1991).

LIF and LIBS techniques are still under development (Wotruba & Riedel 2006). LIF systems uses ultraviolet laser beams to generate fluorescence on a particle surface which is subsequently detected (Rusak et al. 1997). LIBS uses focussed high power laser pulses to ablate small sections of a particle surface. This process generates small plumes of plasma which emit light at characteristic frequencies which are then be used to estimate an assay of the ablated spot (Kinsey 1977).

All of the above sensor technologies have both advantages and disadvantages. For successful sorting multiple parallel detection techniques or a series of sorters may be required. Sorting has historically been closely associated with the minerals industry but it has been the food industry that has driven the developments in modern sorting technology. Consequently the use of ore sorters in the minerals industry peaked and then fell out of favour because the technologies were not driven to meet their needs. However, demands on the minerals industry are changing and with the emergence of new detector technologies, sorting may be part of the way forward (Bamber 2008; Cutmore, N.G., Liu & Middleton 1997; Wotruba & Riedel 2006).

2.1.2 The Sorting Process

Conceptually, there are four sub-processes to a sorting system: presentation, examination, data analysis and separation (Figure 2-1), however, the components of the physical system are often merged together. The presentation stage includes all preparation necessary to arrange the feed material in manner suitable for the examination and separation stages. Depending on the design of the system, the feed can be either randomly distributed on a belt or split into a series of channels. The Model 17 Ore sorter, for example, is fed by a vibratory feeder, uses two stages of 5-channel belts and includes a stabilizer wheel to control particle movement (see Figure 2-2 and Figure 2-3) (Kidd & Wyatt 1982; Salter & Wyatt 1991). The presentation stage may involve several stages of conveyor belts to accelerate the particles, to increase inter-particle distances, and to launch particles in a controlled trajectory.

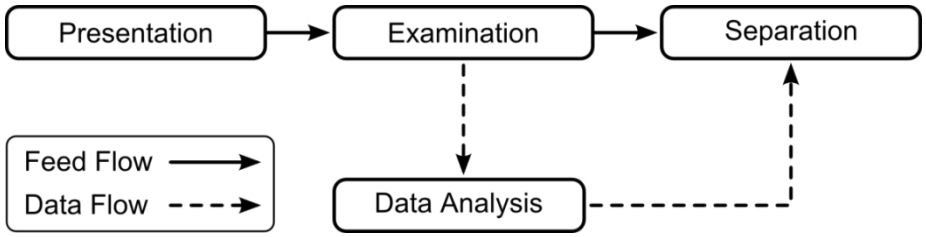

Figure 2-1 – The Conceptual Sub-Processes of Sorting

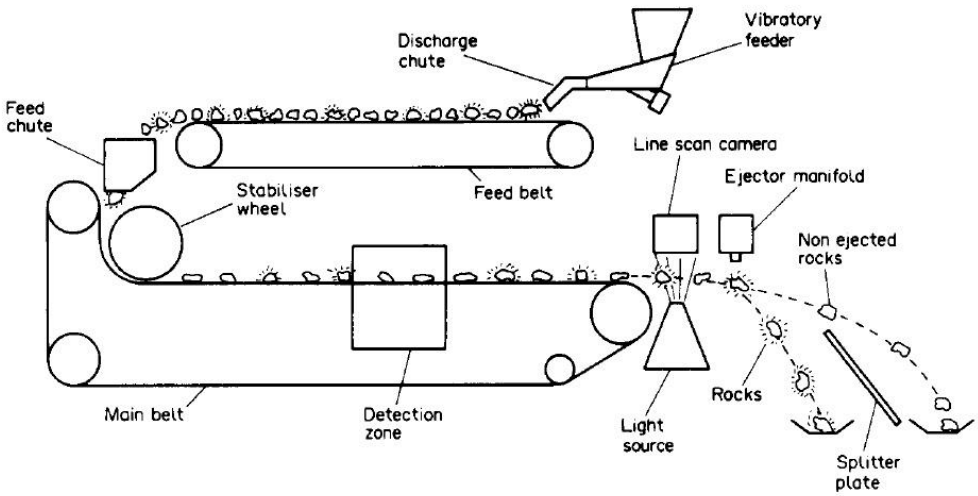

Figure 2-2 - Schematic of the Model 17 Ore Sorter (Salter & Wyatt 1991)

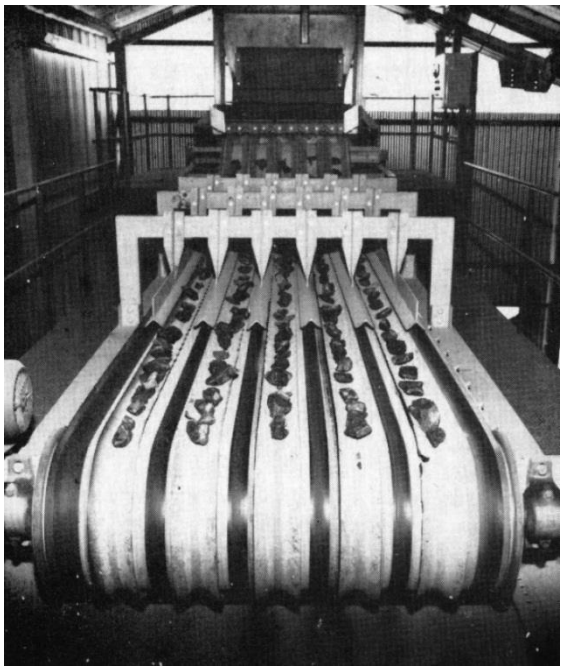

Figure 2-3 – Feed belt of the Model 17 Ore Sorter (Kidd & Wyatt 1982)

The examination process involves measuring the properties of particles with sensors as they pass by on the conveyor belt or in free-fall. The Model 17 Ore Sorter, for example, combines on-belt radiometric, and free-fall optical measurements of particles (Figure 2-2). The data analysis stage manipulates the data gathered by the examination stage into a form where it can be compared to a set of reference criteria. The Model 17 estimates particle mass from optical data then uses the radiometric counts per unit mass of each particle to conclude uranium grade (Kidd & Wyatt 1982). An accept/reject decision is then made for each particle based on the comparison of the measurement data to the reference criteria.

Finally, the particles arrive at the separation stage where the physical separation mechanism enacts the decisions reached in the data analysis. Common separation mechanisms are air jets, which selectively blast particles to change their trajectory and the process stream they report to, and diversion plates with push particles into different streams. More occasionally water jets are used instead of air jets.

Sorting systems in the minerals industry are mainly used to pre-concentrate ore, however, there are rare cases in which it may be used to create a finished product and waste scavenging is also possible. Sorters operating as pre-concentrators typically operate by ejecting barren particles from the feed while scavengers select the valuable particles from material that would otherwise be waste. Sorting run-of-mine material may have a number of benefits, including:

- Reduced cost of operation per unit product by rejecting valueless waste particles early in turn reduces costs of downstream transport, comminution and separation (Sivamohan & Forssberg 1991).
- Reduced ore throughput but at a higher grade which consequently reduces the throughput requirements of comminution and concentration circuits at green-field sites and may avert the need for plant expansions at brownfield sites (Sivamohan & Forssberg 1991).
- Economic recovery of valuable minerals from material that would otherwise be waste (Sivamohan & Forssberg 1991).

These benefits of sorting can mean prolonged mine lifetimes, increased ore reserves, and savings in water and energy (Cutmore, N. G. & Eberhardt 2002). However, the benefits achievable from a sorting operation need to be balanced against the drawbacks which include: the capital cost of the plant and additional operational costs such as sizing, washing and drying, mineral loss to the waste stream, and the unsuitability of some ores within a ore deposit for sorting (Sivamohan & Forssberg 1991).

2.1.3 Conclusion

Sorting has been used as a pre-concentration technique for eons and when used appropriately can offer many benefits to minerals processing plants. Over the last century the use of automated sorting systems in mineral processing has begun, peaked and then fallen out of favour. Recently research

interest in mineral sorting operations has increased, possibly as a result of increased economic pressures on the mining industry and the introduction of new technologies.

2.2 An Overview of Microwaves and Microwave Processing

2.2.1 An Introduction to Microwaves

Clarke et al. (2003) define the microwave region to be the electromagnetic radiation with frequencies between 1 GHz and 150 GHz. In their discussion on the origins of the term 'microwave' and the characteristics that make this portion of the electromagnetic spectrum distinct from others, they present the definition:

> "A microwave is an electromagnetic wave whose wavelength is comparable in linear dimension to the significant functional parts of the equipment that is used to guide, manipulate or measure it"

This definition existed before the advent of modern single-mode optical fibres, which this definition encompasses except fibres guide visible light. Microwaves, as this definition alludes, are at a cross-over point between electronic and optical conceptualizations. In the electronic regime the long-wavelength limit is assumed, in which wavelengths are much larger than the system and are not considered as travelling waves. This assumption gives rise to the lumped circuit model which uses a simple circuit of discrete ideal capacitors, inductors and resistors to describe a system (see Figure 2-4). As the wavelength approaches the circuit size, parasitic capacitances, inductances and resistances appear and distort measurements.

The optical conceptualization operates in the short-wavelength limit, in which the wavelength is considered negligibly small compared to the system and that the waves propagate through it. To do this, the distributed element model is used – this approach is more complex than the lumped

element model and uses continuously distributed infinitesimal capacitors, inductors and resistors to describe a system (see Figure 2-5). Typically, the microwave regime is where the wavelength of radiation matches the size of equipment used. Consequently, this cross-over can make modelling of systems using either the long- or the short- wavelength limits alone difficult. Depending on the operating frequency and the equipment used either lumped or distributed type methods may more appropriate. It is also possible to use resonant methods where the equipment used supports standing waves which are some integer multiple of half-wavelengths in size.

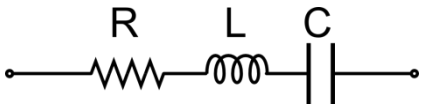

Figure 2-4 – Lumped series RLC circuit

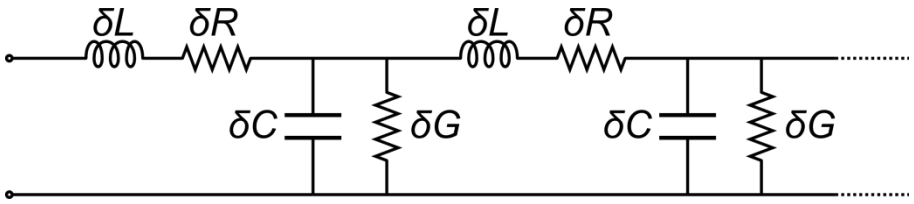

Figure 2-5 – Distributed element model of a lossy transmission line showing the distributed resistance (δR), inductance (δL), capacitance (δC) and conductance (δG)

Cheng (1989) is pragmatic in defining a microwave spectrum:

> "The term "microwave" is somewhat nebulous and imprecise; it could mean electromagnetic waves above a frequency of 1GHz and all the way up to a lower limit of the infrared band, encompassing UHF, SHF, EHF, terahertz and mm-wave regions"

This thesis uses the definition of the International Telecommunication Union (ITU) which states that the microwave region of the spectrum lies between 300MHz and 300GHz, encompassing the

UHF, SHF and EHF bands. The ITU Radio-communications Sector has developed international standards dividing the microwave spectrum into discrete bands, each with designated uses to minimize communications interference. However, the allocation of frequency bands does vary depending on local national regulations. Some sections of the spectrum have been designated as Industrial, Scientific and Medical (ISM) bands which are reserved for unlicensed applications, and are listed in Table 2-2. The usage definition of the ISM bands also includes consumer electronics, such as microwave ovens, cordless phones and other wireless appliances.

Table 2-2 – Microwave ISM Frequencies

Freq. (MHz)	± *(MHz)*	*Regions Permitted*
13.56	0.007	Worldwide
27.12	0.163	Worldwide
40.68	0.02	Worldwide
433.92	0.87	Africa, Europe, Middle East, Former Soviet Union
915	13	North and South America
2450	50	Worldwide
5800	75	Worldwide
24150	125	Worldwide

2.2.2 Electromagnetic Properties of Matter

Any material can be broadly classified into one of three types based on its interaction with microwave fields. These are: Transparent (no absorption and total transmission), Conductor (no absorption and total reflection at the interface) and Absorber (microwave power dissipated in the material which results in heating). This largely correlates with the conductivity of materials. Strongly insulating materials are typically transparent while highly conductive materials reflect microwaves and absorbers are of intermediate conductivity.

The interaction between electromagnetic fields and matter is described by Time-dependent Maxwell's Equations:

$$\nabla \cdot \mathbf{D} = \rho \tag{2.1}$$

$$\nabla \cdot \mathbf{B} = 0 \tag{2.2}$$

$$\nabla \times \mathbf{H} = \frac{\partial \mathbf{D}}{\partial t} + \mathbf{J} \tag{2.3}$$

$$\nabla \times \mathbf{E} = -\frac{\partial \mathbf{B}}{\partial t} \tag{2.4}$$

When an electric field, $\mathbf{E}$, is applied to a medium, the charge carriers in the medium attempt to move or re-orientate themselves with respect to the field and form dipole moments. This can be accomplished in many ways such as ionic conduction, dipolar relaxation, atomic polarization or electronic polarization. The Electric Displacement Field, $\mathbf{D}$, accounts for these the local moments by introducing a term for polarization density, $\mathbf{P}$ (Equation (2.5)).

$$\mathbf{D} = \epsilon_0 \mathbf{E} + \mathbf{P} \tag{2.5}$$

In a linear, isotropic media the polarization density, **P**, is related to electric field intensity by a constant of proportionality called the electric susceptibility, χ_e, which does not depend on field direction (see Equation (2.6)). This allows the electric displacement field to simplify to Equation (2.9). Similar to the polarization density, there is a magnetization, **M**, in which magnetic dipoles re-orientate themselves in response to an applied magnetic field (see Equation (2.10)). The magnetization response of a medium is also proportional to the applied magnetic field, **H**, and in a similar fashion the magnetic flux density, $\mathbf{B}$, simplifies to Equation (2.14) via magnetic susceptibility, χ_v (see Equations (2.10) to (2.13)). In these equations ϵ is the absolute permittivity

and μ is the absolute permeability of the medium. The current density, $\mathbf{J}$, relates to the electric field via the conductivity of the medium, σ, to become Equation (2.15).

$$\mathbf{P} = \varepsilon_0 \chi_e \mathbf{E} \tag{2.6}$$

$$\mathbf{D} = \varepsilon_0 \left(1 + \chi_e\right) \mathbf{E} \tag{2.7}$$

$$\varepsilon_r = 1 + \chi_e \tag{2.8}$$

$$\mathbf{D} = \epsilon \mathbf{E} \tag{2.9}$$

$$\mathbf{B} = \mu_0 \mathbf{H} + \mathbf{M} \tag{2.10}$$

$$\mathbf{M} = \mu_0 \chi_v \mathbf{H} \tag{2.11}$$

$$\mathbf{B} = \mu_0 \left(1 + \chi_v\right) \mathbf{H} \tag{2.12}$$

$$\mu_r = 1 + \chi_v \tag{2.13}$$

$$\mathbf{B} = \mu \mathbf{H} \tag{2.14}$$

$$\mathbf{J} = \sigma \mathbf{E} \tag{2.15}$$

Sinusoidally varying electromagnetic fields (such as microwaves) allow the introduction of phasor notation such that:

$$E\left(x, y, z, t\right) = \Re\left[\mathbf{E}\left(x, y, z\right) e^{j\omega t}\right] \tag{2.16}$$

This notation provides easy solutions of the partial differentials in equations (2.3) and (2.4) which allow the Time-Harmonic Maxwell's Equations to be found:

$$\nabla \times \mathbf{E} = -j\omega\mu\mathbf{H} \tag{2.17}$$

$$\nabla \times \mathbf{H} = \mathbf{J} + j\omega\epsilon\mathbf{E} \tag{2.18}$$

$$\nabla \cdot \mathbf{E} = \frac{\rho}{\epsilon} \tag{2.19}$$

$$\nabla \cdot \mathbf{H} = 0 \tag{2.20}$$

In a simple source free medium ($\rho = 0$) but with non-negligible conductivity, (2.18) becomes (2.21) and (2.22). This allows the definition of a complex permittivity (2.23) where the complex component is given by (2.24). However, this definition of complex permittivity relies on dipolar relaxation being the sole loss mechanism. Ionic species also move in response to an applied field and dissipate energy via resistive heating. This loss is described by ionic conductivity, σ_d .The effective complex permittivity of medium, ε_e'', (see (2.25)) is then the sum of the ionic conductivity and the conductivity due to dipolar relaxation. This can be stated in terms of an effective conductivity, σ_e , using (2.26).

$$\nabla \times \mathbf{H} = j\omega\left(\epsilon - j\frac{\sigma}{\omega}\right)\mathbf{E} \tag{2.21}$$

$$\nabla \times \mathbf{H} = j\omega\epsilon_{Abs}\mathbf{E} \tag{2.22}$$

$$\epsilon_{Abs} = \varepsilon_0\left(\epsilon' - j\epsilon''\right) \tag{2.23}$$

$$\epsilon'' = \frac{\sigma}{\varepsilon_0\omega} \tag{2.24}$$

$$\varepsilon_e'' = \frac{\sigma_d}{\omega\varepsilon_0} + \varepsilon'' \tag{2.25}$$

$$\sigma_e = \omega\varepsilon_0\varepsilon_e'' \tag{2.26}$$

Similarly an expression for complex permeability can be reached which describes the magnetic properties of a medium.

$$\mu_{Abs} = \mu' - j\mu'' \tag{2.27}$$

The complex permittivity and permeability can be written in terms of the permittivity and permeability of free space (ϵ_0 and μ_0 respectively) as shown in (2.28) and (2.29)

$$\epsilon_{Abs} = \epsilon_r \epsilon_0 \tag{2.28}$$

$$\mu_{Abs} = \mu_r \mu_0 \tag{2.29}$$

The majority of materials have negligible interaction with magnetic fields and have a relative permittivity described by equation (2.30), these materials are also called ‘dielectrics’ as they considered to only interact with electric fields. However, highly conductive non-magnetic materials with free charge carriers can inductively heat when exposed to an oscillating magnetic field. Inductive heating occurs when eddy currents form in the material, energy is then dissipated in the material via resistive heating (also known as Joule or Ohmic heating). Since these materials are highly conducting heating is largely a surface effect. This form of magnetic heating is enhanced by non-negligible magnetic properties via hysteresis although this effect ceases when the material exceeds the Curie temperature at which point the magnetic moments become randomly orientated and the material becomes paramagnetic.

$$\mu_r = 1 - j0 \tag{2.30}$$

Microwave power dissipation in lossy, non-magnetic dielectrics can be modelled as an extension of the equations of a parallel plate capacitor with an applied AC field (2.31). In this equation C is the capacitance of the cell, A is the area of the capacitor plates and d is the distance between the plates. The current, I, flowing through the capacitor is given by Equation (2.32), in which V_c is the voltage across the capacitor and ω is the angular frequency of the applied field.

$$C = \frac{A\epsilon}{d} \tag{2.31}$$

$$I = j\omega C V_c \tag{2.32}$$

$$P_{average} = \frac{1}{2}\Re\left(VI\right) \tag{2.33}$$

In the absence of an imaginary component to permittivity, or dielectric loss factor, ϵ'', the current flowing through the capacitor is out of phase with the voltage across it and therefore no power is dissipated in the capacitor. With the inclusion of the imaginary component, the phase of voltage and current relative to each other can be varied and the equation for power dissipation becomes:

$$P = \frac{\omega\epsilon'' A V^2}{d} \tag{2.34}$$

This can be rewritten as power dissipated per unit volume and in terms of electric field and frequency by using: $E = V/d$.

$$P = 2\pi\epsilon'' f E^2 \tag{2.35}$$

In microwave processing, it is common to express the heating potential of a material as the fraction known as the Loss Tangent (2.36) where the loss angle, δ, is the angle formed by the dielectric constant and loss factor in the complex plane.

$$\tan\delta = \frac{\epsilon''}{\epsilon'} \tag{2.36}$$

Using the equation of heat transfer, combined with the equation for power dissipated in a dielectric, the equation that describes microwave heating rate of a lossy dielectric becomes:

$$\frac{\Delta T}{t} = \frac{2\pi\epsilon'' f E^2}{\rho_m C_p} \tag{2.37}$$

In this equation ρ_m is the bulk density and C_p is the specific heat of the material. From this equation it is apparent that there are a number of properties, other than the dielectric loss factor, that influence the microwave heating of a material.

Another important factor to consider for lossy dielectrics is the decrease in microwave power as the wave propagates into the dielectric. This loss per unit volume is proportional to the power flux density and falls off exponentially. The penetration depth of radiation, also known as the skin-depth, is defined as the distance into a material at which the power flux falls to 1/e of the incident power. The skin-depth can be used to approximate the regions in a medium where heating should or should not occur. The equation for the skin-depth is given by Metaxas (1996) to be:

$$D_p = \frac{1}{2\omega\sqrt{\frac{\mu\epsilon_0\epsilon'}{2}}\sqrt{\left(1+\left(\frac{\epsilon''}{\epsilon'}\right)^2\right)^{0.5}-1}} \qquad (2.38)$$

2.2.3 Microwave Assisted Processing

The development of microwave radiation for use in heating began in the 1940s and has since become widespread in both commercial and domestic settings (Osepchuk 1984). Microwave heating has been widely adopted because it has numerous advantages over conventional heating techniques:

- Microwave heating occurs when electromagnetic energy is dissipated directly in a medium while conventional heating techniques require indirect conduction or convection.
- No physical contact with the target is required for heating.
- Heating can be very rapid depending on the dielectric properties of the target.
- Heating is volumetric – it occurs throughout the bulk of the target as opposed to heat conduction inwards from a surface.
- High power magnetron conversion efficiency 80% at 2.45 GHz and 85% at 915 MHz (Meredith 1998).
- Microwave energy can be safely and easily propagated from source to target through waveguides.

Prior to the advent of microwave heating, the dielectric properties of materials were investigated at radio- (3 kHz – 300 MHz) and microwave-frequencies to support the development of radar and telecommunications (Osepchuk 1984). The first investigation of microwave heating in minerals was carried out by Ford & Pei (1967) with particular interest in the sintering of uranium oxide pellets. Their experiments involved heating powdered metal oxides and sulphides in an 800W 2.45 GHz

stirred oven and found dark coloured materials heated faster than light coloured ones and that ore minerals heated faster than gangue minerals (see Table 2-3). This finding was supported by a later study by Chen et al. (1984) who found that significant heating could be achieved in carbon, metal powders, some metal oxides (such as magnetite and uranite) and sulphides (such as pyrite and chalcopyrite), as well as occasional metal halides, while other minerals, such as quartz, calcite, feldspar, zircon and mica experienced little to no heating.

Table 2-3 – Microwave heating results of selected compounds and minerals (Ford & Pei 1967)

Compound	*Colour*	*Heating Rate (K/s)*
Alumina (Al_2O_3)	White	1.3
Calcium Oxide (CaO)	White	0.1
Charcoal (C)	Black	83.3
Covellite (CuS)	Dark blue	2.0
Haematite (Fe_2O_3)	Red	2.8
Magnetite (Fe_3O_4)	Black	16.7
Troilite (FeS)	Black	2.2
Periclase (MgO)	White	0.5
Molybdenite (MoS_2)	Black	150.0
Uranium Dioxide (UO_2)	Dark green	183.3

As ores are heterogeneous mixtures and can contain any number of different minerals, their interaction with microwaves is particularly interesting. The potential for selectively heating specific minerals within a matrix lends itself to a number of different mineral processing applications. To date, an array of microwave assisted physical or chemical processes have been investigated for application to the minerals sector; these include:

- Comminution (Kingman, Vorster & Rowson 2000; Walkiewicz, Clark & McGill 1991)

- Flotation (Sahyoun et al. 2005)
- Carbothermic Reduction and Smelting (Standish & Pramusanto 1991)
- Drying (Haque 1999)
- Leaching (Kruesi & Frahm 1980)
- Waste processing (Hatton & Pickles 1994; Xia & Pickles 2000)
- Sensor based sorting (Djordjevic 2009; Morrison 2010; Salter, Nordin & Downing 1989; van Weert & Kondos 2007; Wotruba & Riedel 2006)

2.2.3.1 Microwave Assisted Comminution and Liberation

Thermally Assisted Liberation (TAL) has its origins in ancient history; prior to the invention of explosives, thermal shock was used extensively to fracture rock (Fitzgibbon & Veasey 1990). Thermal stress occurs when rapid changes in temperature, coupled with low thermal conductivity and high coefficients of expansion, cause regions of a matrix to expand and contract at different rates; if the thermal stress exceeds the strength of the matrix it fractures. This effect is magnified by the heterogeneous nature of rocks and the different thermal properties of the component minerals. Sufficient thermal stress induces fractures and micro-cracking which weakens the surrounding matrix and which in turn reduces the work index. In recent times TAL has been investigated as a way to reduce the work index and fines production of ores in grinding but heating by conventional methods was uneconomic (Fitzgibbon & Veasey 1990).

The application of microwave roasting to ores to induce TAL (Walkiewicz, Clark & McGill 1991) followed earlier work by the US Bureau of Mines characterizing the microwave properties of minerals and compounds (Walkiewicz, Kazonich & McGill 1988). It was found that microwave energy selectively heated minerals in heterogeneous rock matrices and created thermal stresses at grain boundaries; the resulting fractures appeared to follow grain boundaries (Kingman, Vorster & Rowson 2000; Walkiewicz, Clark & McGill 1991; Williamson, Salsman & Tolley 1994).

There have been mixed results from research into liberation and micro-cracking in microwave treated ores. Orumwense & Negeri found no improvement in liberation and that microwave treatment did not necessarily mean preferential inter-granular breakage (2004). It was concluded that there is a different optimal pre-treatment condition for each ore and that excessive microwave exposure may harm liberation (Orumwense & Negeri 2004). These conclusions are supported by research by Kingman et al. (2004) and Rizmanoski (2011) who used high power, short duration microwave exposures, as opposed to longer duration roasting techniques, to find that significant improvements in liberation and strength reduction were achievable.

Initial investigations of microwave assisted comminution focussed entirely on strength reduction and found that microwave roasting did not produce a cost-effective reduction in work index (Walkiewicz, Clark & McGill 1991). Recent investigations have determined that cost-effective weakening and increased liberation may be achieved using short duration, high power density microwave pulses (Bradshaw et al. 2007; KingmanJacksonBradshaw, et al. 2004; Salsman et al. 1996). However, Walkiewicz, Clark and McGill (1991) argue that simple comparisons of applied microwave energy to the reduction in work index do not account for potential downstream benefits which may be achieved from improvements in liberation and grindability. Potential downstream benefits to microwave-assisted ore processing could include increased metal recovery in flotation or leaching processes, a topic discussed in the next section, as well as increased lifetimes for grinding media and mill liners. This means that, while microwave-assisted comminution may add to the processing cost per ton of ore, more effective metal recovery, lower costs for grinding media and less frequent downtime to replace mill liners may result in a net positive outcome.

2.2.3.2 Flotation and Hydrometallurgy

For some processes downstream of comminution, the effect of microwave pre-treatment on flotation and leaching performance has been studied extensively as small changes in the chemical and physical properties of ores due can have a significant impact on metal recovery. To date, the

results of microwave treatment are mixed and have been found to depend on the ore and treatment scheme applied.

Initial flotation tests found no discernible impact on copper recovery due to microwave pre-treatment (Vorster, Rowson & Kingman 2001). This was followed by results showing a negative effect on flotation recovery for a number of different ores which increased with exposure time (Orumwense & Negeri 2004). In the same year another study (KingmanJacksonCumbane, et al. 2004) found that high-power, short duration exposures could lead to improvements in liberation and lead to work by Sahyoun et al. (2005) showing improved flotation rates and product quality.

More recently it has been found that microwave treatment accelerated the oxidation rate on sulphide grain surfaces (Can & Bayraktar 2007). This change in surface chemistry depressed recovery of chalcopyrite, pyrite and galena and consequently degraded flotation performance (Can & Bayraktar 2007; Orumwense & Negeri 2004). Short, high-intensity exposures maximize the internal thermal stresses while simultaneously limiting the time sulphide minerals spend at elevated temperatures. Chemical changes are not necessarily negative, as oxidized pyrite and chalcopyrite have increased magnetic susceptibility and introduces the possibility of magnetic separation (Can & Bayraktar 2007).

Al-Harahsheh & Kingman (2004) comprehensively reviewed the state of microwave assisted leaching. Hydrometallurgy, when compared to pyrometallurgy, has lower recovery, solid-liquid separation issues and impurity problems (Al-Harahsheh & Kingman 2004). The application of microwave technology may be a route improving hydrometallurgical yield and reducing processing time (Al-Harahsheh & Kingman 2004). Despite its shortfalls hydrometallurgy remains an attractive route to research for economic and environmental reasons. Al-Harahsheh & Kingman's review (2004) found that despite over 70 papers on the subject, some showing definite improvements to leaching kinetics, there were no real industrial applications forthcoming.

The majority of research is focussed on microwave pre-treatment, usually in air, followed by normal leaching procedures (Al-Harahsheh & Kingman 2004). Some techniques involve microwave roasting of ores mixed with concentrated acids under varying atmospheres (such as air, chlorine, or nitrogen) then cooling and leaching with different solutions (such as water, brine, or ammonia); others use microwave heating to improve the reaction kinetics while leaching. This has resulted in numerous explanations to justify improvements due to microwaves which may belie an lack of understanding (Al-Harahsheh & Kingman 2004).

It is believed that key issues need to be overcome before microwave assisted leaching can be an effective industrial process (Al-Harahsheh & Kingman 2004). These issues include: accurate in-situ temperature measurement, optimised reactor design, and lack of knowledge regarding the interaction between microwave radiation and highly ionic mixtures.

2.2.3.3 Sorting

As mentioned in Section 2.1.1, the renewed interest in sorting technologies has recently recognised microwave radiation as a potential method of recognizing valuable particles. The first application of microwaves to sort minerals measured microwave absorption to discriminate between gabbro and diamond-bearing kimberlite (Mercer et al. 1988; Salter, Nordin & Downing 1989). Later, Cutmore et al. (1997) used data from a network analyser and dielectric probe to train an artificial neural network (ANN). Once trained, the ANN was capable determining the grade of iron ore samples (Cutmore, N.G., Liu & Middleton 1997). However, this work was limited by the measurement technique – it required samples to be finely ground (<200 μm) and then pressed into a block.

More recently, the combination of microwave heating and thermal-IR measurement is mentioned as being studied at RTWH, Aachen, Germany (Wotruba & Riedel 2006). However, there do not appear to have been any further publications by them on the subject. Initial experiments by Van Weert and colleagues using microwave heating and thermal-IR detection have tentatively found potential in open pit mineable vein and stockwork sulphide deposits (van Weert & Kondos 2007;

van Weert, Kondos & Gluck 2009). While patents regarding various microwave sorting techniques have been issues to the University of Queensland (Djordjevic 2009; Djordjevic & Adair 2010; Morrison 2010) .

2.2.4 Conclusion

A number of potential microwave processing technologies are being researched for use in the mineral processing sector. These technologies offer potential for economically significant improvements in the efficiency of operations while reducing the total energy consumed and the environmental impact of mining and processing and in some cases can substantially increase the size of deposits. To date investigations into microwave technologies have shown promising results for the minerals industry but have not reached the stage where they are economical processes. The combination of Microwave/IR imaging and sorting is an emerging technology and warrants further investigation.

2.3 Dielectric Measurement Techniques

There are many ways to measure the dielectric properties of materials. The most appropriate measurement technique is generally defined by the frequency range of interest and the sample dimensions, as well as the physical phase and dielectric properties of the material. Dielectric measurement techniques can be grouped into resonant and non-resonant methods, the former are restricted to discrete frequencies while the latter are broadband but less accurate (Chen, LF et al. 2004). Measurements at microwave frequencies can be a challenging problem given the wavelength is comparable to the dimensions of the components and diffraction effects become non-negligible (Donovan et al. 1993).

When wavelengths are much longer than the system the lumped equivalent circuit model is used. In this model, the system is represented by a simple circuit with discrete elements (resistors, capacitors and inductors) and measurements are conducted using LCR (inductance, capacitance, resistance)

meters and capacitor-style cells. As the wavelength shortens, and frequency increase, errors are introduced by stray capacitance and residual inductance. When wavelengths are smaller than the size of components, the distributed element model is used; in this model the system is represented by continuous distribution of circuit elements and measurements are performed in terms of scattering parameters.

2.3.1 Non-resonant Techniques

Non-resonant methods measure electromagnetic properties of materials via changes in impedance (Roberts & von Hippel 1946). Transmission lines, such as coaxial lines or rectangular waveguides, are used to deliver a probe wave to the test samples and to deliver the reflected and transmitted waves to the detector (Roberts & von Hippel 1946). The maximum operational frequency range is therefore defined by the working frequency of the transmission line used. Non-resonant techniques are broken into reflection and transmission/reflection techniques based on the return signal utilized.

2.3.1.1 Reflection methods

Reflection methods are one-port techniques which measure changes in the properties of the wave reflected back along the transmission line. The experimental apparatus for these techniques can be simplified to a length of transmission line that terminates in either a short- or open- circuit (see Figure 2-6). The short-circuit technique has been used to measure both permittivity and permeability, while the open-circuit technique is used to measure permittivity of low- to medium-conductivity materials (Chen, LF et al. 2004). The open-circuit reflection method is also useful for measuring the surface impedance of high-conductivity materials (Chen, LF et al. 2004).

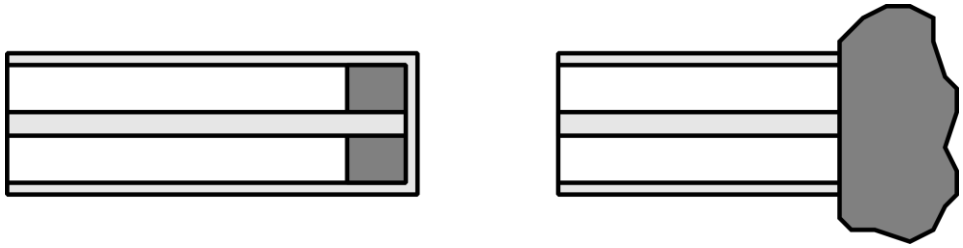

Figure 2-6 – Coaxial short-circuit (left) and open-circuit (right) reflection methods after Chen, LF et al. (2004)

The open-circuit transmission line method, commonly referred to as a dielectric probe, is a popular and versatile measurement technique capable of non-destructively testing solids, semi-solids and liquids (Burdette, Cain & Seals 1980). When a material is brought into contact with the probe head the fringing fields are altered by the dielectric properties of the sample which consequently alters the impedance of the coaxial line. The change in impedance can be observed as a change in the reflection coefficient which is then used to calculate the dielectric properties of the sample (Grant et al. 1989). For ease of measurement it is usually assumed that the sample is non-magnetic and that the change in impedance due to the sample is entirely due to the dielectric properties (Chen, LF et al. 2004; Grant et al. 1989). There are several models for calculation; the simple capacitative model assumes that the sample is sufficiently thick to contain the fringing fields; however at high frequencies the field may radiate out through the sample and require a more nuanced model (Clarke, R N et al. 2003).

Coaxial probes have been used previously for minerals processing research; the US Bureau of Mines (USBM) measured the dielectric properties of minerals and more recently Cutmore et al. (1997) used coaxial probe measurements to deduce mineralogical composition. To accomplish this, Cutmore et al. (1997) trained a set of neural networks to recognise different grades of pressed-powder iron ore samples with accuracy greater than 85% from coaxial probe measurements. Their research was presented as progress towards on-line sorting of gangue and ore particles from a feed stream; however, they concluded that the coaxial probe was an inappropriate measurement technique for the application (Cutmore, N.G., Liu & Middleton 1997). The coaxial probe technique is inappropriate in an industrial setting because it requires samples with very flat surfaces to achieve good electrical contact across the entire probe surface and careful calibration which cannot be achieved in mechanically and electrically noisy environments.

Short-circuit measurements of dielectric properties were pioneered by Roberts & von Hippel (1946). Their technique used measurements of the voltage standing wave ratio (VSWR) in the transmission line from which to calculate dielectric properties. More recently, the short-circuit technique has been adapted to calculate magnetic properties from the scattering parameter S_{11} (Fannin, Relihan & Charles 1995). The boundary condition at the end of the short-circuited line defines the position of electric and magnetic field maxima. Consequently the distance between the sample and the short can play an important role in which property is measured (Chen, LF et al. 2004).

2.3.1.2 Transmission/Reflection Methods

Transmission line measurements developed from reflection methods when the advent of modern network analysers made two-port measurements more accessible (Baker-Jarvis, Vanzura & Kissick 1990). This technique can be broadband (100 MHz to 20 GHz) and be used to calculate both the dielectric and magnetic properties of samples simultaneously (ASTM 2008). They are an effective broadband measurement technique suitable for medium- to high-loss materials and although capable of measuring the permittivity of low loss dielectrics, this technique is not suitable for measuring the loss factor when $\tan\delta < 0.05$ (Clarke, R N et al. 2003). A standardized approach to this measurement technique can be found in ASTM D5568-08, which details the transmission/reflection measurements of solids in a rectangular waveguide (ASTM 2008).

The physical apparatus of the transmission/reflection method is relatively simple; a tightly fitting sample is placed in a section of waveguide, both ends of which are coupled to a network analyser (see Figure 2-7). Depending on the complexity of the measurement and the calculation algorithm, the data used ranges from a transmission measurement (S_{21}) to a full two-port scattering parameter set (S_{11}, S_{22}, S_{21}, S_{12}) (ASTM 2008). High precision sample machining is required to minimize the size of air-gaps between the sample and the transmission line walls. Air gaps reduce the measured electromagnetic properties, and at higher frequencies may cause significant error by launching high order modes (Vanzura et al. 1994). Samples for use in rectangular waveguides are easier to

manufacture than for coaxial lines, however, the working frequency range is not as large (Clarke, R N et al. 2003).

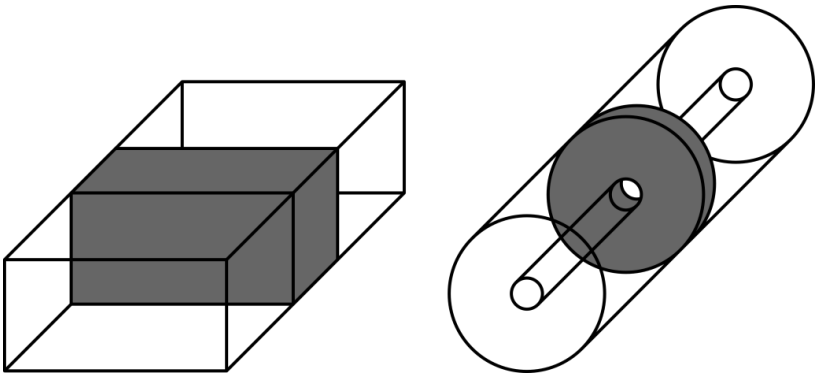

Figure 2-7 – Waveguide (left) and coaxial (right) transmission line elements

There are two main methods for calculating electromagnetic properties from a transmission/reflection measurement; the explicit solution and iterative algorithms. The explicit solution fails when the sample length is an integer number of half-wavelengths due to numerical instability caused by large uncertainties in phase (ASTM 2008). The sample length, volume and position are also sources of uncertainty in the explicit solution. Iterative algorithms were subsequently developed by Baker-Jarvis, Vanzura and Kissick (1990) to provide more stable solutions. This work produced a number of different combinations of iterative equations for solving dielectric properties that were stable for samples with lengths equal to an integer numbers of half-wavelengths (Baker-Jarvis, Vanzura & Kissick 1990). By selecting different combinations of equations, solutions were possible with or without knowledge of sample position or size.

2.3.2 Resonant Techniques

There are many varieties of resonant dielectric measurement at microwave frequencies including closed cavity resonators, open resonators and dielectric resonators. Central to this style of measurement are the changes in standing waves formed within the resonator. Consequently measurements are restricted to those resonant modes.

2.3.2.1 Cavity Perturbation

Closed cavity perturbation measurements are an established and versatile technique for measuring electromagnetic properties at microwave frequencies. Perturbation theory was first considered in terms of small deformations of the cavity boundaries by Bethe and Schwinger (1943), and later extended to the case of a small body impinging on the cavity by Casimir (1951). Cavity perturbations experiments were reported by Waldron (1956) and Spencer et al. (1956) who calculated permeability and permittivity from the changes in cavity resonant frequency and quality factor due to the test material. The cavity may be completely or partially filled by the sample but does not require physical contact and has been used to measure properties at elevated temperatures. An outline of the design and measurement procedure for a rectangular waveguide based cavity was formalized by the standards organization ASTM International (ASTM 2001) but was withdrawn in 2010. The withdrawal of this standard was in accordance with ASTM regulations which require standards to be withdrawn if they are not updated within eight years of last approval.

Cavities are typically either cylindrical or rectangular for both ease of manufacturing and easily understood resonant modes (Donovan et al. 1993). Rectangular cavities commonly use the Transverse Electric (TE) mode, which has no electric field components in the direction of propagation; whereas cylindrical cavities commonly use either Transverse Magnetic (TM), which has no magnetic components in the direction of propagation, or TE modes (ASTM 2001; Chen, L, Ong & Tan 1996; Donovan et al. 1993; Hutcheon, de Jong & Adams 1992). Closed cavities are most commonly used in the high MHz and low GHz regions of the microwave spectrum, as cavity sizes become inconveniently large at lower frequencies and small at higher frequencies (Clarke, R N et al. 2003).

In the simplest sense, a closed cavity resonator is a void bounded by conductive walls which confine electromagnetic fields. The boundary conditions imposed by the dimensions and geometry of the cavity only permit specific resonant modes (which correspond to standing waves) to exist within (Waldron 1960). When an object with different electromagnetic properties is introduced into

the cavity, it perturbs the standing waves and shifts the resonant frequency. The positioning of the sample in the cavity determines the property measured: electric, magnetic, a mixture thereof. To measure the dielectric properties the sample is positioned in the standing waves at an electric field anti-node, where the electric field amplitude is greatest; this location is also a magnetic field node, where the magnetic field is smallest. Similarly magnetic properties are measured at a magnetic field anti-node which is also an electric field node.

The object also increases the energy loss rate in the cavity which can be deduced from the quality factor (Q) of the cavity. Q is a dimensionless parameter determined from the ratio of the energy stored at the resonant frequency, W, and the energy dissipated in a single period of that frequency, L (Klein et al. 1993). Q may also be expressed as ratio of resonant frequency, f_r, and bandwidth, Δf_r, as defined by the full-width half maximum (see Equation (2.39)) (Klein et al. 1993). Cavities with high Q-factors are desirable for their higher sensitivity because small changes in bandwidth are easier to resolve with steeper gradients of forward energy loss (S_{21}) in frequency (Donovan et al. 1993). Additionally, the narrower bandwidths of high Q cavities are desirable because the loss due the insertion of a sample constitutes a larger proportion of the overall cavity losses. Klein et al. (1993) state that measurement cavities should have a Q-factor on the order of 10^4 while ASTM 2520-01 requires Q-factors exceeding 2000 (ASTM 2001).

$$Q = \frac{f_r}{\Delta f_r} = \frac{\omega_0 W}{L} \tag{2.39}$$

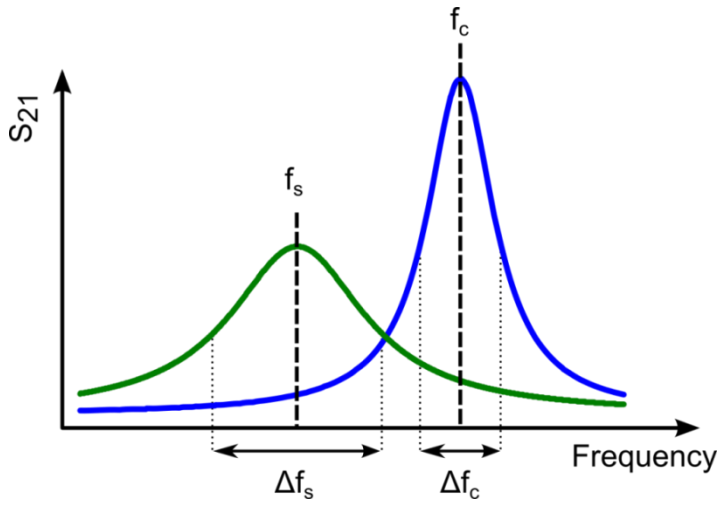

Figure 2-8 – Perturbation measurement of an unloaded (blue, f1 and Δf1) and loaded (green, f2 and Δf2) cavity after Clarke, R N et al. (2003).

For each calculation of dielectric properties two sets of two parameters are required: the resonant frequency and Q of the cavity both when empty and when loaded with a sample. These values are obtained by measuring the transmitted power, S_{21}, over a range of frequencies and generating a power absorption spectrum (see Figure 2-8). For small samples at an electric field anti-node, the dielectric properties may then be calculated using Equations (2.40) and (2.41) (Chen, LF et al. 2004). Equations for a cylindrical TM_{010} cavity perturbed by a prolate ellipsoid were reported by Parkash, Vaid and Mansingh (1979) who followed the of theory Waldron (1960) (see Equations (2.42) and (2.43)). Additionally, due to the nature of Bessel Functions, these equations can be applied to higher order TM_{0n0} modes which also have axially aligned electric field maxima at the centre of the cavity.

A perturbing body can be considered discontinuity in the space where a uniform electric field would have existed. The changes in the electric field both in and around the perturber are due to its geometry and dielectric properties. The changes in electric field can be expressed as a depolarization field which is a correction to the externally applied field, similar to the electric displacement field discussed previously (see Section 2.2.2). Generally the field in a perturbing body is not uniform; however, most analyses of resonant cavity perturbation approximate the perturber as

an ellipsoid. Ellipsoidal shapes are a special case in which the field internal field is uniform and consequently simplify calculations (Klein et al. 1993). A depolarization factor, N_e, describing the geometry of the perturber is still required; in the case of a cylindrical TM_{010} cavity it is governed by the ratio of the perturbers radius to its height as well as the ratio of perturber height to cavity height (Parkash, Vaid and Mansingh 1979). The assumption that the perturber is thin or the same height as the cavity means that the depolarisation factor becomes negligible and leaves equations (2.44) and (2.45).

$$\epsilon' = A\frac{V_c}{V_s}\frac{\delta f}{f_c} + 1 \tag{2.40}$$

$$\epsilon'' = B\frac{V_c}{V_s}\left(\frac{1}{Q_s} - \frac{1}{Q_c}\right) \tag{2.41}$$

$$\epsilon' = \frac{V_c\frac{\delta f}{f_c}\left[\frac{V_s}{2J_1^2(ka)} - N_eV_c\frac{\delta f}{f_c}\right] - N_eV_c^{\,2}\left[\frac{1}{2}\left(\frac{1}{Q_s} - \frac{1}{Q_c}\right)\right]^2}{\left[\frac{V_s}{2J_1^2(ka)} - N_eV_c\frac{\delta f}{f_c}\right]^2 + \left[\frac{N_eV_c}{2}\left(\frac{1}{Q_s} - \frac{1}{Q_c}\right)\right]^2} + 1 \tag{2.42}$$

$$\epsilon'' = \frac{\frac{V_c}{2}\left(\frac{1}{Q_s} - \frac{1}{Q_c}\right)\left[\frac{V_s}{2J_1^2(ka)} - N_eV_c\frac{\delta f}{f_c}\right] + N_eV_c^{\,2}\frac{\delta f}{f_c}\left[\frac{1}{2}\left(\frac{1}{Q_s} - \frac{1}{Q_c}\right)\right]^2}{\left[\frac{V_s}{2J_1^2(ka)} - N_eV_c\frac{\delta f}{f_c}\right]^2 + \left[\frac{N_eV_c}{2}\left(\frac{1}{Q_s} - \frac{1}{Q_c}\right)\right]^2} \tag{2.43}$$

$$\epsilon' = 2J_1^2(ka)\frac{V_c\delta f}{V_s f_c} + 1 \tag{2.44}$$

$$\epsilon'' = J_1^2(ka)\frac{V_c}{V_s}\left(\frac{1}{Q_s} - \frac{1}{Q_c}\right) \tag{2.45}$$

Where:

- V_c and V_s are the volume of the cavity and sample respectively.
- f_c and f_s are the resonant frequencies of the cavity when empty and loaded with a sample respectively and $\delta f = f_c - f_s$.
- Q_c and Q_s are the quality factors of the empty and sample-loaded cavities respectively.
- N_e is a depolarizing factor governed by the dimensions of the prolate ellipsoid, and its height relative to the height of the cavity (Parkash, Vaid & Mansingh 1979).
- $J_1(ka)$ is a first-order Bessel function describing the field in the cavity. See Section 8.3.4 of the Appendix for numerical solutions of when electric field boundary conditions demand zero field at the walls and consequently $J_0(ka) = 0$ (Parkash, Vaid & Mansingh 1979).
- A and B are factors governed by the working mode of the cavity, shape of the cavity and the sample, as well as the location of the sample within the cavity – they are typically determined by calibration (Chen, LF et al. 2004). ASTM D2520 provides equations to solve for the dielectric properties of numerous different sample geometries within a rectangular waveguide cavity (see Section 8.1.1 of the Appendix) (ASTM 2001).

The equations for calculating the magnetic properties of a small sample at a magnetic field anti-node are identical to those for calculating dielectric properties (see Equation (2.46) and (2.47). The magnetic properties can potentially be measured using the same resonant mode as those used for dielectric measurements as long as the sample can be placed in the magnetic field maxima. Selection of the appropriate resonant mode for magnetic property measurement depends on the cavity size & shape, the measurement frequency desired and the accessibility of the relevant magnetic field maxima.

$$\mu' = \frac{V_c \left(f_c - f \right)_s}{A V_s f_s} + 1 \tag{2.46}$$

$$\mu'' = \frac{V_c}{B V_s} \left(\frac{1}{Q_s} - \frac{1}{Q_c} \right) \tag{2.47}$$

The small sample condition requires that the object inserted into the cavity must be small with respect to the volume of the cavity and the spatial variation of the resonant field. This condition prevents cavity mode hops, allows the assumption of quasi-static limit, and ensures that the samples are not multiple skin-depths thick (Klein et al. 1993; Landau & Lifschitz 1984). In general, resonant perturbation techniques have a high degree of accuracy; however, there are sources of uncertainty in these methods:

- Wall losses decrease the cavity Q and consequently increase the uncertainty of bandwidth measurements. The wall losses are controlled by the surface area to volume ratio of the cavity hence cylindrical cavities have higher Q in comparison to rectangular waveguide cavities (Donovan et al. 1993).
- Uncertainty due to electrical noise and digitization error (Clarke, R N et al. 2003).
- Assumption in perturbation calculations include of first order perturbation (homogeneous, isotropic perturber, small perturbation, constant field within the perturber) and neglect of high-field effects (Carter 2001; Klein et al. 1993; Waldron 1960). Therefore sample properties such as particle shape or the size distribution and packing density of powder samples add uncertainty to measurements. An alternative to perturbation calculations can be obtained through computer-based numerical analysis of cavities (Adams, de Jong & Hutcheon 1992).
- Uncertainty in the dimensions and volume of both the sample and cavity due to effects such as measurement error or thermal drift (Dressel et al. 1993).

2.3.2.2 Other Resonant Techniques

2.3.2.2.1 Open Resonators

At the millimetre end of the microwave spectrum closed cavity resonators become impractically small and open resonators are used instead. Open resonators are formed when two reflectors are arranged to support a standing wave between them; in optical spectroscopy this is known as a Fabry-Perot interferometer (Clarke, R. N. & Rosenburg 1982) and has numerous uses including laser resonators, dichroic filters, and frequency references. When the reflectors are correctly aligned, the standing waves operate in the transverse electromagnetic mode TEM_{00n} , in which neither the electric nor the magnetic fields have components in the direction of propagation (Jones, RG 1976). This technique is suitable for thin-sheet specimens which have a diameter larger than the beam waist and a thickness smaller than a half wavelength in the medium.

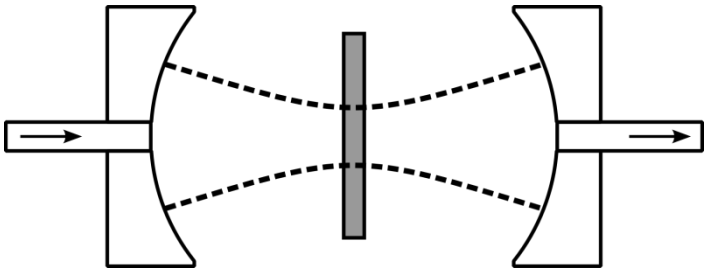

Figure 2-9 – Conceptual diagram of an open resonator measurement with a sample centred between two reflectors

2.3.2.2.2 Dielectric Resonators

In the dielectric resonator technique a well-machined sample forms the resonator and dielectric properties are calculated from the properties of the resonant frequency and Q-factor. Electromagnetic fields are coupled into and out of dielectric resonators by use of the evanescent field. Well-machined, puck shaped resonators, in conjunction with numerical modelling, are potentially the best way of measuring the dielectric properties of low-loss materials in a both highly

sensitive and accurate manner. This technique is capable of operating at lower frequencies than cavity perturbation techniques of comparable size because the dielectric properties of the resonator shorten the effective wavelength of the field. The split-post resonator method is an adaption of dielectric resonator measurements. In this technique, thin sheet samples are placed between two identical cylindrical dielectric resonators and dielectric properties are calculated from changes in the resonant frequency and Q-factor of the system (see Figure 2-10) (Krupka et al. 2001).

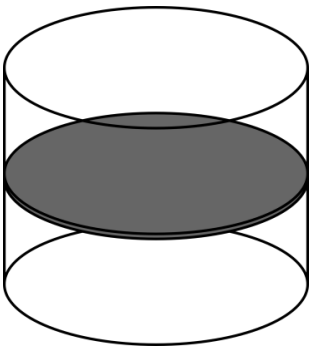

Figure 2-10 – Conceptual arrangement of resonators in a split-post resonator experiment

2.3.3 Conclusion

Dielectric measurement techniques are diverse and it is important to select the measurement technique appropriate for the application. Non-resonant techniques provide broadband ways to quickly characterize dielectric properties while resonant techniques accurate and capable of measuring the properties of low-loss minerals, such as quartz. Additionally, all the measurement techniques surveyed produce values assuming a homogeneous sample and struggle with heterogeneous samples.

2.4 Microwave Characterization of Minerals

To date, data on the electrical properties of minerals at microwave frequencies is sparse but growing, and interest at these frequencies has largely centred on the application of microwave

heating technology. For this reason many investigations have concerned themselves with characterizing the microwave heating rates of broad sets of minerals without addressing the dielectric properties, the variability within a mineral species, or the nature of the charge carriers which form dipoles in response to the applied field. Other investigations have examined the dielectric properties of specific minerals and focused on the conduction mechanisms responsible (Davidson & Yoffe 1965, 1968; Husk & Seehra 1978; Meunier et al. 1983; Pridmore & Shuey 1976).

In order to apply a selective microwave heating process to ores, a basis for the selective heating is needed and to establish this, an understanding of the relative dielectric properties of both the valuable minerals and the gangue matrix is required. In a sorting application, the assumption is that valuable minerals heat preferentially in a microwave field. However, if there is an incomplete understanding of the dielectric properties of minerals in the gangue matrix, there is a chance that a moderately lossy gangue mineral could negate any potential benefits in sorting. The variability of mineral dielectric properties and the way in which the dielectric properties mix together to form a heterogeneous solid also need to be addressed.

One of the first investigations into microwave heating in minerals was by Ford & Pei (1967). They exposed ten different mineral species in a (2.45 GHz) multimode oven and measured sample heating with an infrared thermometer. It was found that oxides and sulphides of metals heated easily and that dark coloured minerals heated faster than light coloured ones (See Section 2.2.3, Table 2-3). Later, a more quantitative study of microwave (2.45 GHz) heating rates and reaction products was performed by Chen et al. (1984) which reinforces the work of Ford & Pei (1967) in finding that ore minerals heat readily while gangue minerals do not (see Section 8.2, Table 8-4 of the Appendix). This investigation involved microwave heating of 45 different minerals species in a single mode applicator whilst recording forward and reflected power and infrared measurements of temperature. However, the authors refrained from publishing temperature data citing inaccuracies in the infrared camera technique (Chen, TT et al. 1984). Crucially, the research of Chen et al. (1984) recognizes the role of chemical composition in heating variability, such as the role of iron in heating sphalerite.

The now defunct US Bureau of Mines (USBM) investigated both the heating rate and dielectric properties of minerals at microwave frequencies between 1988 and its closure in 1996. The work began with microwave heating experiments by Walkiewicz et al. (1988), which built upon the work of Ford & Pei (1967) and Chen et al. (1984), and was complemented by the filled coaxial waveguides measurements of Church et al. (1988) in measuring dielectric properties. Walkiewicz et al. (1988) demonstrated that, despite considerable spread in heating rates, ore minerals almost always heated faster in microwave fields than gangue minerals (see Section 8.2, Table 8-7 of the Appendix). Furthermore, the work of Walkiewicz et al. (1988) identified that microwave radiation selectively heated ore minerals in a gangue matrix and lead to stress cracking which was investigated further as a route to an economic thermally assisted liberation process.

Church et al. (1988) characterized the dielectric properties of many low-loss minerals at microwave frequencies (300 MHz to 1 GHz) using a filled coaxial waveguide technique (see Table 2-4) and estimated their uncertainty to be less than 3%. This work was followed by that of Nelson et al. (1989), who measured the dielectric properties of ten minerals they considered to be important constituents of ore (see Table 2-5). Nelson et al. (1989) used a short-circuited waveguide technique between 1 to 22 GHz to measure the dielectric properties of pulverized samples at a range of densities. They then applied the Landau-Lifschitz-Looyenga mixing equation (discussed further in Section 2.5 below) to calculate the dielectric properties of the solid mineral. They observed that the dielectric properties of Salite and Goethite were almost independent of frequency, while Hollandite peaked between 2.45 and 11.7 MHz, and all other minerals moderately to significantly decrease with increasing frequency (Nelson, Lindroth & Blake 1989). This means that while constrained to ISM bands, frequency is an important consideration when attempting to optimize a selective heating process. Both Church et al. (1988) and Nelson et al (1989) use the relationship $\sigma = f_0 \omega \varepsilon''$ when linking conductivity to the dielectric loss factor.

Table 2-4 – Electrical properties of minerals at 915 MHz after Church et al (1988)

Mineral	ϵ'	$\epsilon''(10^{-3})$	*Mineral*	ϵ'	$\epsilon''(10^{-3})$
Anhydrite	6.27	0.61	Magnesite	6.61	1.04
Apatite	9.39	0.65	Malachite	6.65	1.44
Aragonite	8.18	0.98	Monazite	12.34	1.47
Barite	9.48	1.01	Muscovite	4.23	0.76
Bauxite	6.4	1.62	Nephelene	6.71	0.54
Beryl	6.38	1.21	Orthoclase	4.34	0.19
Biotite	5.61	0.59	Periclase	9.45	0.43
Calcite	8.91	0.42	Pollucite	5.95	0.87
Celestite	11.23	0.55	Quartz	3.94	0.63
Cerussite	22.98	10.50	Rhodochrosite	8.26	5.79
Chromite	11.22	1.83	Scheelite	10.69	1.41
Columbite	25.24	15.60	Sericite	6.08	1.00
Corundum	9.81	0.72	Siderite	7.1	1.90
Cryolite	6.33	2.60	Smithsonite	9.58	2.06
Dolomite	7.26	3.14	Sphalerite	9.66	7.11
Fluorite	6.58	0.48	Spodumene	6.95	0.92
Goethite	9.6	4.63	Tourmaline	5.29	0.54
Halite	4.83	0.44	Witherite	7.01	3.03
Kyanite	8.65	0.33	Wolframite	15.53	3.88
Lepidolite	4.95	1.17			

Table 2-5 – Dielectric Properties of Solid Minerals at 2.45 GHz (Nelson, Lindroth & Blake 1989)

Mineral	ϵ'	ϵ''
Richterite	7.37 ± 0.06	0.026 ± 0.009
Clinochlore	7.06 ± 0.04	0.137 ± 0.019
Labradorite	6.01 ± 0.14	0.090 ± 0.042
Muscovite	8.69 ± 0.12	0.091 ± 0.009
Phlogopite	9.77 ± 0.39	0.14 ± 0.04
Salite	7.18 ± 0.04	0.17 ± 0.01
Goethite	13.6 ± 0.3	0.38 ± 0.01
Hematite	18.3 ± 0.2	2.23 ± 0.17
Ilmenite	23.6 ± 0.8	11.2 ± 0.4
Hollandite	61.9 ± 9.3	10.7 ± 1.1

Holderfield & Salsman (1992) extended the works of Church et al. (1988) and Nelson et al. (1989) to measuring the dielectric properties of more conductive minerals (such as bornite, chalcocite and galena) and unsuccessfully attempted to correlate dielectric properties of minerals with the crystallographic structure (see Appendix Section 8.2, Table 8-4). Differences in the bonds between atoms in a crystalline structure affect how easy or hard it is for charge carriers to move in each direction. This results in dielectric anisotropy whereby the effective dielectric properties of a crystal depend on its orientation with respect to an applied field.

An example of crystalline anisotropy at low frequencies can be found in the work of Rüscher & Gall (Rüscher & Gall 1995, 1997). These authors measured the conductivity of natural biotite and vermiculite both perpendicular ($E\perp(001)$) and parallel ($E\parallel(001)$) to the sheet structure between 0.1 kHz and 1 MHz (Rüscher & Gall 1995, 1997) and also characterized the chemical composition of the samples using an electron microprobe. The work was inspired by debate in literature regarding

the scale of changes in anisotropy as a result of increasing the iron to magnesium ratio. Some groups claimed up to four orders of magnitude difference between $E_{\perp}(001)$ and $E_{\parallel}(001)$, while the data of others could not support anisotropy more than a factor of three (Crine et al. 1977; Meunier et al. 1983; Rüscher & Gall 1995; Tolland & Strens 1972). Despite their disagreement regarding the magnitude of anisotropy, there was agreement regarding the link between conductivity and iron concentration (Crine et al. 1977; Rüscher & Gall 1995).

Table 2-6 – Dielectric Properties of Chalcopyrite and Chalcocite at 915 and 2450 MHz after Salsman (1991)

Frequency:	*915 MHz*		*2450 MHz*	
Mineral	ϵ'	ϵ''	ϵ'	ϵ''
Chalcopyrite	13.1	11.5	11.0	7.7
Chalcocite	17.2	1.1	16.8	1.6

Table 2-7 – Dielectric Properties of minerals at 915 and 2450 MHz after Salsman and Holderfield (1994)

Frequency:	*915 MHz*		*2450 MHz*	
Mineral	ϵ'	ϵ''	ϵ'	ϵ''
Chalcopyrite	84.8	70.5	60.6	28.2
Chalcocite	245.4	94.3	189.8	42.5
Cobaltite	27.2	2.6	28.3	0.1

Further work published by the USBM, such as Salsman (1991) and Salsman & Holderfield (1994), present dielectric properties of chalcopyrite and chalcocite (among other minerals). In these two publications (see Table 2-6 and Table 2-7) there are large differences in the magnitude of the dielectric properties, which are not expounded by the authors. Some potential reasons for the differences in Table 2-6 and Table 2-7 can be found in the work of Xiao (1990), who used the resonant cavity perturbation method to measure the properties of hundreds of rock and mineral samples at 9.37 GHz. Xiao (1985) lists many complicating and inter-relating factors that may

influence dielectric properties of minerals, including: electromagnetic frequency, composition, texture, moisture, temperature, pressure, density, porosity, geological occurrence and metamorphic degree. Although the study does not address all the factors above, Xiao (1990) does reach a number of important conclusions:

- In both extrusive and intrusive magmatic rocks-types the dielectric properties decrease from ultrabasic through basic and intermediate to acidic (Xiao 1990). (see Appendix Section 8.2,)
- Dielectric properties of magmatic rocks decreased with increasing silicon, potassium, sodium; and increased with increasing iron, manganese, titanium and calcium (Xiao 1990). (see Appendix Section 8.2, Table 8-8)
- Dielectric properties in sedimentary and metamorphic rocks-type vary in a similar but more complex manner than the magmatic types because they have the added factors of metamorphic condition and sedimentary environment (Xiao 1990). (see Appendix Section 8.2, Table 8-9)
- There appeared to be no effect on dielectric properties due to structural water, however, the effect of adsorbed water varied depending on the thickness of the adsorbed layer (Xiao 1990). (see Appendix Section 8.2, Table 8-10)

These conclusions aid in the understanding of microwave heating of ores and particularly in identifying rock-types that may give the best selective heating. Xiao (1990) identifies several elements, including iron (as observed by Chen et al. (1984) in sphalerite), that typically increase the dielectric properties of rocks and hence raise the average heating rates.

At much lower frequencies (100 Hz to 1 MHz) water can have a significant effect on the properties of minerals, however at microwave frequencies the effect of water is more nuanced (Rüscher & Gall 1997; Wang & Schmugge 1980). The effect of adsorbed water at microwave frequencies was studied Wang & Schmugge (1980) who found a transition point in the water content of soils below which adsorbed water appeared to have the dielectric properties of ice. Their modelling found that the transition points occurred between 16% and 33% water, and clays had higher transition points than sandy soils. They suggest that this effect is due to the first few layers of adsorbed water being

closely bound and therefore difficult for an applied field to polarize. The works of Wang & Schmugge (1980) along with Xiao's (1990) conclusions suggest that the effect of water on dielectric properties can be minimized with careful drying of samples.

Both Chen et al. (1984) and Xiao (1990) have demonstrated that the elemental composition of rocks and minerals is an important consideration in microwave heating performance. Natural minerals are not pure compounds and their elemental composition can be very loosely defined (solid solutions of end-members, natural deviations in stoichiometry, as well as both intrinsic and extrinsic impurities) and depend heavily on both the temperature and geochemical environment in which they formed. Metal sulphides and oxides have high dielectric properties, which make them good targets for selective microwave heating, but because they are semiconductors their dielectric properties are also particularly variable. The variability of semiconducting ore minerals is demonstrated in Table 2-8, which shows the considerably wide conductivity ranges of six selected minerals.

Semiconductors have three, non-exclusive, sources of free charge carriers: deviations from stoichiometry; trace elements in solid solution; and electron thermal excitation. Deviations from stoichiometry are typically point defects such as vacancies. Trace element dopants are also point defects and can, even in very low concentrations, alter the electrical properties of a semiconductor by introducing acceptor or donor impurities either interstitially or by substitution. Thermal excitation of electrons is a process by which electrons gain enough thermal energy to be promoted to the conduction band from the valence band. The dielectric properties of individual semiconducting minerals can be counter-intuitive – a detailed discussion of conductivity at low frequencies on a mineral by mineral basis can be found in Shuey's monograph (1975). The behaviour of charges in dielectrics has been observed to follow a universal relaxation law and the implications of this, specifically for semiconductors, are discussed in Jonscher's monograph (1996).

Table 2-8 – Selected low frequency mineral conductivity ranges – adapted from Shuey (1975)

Mineral	*Conductivity Range (S/m)*	
	Min	Max
Bornite	1.3E+01	6.3E+05
Chalcocite	2.4E+01	1.3E+04
Chalcopyrite	1.0E+02	1.0E+04
Pyrrhotite	6.3E+03	1.5E+05
Pyrite	1.0E+00	1.0E+05
Magnetite	1.0E-02	2.0E+04

Pridmore & Shuey (1976) concluded that the conductivity, and hence the dielectric properties, of chalcopyrite is dominated by deviations from stoichiometric $CuFeS_2$ while extrinsic defects caused by impurities playing no detectable role. The natural chalcopyrite samples surveyed by Pridmore & Shuey (1976) had an excess of metal (typically on the order of 0.1%) and were all consequently n-type semiconductors, although p-type chalcopyrite has been synthesized. Since chalcopyrites have an excess of metal, the electrical properties are governed by the copper/iron ratio – a property which can be measured using energy- or wavelength dispersive X-ray spectrometry (EDS or WDS).

Due to the temperature and sulphur pressure of formation natural galena can be either an n- or p-type semiconductor by exhibiting either a lead or sulphur excess respectively. Almost all galena surveyed by Pridmore & Shuey (1976) was n- and mixed-type. However, p-type galena did occur, along with mixed- and n-type galena, in high- and very low-silver deposits (Pridmore & Shuey 1976) where lead vacancies and silver substitution for lead resulted in additional acceptor defects.

The formation temperature of pyrite and the associated impurities play an important role in defining its semiconductor nature. Pyrites found in deposits associated with high formation temperatures are almost universally n-type due to sulphur deficiency (Pridmore & Shuey 1976). However, arsenic is a very effective acceptor impurity, and high-temperature pyrites can result in p-type semiconductors

even at very low concentrations of As (Pridmore & Shuey 1976). On the other hand, pyrites found in sedimentary and epithermal deposits are usually p-type semiconductors except when copper bearing sediments are also present (Pridmore & Shuey 1976).

The dielectric properties of minerals at microwave frequencies have been studied by a number of groups and there is evidence that valuable minerals will heat faster than gangue minerals. However, data is sparse and complicating factors, such as chemistry, anisotropy and moisture, are not always addressed. Despite the large variations in published data, there do not appear to have been any systematic investigations into the permittivity ranges of minerals at microwave frequencies. While the details of conduction mechanisms do not need to be known, it is clear that a better understanding of the relationship between chemical composition and dielectric properties of minerals is required.

It is clear that the dielectric properties of mineral specimens from different deposits, or even within the same deposit, may significantly differ. Therefore, it may be unwise to look solely to scholarly articles for dielectric property values. The properties of minerals in a deposit and their inherent variation need to be carefully considered when designing a microwave/IR sorting system and characterization of the deposit, or ore-types within it, may be necessary.

2.5 Dielectric Mixture Equations

Understanding how electromagnetic waves interact with materials has applications in many fields including communications, medical imaging and industrial processing. Central to this is the calculation of the effective dielectric properties of mixtures which is a non-trivial problem and has received considerable attention in many frequency regimes. Exact solutions for the dielectric properties of mixtures are only possible for an idealized system with well-defined geometry. Consequently, a variety of mixture approximations have been created each describing systems with different sets of properties, geometries and boundaries. A detailed account of different dielectric mixing theories can be found in the monograph edited by Priou (1992).

The Maxwell-Garnet Theory is one of the first mixture theories and dates back to the 1890s (Tinga 1992). Lord Rayleigh later demonstrated that the Maxwell-Garnet theory is a good first order approximation for cubically arranged spheres in a host matrix and presented a simpler formulation (Tinga 1992). The later theories of both Bruggeman and Böttcher attempted use the long range interaction of inclusions to account for higher order effects (Tinga 1992). Central to the long range interaction theories is the recognition that the apparent local permittivity of the host matrix is not equal to the permittivity of the host matrix as a result of nearby inclusions altering the local electromagnetic field.

The quasistatic limit is a common assumption in mixture theories and requires that the spatial variation of dielectric structures has to be much smaller than the wavelength and hence spatial variation of the applied field (Landau & Lifschitz 1984). The quasistatic limit simplifies mixing rule calculations by assuming the structure and geometry of components within the mixture are negligibly small compared to the variation of the field. However, when structures are comparable in size to the diffraction limit (one half-wavelength), scattering effects become non-negligible. Experimentally, it has been shown that the permittivity of a mixture strongly depends on: the permittivity of the component phases, the volume fraction occupied by each component and the quantity of water adsorbed (Greffe & Grosse 1992). Additionally, the permittivity is weakly affected by the applied field intensity as well as the ordering, shape and size variation of the inclusions (Greffe & Grosse 1992).

Numerical simulation of mixtures, with both random and periodic inclusions has led to further understanding of mixtures. Amongst the issues studied are the shape and interconnectedness of inclusions. In their work, Brosseau & Beroual (1999) demonstrated computationally that the effective permittivity of a medium changed with the angle between the applied field and a periodic array of rod-shaped inclusions. This work was followed by Beroual et al. (2000) and Jones & Freidman (2000), both of whom computationally demonstrated that the aspect ratio of inclusions can strongly effect dielectric properties to such an extent that the effective permittivity along the axis of a rod or prolate spheroid array approaches that of the of the inclusions. This work is similar

to earlier work by Carmona & El Amarti (1987) who experimentally demonstrated anisotropic conductivity in carbon-fibre reinforced polymer and a relationship between the degree of anisotropy and the aspect ratio of the fibres.

Nelson & You (1990) exploited the low degree of shape anisotropy in pulverized material to compare the effectiveness of six mixture equations (see Table 2-9) at predicting the dielectric properties of solid polymers. In these equations v_1 and v_2 represent the volume fractions of mixture components one and two respectively. Of the six equations, they found that the Landau-Lifschitz-Looyenga (LLL) and Complex Refractive Index (CRI) equations performed best. The LLL equation represents general systems of both continuous and discretized mixtures by considering inclusions to be infinitesimal spheres (Greffe & Grosse 1992 and Sihvola & Lindell 1992). Similar results were found by Arai et al. (1995) at low temperatures for solid, sintered and compact powder ceramics. However, changes in the density of compacted powders above 400°C lead the mixture equations to deviate from the measured properties of the solids (Arai, Binner & Cross 1995).

Table 2-9 – Selected Mixture Equations ($v_1 + v_2 = 1$)

Complex Refractive Index (CRI)	$\epsilon^{1/2} = v_1\epsilon_1^{1/2} + v_2\epsilon_2^{1/2}$
Landau-Lifschitz-Looyenga (LLL)	$\varepsilon^{1/3} = v_1\varepsilon_1^{1/3} + v_2\varepsilon_2^{1/3}$
Böttcher	$\frac{\epsilon - \epsilon_1}{3\epsilon} = v_2 \frac{\epsilon_2 - \epsilon_1}{\epsilon_2 + \epsilon_1}$
Bruggeman-Hanai	$\frac{\epsilon - \epsilon_2}{\epsilon_1 - \epsilon_2}\left(\frac{\epsilon}{\epsilon_1}\right)^{1/3} = 1 - v_2$
Rayleigh (also Maxwell-Garnett)	$\frac{\epsilon - \epsilon_1}{\epsilon + 2\epsilon_1} = v_2 \frac{\epsilon_2 - \epsilon_1}{2\epsilon_1 + \epsilon_2}$
Lichtenecker	$\ln\epsilon = v_1 \ln\epsilon_1 + v_2 \ln\epsilon_2$

A measurement technique published by Nelson & Kraszewski (1998) was capable of determining the percentage of coal from the dielectric properties of a limestone-coal mixture. This technique measured the perturbation of a resonant cavity due to powdered samples and a calibration data set to determine the quantity of coal. This work was followed by that of Nelson (2001) who adapted the LLL equation to predict the dielectric properties of a ternary mixture with a high degree of accuracy. There does not, however, appear to be any work that reverses the procedure and attempts to calculate the dielectric properties of mixture components from the measured properties of mixtures.

Rocks and ores are aggregates of minerals and the microstructure can have many different forms, and include small finely disseminated crystals, or aligned veins and needles of highly conductive minerals. Consequently, the microstructure of a rock matrix will have a non-negligible effect and the effective dielectric properties may depend heavily on its orientation with respect to an applied field. Care needs to be taken when pulverizing rock samples for measurements in, for example a resonant cavity, as the textural effects will disappear.

Nelson's (2001) successfully demonstrated a technique for estimating the fractional content of coal in coal-limestone mixtures based on the LLL equation yet there appears to be room in the literature for a reverse calculation. This calculation would approximate the dielectric properties of individual mixture components from sets of mixture data. Pulverized samples would be appropriate in this case, as microstructural effects would complicate the calculation.

2.6 Conclusion

Published literature shows differences between the dielectric properties and heating rates of ore and gangue minerals at microwave frequencies. These differences result in selective heating of the valuable mineral phase and has inspired research into mineral processing technologies such as microwave assisted comminution, liberation and flotation. While still in its infancy, new research

into combined selective microwave heating, infrared imaging and automated sorting has suggested there could be significant economic advantage in microwave/IR sorting.

However, the dielectric properties of minerals can vary significantly, and while the general reasons for variation are understood, they are not always addressed in processing. As the geological origins of minerals and ores can impact the dielectric properties they may also impact the degree of selective heating and potentially spoil sorting performance. A simple method for determining the potential for microwave/IR sorting in an ore is to process a large batch of particles and assay each particle individually. This is an appropriate technique for assessing the economics of a system but it does not shed light on the mechanisms behind the result or the controls that might be used to improve sorter performance for that ore. For this reason the design of microwave/IR based sorting devices would benefit from dielectric property characterization of ores and their component minerals.

The determination of dielectric properties of mixtures is a non-trivial problem in which the shape and arrangement of inclusions in a host matrix play an important role. As rock is a complex mixture, it is evident in the literature that the shape and arrangement of inclusions will affect selective heating. In powdered and granular samples, however, the LLL dielectric mixing theory has been shown to work well and been used to gauge the volume fraction of components in binary and ternary mixtures. There does not appear to have been any work in back-calculating the properties of mixtures to approximate the dielectric properties of mixture components if volume fractions are known. This calculation potentially leads to a method for characterizing the dielectric properties of all minerals in an ore sample and therefore warrants further investigation.

3 MW/IR and Dielectric Property Characterisation

3.1 Introduction

The premise of sorting using the Microwave/IR technique relies on a detectable relationship between heating rate and valuable mineral content. This relationship is simplified when gangue minerals are assumed to not interact with the microwave field and all heating is then due to the valuable minerals. As described in Section 2.1.2 of the Literature Review, a microwave/IR based pre-concentration process would likely eject the mostly barren particles, while a process generating a finished product would select only the particles which meet the requisite grade.

Some gangue minerals, such as ferromagnesian silicates, which are particularly common in monzonite ores, may be good microwave absorbers and thereby complicate sorting. Microwave absorbent gangue minerals negate the assumption that microwave heating is entirely due to valuable minerals, and may cause barren particles to displace valuable particles in the product stream. This could cause both barren particles to report to the product stream (false positives), which increases the cost of downstream processing, and valuable particles to report to the waste stream (false negatives) which are a direct economic loss.

The aim of this chapter is firstly to characterise the microwave heating of particles from different ores. To accomplish this, the temperature of particles needs to be measured both pre- and post-exposure to a microwave field. The second aim is to characterise the microwave dielectric properties of the ore particles along with selected mineral samples. These characterisation experiments are then used to establish a relationship between the microwave heating and dielectric properties of ore particles.

3.2 Sample Preparation and Microwave Characterisation

Six ores were selected for microwave heating characterisation. Each ore type was expected to exhibit a unique microwave heating behaviour related to factors such as mineral composition and chemistry, grain size, heterogeneity and structure, as well as the shape and size of particles. The impact these factor have on microwave heating can be hard to quantify. However, insights on their magnitude can potentially be found in the standard deviation of average particle temperatures resulting from repeated MW/IR experiments. `

3.2.1 Selection and Preparation of Ore Samples

The six ores selected are detailed in Table 3-1. These ores were chosen to represent a broad range of minerals and to have large variations in the relative contents of the component minerals. The ores were also chosen to gain insight into the effects of different petrologies on microwave heating. Monzonite ores are similar in both petrology and gangue mineral composition – all containing appreciable quantities of ferromagnesian silicates – and it is for this reason they are over-represented. For each of the ores, a thirty-three particle sample set of -22.4 +19.0 mm material was obtained by sizing and splitting from a much larger sample. Each particle in each sample set was then labelled with an identifying number.

All ore samples were sourced from different locations at the Bingham Canyon operation of Kennecott Utah Copper. This is a porphyry copper deposit formed by an igneous intrusion into the local sedimentary rocks. The QZ samples is quartzite ore which is predominantly quartz but with finely disseminated sulphides, such as chalcopyrite and pyrite. The monzonite ore samples are veined and contain many different silicate minerals, some of which may heat reasonably well. The SKN sample is from a skarn ore, which is highly heterogeneous, contains a large amount of garnet as well as both disseminated and veined sulphides.

Table 3-1 – Ores selected for multimode heating characterisation

Ore Name	*Description*
QZ	A quartzite ore with finely disseminated sulphides
SKN	Skarn ore
MZ1	Veined Monzonite ore
MZ2	Veined Monzonite ore
MZ3	Veined Monzonite ore
MZ4	Veined Monzonite ore

3.2.2 Microwave-Infrared (MW/IR) Characterisation

Microwave heating was used to characterize particle heating behaviour and then to guide the selection of particles for further investigation. When coupled with infrared (IR) thermal imaging, a domestic microwave oven can be used to quickly and easily gauge the relative heating of particles. Heating in a domestic oven is a batch process rather than a continuous process, expected in an industrial setting. In both domestic and industrial systems particles are exposed to, and move through, a multimode field. The complex field patterns in multimode cavities allow more uniform fields than resonant cavities. Uniform fields mean that differences in particle heating are more likely to be due to dielectric properties rather than differences microwave field exposure. While domestic ovens only have a single microwave feed, industrial scale systems can have multiple feed to further improve field uniformity. In the absence of large proportions of highly conductive mineral phases the rock particles can be considered insulators and consequently dielectric heating will be the dominant heating mechanism. Assuming particles behave solely as dielectrics (i.e. no interaction with the magnetic field), have a permittivity of six and a loss factor of 0.2 the penetration depth is approx. 240 mm which is an order of magnitude larger than the particle size fraction.

There were five stages to the MW/IR characterisation process: randomised particle positioning; pre-exposure thermal imaging; microwave heating; post-exposure thermal imaging; and thermal

analysis. Three random positioning sets were generated for each ore; particles were arranged on the cavity turntable according to the sets and then exposed once with the labels facing up and again with the labels facing down.

For each ore, three random particle ordering permutation sets were generated using the inbuilt MATLAB function 'randperm'. Each permutation set was then cut in two: the first 17 (batch A) and last 16 particles (batch B). Despite the difference in number of particles between batches A and B, there is no statistically significant difference in mass or volume (see Appendix Section 8.3.1, Table 8-12and Table 8-13) and therefore these factors will not unduly influence heating results. Furthermore, the permutation sets draw from the full 33 particle pool, so the combination of particles is different in each permutation set and each repeat of microwave heating. The randomization procedure allows the variability in cavity loading and potential field dragging effects (due to particle size, shape and dielectric properties) to be exhibited as variability in the average temperature increase of individual particles resulting from microwave heating.

Particles were placed on the domestic oven turntable according to their random permutation with the labelled side facing upwards. The whole turntable was then imaged using the thermal camera (Cedip Silver 420) to obtain initial particle temperatures (see Figure 3-1, left) at a sensitivity of 20 mK. Once imaged, the particles were exposed in a 2.45 GHz, 1200 Watt domestic oven (Sharp R380L-(W)) on 'High' for a single rotation of the microwave turntable (12 seconds). While the microwave energy applied per particle differed between exposures of 16 and 17 particle batches, the energy per unit mass or volume of material is statistically indistinguishable. A second thermal image was taken approximately 5 seconds after the microwave exposure (see Figure 3-1, right) to obtain the heated particle temperatures. The particles were then allowed to cool to room temperature and then procedure was repeated with the same arrangement of particles set with the labelled side facing down. This process (exposure and imaging with labels both up and down) was repeated for a further two permutation sets.

The thermal images, such as those in Figure 3-1, were analysed using the Altair radiometric analysis software suite which was provided with the camera. The minimum, maximum and average

pixel temperature as well as pixel standard deviation were collected for each particle using the area polyline tool to identify each particle. This process was used to analyse all pre- and post-exposure thermal images. The data was collected in a spread-sheet and then used to calculate average changes in particle temperature due to microwave heating. The data can be graphically represented as a 'temperature profile', where particles are sorted by ascending average temperature which is then plotted versus the cumulative mass percent. When the temperature profiles of the six ores are plotted together, in Figure 3-2, three distinct heating behaviours become apparent: Quartzite, Monzonite, and Skarn – refer to Appendix Section 8.3.2 for individually plotted profiles with error bars.

The emissivity of materials changes the apparent temperature of an object as observed by the infrared camera. Emissivity is a complex property defined as the ratio of the energy emitted by a body to the energy radiated by a blackbody. Factors that affect emissivity include: temperature, emission angle, wavelength, geometry, colour, composition and surface roughness. Differences in emissivity are an important consideration when comparing the thermographic measurements of targets with very different properties, for instance polished silver and paper. However, since all particles are sourced from a single deposit and have undergone the same preparation (crushing, screening etc.) it can be assumed that particles have effectively identical emissivity. In the radiometric calculations performed particles were assumed to have an emissivity of 1, which is identical to a blackbody and a commonly used value for rock faces (for example Feely & Christensen 1999). The small spread in particle emissivity can be observed in the distribution of particle temperatures when at equilibrium with room temperature (see Figure 3-1). Since all objects above 0 Kelvin emit radiation, heating the particles to an arbitrary temperature is not necessary. Furthermore the effect of emissivity is mitigated by the use of temperature changes rather than absolute temperatures.

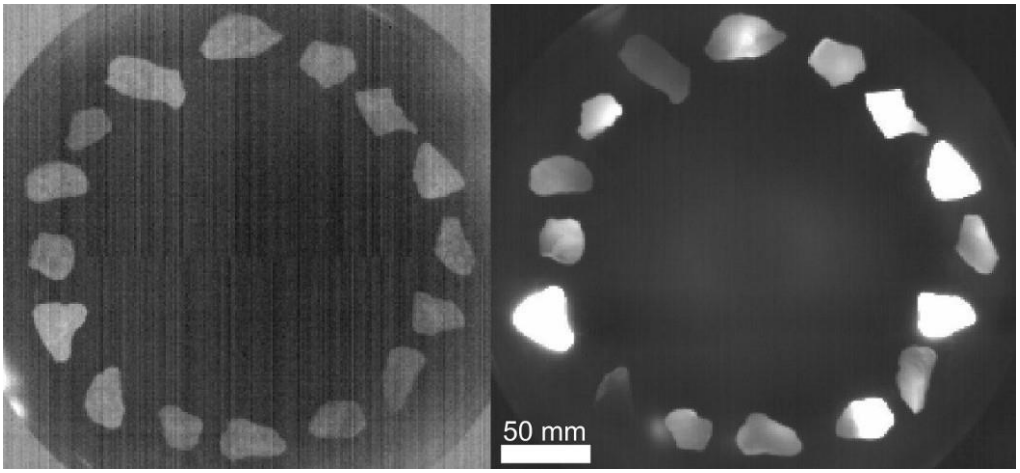

Figure 3-1 – Thermal images of the SKN sample before (left, greyscale palette 23 to 25 °C) and after (right, greyscale palette 20 to 40 °C) heating.

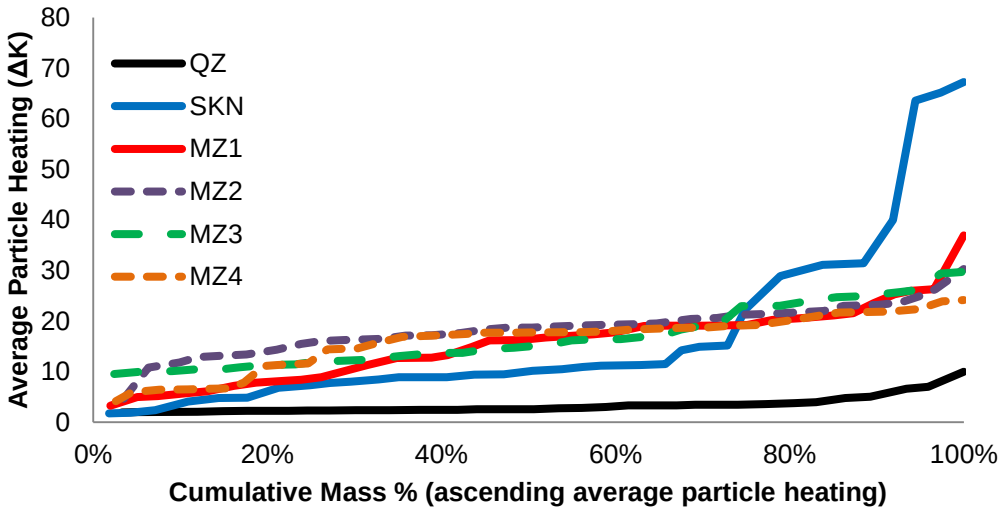

Figure 3-2 – Whole particle multimode heating profiles (Error bars omitted for clarity)

As can be seen in Figure 3-2, the quartzite does not heat much compared to the other ores – the average increase in particle temperature due to microwave exposure is approx. 3.3 °C. The low- and mid-heating sections of QZ are almost indistinguishable with only a small upswing in the temperatures of the hottest particles. The monzonite ores all have similar heating profiles; although there is some divergence among the cooler particles, presumably due to different gangue mineral compositions. The average increase in particle temperature in these four ores is approx. 16.6 °C.

The SKN sample has a pronounced heating profile – the coldest particles are heated similarly to the quartzite particles with the temperatures remaining cooler than the monzonite ores into the mid-heating region, the profile then swings sharply upward to particles considerably hotter than measured in any of the other ore samples.

3.2.2.1 Relative Standard Deviation

The distinct heating behaviours observed in the temperature profiles can also be found in microwave heating inhomogeneity on individual particle surfaces. This effect can be directly seen when visually comparing thermal images of QZ and SKN (see Figure 3-3). To analytically measure variation in particle temperature the relative standard deviation (RSD) is used – this is the pixel standard deviation divided by the average of pixel temperatures of the particle surface. When the RSD profiles are plotted (see Figure 3-4), the ores again form three groups: quartzite particles show the least temperature variation on their surfaces, which corresponds with both the highly disseminated nature of the sulphide mineralization and the predominantly quartz matrix; the monzonite ores with predominantly feldspathic matrices and veined sulphide mineralization form a distinct group, while the skarn sample has the highest variations, reflecting its petrology. Rather than absolute temperature rise this analysis uses the relative variation in pixel temperatures on particle surfaces and for this reason the energy each particle is exposed is of less importance than the mineralogy or texture.

The connection between variation in particle surface temperature and petrology is an interesting finding and warrants further investigation. However, this work has only been conducted at a single size fraction (-22.4 +19.0 mm) and work extending the characterisation to other sizes fractions and other microwave frequencies, such as 915 MHz, may be necessary to develop the property for ore sorting. If the heterogeneity of particles can be connected to gangue liberation this data may be useful for determining the appropriate size fractions for pre-concentration sorting. Finally, measuring surface temperature variations after microwave heating could potentially be an online method for distinguishing the ore-type of particles in a mixed stream and add another variable to sorting logic.

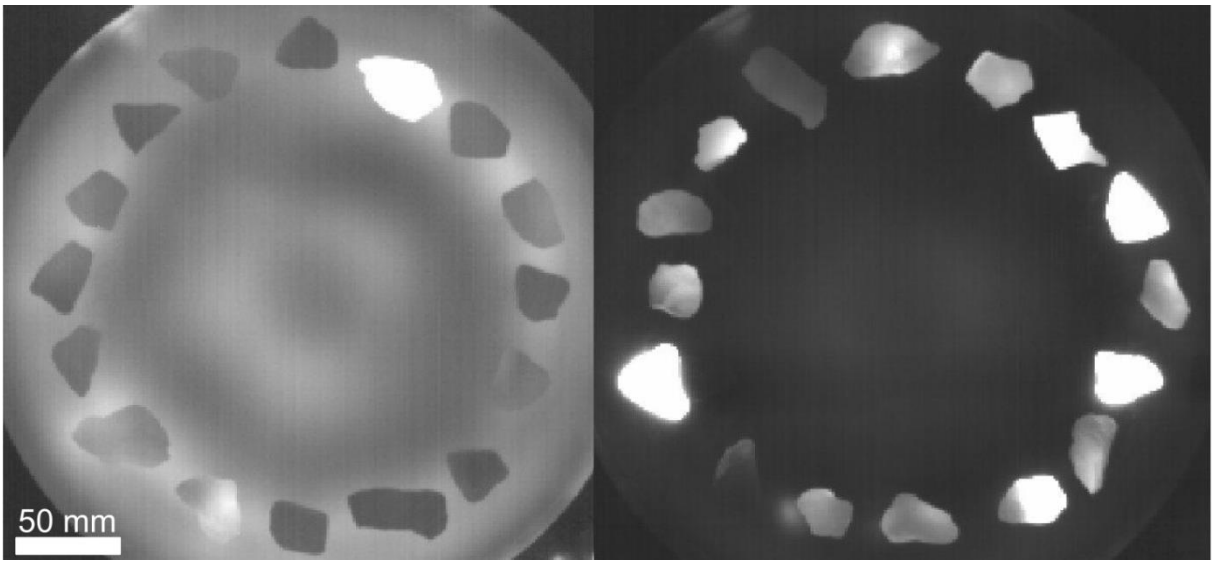

Figure 3-3 – A comparison of QZ (left, greyscale palette 20 to 30 °C) and SKN (right, greyscale palette 20 to 40 °C) after heating

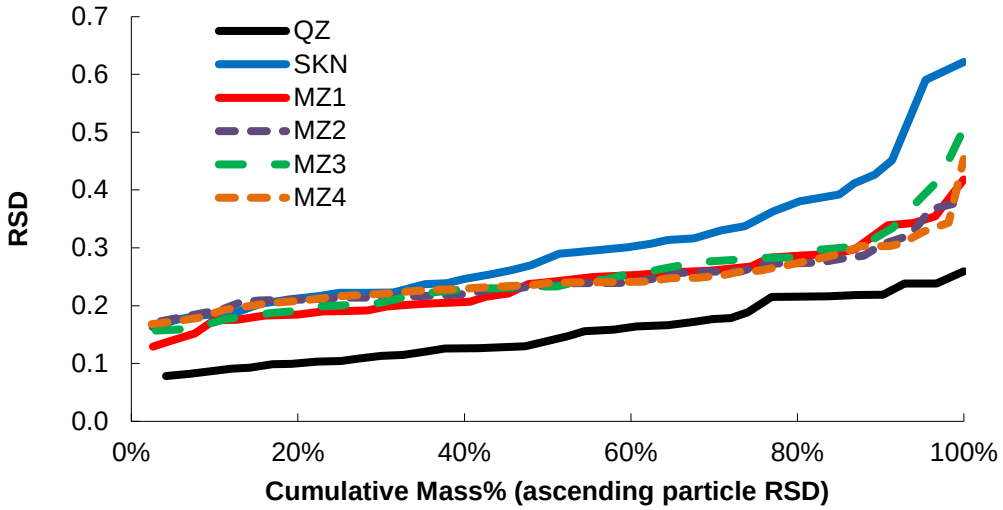

Figure 3-4 – Profiles of particle surface temperature RSDs for each ore

3.2.3 Sample Thinning

The microwave-infrared characterisation process produced 198 characterised particles. A number of strategies were used to reduce the number of particles prior to pulverisation and dielectric measurement at the University of Nottingham. The first strategy was the exclusion of entire ores; the four monzonite samples produced similar microwave heating results and for this reason MZ3 and MZ4 were discarded.

In a commercial application, the greatest sorting operational efficiency is found when focussing on either the hottest or coldest particles and therefore an understanding of the minerals responsible for these behaviours is required. For this reason the five hottest and five coldest particles were selected from the four remaining ores (QZ, SKN, MZ1 and MZ2) along with five mid-temperature chosen using a random number generator. Focussing on the hottest and coldest particles in this manner means that a direct comparison between dielectric data and sorting feasibility studies cannot be made.

3.2.4 Sample Processing

A three-step sample preparation process was developed and applied to the selected and characterized ore particles. This method produced solid cores and powders for resonant cavity measurements, as well as rock fragments with smooth faces for potential further investigation. Figure 3-5 illustrates the sample processing method – the grey areas were retained as a solid half and core, while the blue area was pulverized in a ring mill.

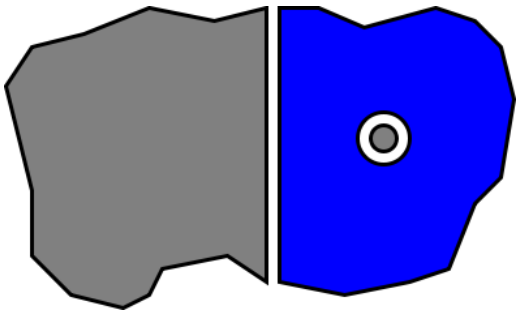

Figure 3-5 – Particle processing

3.2.4.1 Coring

The Nuclear Magnetic Resonance (NMR) tubes used to suspend samples in the resonant cavities at the University of Nottingham are available in three sizes: 2, 3, and 4mm inner diameter. The diameters of core samples need to be consistently smaller than the tube inner diameters to fit.

Initial testing with commercially available 6mm Outer Diameter (OD) diamond core drills-bits produced cores under the 4mm limit. However, wear on the inner surface of these drill-bits resulted in core diameters which crept to 4mm after only a few uses. This problem was resolved by purchasing custom-made 3.5mm Inner Diameter (ID) electroplated diamond core drill bits which were much less susceptible to wear and cores remained under the 4mm limit after many uses. To improve the success rate of core cutting, the drill-bit was attached to a drill-press via a water swivel, which injected water down the barrel of the bit and to the cutting face.

Considerable effort was made to keep one half of the particle whole in the core drilling process; however, it was not universally successful. Some particles, due to their friability or existing fractures, fragmented when exposed to water and stress in the drilling process. When core drilling was unsuccessful, all material was retained for later pulverization. Manufactured cores were placed in numbered bags and dried in an oven at 90°C overnight.

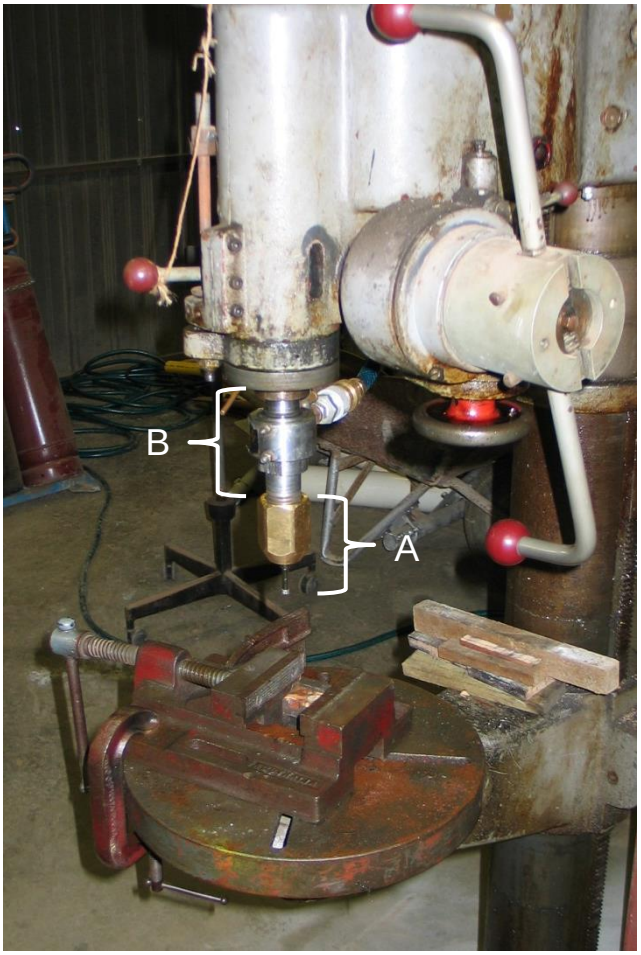

Figure 3-6 – Rock core cutting apparatus showing diamond plated drill-bit (A), water swivel with hose (B)

Table 3-2 – Tally of cores produced

Ore	*Number of Cores*
QZ	13
SKN	13
MZ2	10
MZ1	8

3.2.4.2 Particle Halving

After coring, the particles were cut in half using a diamond saw. As described in the previous section, the coring process attempted to keep half of the particle solid. Once cut, the half with the core-hole, and any other fragments, were placed in numbered bags and dried overnight in a 90°C oven. This material was used in the later pulverization stage. The half without the core-hole were separately bagged and dried in the same oven overnight. Some particles fragmented when being cut with the diamond saw and no solid halves were produced. In these cases, all fragments were used in the pulverization stage.

Table 3-3 – Tally of halves produced

Ore	*Number of Halves*
QZ	15
SKN	15
MZ2	14
MZ1	13

3.2.4.3 Pulverization

The cored halves or the entirety of fragmented particles were then pulverized in a ring mill (ROCKLABS SRM) for 1 minute and 30 seconds to achieve a powder typically less than 100 µm. The resulting powders of each particle were then placed in numbered bags and dried overnight in an oven at 90°C to reduce moisture.

3.2.4.4 Pure Minerals

Knowledge of the dielectric properties of pure minerals provides insight into the dielectric properties of ores. To this end, a selection of pure minerals specimens were obtained from the minerals dealer Gregory Bottley and Lloyd and a mica sample was donated from Prof. Ben Adair's personal collection (see Table 3-4 and Figure 3-7). None of the pure mineral samples were suitable for cutting with the diamond saw but some were suitable for coring (see Table 3-4). Powders were obtained from all minerals using the same methods as for the ore samples.

The minerals obtained were in highly phase-pure forms with the exception of the molybdenite specimen which was heavily mineralized. The molybdenite sample was first crushed in both jaw and rolls crushers and then concentrated by heavy liquid separation with lithium heteropolytungstate (LST, specific gravity = 2.8). The molybdenite concentrate was then washed, dried and pulverized using the ring mill whilst the tailings were discarded. The samples with significant mass, quartz, pyrite, chalcopyrite and garnet were split into three size fractions: -75 μm, -212 μm +75 μm, and +212μm. Measurements with a Niton X-Ray Fluorescence (XRF) analyser on the powdered mineral samples produced poor totals but indicated that the quartz sample is 99% pure, the pyrite and chalcopyrite samples are 97% pure while the molybdenite sample is 83% pure.

Figure 3-7 – Unprocessed mineral specimens: molybdenite (A), feldspar (B), chalcopyrite (C), quartz (D) and pyrite (E)

Table 3-4 – Pure mineral samples

Mineral	*Origin*	*Core*
Quartz	Unknown	✓
Feldspar	Unknown	✓
Garnet	Nigeria	×
Pyrite	Peru	✓
Chalcopyrite	Peru	✓
Molybdenite	Peru	×
Mica	USA	×

3.3 Microwave Dielectric Measurements

The dielectric properties of prepared ore and mineral samples were measured via perturbation of a cylindrical cavity at the National Centre for Industrial Microwave Processing (NCIMP), at The University of Nottingham. The majority of these measurements were performed at room temperature; however, data was collected on the behaviour of dielectric properties at elevated temperatures for the pure mineral samples. Additional experiments were performed using mixtures of quartz and pyrite powder to better understand the uncertainty in cavity perturbation measurements.

3.3.1 Microwave Test Cavity

The Dielectric Measurement Laboratory of the NCIMP, at The University of Nottingham has two, cylindrical TM_{0n0} resonant cavities – named 'C1' and 'C2'. All microwave frequency dielectric measurements reported in this thesis were conducted using the larger, C1 system (see Figure 3-9). The C1 cavity has a volume of 15190473 mm^3, it is approx. 54 mm high and has a diameter of approx. 598 mm. The system primarily consists of the resonant cavity, a Hewlett-Packard (8753C) network analyser, and a PC with custom control and acquisition software. The system also has a furnace and temperature controller, cavity cooling system, and linear positioning system for dielectric measurements at elevated temperatures. The network analyser is coupled to the magnetic field in the resonant cavity via loop antennas and coupling efficiency can be controlled by changing the diameter of the loops. The cavity supports a number of TM modes which can be used to measure dielectric properties, of these modes TM_{010}. TM_{020} and TM_{050} are the most interesting due to their proximity to ISM bands (see Table 3-5).

Dielectric properties are calculated from measurements of resonant frequency and bandwidth using perturbation equations (3.1) and (3.2) detailed in the Literature Review (see Section 2.3.2.1). Dielectric property calculations were performed in the limit of a negligible radius sample. This means that, while samples do not extend the full height of the cavity, the depolarization factor (N, which is determined from the ratios of sample axis lengths) is still negligible and reduces Equations

(2.42) and (2.43) of the Literature Review to Equations (3.1) and (3.2) below. This is reinforced by using small and powdered (low density) samples which are much smaller than the wavelength of the applied field. Using this approach with high permittivity and large samples introduces a systematic offset into measurements. When samples are identified as having a high permittivity this systematic error is mitigated by repeating the measurements with increasingly smaller samples until the results converge.

$$\epsilon' = 2J_1^2(ka)\frac{V_c \delta f}{V_s f_c} + 1 \tag{3.1}$$

$$\epsilon'' = J_1^2(ka)\frac{V_c}{V_s}\left(\frac{1}{Q_s} - \frac{1}{Q_c}\right) \tag{3.2}$$

Where:

- V_c and V_s are the volume of the cavity and sample respectively.
- f_c and f_s are the resonant frequencies of the cavity when empty and loaded with a sample respectively and $\delta f = f_c - f_s$.
- Q_c and Q_s are the quality factors of the empty and sample-loaded cavities respectively.
- $J_1(ka)$ is a first-order Bessel function describing the field in the cavity. See Section 8.3.4, Table 8-14 of the Appendix for numerical solutions of when electric field boundary conditions demand zero field at the walls and consequently $J_0(ka) = 0$ (Parkash, Vaid & Mansingh 1979).

Table 3-5 – Mode details of the C1 cavity

TM Mode	f_0 *(MHz)*	Q_{empty}	$J_1^2(ka)$
010	397	9983	0.269
020	912	12774	0.116
030	1431	14692	0.073
040	1951	16729	0.054
050	2472	18187	0.043

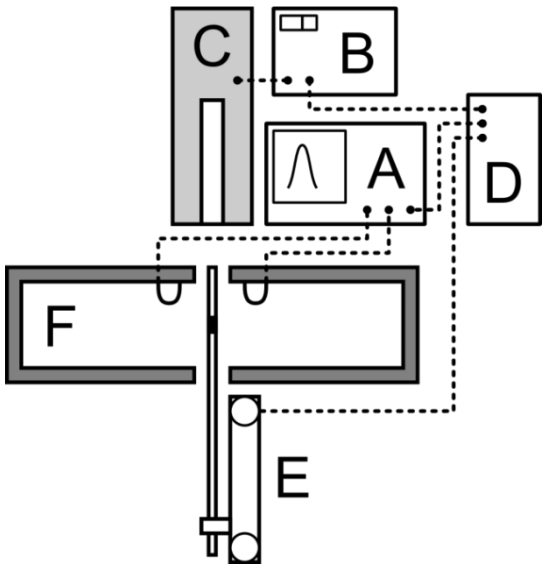

Figure 3-8 – Conceptual schematic of the C1 cavity and associated systems (A network analyser; B furnace control system; C furnace; D PC with control and acquisition software; E electromotor system for moving the sample tube between cavity and furnace; F physical cavity containing a glass sample tube and excited by the magnetic field)

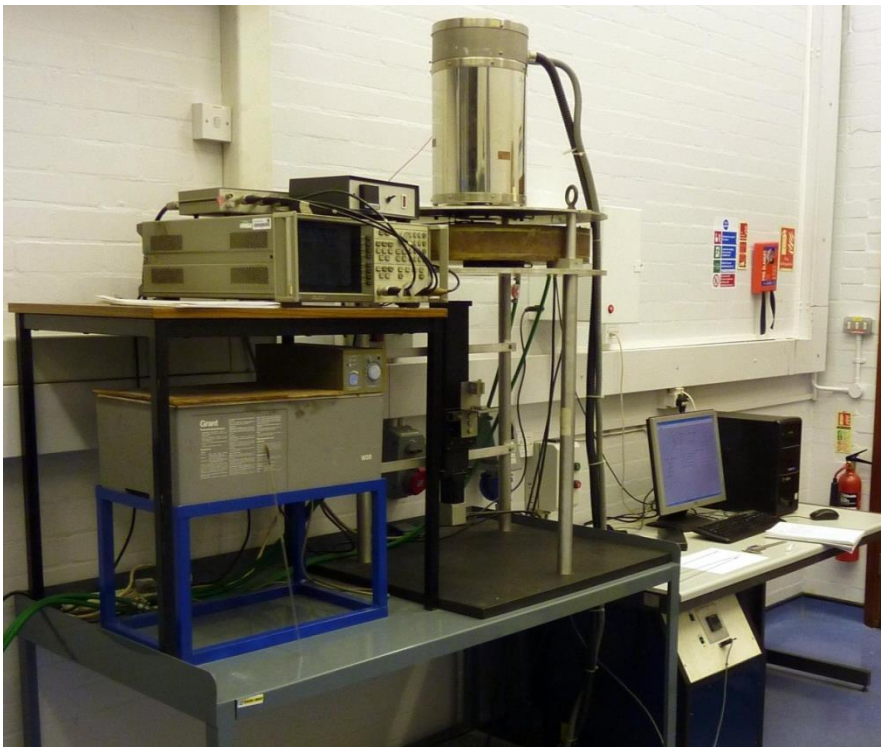

Figure 3-9 – The NCIMP C1 Cavity

3.3.2 Measurement Procedure

Dielectric measurements in the C1 cavity are a two-stage process involving a sample tube calibration measurement and then the sample measurement. The calibration measurement represents the effective empty cavity measurement and separates the perturbation due to the NMR tube and kaolin-wool plug suspending the sample in the cavity (sample tube) from the perturbation due to the sample itself.

Sample tubes are prepared by first inserting a kaolin-wool plug into the quartz tube. A reference mark is then made on the tube so that the top of the plug sits just below the mid-point of the cavity when the tube extends through to the top of the cavity. The kaolin-wool plug is then tamped down with a metal rod to form a flat top surface. The weight of the tube is then measured on a high precision balance. The tube with plug is then placed in the cavity according to the reference

marking and the cavity resonant frequency, f_r, and bandwidth, Δf_r, are recorded. These recorded frequencies and bandwidths are later used as the 'empty cavity' values for calculating dielectric properties of samples.

The tube is then removed from the cavity and a small amount of sample, either solid or powder, is added. Powder samples are then gently tamped down with a metal rod or compacted using a specific 'tapping' regime in which the sample tube is held upright and gently tapped on the lab bench a set number of times to settle the powder. The weight of the sample tube with sample is then measured on the high-precision balance and the height of the sample in the tube is measured with Vernier Calliper (average sample height: 22 mm ±3 mm). The sample volume and density are later used to calculate the dielectric properties of a bulk solid. The average density of the solid particles was 2.66 g/cm^3 (standard deviation: 0.23) while the average density of powders was 1.53 g/cm^3 (standard deviation: 0.20).

The sample tube is then reinserted into the cavity. In a perfect empty and sealed cylindrical cavity there is no electric field variation in vertical direction. Modelling by Pipiskova & Lukac (1970) has shown that the combination of access holes, glass tube and sample alters the field distribution and induces variation in the vertical direction. For this reason the vertical position of the tube is then adjusted to achieve largest perturbation (i.e., the lowest centre frequency) by observing one of the TM_{0n0} resonances on the network analyser (see Figure 3-10). This position of maximum perturbation corresponds to the position where the sample has the strongest interaction with the resonant electric field.

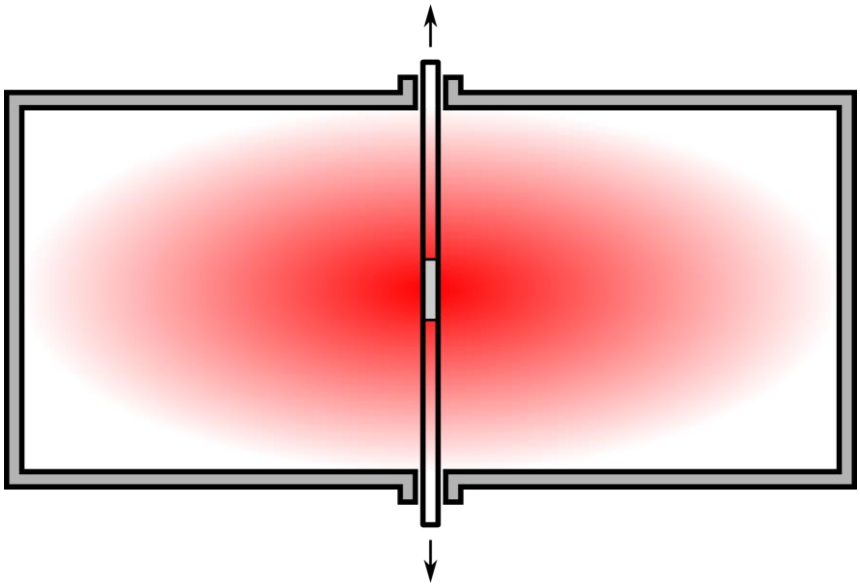

Figure 3-10 – Positioning samples in the cavity to achieve the largest perturbation of the electric field (illustrative purposes only)

At this point the measurement technique diverges. Room temperature measurements only require another measurement of the centre frequency and bandwidth of the resonant modes and then the sample is discarded and the process begins with a fresh sample tube and kaolin-wool plug. On the other hand, measurements at elevated temperatures continue for another several hours. In elevated temperature measurements, the sample is lifted into a furnace by the linear positioning system, heated to the desired temperature and then held at the desired temperature for a further ten minutes to reach thermal equilibrium. The positioning system then quickly lowers the sample into the cavity for measurement of the centre frequency and bandwidth and then returns it to the furnace in a process taking no more than a couple of seconds. This introduces a level of uncertainty into the temperature measurement that was not characterised although is deemed small due to the short amount of time the sample spends outside the furnace. The process of heating and cavity measurement is then repeated at specified temperature intervals until an end temperature is reached. Heating a resonant cavity is undesirable because thermal expansion changes the centre frequency and the temperature-resistance relationship of metals increases wall losses and therefore simultaneously decreases the Q-factor.

For core samples, after computation of the dielectric properties using Equations (3.1) and (3.2) no further analysis is required. However, powder samples can be considered as an air-solid mixture and to obtain the dielectric properties of the solid material a mixture equation is required. Nelson (2005) found that the Landau-Lifschitz-Looyenga (LLL) mixture equation provided the best estimates of solid dielectric properties most often from powdered and granular mixtures. To this end Nelson (2005) provides a most modified version of the LLL equation (see Equation (3.3)). To accomplish these calculations, the mass and volume of powder in the sample tube were used in combination with the previously measured density of the original particle to arrive at a value for solid permittivity.

$$\epsilon_{solid} = \left[\frac{\left(\epsilon_{powder}^{1/3} - 1\right)\rho_{solid}}{\rho_{powder}} + 1 \right]^3 \tag{3.3}$$

3.3.3 Uncertainty Characterisation

It is important to understand the magnitude of the uncertainty in cavity perturbation dielectric measurements and several sources were identified. A factorial experiment was designed focussing on 3 specific sources of uncertainty: density, mass and dielectric property. Other sources of uncertainty included measurement noise and sample tube position within the cavity. The uncertainty associated with the use of the LLL mixture equation is not quantified in this thesis; however, it was studied in geological mixtures by Nelson (2005) and found to be generally less than 2%.

3.3.3.1 Measurement Noise

A fundamental level of uncertainty can be found in the repeated measurement of cavity resonant frequency and bandwidth. This uncertainty is due to sources such as electrical noise and interference, digitization error, thermal drift and represents the noise floor. Some of this uncertainty can be reduced by adjusting the Intermediate Frequency Bandwidth (IFBW) – which reduces

measurement noise resulting from the network analyser local oscillator – as well as the averaging and smoothing parameters on the network analyser. This uncertainty can be found by recording sets of repeated measurements of resonant frequency and bandwidth data for both calibration and sample measurements. The equations for calculating dielectric properties ((3.1) and (3.2)) can be modified to estimate the standard deviation due to noise in calibration and sample measurements in terms of the dielectric properties (see Equations (3.4) and (3.5)).

$$\sigma_{\varepsilon'} = \frac{aM}{\bar{f}_0}\sqrt{\left(\frac{a\sigma_M}{M}\right)^2 + \left(\frac{\sigma_{f_0}}{\bar{f}_0}\right)^2} \tag{3.4}$$

$$\sigma_{\varepsilon''} = \frac{v_c}{v_s} J_1(ka)^2 \sqrt{\left(\frac{\sigma_{Q_s}}{\bar{Q}_s^2}\right)^2 + \left(\frac{\sigma_{Q_c}}{\bar{Q}_c^2}\right)^2} \tag{3.5}$$

Where:

$$a = \frac{2v_c}{v_s} J_1(ka)^2 \tag{3.6}$$

$$M = \bar{f}_0 - \bar{f}_s \tag{3.7}$$

$$\sigma_M = \sqrt{\sigma_{f_0}^2 + \sigma_{f_s}^2} \tag{3.8}$$

3.3.3.2 Tube Positioning

The purpose of this measurement was to determine the error associated with positioning the sample tube in the cavity as it was identified as the main source of operator error. The measurement procedure calls for the tube position to be optimized by observing cavity perturbation on the network analyser. To determine the magnitude of this uncertainty, a single sample tube filled with a quartz-pyrite mixture (80%-20% respectively, size fraction: -212 +75 μm) with a fixed mass and volume was then measured five times in the resonant cavity. Between each of the measurements the

sample tube was removed from the cavity, reinserted and then the perturbation signal was re-optimized. The results of this experiment can be found in Table 3-6.

The standard deviations reported in Table 3-6 are calculated using Equations (3.4) and (3.5) from the results of eight successive measurements with no change in tube positioning. The averages (and standard deviations) of the measurements are 5.3753 (0.0279) for the real and 0.0911 (0.0006) for dielectric loss factor. When these values are compared to the average and standard deviation of the individual measurements set it can be seen that uncertainty in the dielectric constant due to tube positioning is substantial as the standard deviation of the set is an order of magnitude larger than the standard deviation of individual measurements. However, the uncertainty in loss factor does not appear to be sensitive to tube position, as the standard deviation of the set is smaller than the noise of individual measurements.

Table 3-6 – Dielectric property results of a single sample tube measured multiple times at 2470 MHz (with Std. Dev. of measurement noise)

Measurement	ϵ'	ϵ''
1	5.4126 (0.0042)	0.0909 (0.0023)
2	5.3409 (0.0037)	0.0903 (0.0023)
3	5.3841 (0.0037)	0.0910 (0.0022)
4	5.3831 (0.0026)	0.0918 (0.0022)
5	5.3556 (0.0026)	0.0915 (0.0025)
Mean	5.3753	0.0911
St. Dev.	0.0279	0.0006

3.3.3.3 Volume, Mass, and Dielectric Properties

Three further potential sources for uncertainty were identified which feed into the calculation of dielectric properties: volume, mass and the dielectric properties of the mixture. To study these effects a randomized 3x3x3 factorial experiment with a blocked repeat was designed. The experimental design requires three different sample masses, three different sample densities and three different mixtures for a total of 27 observations in a randomized order. As the experiment has a blocked repeat, the 27 measurements are then repeated in a different randomized order. To ensure the independence of observations, no sample tube was reused.

The dielectric properties for all observations in the factorial experiment were projected to values for solids using the modified LLL equation (3.3) which also used densities measurements of the solid pyrite and quartz stock from which the powder samples were generated (see Appendix Section 8.3.5, Table 8-15 and Table 8-16). The factorial design used in this manner includes effects such as measurement noise and tube positioning in its estimation of the standard measurement error.

Sample Mass

The purpose of this measurement was to examine the effect varying sample masses have on calculated dielectric properties. The mass of a sample does not directly factor in perturbation measurements; it appears in the calculation of sample density which is later used to estimate the solid dielectric properties. However, the quantity of sample also influences the measurement via the assumptions in perturbation theory (see Literature Review Section 2.3.2.1), namely that the perturbing sample is small and the field within the electric sample is constant. This introduces a systematic error as samples with high dielectric properties perturb the field more than samples with low dielectric properties.

Three sample masses were chosen for the factorial experiment: 0.05, 0.1 and 0.15 grams. Precisely filling the sample tubes with the powder mixture is difficult and there is an additional level of uncertainty in sample mass due to burrs on the ends of the quartz NMR tubes. These burrs can cause the sample tube to lean in different directions which thereby alter the mass perceived by the balance. This effect was mitigated by using marks on the bottom of sample tubes to orientate the tubes in a repeatable manner. The deviation between actual sample mass and target sample mass was, on average 0.001 grams (St. Dev. 0.003 grams). This corresponds to average 2% error in mass for the 0.05 gram samples.

Sample Volume

The volume of the sample appears twice in the equations used to calculate the dielectric properties bulk solid from a perturbation measurement. It first appears in the calculation of the powder dielectric properties resulting from the perturbation measurement and appears again in the calculation of density as part of the LLL estimation of solid properties.

To study the effect different volumes had on dielectric properties a method was required to control sample powder compaction. This was accomplished by tapping filled sample tubes on the laboratory bench a specified number of times. Three different volume levels were required by the factorial design experiment, these were: 45, 90 and 135 taps.

Sample Properties

Initial cavity perturbation experiments on pure mineral powders revealed that low-loss samples, such as quartz, could produce negative values for the dielectric properties. In those measurements, this was mitigated by using slightly larger quartz samples. Pyrite, on the other hand, is a highly conductive material and only very small samples were needed. This effect is due to the assumptions in the cavity perturbation theory such as constant electric field within the sample. This assumption

does not hold true for highly conductive samples where a measurement of bulk dielectric properties can turn into one of surface impedance. It follows that, while not expressed in the calculations, there is therefore some relationship between the uncertainty in dielectric property results and the dielectric properties of the sample itself. This may be further complicated by factors such as imperfect mixing and shielding due to very small penetration depths in highly conductive grains. To test this effect, three powders with different dielectric properties were included in the factorial design. These powders were made by mixing different proportions of quartz and pyrite powder (see Appendix Section 8.3.5, Table 8-16).

3.3.3.4 Factorial Design Results

The experimental design was generated using the Minitab 16 statistical software suite. Once the data was collected, this software was used to analyse the results. Analysis of variance (ANOVA) was used to examine the results of the factorial experiment with general linear models, the basic results of which can be found in Table 3-10 – Table 3-13, more extensive reports generated by Minitab can be found in Section 8.3.5.1 of the Appendix. A benefit of analysing the factorial experiment in this manner is that an error term, S, is generated which estimates the standard deviation in the experiment.

General Results

Initial ANOVA for volume, density, both the dielectric constant and loss factor show that Blocking the repeated observation set did not produce a significant effect (see Table 3-7). The analyses were repeated with blocking removed from subsequent analyses.

Table 3-7 – ANOVA results for the significance of blocking the repeated data

Result Analysed	*P-value (Blocks)*
ϵ'	0.596
ϵ''	0.198
Volume	0.307
Density	0.105

Volume and Density

Analysing the factorial experiment with respect to sample volume and density is a check that the tapping method for powder compaction worked. The ANOVA for volume (see Table 3-9) shows only sample mass to be a statistically significant factor (95% confidence). This finding, in essence, means that the only factor influencing the sample volume is the amount of sample. However, there is evidence for interactions between Taps & Mixture (P = 0.095), and Mass & Mixture (P = 0.077) which is potentially due to the different mixture densities. An ANOVA for density shows none of the control factors had a statistically significant effect on the sample powder density (see Table 3-10) however there is evidence for a Taps-Mixture interaction. These results demonstrate that tapping is an inadequate method for controlling powder compaction. A more reproducible powder compaction technique needs to be investigated if control of this property is required in future measurements.

Table 3-8 – Key to abbreviations used in ANOVA analyses

Abbreviation	*Definition*
DF	Degrees of Freedom
Seq SS	Sequential Sum of Squares
Adj SS	Adjusted Sum of Squares
Adj MS	Adjusted Mean Squares
F	F statistic
P	Probability of the null hypothesis

Table 3-9 – ANOVA for powder volume using Adjusted SS for tests

Source	*DF*	*Seq SS*	*Adj SS*	*Adj MS*	*F*	*P*
Taps	2	13.50	13.50	6.75	0.14	0.866
Mass	2	21649.86	21649.86	10824.93	231.77	0.000
Mixture	2	44.55	44.55	22.28	0.48	0.626
Taps*Mass	4	324.26	324.26	81.06	1.74	0.171
Taps*Mixture	4	411.68	411.68	102.92	2.20	0.095
Mass*Mixture	4	444.76	444.76	111.19	2.38	0.077
Taps*Mass*Mixture	8	495.61	495.61	61.95	1.33	0.273
Error	27	1261.03	1261.03	46.70		
Total	53	24645.26				

Table 3-10 – ANOVA for powder density using Adjusted SS for tests

Source	*DF*	*Seq SS*	*Adj SS*	*Adj MS*	*F*	*P*
Taps	2	4050	4050	2025	0.02	0.979
Mass	2	113862	113862	56931	0.60	0.558
Mixture	2	58012	58012	29006	0.30	0.741
Taps*Mass	4	354709	354709	88677	0.93	0.462
Taps*Mixture	4	809949	809949	202487	2.12	0.106
Mass*Mixture	4	489958	489958	122490	1.28	0.302
Taps*Mass*Mixture	8	608438	608438	76055	0.80	0.611
Error	27	2579901	2579901	95552		
Total	53	5018879				

Dielectric Constant

ANOVA of the factorial experiment using estimated solid dielectric constant results reveals that all three controlled factors (Taps, Mass and Mixture) have a statistically significant effect (see Table 3-11). Different mixtures are expected to have different dielectric properties and therefore appear as a significant factor in the ANOVA. The significance of mass supports the premise that different quantities of sample affect the results via the perturbation assumptions. This is additionally supported by the evidence for an interaction between Mass & Mixture (P = 0.093) which suggests that the perturbation calculation is effected by the degree of perturbation. It is surprising that Taps is significant (98.9% confidence) in these results given that it explains neither volume nor density. The ANOVA also produces an estimated standard deviation of the experiment (S=0.38), which is small compared to the mean of the real part for all observations (5.898) and correspond to a relative standard deviation of approx. 6% (see Table 3-12).

Table 3-11 – ANOVA for ϵ' using adjusted SS for tests

Source	*DF*	*Seq SS*	*Adj SS*	*Adj MS*	*F*	*P*
Taps	2	1.5511	1.5511	0.7755	5.33	0.011
Mass	2	0.9835	0.9835	0.4917	3.38	0.049
Mixture	2	6.6996	6.6996	3.3498	23.04	0.000
Taps*Mass	4	0.2376	0.2376	0.0594	0.41	0.801
Taps*Mixture	4	0.1886	0.1886	0.0471	0.32	0.859
Mass*Mixture	4	1.2917	1.2917	0.3229	2.22	0.093
Taps*Mass*Mixture	8	0.6982	0.6982	0.0873	0.60	0.769
Error	27	3.9256	3.9256	0.1454		
Total	53	15.5758				

Table 3-12 – Estimated error results from ANOVA for ϵ'

S	R^2	R^2*(adj)*
0.381303	74.80%	50.53%

Dielectric Loss Factor

ANOVA of the factorial experiment using estimated solid loss factor results shows that both Mixture and Mass are very significant factors (>99.9% confidence) although Taps is not significant. It is interesting that there is an interaction between Taps and Mass (99.6% confidence) as it was not observed in the results for the dielectric constant and the results were obtained simultaneously. In this case, the estimated standard deviation is a significant fraction of the mean loss factor of all observations (0.075) and corresponds to a relative standard deviation of approx. 25% (see Table 3-14).

Table 3-13 – ANOVA for ϵ'' using adjusted SS for tests

Source	*DF*	*Seq SS*	*Adj SS*	*Adj MS*	*F*	*P*
Taps	2	0.000763	0.000763	0.000381	1.15	0.330
Mass	2	0.00706	0.00706	0.00353	10.69	0.000
Mixture	2	0.052758	0.052758	0.026379	79.87	0.000
Taps*Mass	4	0.006424	0.006424	0.001606	4.86	0.004
Taps*Mixture	4	0.001369	0.001369	0.000342	1.04	0.407
Mass*Mixture	4	0.001627	0.001627	0.000407	1.23	0.321
Taps*Mass*Mixture	8	0.00377	0.00377	0.000471	1.43	0.231
Error	27	0.008917	0.008917	0.00033		
Total	53	0.082688				

Table 3-14 – Estimated error in loss factor results from ANOVA for ϵ''

S	R^2	R^2*(adj)*
0.0181731	89.22%	78.83%

3.3.3.5 Uncertainty Conclusions

Experiments gauging operator error demonstrated that the positioning of the sample tube in the cavity, while not important for measurements of loss factor, is an important factor when measuring the dielectric constant. The factorial experiment has revealed that tapping is not a good method for controlling powder compaction. ANOVAs of the results for both the real and imaginary components of permittivity have shown that Mass and Mixture are significant factors in the measurement of both and supports the premise that both the quantity and sample dielectric properties affect the results of perturbation measurements.

Analysis of the factorial experiment also produced estimates for the standard deviations of measurements; 0.381 for dielectric constant and 0.018 for the loss factor. These estimated standard deviations include all sources of uncertainty (such as tube positioning) and can then be used to gauge the uncertainty in further measurements. These estimates of uncertainty mean that the loss factor of low-loss materials, such as quartz, may be difficult to accurately measure and these measurements may occasionally produce negative loss factors. Additionally, the finding that the controlled factor (taps, mass and mixture) affects the outcome of dielectric property measurements means that future measurements of ores should be conducted using a standardised procedure. Furthermore, this uncertainty characterisation experiment was accomplished with powdered samples and includes a step that calculates the properties of a solid from the powder. The uncertainty in dielectric measurements of solid samples is expected to be smaller.

3.3.4 Microwave Dielectric Results

This section presents and discusses the dielectric measurement results of mineral and ore samples at 2470 MHz (corresponding results for measurements at 912 MHz can be found in Section 8.3.6.1 of the Appendix). Present dielectric properties of particles in terms of their characterized microwave heating results and compare the results of core and powder measurements.

3.3.4.1 Ore Powder and Core Results

The results of cavity perturbation measurements on ore powder samples are presented in Figure 3-11 and Figure 3-12 below. In these graphs, the real and complex components of permittivity as well as dielectric loss tangent for each sample in the four ores are plotted against their respective average whole particle microwave heating, characterised earlier (see Section 3.2.2). Plotting in this manner allows the relationship between dielectric properties and microwave heating to be observed.

In Figure 3-11, visual inspection suggests the possibility of a weak linear relationship between permittivity and microwave heating across all ores (Figure 3-11). However, this relationship only

appears to extend to loss factors for low microwave heating (Figure 3-12). When powder loss tangents are plotted against microwave heating (Figure 3-13), the data suggests that ores may have a common relationship with the exception of specific samples in the SKN, MZ1 and MZ2 ore which deviate considerably. The relationship between loss tangent and microwave heating for all ore powders combined was analysed using linear regression in Minitab but produced a poor fit (R^2 = 40.7%).

In the results of the Minitab linear regression routine six data points are identified as unusual observations – points that have a disproportionate effect on the regression. A subsequent fitting identified another poorly fitting measurement (See Section 8.3.6.2 of the Appendix for full regression reports). The final dataset with a linear regression fitting (R^2 = 89%) can be found in Figure 3-14 below. Also in Figure 3-14 are the re-measured data for the anomalous ore powder samples which support the anomalous behaviour, particularly at higher temperatures. Re-measurement of microwave heating is inappropriate because the sample processing technique was partially destructive; furthermore, the microwave heating data presented already represents the average of six heating measurements.

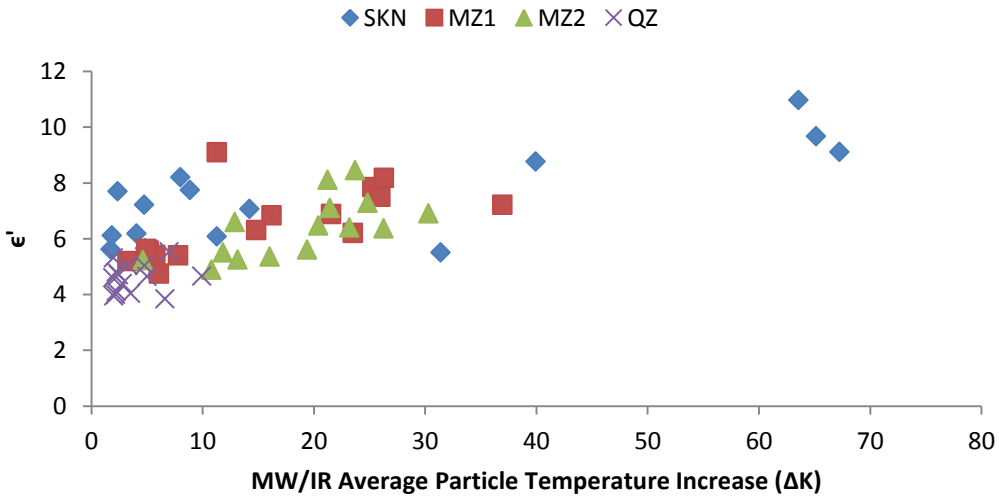

Figure 3-11 – Measured ϵ' for ore powders at 2470 MHz

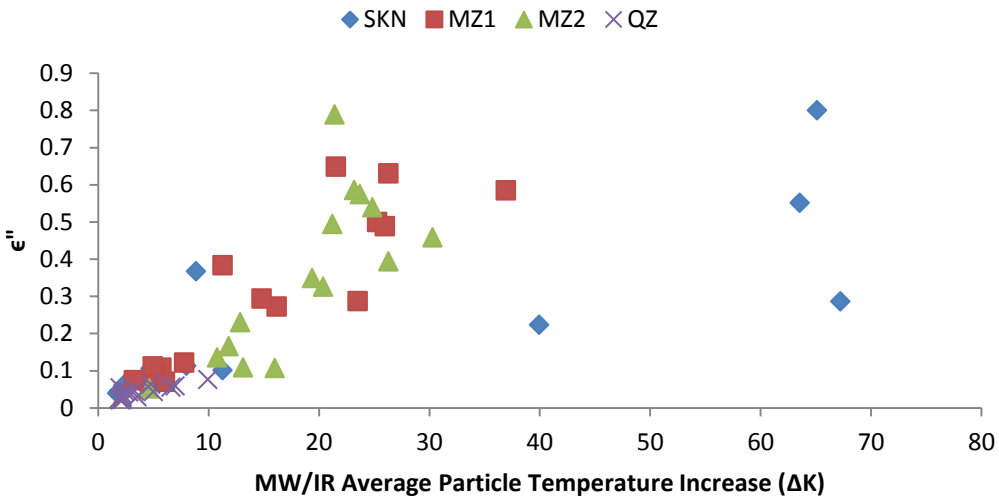

Figure 3-12 – Measured ϵ'' for ore powders at 2470 MHz

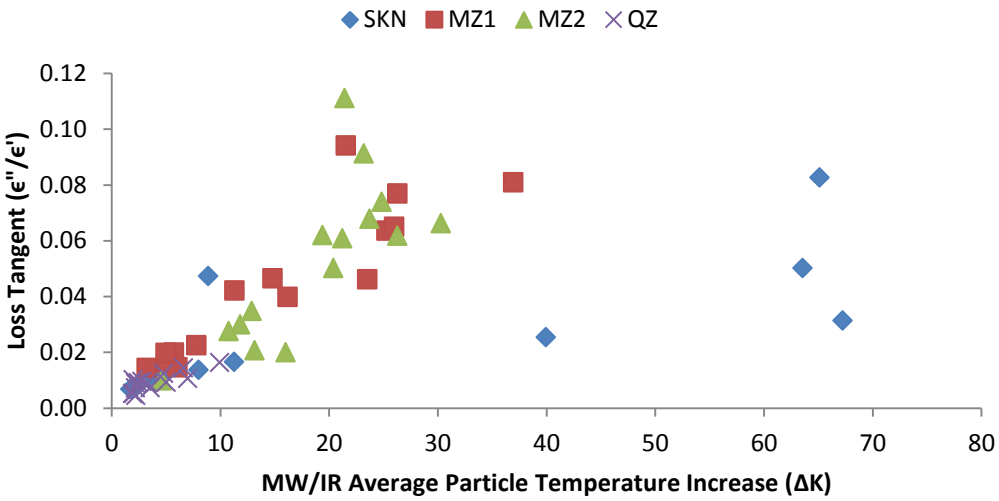

Figure 3-13 – Loss tangent of powders at 2470 MHz

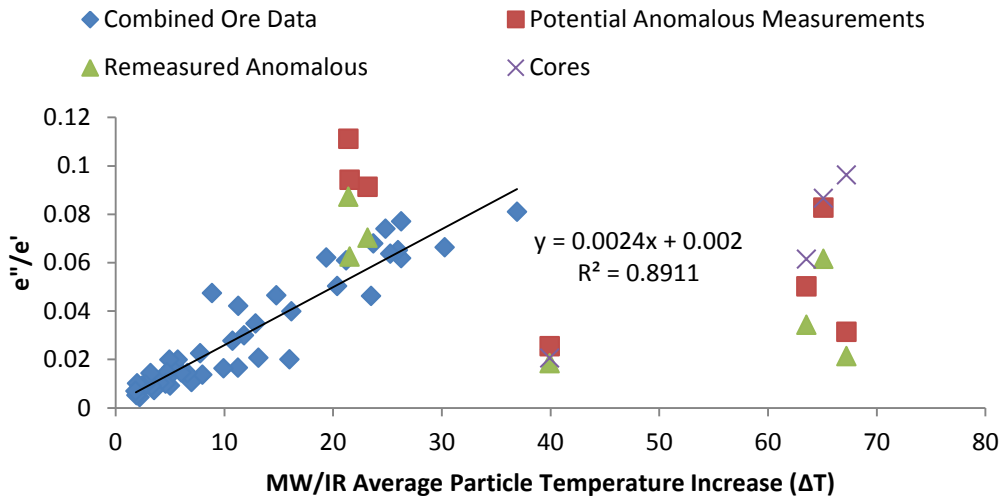

Figure 3-14 – Fitting of combined ore powder loss tangent data and excluding anomalous measurements

In the Literature Review (see Section 2.2.2), the heating rate of a lossy dielectric was given as Equation (3.9), below. In the MW/IR characterisation of ore particles, exposure times were set (12 seconds) as was the exposure frequency (2.45 GHz) and power (1200 W). Assuming that particles have similar density and specific heat the particle temperature change, ΔT, will be a function of the loss factor and the electric field intensity only. The electric field within an object does not necessarily have the same magnitude as the field in air and ranges from Equation (3.10) for field components tangential to the interface between the body and the external medium, to Equation (3.11) for field components normal to the interface (Landau & Lifschitz 1984). It is therefore possible that temperature changes due to microwave heating will be a function of ϵ''/ϵ'^2 rather than the loss tangent, ϵ''/ϵ'.

$$\frac{\Delta T}{t} = \frac{2\pi\epsilon'' f E^2}{\rho_m C_p} \tag{3.9}$$

$$\mathbf{E}_{t2} = \mathbf{E}_{t1} \tag{3.10}$$

$$\mathbf{E}_{n2} = \frac{\epsilon_1'}{\epsilon_2'}\mathbf{E}_{n1} \tag{3.11}$$

Regression analysis of the ϵ''/ϵ'^2 model with Minitab produces very similar results to the loss tangent regression above. Initial fitting of the entire data set a produces poor fit (R^2 = 39.9%) but again identifies the six anomalous data points. The subsequent regression again identifies the other poorly fitting measurement (See Section 8.3.6.2 of the Appendix for full regression reports). The final dataset with a linear regression fitting (R^2 = 88%) can be found in Figure 3-15 below, which also includes re-measured data for the anomalous ore powder samples which supports their anomalous behaviour. The regressions of both loss tangent and modified loss tangent produce a very similar R^2 value which means that either of these models may be used to describe heating equally well.

There are two distinct groups of anomalous samples, low-heating and high-heating. High-heating samples may be the result of textural effects (which is destroyed by pulverization) or interaction with the magnetic component of the field in the heating cavity. The loss tangent data for core measurements (see Figure 3-16) shows that the anomalous particles appear to conform to the same trend as the rest of the data. Linear regression of the combined core dataset (see Figure 3-17) produces a reasonable fit (R^2 = 75.7%). This indicates that the anomalous powders interact with the electromagnetic field differently to the cores and implies textural effects are the cause. Individual graphs of permittivity and loss factor data for core samples can be found in the Appendix (See Section 8.3.6.4).

Dielectric property measurement of cores for low-heating particles could not be accomplished as they were not successfully cut from the original particles. It is possible that the anomalous nature of both the high- and low- heating samples is due to the heterogeneity of the original particles and their halving. In this instance the cored and powdered halves of the high-heating samples would contain an unrepresentatively low fraction of microwave active minerals, while the low-heating samples contain unrepresentatively high fractions.

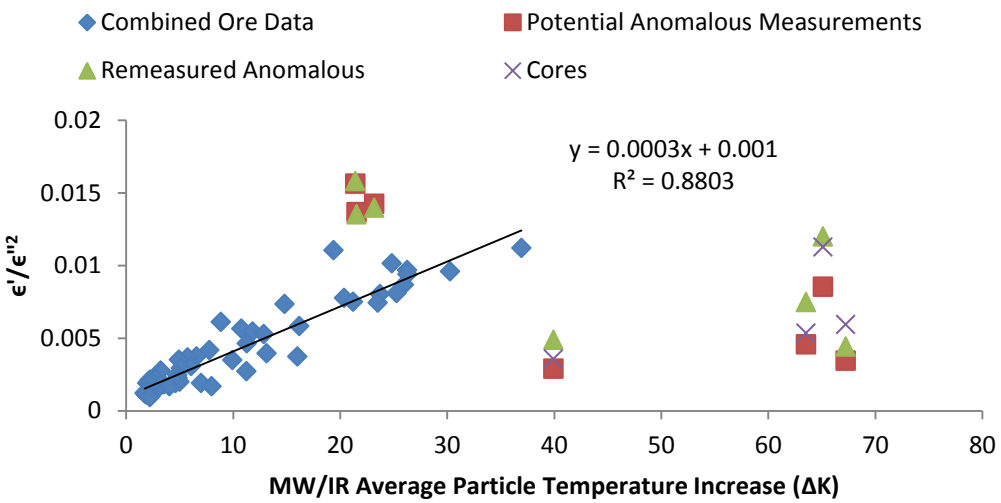

Figure 3-15 – Fitting of combined ore data using a modified loss tangent and excluding anomalous measurements

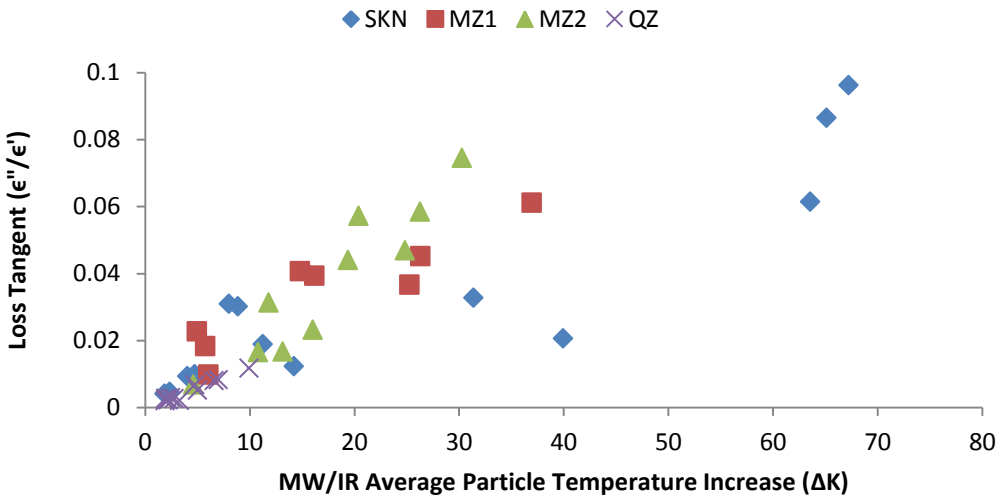

Figure 3-16 – Loss tangent of ore cores samples at 2470MHz

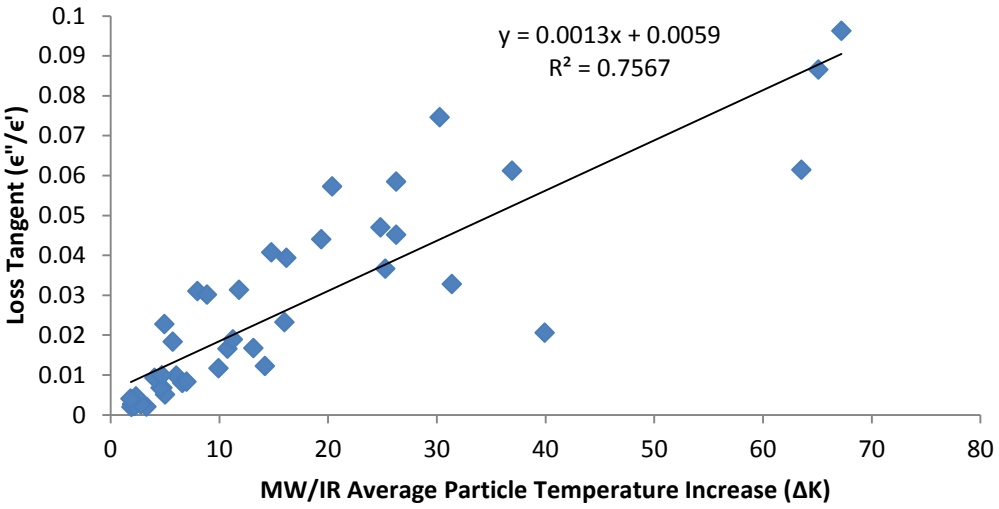

Figure 3-17 – Fitting of combined ore core loss tangent data

When logarithmic axes are used to plot the combined loss tangent data, the anomalous particles appear to fit better (see Figure 3-18). This log-log relationship is then analysed by combining the data into a single series (see Figure 3-19) and fitted with a power function. The resulting function, (3.12), shows a reasonable fit (R^2 = 0.79). A similar correlation can be observed when using the Loss Tangent data measured at 912 MHz although with slightly lower R^2 (0.71), potentially because the MW/IR characterisation was performed using a 2.45 GHz oven (See Section 8.3.6.3 of the Appendix). A linear regression of data on log-log plot is generally an invalid method for confirming a power law without further statistical analysis (Clauset, Shalizi & Newman 2009). A log-log relationship in this instance was used because it tends to collapse many trends to a line in log-log space. This provides a simple model of the entire dataset, including the anomalous measurements, with a reasonable quality of fit but with reduced statistical power. For this reason the log-log relationship should be considered qualitative.

$$y = 0.0041x^{0.78} \tag{3.12}$$

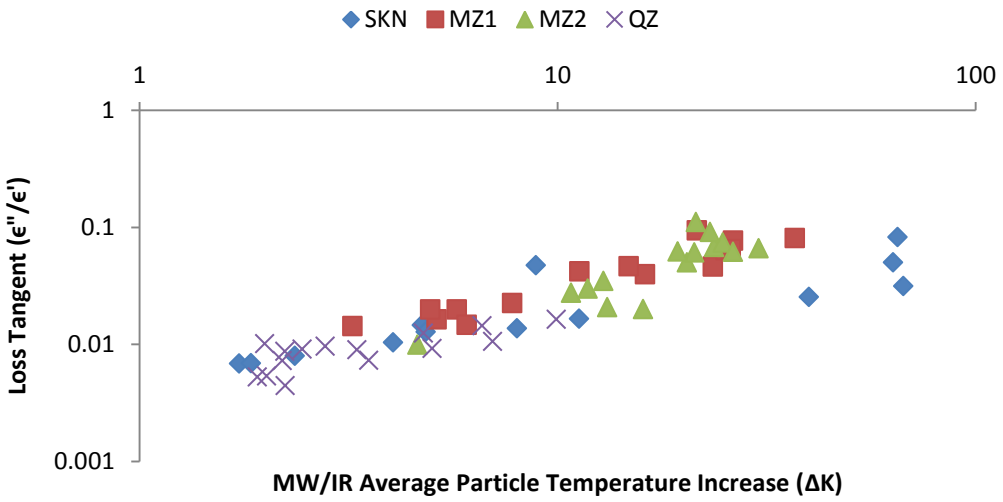

Figure 3-18 – Log-Log plot of loss tangent v. Average MW/IR temperature increase for powders at 2470 MHz

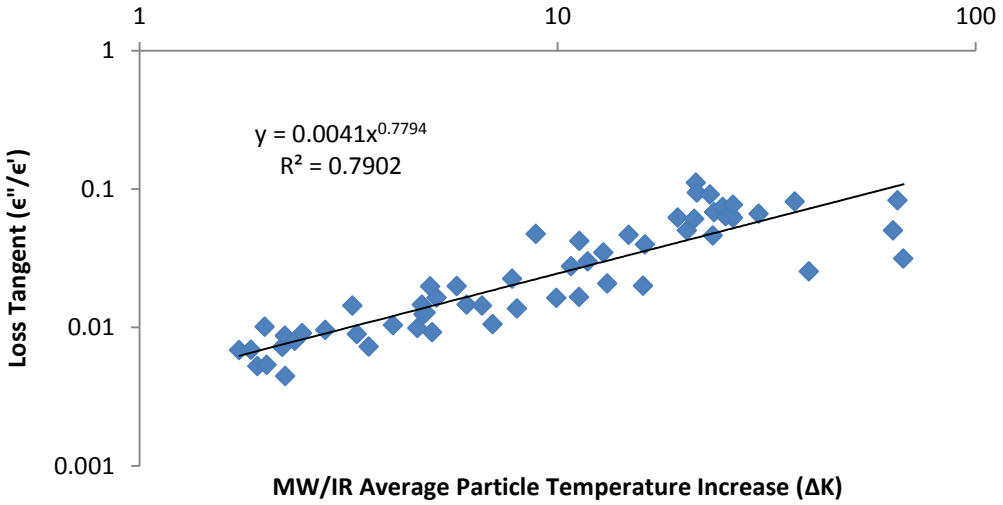

Figure 3-19 – Loss tangent data for all ore powders combined at 2470 MHz

3.3.4.2 Correlation of Ore Powder and Core Dielectric Data

Comparisons of both real and imaginary components of permittivity as well as loss tangent for core and powder samples at 2470 MHz can be found in Figure 3-20, Figure 3-21 and Figure 3-22 below. In these graphs the dielectric properties of powdered samples (ϵ', ϵ'' and loss tangent) are plotted

against the corresponding dielectric properties of cores taken from the original particles. Two SKN powder measurements produced unphysical, negative values for loss factor and were excluded from these graphs. These comparisons show general agreement between the core and powder samples with exceptions at high ϵ' and ϵ'' values due to SKN samples. That SKN core samples have higher permittivity than is predicted by the powdered sample which implies several effects including heterogeneity (resulting in unrepresentative cores) or mineral structural effects i.e. the extent of the conductive minerals.

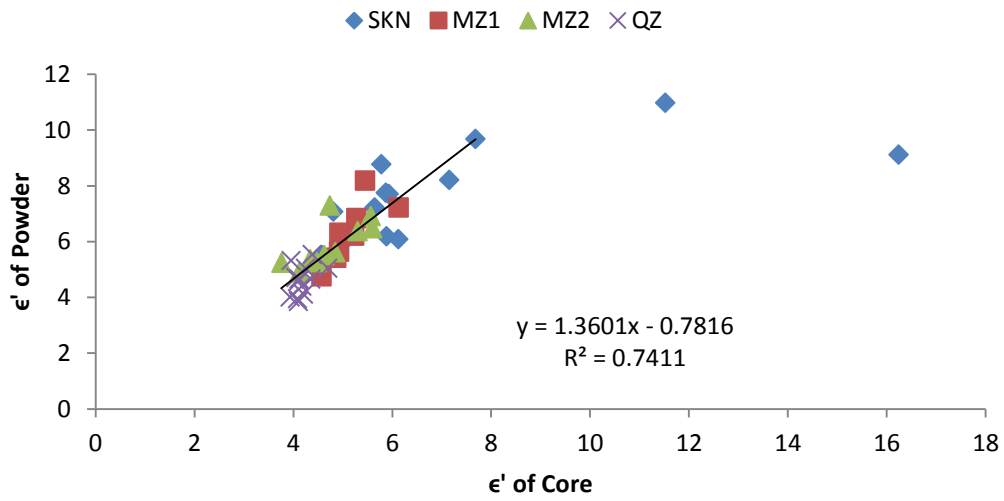

Figure 3-20 – The correlation of core and powder ϵ' at 2470 MHz (fit excludes two SKN samples)

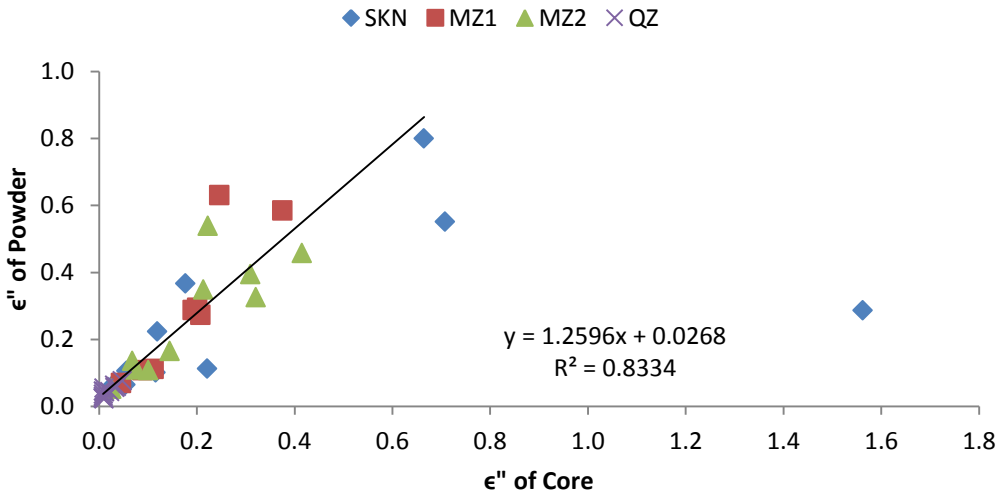

Figure 3-21 – The correlation of core and powder ϵ'' at 2470 MHz (fit excludes two SKN samples)

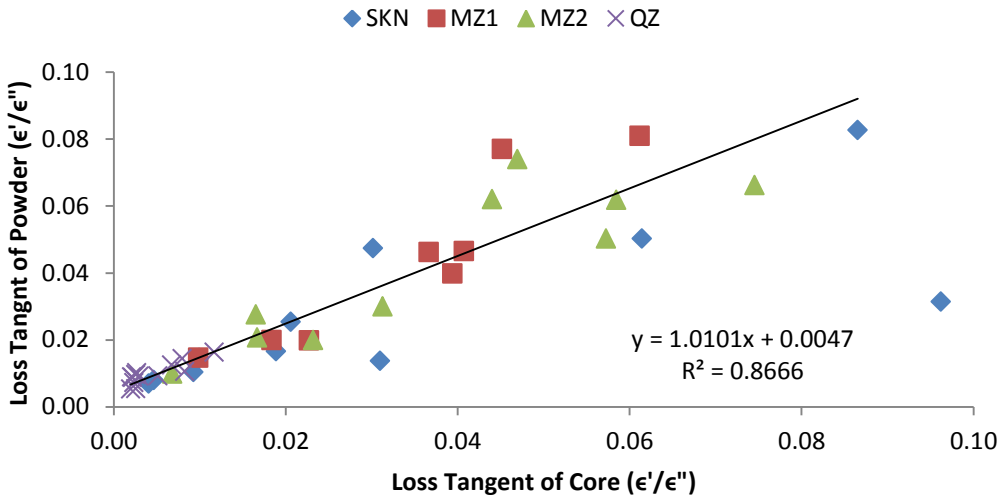

Figure 3-22 – The correlation of core and powder loss tangents at 2470 MHz (fit excludes two SKN samples)

3.3.4.3 Dielectric Properties of Ore Samples at Different Frequencies

Measurements were conducted at different frequencies to understand how dielectric properties may change with frequency. The correlation of 912 and 2470 MHz measurements was used to study frequency effects. Figure 3-23, Figure 3-24, and Figure 3-25 show a strong correlation between the dielectric properties of ore powders at 912 and 2470 MHz. Combined ore powder data can be found in Figure 3-26 and Figure 3-27 below. An almost perfect 1:1 correlation is visible in the dielectric constant (Figure 3-26); however, Figure 3-27 shows that loss factors are consistently larger at 912 MHz by approx. 1.35:1. The increase in loss factor at 912 MHz is also reflected in the correlation of loss tangent data (Figure 3-28).

When the larger, 912 MHz, loss factors are used in the power relationship between loss tangent and microwave heating (See Equation (3.12)), it can be found that the 35% increase in loss tangents equates to an increase in microwave heating of approx. 46%. It would therefore appear that 912 MHz is a preferable operating frequency for microwave heating. However, this interpretation does not take in to account the frequency term in the numerator of the heating rate formula (See Equation

(2.37) in Section 2.2.2 of the Literature Review). This means that, under the assumption of bulk heating, for the identical field strengths and exposure times, particles in a 912 MHz field should only experience approx. 54% of the heating of those heated in a 2470 MHz field. A MW/IR characterisation scheme procedure that includes sets of particle heating measurements in a 915 MHz field would confirm this finding.

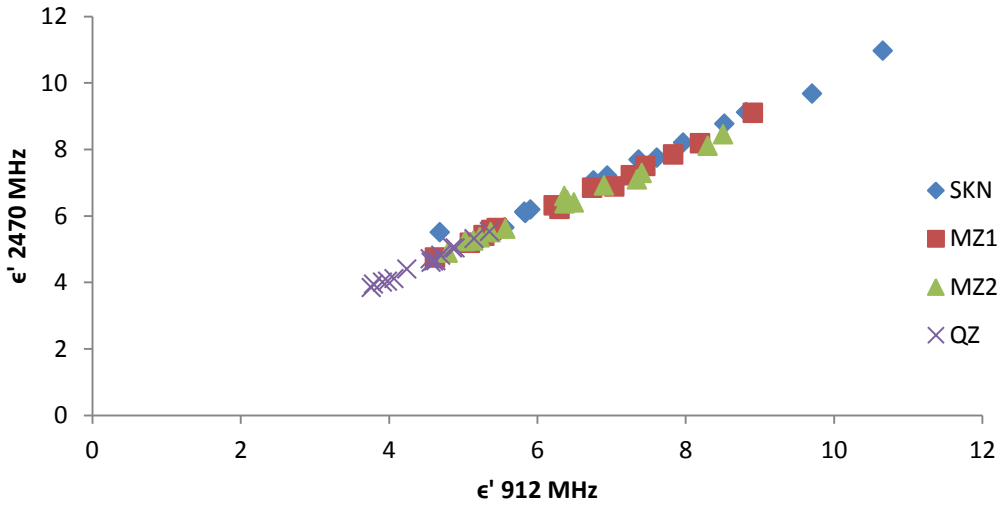

Figure 3-23 – The correlation of 912 and 2470 MHz ϵ' measurements of ore powders

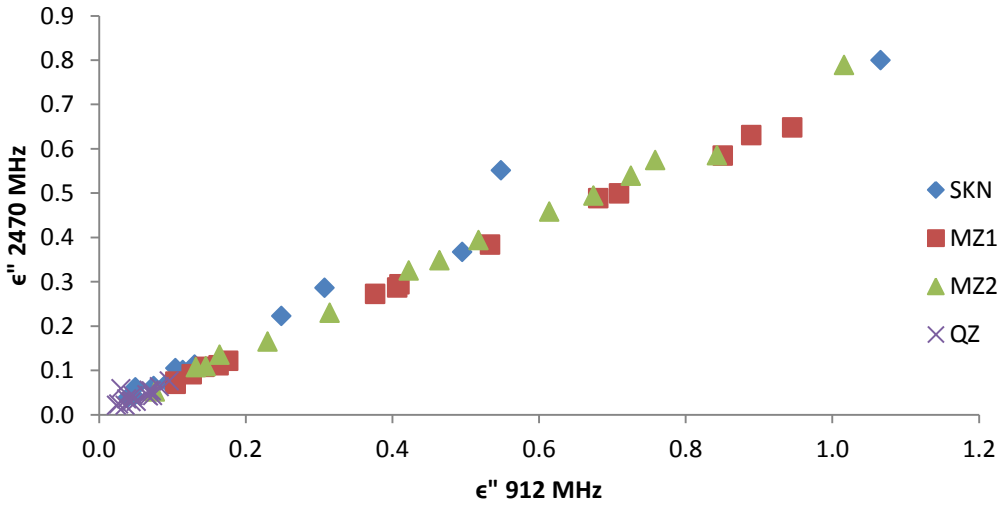

Figure 3-24 – The correlation of 912 and 2470 MHz ϵ'' measurements of ore powders

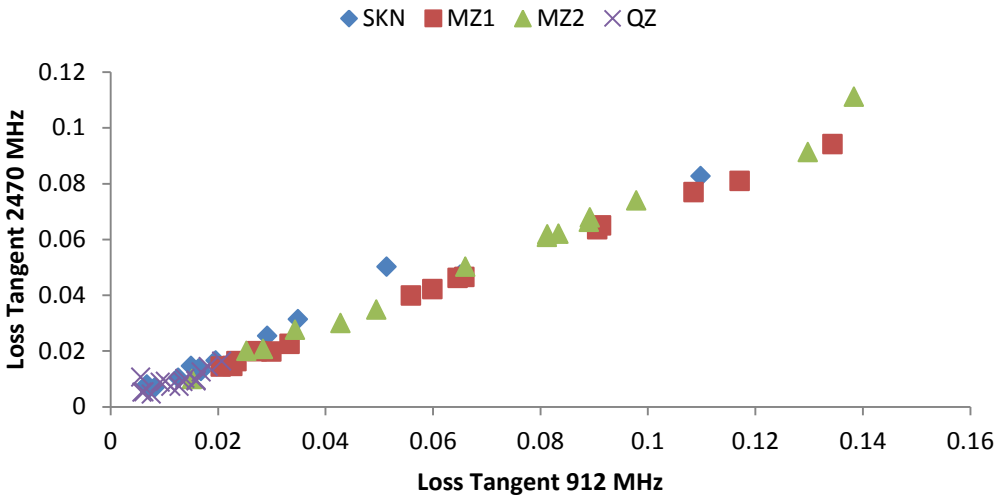

Figure 3-25 – The correlation of 912 and 2470 MHz loss tangent measurements for ore powders

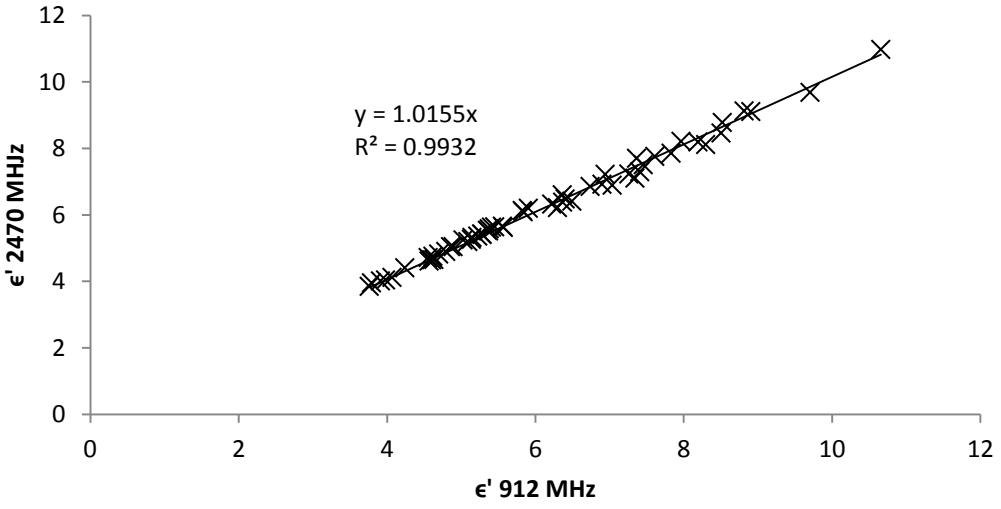

Figure 3-26 – The correlation of 912 and 2470 MHz ϵ' measurements for combined ore powders

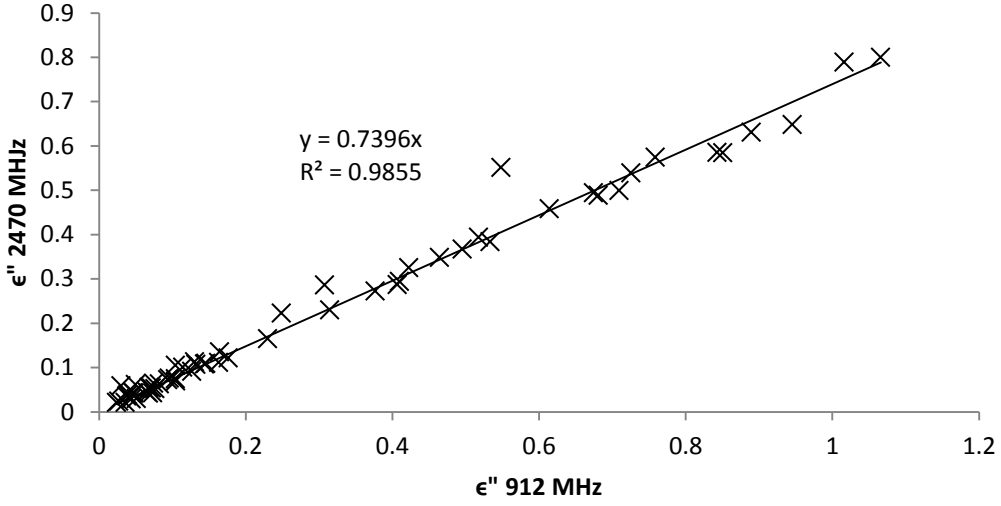

Figure 3-27 – The correlation of 912 and 2470 MHz ϵ'' measurements for combined ore powders

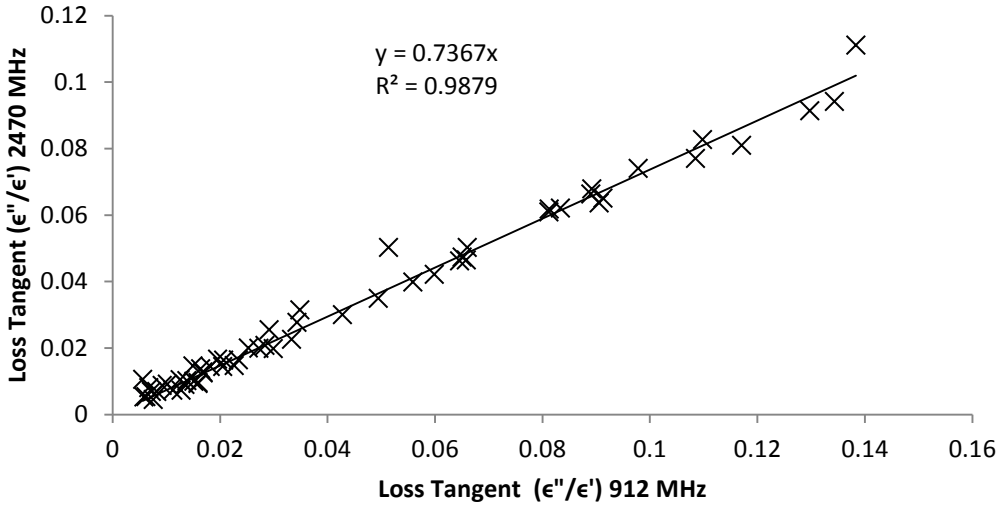

Figure 3-28 – The correlation of 912 and 2470 MHz loss tangent measurements for combined ore powders

3.3.4.4 Mineral Dielectric Properties

In addition to the dielectric measurements of characterized ores, cavity perturbation measurements were performed on a set of pure mineral specimens. In addition to measurements at room temperature, further measurements were made to investigate the behaviour of dielectric properties

at elevated temperatures. The results of cavity perturbation measurements of both powder and core samples of mineral can be found in Table 3-15 and Table 3-16. Immediately visible in these tables are the discrepancies between sulphide (chalcopyrite and pyrite) core and powder measurements. However, there do not appear to be significant differences in the results for quartz or feldspar samples. The values obtained from sulphide cores are lower than those for powder samples but the reasons for this are unclear. One reason for the disparity is that the solid core samples are conductive and have a large effect on the field in the cavity which results in either measurements of surface impedance or invalid perturbation equations. It is unlikely that these discrepancies are due to heterogeneity as was observed above in the ore samples (See Section 3.3.4.2) because of the phase purity of the mineral specimens.

The loss factors of feldspar, garnet and quartz powders are statistically indistinguishable when using the standard deviation (0.018) determined by analysis of the factorial experiment (see Section 3.3.3.3). Similarly, the permittivity of quartz and feldspar powders are indistinguishable using the standard deviation obtained (0.381) from the factorial experiment.

Table 3-15 – Measured dielectric properties of mineral powder specimens at 2470 MHz

Mineral	ϵ'	ϵ''	ϵ''/ϵ'	ϵ''/ϵ'^2
Pyrite	26.38	5.94	0.2252	0.0085
Chalcopyrite	21.81	1.51	0.0692	0.0032
Molybdenite	15.42	2.18	0.1411	0.0092
Garnet	10.64	0.017	0.0016	0.0002
Mica	8.17	0.089	0.0109	0.0013
Quartz	4.63	0.018	0.0039	0.0008
Feldspar	4.60	0.018	0.0040	0.0009

Table 3-16 – Measured dielectric properties of mineral core specimens at 2470 MHz

Mineral	ϵ'	ϵ''	ϵ''/ϵ'	ϵ''/ϵ'^2
Pyrite	13.12	0.7978	0.0608	0.0046
Chalcopyrite	11.73	0.3400	0.0290	0.0025
Feldspar	5.12	0.0314	0.0061	0.0012
Quartz	4.36	0.0013	0.0003	0.0001

The measured dielectric properties of chalcopyrite fit within ranges in scholarly literature which start at ϵ' = 8.4, ϵ'' = 0.2 for chalcopyrite powders (Lovás et al. 2010) and reach ϵ' = 77.5 (Holderfield & Salsman 1992). Lovás et al. (2010) also published values for a pyrite powder (ϵ' = 8, ϵ'' = 0.2), showing similar values to the chalcopyrite powder; which is echoed in the measured properties. Although no dielectric property data could be found, molybdenite is known to heat rapidly in a microwave field (Ford & Pei 1967) and this supports the measured dielectric properties.

A medium is considered a good conductor when it fulfils the inequality in Equation (3.13) and a good insulator when it fulfils the inequality given in Equation (3.14). When the Equation (2.26) of the Literature Review is applied to Equations (3.13) and (3.14) we arrive at inequalities purely in terms of the loss tangent – good conductors have a loss tangent much greater than unity (3.15), while good insulators have loss tangents much less than unity (3.16). In Table 3-15 and Table 3-16 it can be seen that all minerals species measured had a loss tangent less than one – the largest being pyrite at 0.23. This illustrates that the gangue minerals are good insulators and that, while semiconductors, the sulphides cannot be considered good conductors.

$$\frac{\sigma}{\omega\varepsilon_0\varepsilon'} \gg 1 \qquad (3.13)$$

$$\frac{\sigma}{\omega\varepsilon_0\varepsilon'} \ll 1 \qquad (3.14)$$

$$\frac{\varepsilon''}{\varepsilon'} \gg 1 \quad (3.15)$$

$$\frac{\varepsilon''}{\varepsilon'} \ll 1 \quad (3.16)$$

The dielectric properties of the quartz core is comparable to the values published by Church, Webb and Salsman (1988) (ϵ' = 3.94 ϵ'' = 0.00063) and the 95% confidence interval, as defined by the uncertainty characterisation, of the measured quartz powder data also encompasses literature data. The dielectric properties from powdered feldspar sample are somewhat similar to the values published by Church, Webb and Salsman (1988) (ϵ' = 4.34 ϵ'' = 0.00019) for Orthoclase, although the results for the core sample differ slightly. The measured mica sample have dielectric properties similar to phlogopite ϵ' = 9.77 ϵ'' = 0.41 (Nelson, Lindroth & Blake 1989). Unfortunately no dielectric properties for garnet are found in scholarly literature to compare with the measurement results. These measurements highlight two issues: there are not many mineral dielectric properties published in scholarly literature; and when dielectric data are published the mineral samples are not well characterized in terms of chemical composition.

3.3.4.5 Evolution of Mineral Dielectric Properties with Temperature

A series of measurements were performed to investigate the effect of temperature on mineral dielectric properties. These measurements were accomplished on the C1 cavity using the elevated temperature measurement technique described in Section 3.3.2 and the results of which can be found in Figure 3-29, Figure 3-30 and Figure 3-31. In these figures, the dielectric properties of mineral samples are plotted against the temperature at which the properties are measured. The figures demonstrate that temperature can influence the real and complex permittivity components, along with loss tangent, of each mineral in different ways. These experiments began at room temperature and were set to reach 700°C with measurements performed in either 20°C or 25°C intervals. Intermittent software failures cut short the measurement runs of the gangue minerals (feldspar, garnet, mica and quartz). Despite being restricted to lower temperatures the gangue

minerals show very little movement in dielectric properties between room temperature and approx. 200 °C when compared to the sulphides.

Figure 3-29 shows that the dielectric constant is stable for all minerals, barring molybdenite, between room temperature and approx. 475°C. At 475°C the dielectric constants for both chalcopyrite and pyrite increase sharply as do the loss factors (see Figure 3-30). This is most likely the result of chemical changes. In pyrite this is most likely a reduction to pyrrhotite and hematite somewhere between 300°C and 600°C (Music, Popović & Ristić 1992). However, before the chemical change the loss factor of pyrite drops considerably between room temperature and approx. 200°C, reminiscent of metallic rather than semiconductor conduction behaviour. Above 200°C the loss factor remains stable until approximately 475°C where it experiences a sharp increase. The loss factor of chalcopyrite increases between room temperature and approx. 100°C but, like pyrite, also falls considerably between 200°C and 475°C. The drop in loss factors of pyrite and chalcopyrite is reflected in the loss tangent which reduces them to a level comparable with the gangue minerals (feldspar, garnet, mica and quartz).

A consequence of the drop in loss tangent is that pyrite and chalcopyrite will experience lower heating rates at elevated temperatures. For pyrite, any increase in temperature above room temperature will slow its heating rate, while chalcopyrite heating rates slow above approx. 100°C. These reduced heating rates at higher temperatures mean that the degree of selective heating in chalcopyrite and pyrite decreases. To contrast with the temperature behaviour of chalcopyrite and pyrite, the dielectric constant of molybdenite increases with temperature all the way to the termination of the experiment at 625°C. The loss factor of molybdenite increases slowly from room temperature to a peak at approx. 275°C. Molybdenite's loss factor then slow decreases to approx. 500°C where a physical or chemical change causes a much sharper drop. The implication of this is that the discrimination of MW/IR system focussing on the recovery of molybdenite may achieve selective heating all the way up to 500°C.

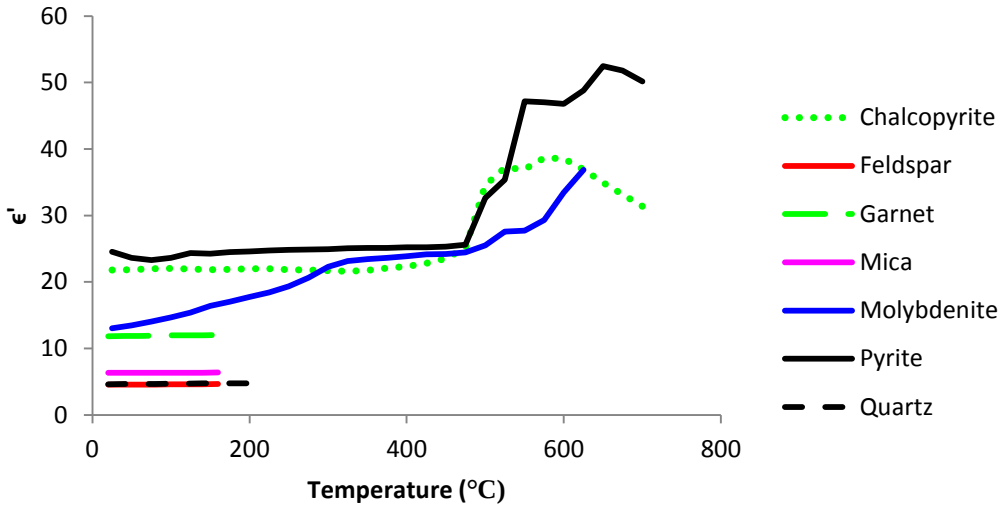

Figure 3-29 – Evolution of ϵ' with temperature of minerals at 2470 MHz

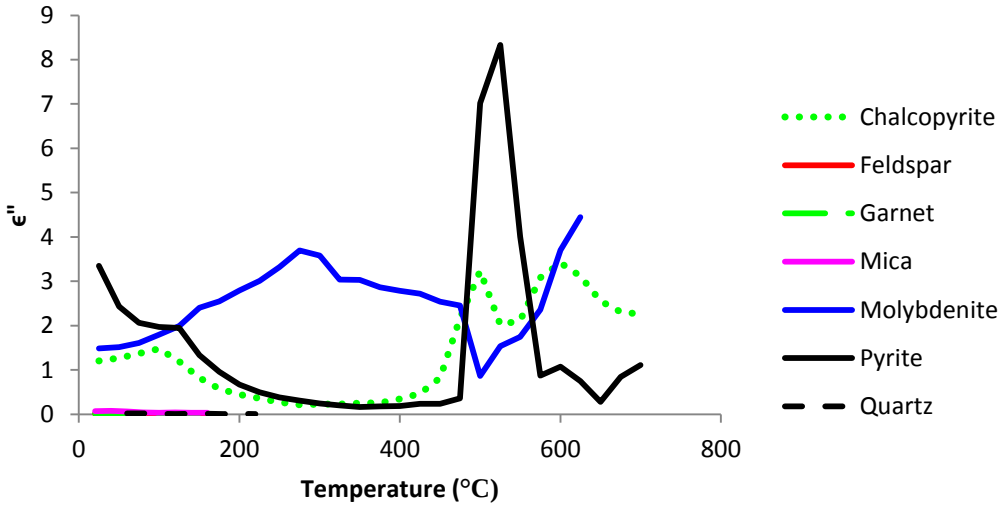

Figure 3-30 – Evolution of ϵ'' with temperature for minerals at 2470 MHz

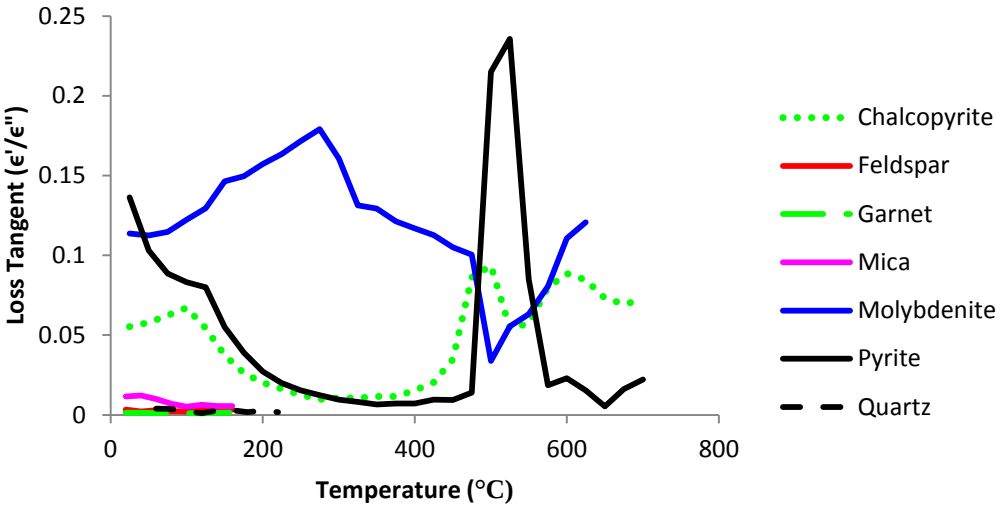

Figure 3-31 – Evolution of the dielectric loss tangent of minerals at 2470 MHz with temperature

3.4 Conclusion

Heating of particles from six different ores was characterized using infrared thermography. Of the six ores, four were chosen and each particle in those sets was processed into core, halve and powder samples. While performing the MW/IR characterisation it was found that a degree of discrimination between ores could be found using relative standard deviation of IR pixel temperatures on particle surfaces.

Once, characterized and processed the ore samples, along with a small set of mineral samples, were taken to the University of Nottingham for cavity perturbation measurements. Before measurement of the ore samples, a factorial design uncertainty characterisation experiment was conducted using mixtures of quartz and pyrite. This experiment analysed the significance of sample mass, volume and dielectric properties as well as provided an overall estimate of the error in dielectric measurement using the C1 cavity. It was firstly found that there is no additional uncertainty in the dielectric loss factor beyond the measurement noise when the position of the sample tube within the cavity is optimized. However, permittivity measurements are sensitive to tube position and, even when optimizing the position, the measurement uncertainty exceeds the noise floor. Analysis of the factorial experiment revealed that tapping was a poor method for controlling powder compaction,

while both mass and mixture have a statistically significant effect on the dielectric constant and loss factor. The analysis also produced general estimates of the standard deviation in dielectric properties; 0.381 for dielectric constant and 0.018 for the loss factor.

Analysis of dielectric data for ore samples revealed that the loss tangent and modified loss tangent produced good fits (89% and 88% respectively) to describe the bulk of measurements but only when specific, anomalous, samples were excluded. As expected, a log-log relationship between loss temperature and the MW/IR temperatures for both powders and cores collapsed anomalous measurements to a single relationship. This log-log relationship qualitatively produced a good fit (79%) capable of describing heating behaviour for the entire data set, including the anomalous samples but, in the absence of further analysis, lacks statistical power. A linear correlation was found in dielectric measurements at 2470 and 912 MHz, and the loss tangents of samples at 912 MHz were found to be approx. 35% larger than at 2470 MHz. Using the power relationship (3.12) and accounting for the effect of frequency, it was calculated that particles exposed to 912 MHz radiation should heat at approx. 54% the rate of those in a 2470 MHz field. A general correlation was found between powder and core measurements; however there was significant deviation, particularly in the SKN sample, presumably due to the properties, such as heterogeneity, of samples and the core sampling method, and warrants further investigation.

Dielectric measurement of most mineral samples is supported by values found in literature. The measurements confirm that sulphides have much higher dielectric properties than gangue mineral and are good targets for selective heating. However the loss tangents of all sulphide minerals were found to be less than unity therefore cannot be considered conductive. Unlike the ore samples, the behaviour of mineral dielectric properties with temperature was investigated. The results of these measurements show that, despite stable dielectric constants, the loss factor and loss tangent of chalcopyrite and pyrite drop considerably between room temperature and about 200°C. However, the loss tangent of molybdenite remains high to approx. 500°C. This indicates that a MW/IR sorting process targeting copper recovery will have better selective heating, and hence thermal contrast, when minerals remain below 100°C. Above 500°C the chalcopyrite, pyrite and molybdenite experience several phase or chemical changes which create sharp peaks in permittivity.

These outcomes of this chapter suggest two avenues of research. The first is to explore the reasons that anomalous samples do not heat like their dielectric properties suggest they should. Magnetic field interactions and mineral structuring have been identified as the possible mechanisms for anomalous heating and are further investigated in the Chapter 4. The second avenue of research is to form an understanding of the mineralogical compositions and underlying mineral chemistry in different ores and how these relate to dielectric properties and microwave heating; this is addressed in Chapter 5.

4 Magnetic Measurement and Resonant Cavity Texture Characterisation

4.1 Introduction

In the previous chapter a small number samples were identified which did not follow the correlation between loss tangent and microwave heating observed in all other particles (see Section 3.3.4.1, Figure 3-14). Two different behaviours were observed in these anomalous samples; heating above and heating below what would be expected due to the dielectric properties. Re-measurement of the powder samples as well as their solid cores continued to support their anomalous behaviour. This chapter focuses on the anomalous samples in an attempt to understand why these particles behaved differently in MW/IR characterisation and dielectric property measurement.

There are a number of possible reasons for the unusual relationships between microwave heating and dielectric properties observed in the anomalously heating samples. For samples to heat at rates up to approx. 4.6 K/second above the rate anticipated by dielectric properties suggests that microwave energy is being dissipated in those samples in some other manner. This could be the result of a strong interaction with the magnetic field components, high permittivity structures within particles which improve the coupling of particles to the electric field (texture), or effects external to the particle such as higher than expected electric field concentrations.

Dielectric measurement of sulphide minerals revealed loss tangents less than unity, for this reason it is unlikely that these minerals have the ionic charge carriers available for induction heating to occur. The pulverization of samples destroys the texture of particles so, while it can potentially explain the high-heating samples, it cannot explain occurrence of low heating samples (up to approx. 2 K/second below the rate expected by dielectric properties). The natural heterogeneity of the rock particles used can potentially explain both low- and high-heating samples. While particles are effectively homogenized when powdered, the processing regime included halving particles with a diamond saw to retain a solid section. Therefore powder samples only represent a sub-section of the whole particle and this potentially leads to an unrepresentative powder sample.

There are three aims to the investigations detailed in this chapter. Firstly, to determine whether ore samples can be consider purely as lossy dielectrics by measuring their magnetic permeability and comparing it to microwave heating rates. This is accomplished by measuring the permeability of ore samples at radio frequencies (RF) using a magnetic susceptibility meter (Ultra-Dynamics bench-top Magnasat) and compared to microwave heating data from Chapter 3. Secondly, to determine whether mineral structuring in particles can influence microwave heating by rotating cylindrical samples in a resonant cavity. Thirdly, to qualitatively determine whether the heterogeneity of sulphides may lead to unrepresentative sampling when halving particles by examining retained solid sections of anomalous samples using automated scanning electron microscopy (FEI Quanta 600 Mk 1), also referred to as a Mineral Liberation Analyser (MLA).

4.2 Magnetic Properties

A strong coupling to the magnetic field is one explanation for samples, particularly from the SKN ore, which heats much more than their dielectric properties alone suggest. Poynting's Theorem (see Equation (4.1) and (4.2) below) describes the rate of electromagnetic energy transfer through and into a medium. These equations show energy is stored in both the electric and magnetic portions of the field. Therefore a strong interaction with the magnetic field and heating will result from minerals with significant magnetic permeability such as magnetite or pyrrhotite. However, skarn ores, such as the SKN sample, commonly contain the mineral garnet which can also be ferrimagnetic depending on its chemical composition and therefore have a non-negligible interaction with magnetic fields too. Measurements of the magnetic properties of ore samples were accomplished using an inductance measuring device called a 'Magnasat'. Two sets of magnetic measurements were performed. An initial investigation into the relationship between magnetic properties and measurement frequency was performed in a reduced sample set and then all powdered samples were measured at a single frequency.

$$\frac{\partial u}{\partial t} = -\nabla \cdot \mathbf{S} - \mathbf{J}_f \cdot \mathbf{E} \qquad (4.1)$$

Where the energy density, u, is given by:

$$u = \frac{1}{2}\left(\mathbf{E}\cdot\mathbf{D} + \mathbf{B}\cdot\mathbf{H}\right) \tag{4.2}$$

4.2.1 Magnasat Device and Measurement Procedure

The Magnasat is a device for measuring magnetic susceptibility of materials between 348 and 14177 Hz (see Figure 4-1). Although this is well below the microwave regime, measurements at these frequencies give an insight into the presence of a magnetic fraction. The permeability of ferromagnetic materials is known to decrease sharply in the microwave regime (Hodsman, Eichholz & Millership 1949; Kittel 1946). However, this means that measurements at RF frequencies will exaggerate the permeability of microwave frequencies and make identification of particles heating due to strong interactions with the magnetic field easier. The Magnasat has three main sub-systems: the send/receive solenoids, the solenoid electronics, and a PC running control and data logging software. There are two solenoids in a Magnasat; on each solenoid send coils are wound on top of receive coils. On the first solenoid the receive coil is wound in the same direction as the send coil but is wound the opposite direction on the second coil (Cavanough 2003). As a result of the flux linkage between the send and receive coils, when a sample is placed in a solenoid it changes the amplitude of the voltage in the receive coil circuit proportional to its magnetic susceptibility (Cavanough & Holtham 2000). The proportional response is then calibrated with a material of known susceptibility. This configuration was adopted to minimize temperature drift issues encountered in systems using a single solenoid and bridge circuit (Cavanough & Holtham 2000).

Figure 4-1 – The Magnasat, $MnCl_2$ calibrant and control PC

Calibration of the Magnasat is required every time one of the measurement conditions, such as gain or frequency, is changed. To do this, a calibrant with known mass and magnetic susceptibility are required. In this case calibration was performed with a 45 gram manganese chloride ($MnCl_2$) calibrant (χ_m = 9.49 x 10^{-7}). Once calibrated, measurements using the Magnasat are simple; firstly powder samples are transferred to an appropriately sized vial and both their mass and volume measured. The sample name and mass are then entered into the control and logging software and the measurement trigged. To produce a value for magnetic susceptibility, the Magnasat needs to measure the receive signals twice; first with the sample in the solenoid and then whilst the solenoid is empty. The result of the magnetic susceptibility measurement is then both displayed on-screen and logged in a comma-separated values (CSV) file.

The data produced by Magnasat measurements requires further processing to arrive at results in terms of volume magnetic susceptibility. The Magnasat requests the sample mass prior to measurement and then measures the change in flux linkage. This means that the Magnasat can only produces data in form of mass susceptibility (measured in m^3/kg), χ_m. This is then converted to volume susceptibility, χ_v, using the density of the sample, ρ (see Equation (4.3)), calculated from the sample mass and volume measured previously, and related to real component of permeability via Equation (4.4).

$$\chi_v = \rho \chi_m \tag{4.3}$$

$$\mu' = \chi_v + 1 \tag{4.4}$$

Given the duality of electrostatic and magnetostatic problems (Sihvola & Lindell 1992), the Landau-Lifschitz-Looyenga dielectric mixing equation can be applied to calculate the magnetic properties of solids from powders (see Equation (4.5)).

$$\mu_{solid} = \left[\frac{\left(\mu_{powder}^{1/3} - 1 \right) \rho_{solid}}{\rho_{powder}} + 1 \right]^3 \tag{4.5}$$

4.2.2 The Effect of Frequency on Magnetic Permeability

In order to investigate the magnitude of frequency dependence in Magnasat measurements, one sample of each ore was selected and measured across a range of frequencies (see Table 4-1). Since calibrations are required for each frequency change, the four samples were measured in order, three times at each frequency, for a total of twelve measurements per calibration. Regression analyses (both linear and quadratic) were performed on each data series displayed in Figure 4-2 (see Section 8.4.1 of the Appendix for full regression reports). Of these analyses only the QZ sample had statistically significant linear and quadratic terms, however, the magnitude of these terms was very small (of the order 10^{-8} and 10^{-12} respectively). In the other three ore samples, no significant permeability response to frequency was found in the samples chosen. Therefore any measurement within the frequency range of the Magnasat (348 to 14177 Hz) will produce results similar to any other frequency within the range.

Table 4-1 – Magnasat measurement frequencies and their gain settings

Frequency (Hz)	*Gain*
348	50000
1391	10000
2704	5000
9489	2000
14177	2000

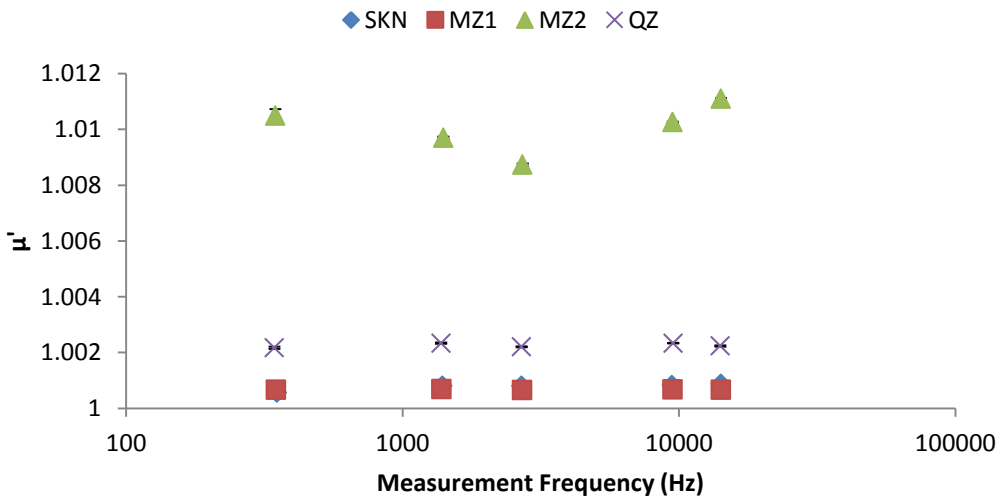

Figure 4-2 – The evolution of permeability with frequency in four ore samples

4.2.3 Comparison of Magnetic Permeability and Microwave Heating

Measurements of the permeability of ore powder samples were conducted at 9489 Hz using the Magnasat. The results of these measurements can be found in Figure 4-3 below plotted against the MI/IR temperature changes observed for whole particles in Chapter 3 (see Section 3.2.2). Figure 4-3 shows no correlation between permeability and microwave heating, although it is interesting to note that QZ samples on average have higher RF permeabilities than the other ores. Linear and

quadratic regression of these data shows no relationships between ore powder permeability and the whole particle MW/IR characterized temperatures (see Section 8.4.2 of the Appendix for full regression reports).

One MZ2 particle appears to be significantly more magnetic than all other particles (see Figure 4-3). If heating due to a strong magnetic field interaction is affecting the anomalous samples, this particle should also have MW/IR heating behaviour that cannot be predicted using the dielectric loss tangent. To test this, the MZ2 particle is identified in a plot of dielectric loss tangent and MW/IR characterised heating (see Figure 4-4). It is evident in Figure 4-4 that the high permeability sample heats indistinguishably from the combined ore data and can consequently be considered as a lossy dielectric. Similar to Figure 4-3 RF permeability is plotted against MW/IR heating in Figure 4-5 although the data is separated into anomalous and normal samples. It can be seen in Figure 4-5 that anomalous samples do not express any significantly greater magnetic properties. This indicates that magnetic heating is unlikely to be responsible for anomalous microwave heating behaviour.

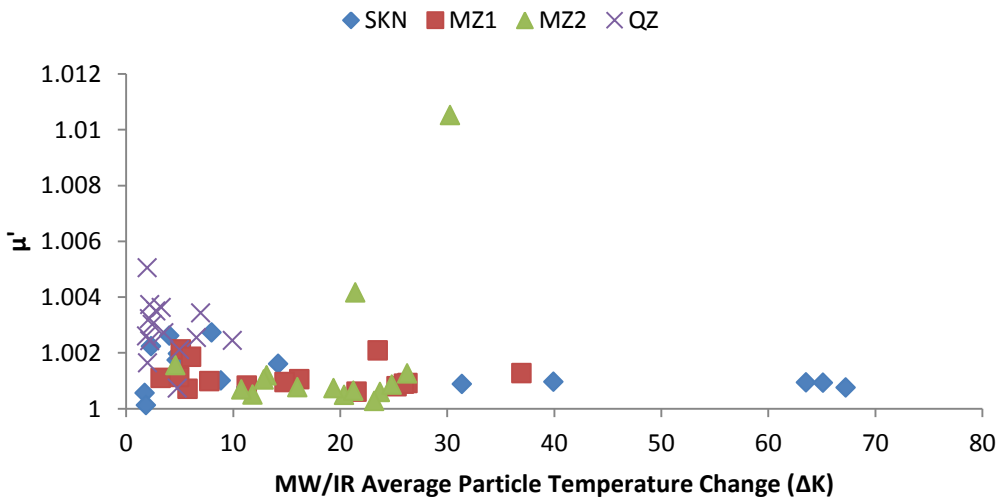

Figure 4-3 – The magnetic permeability of ores (9.5 kHz)

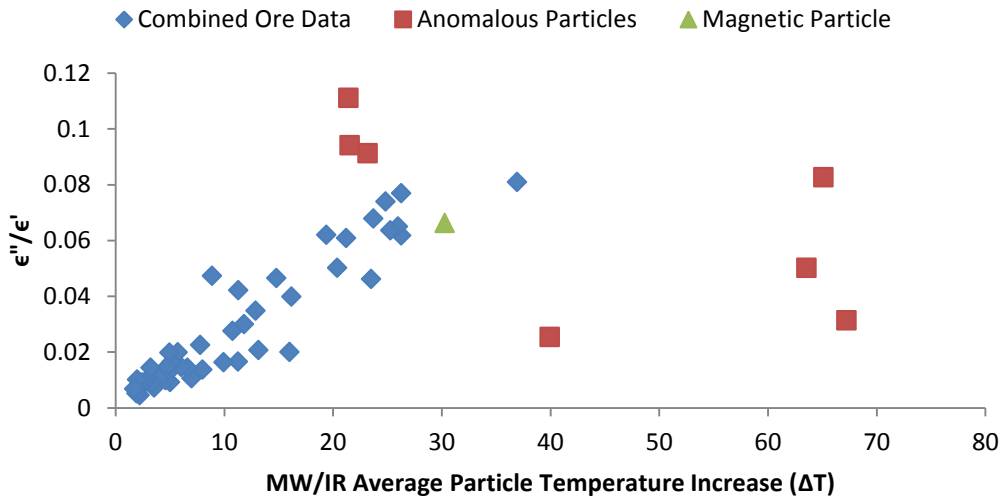

Figure 4-4 – Identification of the magnetic and anomalous particles in dielectric properties and microwave heating

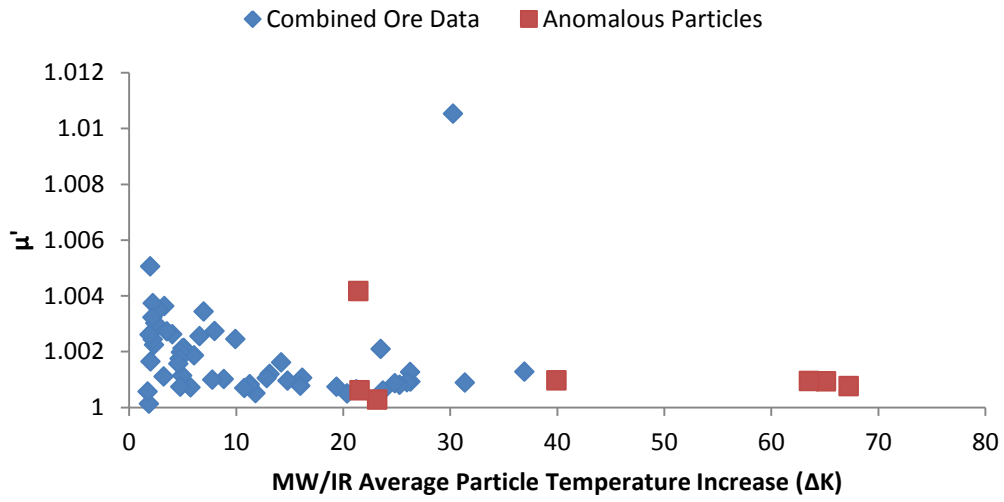

Figure 4-5 – Identification of the anomalous particles in heating and permeability

4.2.4 Conclusion

Regression analysis has shown there is no, or vanishingly small, relationship between frequency and permeability in the range 348 to 14177 Hz in the four specimens examined. Measurements were

then conducted on the full set of ore powder samples at 9489 Hz. Regression analysis of these measurements found no relationship between permeability and the characterized microwave heating of the original particles. Additionally, the permeability of the anomalously heating particles was indistinguishable from the other ore samples. Consequently the heating of ore particles as a result of interactions with the magnetic field components in a cavity does not explain the anomalously hot specimens. Furthermore, the most magnetic sample was not a member of the anomalously heating set and heats similarly to all other samples.

4.3 Texture Properties

Depolarisation resulting from needle, or rod, shaped inclusions in mixtures has been shown to cause an apparent bulk dielectric anisotropy in studies of dielectric mixing equations (see Section 2.5 of the Literature Review). This apparent anisotropy could help explain the anomalous relationship between dielectric properties and MW/IR characterization seen in the SKN samples. In a solid ore particle, texture or heterogeneous mineral structures, such as veins, may result in an apparent bulk dielectric anisotropy in additional to other factors such as shape. Consequently, when electromagnetic fields are applied to ore particles, such as in MW/IR characterization, the strength of a particles interaction with the field will depend on its orientation. When particles are pulverized for dielectric measurement these structures disappear and result in a disagreement between measured values and a possible explanation for the anomalously heating particles.

The effects of dielectric anisotropy can be investigated by rotating solid samples in a resonant electric field and examining the change in perturbation at each angular position. Cylindrical samples are preferable in this case because they do not change shape when rotated about their axis. However, if samples are placed vertically in an electric field, similar to the Nottingham C1 cavity, the effects of dielectric anisotropy are masked. Under the assumption of a spatially invariant field, rotation of an object about the axis of the E-field does not change the extent of an inclusion that couples to the field (see Figure 4-6). Instead, cylindrical samples need to be rotated about an axis normal to the electric field for the apparent bulk dielectric anisotropy to be observed (see Figure 4-7). This approach is somewhat complicated by the electromagnetic field distribution. When a thin

sample is oriented vertically it is not exposed to magnetic fields; however, when the sample is horizontal the centre is in an E-field maximum whilst the ends are exposed to magnetic fields (see Figure 4-8 for the electric, E, and magnetic, H, field distribution in a TE_{101} cavity). Since the horizontal sample is exposed to both electric and magnetic fields the resulting perturbation will couple both permittivity and permeability. Since these samples have negligible magnetic properties perturbation is assumed to be due to the dielectric properties.

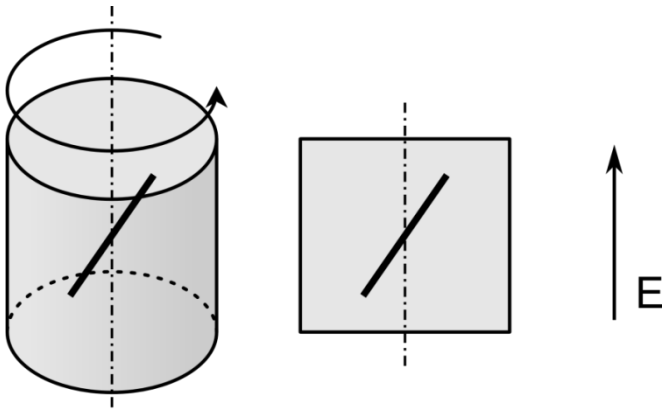

Figure 4-6 – Rotation of a cylinder about the E-Field axis does not change the length component of an inclusion in line with the E-field.

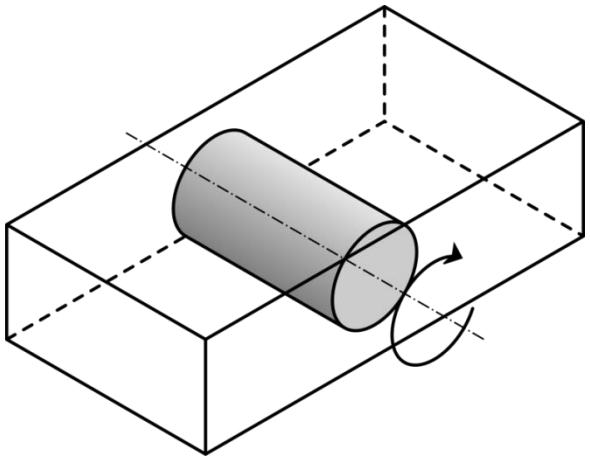

Figure 4-7 – Dielectric anisotropy measurement by axial rotation

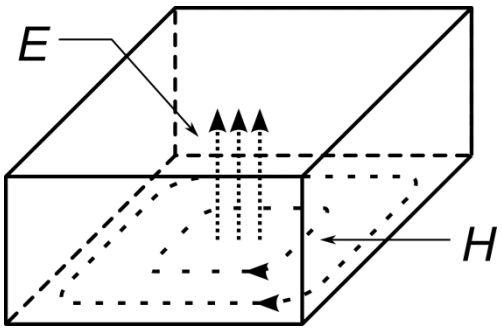

Figure 4-8 - E and H field distribution in a rectangular TE_{101} cavity

To qualitatively observe bulk dielectric anisotropy, large SKN particles were machined into cylinders, with comparable size to the particles used in MW/IR characterization. Further details on core preparation can be found in Section 4.3.1.2 below. This size was necessary to preserve mineral structures and their potential extent. The hypothesis that samples are complex heterogeneous mixtures with structuring precludes manufacturing cores for a single sample with different orientations and also means that the dielectric properties of samples machined from different ore particles cannot be compared. The measurement procedure therefore requires multiple measurements of individual samples from different orientations while preserving a rotationally symmetric shape in the cavity. To measure bulk dielectric anisotropy in the SKN core samples a rectangular waveguide cavity was designed and constructed from WR340 waveguide stock (see Section 4.3.2 below). The cavity was formed between two iris endplates and connected to a network analyser (Agilent E5071C) via waveguide-coaxial transitions. The network analyser was then used to record cavity Q-factor and resonant frequency of the empty cavity (see Section 4.3.2.2) and then of samples as they were rotated in 45° increments (see Section 4.3.3 below).

4.3.1 Sample Preparation

The skarn ore, SKN, was chosen for the investigation of dielectric anisotropy because it is known to have a high degree of heterogeneity, and in the previous chapter it was found that some SKN samples heated approx. 55 K more than dielectric properties suggest in a 2.45 GHz multimode oven (see Section 3.3.4.1 of Chapter 3). The approximate dimensions of cores were calculated to mimic the -22.4 +19.0 mm particles used in the microwave/IR characterization of the previous chapter.

Particles from the -75 +63 mm size fraction were selected from which to manufacture suitably sized cores using a drill press and diamond core drill bits (see Section 4.3.1.2 below).

4.3.1.1 Core Size Calculation

There are competing pressures on the construction of the samples. The sample cylinder needs to be large enough to capture mineral texture features while also being small enough to not overly perturb the fields within the resonant cavity. All ore samples used in the previous characterization and dielectric measurement were from the -22.4 +19.0 mm size fraction, of these 60 particles and the average volume was 5.59 cm^3 (standard deviation 1.78). Cores manufactured for this investigation are to demonstrate the presence of a dielectric anisotropy effect in -22.4 +19.0 mm particles. Therefore the cores need to be somewhat comparable in volume to preserve any texture features present.

Formulae describing the volume of ore particles in terms of size fraction can be found in the work of Michaux (2005). Equation (4.6) describes the average particle volume, β, while Equation (4.7) describes the standard deviation of the average particle volume, δ. Both of these equations depend solely on φ, the size fraction mean, which is the average of the opening and closing sieve sizes used to create sample population. In Equation (4.6) the shape factor, 0.68, describes the average geometry of particles – a cube would have a shape factor of 1 whereas a sphere would have a shape factor of $\pi/6$ (approx. 0.5236). These equations were used to calculate the volumes and standard deviations of the -22.4 +19.0 mm size fraction, as well as the next three smaller size fractions (see Table 4-2). Assuming a diameter of 15mm, a cylindrical sample would require a length of 20.6 mm to have a volume equal to the average -19.0 +16.0 mm particle.

$$\beta = 0.68\varphi^3 \qquad (4.6)$$

$$\delta = 0.18\varphi^3 \qquad (4.7)$$

Table 4-2 – Average particle volume and standard deviation calculated using (1.6) and (1.7)

Top size (mm)	*Bottom Size (mm)*	β (cm^3)	δ (cm^3)
22.4	19.0	6.03	1.60
19.0	16.0	3.64	0.96
16.0	13.2	2.12	0.56
13.2	9.5	0.99	0.26

4.3.1.2 Core Preparation

SKN core samples were manufactured using the same drill press and water swivel that was used to the produce the 3.5mm cores for measurement in a cavity perturbation system (C1) at The University of Nottingham (See Section 3.2.4.1 of Chapter 3). However, in this instance, larger cores were obtained using a commercially available 15mm outer diameter (OD) diamond core drill bits and cut from +75mm particles. Custom drill bits were not used for this procedure since there was no maximum OD constraint. Fourteen cores were successfully produced using this method and were then measured using Vernier callipers, a summary of their dimensions can be found in Table 4-3 below. Using the average volume and length, the cores were found to have an average volume of 1.93cm^3 (St. Dev. 0.24 cm^3) which lies within the -16.0 +13.2mm size fraction.

Table 4-3 – Average and standard deviation of SKN core dimensions (14 cores)

	Average	*St. Dev.*
Diameter (mm)	11.53	0.20
Length (mm)	18.46	2.08

4.3.2 The Texture Measurement Cavity

A rectangular waveguide cavity was constructed to create an appropriate electric field with which to investigate the existence of dielectric anisotropy and its magnitude (see Figure 4-9). The resonant modes of the cavity were first calculated and then compared to the measured modes.

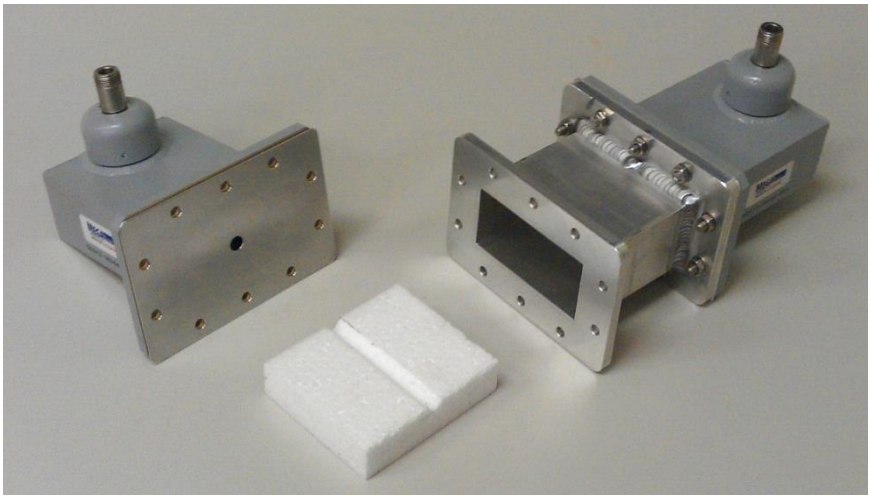

Figure 4-9 – The rectangular waveguide resonant cavity, polystyrene sample holder, waveguide-coaxial transitions and 9mm iris.

4.3.2.1 Cavity Design

The rectangular waveguide cavity was largely designed in accordance with the ASTM D2520-01 standard (ASTM 2001). However, vertical sample access holes through the cavity were not added, instead access to samples within the cavity is via removal of an end-plate. The ASTM D2520 standard uses a length of rectangular waveguide with iris-coupled endplates affixed to either end to form the body of the resonant cavity. Waveguide-coaxial transitions were then attached to either end of the cavity to launch and receive the electromagnetic signals from a network analyser.

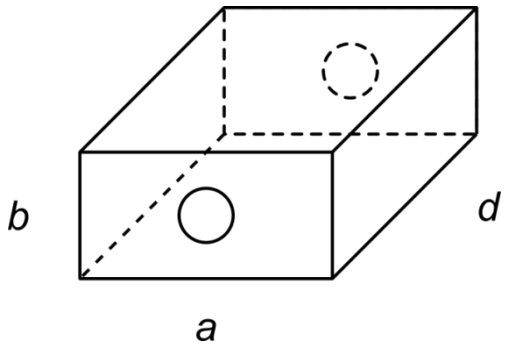

Figure 4-10 – Conceptual design of a rectangular waveguide cavity (a – width, b – height, d – length)

There are a number of different parameters that need to be considered when designing the cavity: the dimensions of the waveguide, the length of the cavity, and the diameter of the irises (see Figure 4-10). Selecting WR340 waveguide constrains both the width and height of the cavity and leaves only the cavity length to be determined (see Table 4-4 for dimensions). In a rectangular resonant cavity, the frequency of the resonant mode, f_{mnp}, and can be calculated using Equation (4.8) (Cheng 1989). The TE_{101} mode is the lowest frequency mode since the lowest possible transverse magnetic mode is TM_{110}. Using this equation and the WR340 waveguide dimensions it is possible to show how changes in the length of the resonant cavity affect its resonant frequency (see Figure 4-11). A cavity length of 100mm was selected and corresponds to a TE_{101} resonant frequency 2.293 GHz which is lower than the ISM band at 2.45 GHz and the 2.47 GHz resonance in the Nottingham C1 cavity.

$$f_{mnp} = \frac{c}{2}\sqrt{\left(\frac{m}{a}\right)^2 + \left(\frac{n}{b}\right)^2 + \left(\frac{p}{d}\right)^2} \qquad (4.8)$$

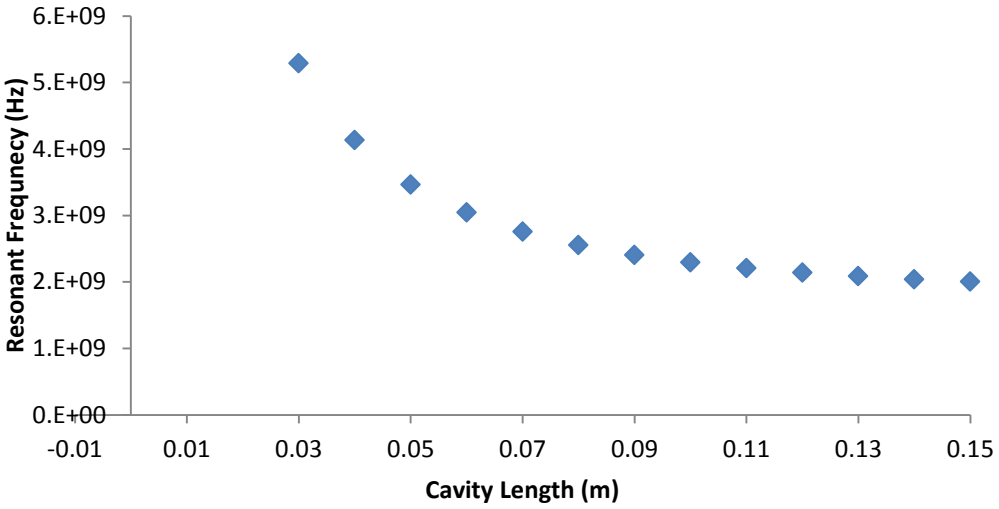

Figure 4-11 – Calculated resonant frequencies of different length TE_{101} cavities made from WR340 waveguide

Table 4-4 –WR340 Rectangular Waveguide Cavity Dimensions

Width, *a*	3.4 inches (8.636 cm)
Height, *b*	1.7 inches (4.318 cm)
Length, *d*	10 cm
Volume	307.1 cm^3

The iris diameter of the end-plates is specified in ASTM D2520-01 using Equation (4.9) in which $x = 2.2$ and *b* is the wall height of the cavity. When using WR340 waveguide stock to form the cavity, this means an iris diameter of 19.6 mm. However, the iris diameter controls the coupling of energy into and out of the cavity and thereby defines two parameters in cavity measurements; the signal-to-noise ratio, and cavity Q-factor. Irises with smaller diameters will increase the cavity Q-factor at the expense of the signal-to-noise ratio. Four sets of endplates were made with diameters: 9, 14, 17 and 20 mm.

$$D_{iris} = \frac{b}{x} \tag{4.9}$$

Calculation of dielectric properties may be accomplished using equations found in ASTM D2520-01 (ASTM 2001). The standard provides a number of different dielectric property equations to cover different geometry objects and their orientations to the electric field (see appendix Section 8.1.1). Equations (4.10) and (4.11) are used to calculate the permittivity and loss factor of a cylindrical object which has its long axis in line with the field in the cavity (vertical cylinder). The dielectric properties of a cylindrical object perpendicular to the field axis (horizontal cylinder) are then calculated using Equations (4.12) and (4.13), which are extension of equations (4.10) and (4.11).

The relationship between equations describing the dielectric properties of a horizontal cylinder and a vertical cylinder are examined in Figure 4-12 and Figure 4-13 below. In both permittivity and loss factor these figures show an asymptotic behaviour about ϵ'_{vert} = 2 (equivalent to a change in cavity resonance due to the sample of approx. 2.3673 x 10^7 Hz). This means that, when using Equation (4.12), samples with large permittivity when measured vertically approach zero from negative values when they are measured horizontally. As a consequence any horizontal sample that perturbs the cavity more than 2.3673 x 10^7 Hz will produce a negative permittivity. Additionally, samples perturbing the cavity near to 2.3676 x 10^7 Hz will produces strongly negative or positive results (division by zero means the function is not defined when ϵ'_{vert} = 2). The behaviour of Equation (4.13), under the assumption that ϵ''_{vert} = 1, is shown in Figure 4-13 which demonstrates that the apparent loss factor is small for a samples with a large permittivity but becomes very large when the permittivity of the sample approaches 2 (again, the function is undefined at ϵ'_{vert} = 2). For these reasons the ASTM D2520-01 equations were not used to calculate dielectric properties and texture was assessed via changes in resonant frequency and Q- factor instead.

$$\epsilon'_{vert} = \frac{V_c}{2V_s}\frac{(f_c - f_s)}{f_s} + 1 \qquad (4.10)$$

$$\epsilon''_{vert} = \frac{V_c}{4V_s}\left(\frac{1}{Q_s} - \frac{1}{Q_c}\right) \qquad (4.11)$$

$$\epsilon'_{horiz} = \frac{\epsilon'_{vert}}{2 - \epsilon'_{vert}} \tag{4.12}$$

$$\epsilon''_{horiz} = \frac{2\epsilon''_{vert}}{\left(2 - \epsilon'_{vert}\right)^2} \tag{4.13}$$

Where:

- V_c and V_s are the volume of the cavity and sample respectively.
- f_c and f_s are the resonant frequencies of the cavity when empty and loaded with a sample respectively.
- Q_c and Q_s are the quality factors of the empty and sample-loaded cavities respectively.

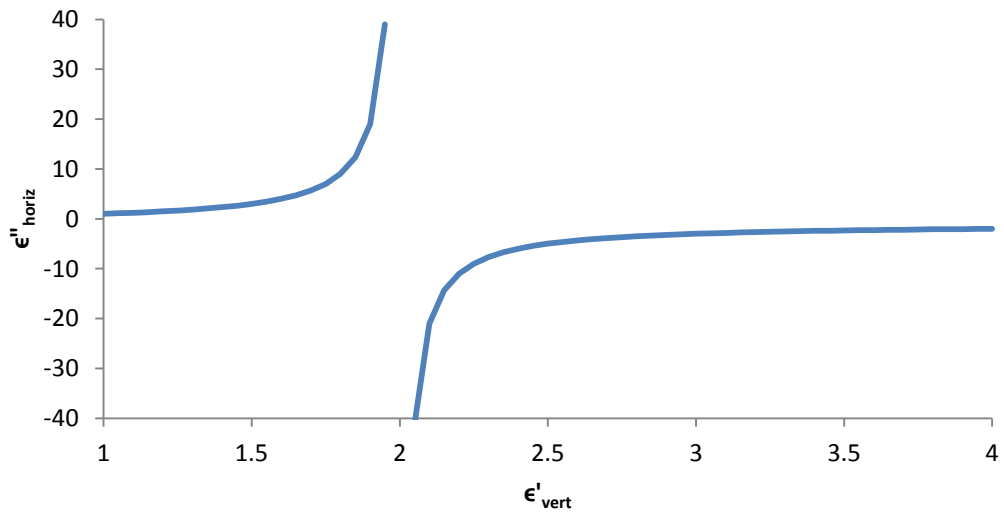

Figure 4-12 – Calculation of the permittivity of a horizontal rod according to ASTM D252-01

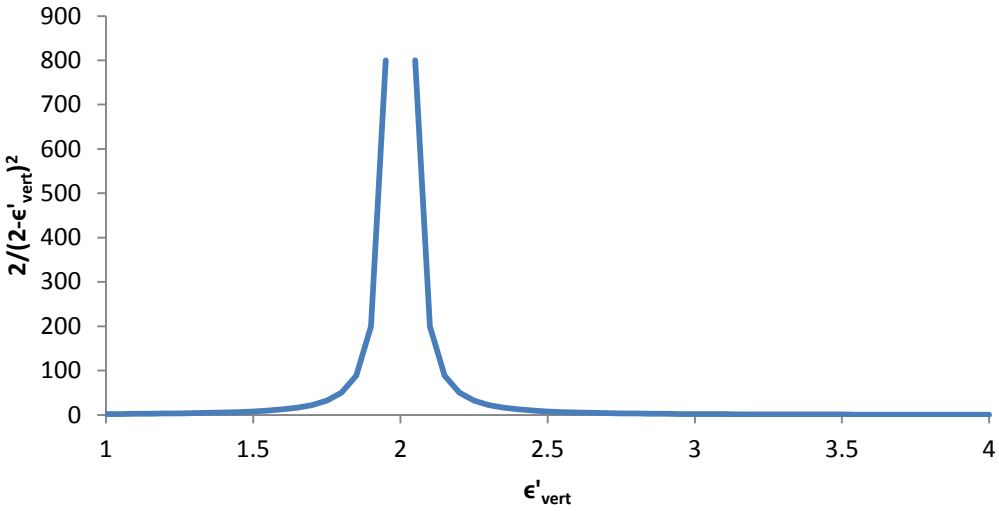

Figure 4-13 – Calculation of the loss factor of a horizontal rod according to ASTM D2520-01

4.3.2.2 Cavity Characterization

The resonant cavity with 9mm iris-coupled endplates was characterized by firstly measuring cavity transmission (S_{21}) on a network analyser (Agilent 5071C) between 2 and 4 GHz (see Figure 4-14). Two primary resonances are visible in Figure 4-14; the first is the TE_{101} mode and occurs at approx. 2.3 GHz. The TE_{101} resonance was further analysed by centring the sweep on the resonance and narrowing the bandwidth to 2 MHz. The TE_{101} resonance was found to have a centre frequency of 2.296 GHz, which is close to the calculated value of 2.293 GHz (see Section 4.3.2.1), and a Q-factor of approx. 8500 when using 9mm iris coupled end-plates. The forward attenuation of each 9mm iris at 2.29 GHz was approx. 52 dB. The second resonance can be found in Figure 4-14 at approx. 3.465 GHz, this is likely to be the TE_{010} mode calculated using Equation (1.8) to occur at 3.47 GHz.

The resonant frequency and Q-factor of the TE_{101} mode was further characterized using each of the iris endplate pairs (see Figure 4-15) on the completely empty cavity. These measurements show that the resonant frequency and Q-factors increase with decreasing iris size. For this reason, the 9mm irises were used for all further cavity measurements.

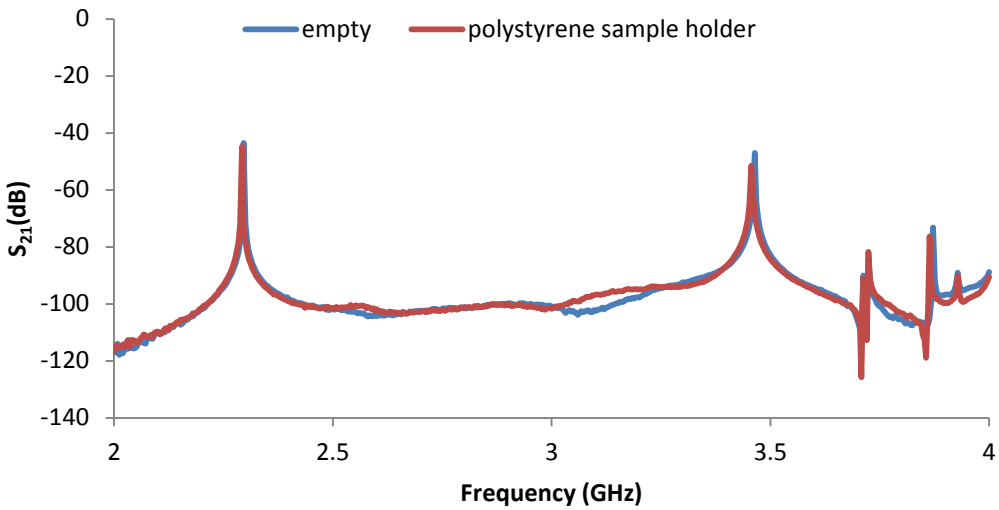

Figure 4-14 – Resonant modes in the resonant waveguide cavity (9mm iris)

A polystyrene foam sample holder was required to support the rock core samples in the cavity and the effect this has on the cavity needs to be accounted for (see Figure 4-9). An initial transmission measurement between 2 and 4 GHz demonstrated that the sample holder made no significant changes to the cavity modes (see Figure 4-14). For the purposes of sample measurements the polystyrene samples holder in the cavity represents the unloaded case. Therefore when calculations are performed, the values for the unloaded cavity centre frequency and Q-factor are taken from Table 4-5.

Access to samples in the cavity is via removal of a waveguide-coaxial transition and iris-coupled endplate. Eight measurements of the resonant cavity were performed to define the uncertainty associated with accessing the cavity. In this experiment the sample holder, iris coupled endplate and waveguide coaxial transition were removed and then replaced between each measurement. The results of these measurements can be found in Table 4-5.

Table 4-5 – Resonant Frequency and Q-factor of the rectangular cavity with polystyrene sample holder

	Average	*Standard Deviation*
Resonant Frequency	2.291813 GHz	14.9 kHz
Q-factor	5865	169

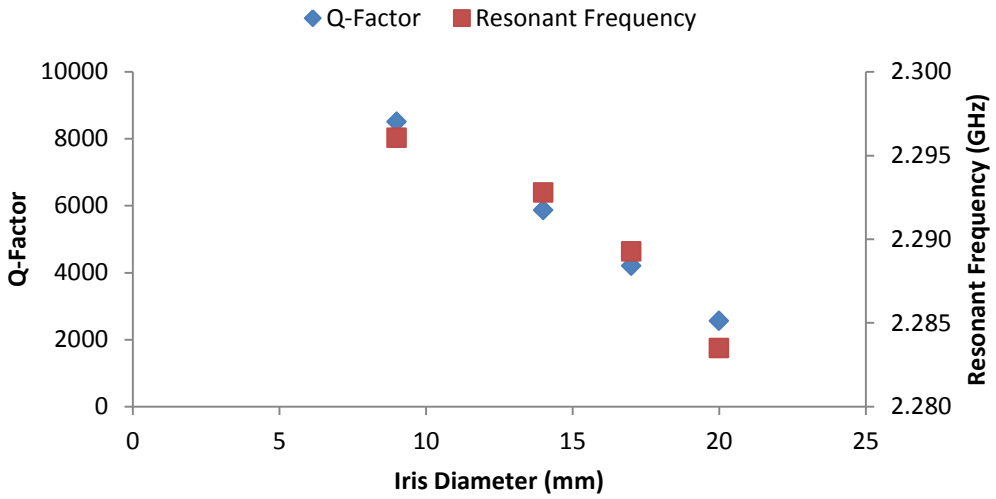

Figure 4-15 – Q-Factors and resonant frequencies of the TE_{101} mode of the empty rectangular waveguide cavity with different sized coupling irises

4.3.3 Measurement of Textures

Texture measurements were accomplished by first making a small mark on the rim of the cores. The cores were then centred on the sample holder and rotated so that the mark pointed upwards. The sample holder and core were then placed in the cavity. S_{21} was recorded on the network analyser in a 20MHz bandwidth roughly centred on the TE_{101} mode. The centre frequency and Q-factor of the resonance were then calculated from the sweep data using a MATLAB function which includes noise filters, finds the centre frequency of the resonance and then interpolates the full-width half-maximum to calculate bandwidth (refer to Section 8.5.1 of the Appendix for MATLAB code). The core was then removed from the cavity, re-centred on the sample holder, rotated clockwise by 45

degrees, returned to the cavity and then re-measured. This was done until a 180 degree rotation of the core had been achieved – a total of five measurements. Ten cores were measured in this manner.

While dielectric properties are not calculated using the ASTM method (see Section 4.3.2.1 above) it is still possible to qualitatively examine bulk dielectric anisotropy by means of changes in resonant frequency and Q-factor of a cavity due to core rotation. However, sample cores have different lengths and consequently volumes. Equations (4.14) and (4.15) are used to account for the different volumes by calculating values analogous to permittivity and loss factor. These equations neglect the constants which ordinarily account for factors such as the geometry of the sample and cavity mode but preserve the ratio of cavity volume to sample volume. Therefore, the *P* and *L* values generated are proportional to the true permittivity and loss factor expected from an ideal measurement; similarly *L/P* will be proportional to the loss tangent. The assumptions in the perturbation calculations mean that in ideal dielectric measurements the samples extend the full height, or width depending on orientation, of the cavity. As the E-field decays in strength away from the centre of the cavity there will be differences in the perturbation due to longer or shorter samples. Since samples are centred in the cavity and on average approx. 21% (±5%) of the cavity width these differences should be subtle, consistent and largely be reflected in the absolute magnitude of *P* and *L* rather than the relative variation of individual cores due to rotation. The average *P* and *L* values for cores can be found in Table 4-6.

$$P = \frac{V_c}{V_s}\frac{\left(f_c - f_s\right)}{f_s} \tag{4.14}$$

$$L = \frac{V_c}{V_s}\left(\frac{1}{Q_s} - \frac{1}{Q_c}\right) \tag{4.15}$$

Table 4-6 – Average P and L values for measured cores

	Average	*Standard Deviation*
P	3.97	0.19
L	0.14	0.05

Bulk dielectric anisotropy is not examined using the absolute values of *P* and *L* for each sample but in their variation as the sample is rotated. Once the *P* and *L* values are calculated for each rotation position of the measured cores, the variation due to rotation can be calculated. This was accomplished by subtracting minimum value from the maximum and then dividing by the average as shown in Equation (4.16). This procedure was used for calculation of *L*, *P* and *L/P*. The results of these calculations can be found in Table 4-7. It can be seen in Table 4-7 that there are small variations in *P* values, indicating the permittivity of cylinders remains relatively constant throughout rotation. These results also show a significant degree of variation (>10%) in *L* values in six of the ten cores studied and indicates large changes in the loss factor of these cores due rotation. Furthermore, the large spread in L variations indicates that every core has a different interaction with the E-field, potentially arising from mineral structures. This finding clearly demonstrates bulk dielectric anisotropy in SKN cores and supports the explanation of internal mineral structuring as a reason for abnormal heating in particles. Graphs of *P* and *L* for 180° rotations of all measured cores can be found in the Appendix (see Section 8.5.2, Figure 8-30and Figure 8-31).

$$L_{variation} = \frac{L_{max} - L_{min}}{L_{average}} \tag{4.16}$$

Table 4-7 – Variation in P and L measurements due to the rotation of cores

Core	*L*	*P*	*L/P*
16b	83.59%	3.88%	80.06%
15a	80.03%	2.97%	76.82%
9a	42.98%	2.49%	40.48%
3b	37.05%	1.84%	35.30%
1b	28.44%	3.07%	25.40%
3a	18.08%	1.19%	17.20%
6b	8.01%	0.82%	7.20%
13a	6.11%	0.59%	5.52%
14b	5.20%	0.44%	4.93%
8b	2.92%	0.24%	3.09%
Average	*31.24*	*1.75%*	*29.60%*
Standard Deviation	*30.04%*	*1.28%*	*28.85%*

To further understand the variability in measurements cores 16B and 8B were subjected to repeated measurements. For these cores, the measurement procedure from 0° to 180°, as described above, was repeated three times. The *P* and *L* values for both cores at each rotation increment can be found in Figure 4-16 and Figure 4-17 respectively. These measurements show both *P* and *L* have sinusoidal shape, are in-phase and have a 180° period – behaviour strongly indicating a bulk dielectric anisotropy. Additionally, the error in these measurements, despite removing the waveguide-coaxial transition and iris-coupled end-plate between each measurement, is small – the relative standard deviations are 0.2% and 2% for *P* and *L* values respectively.

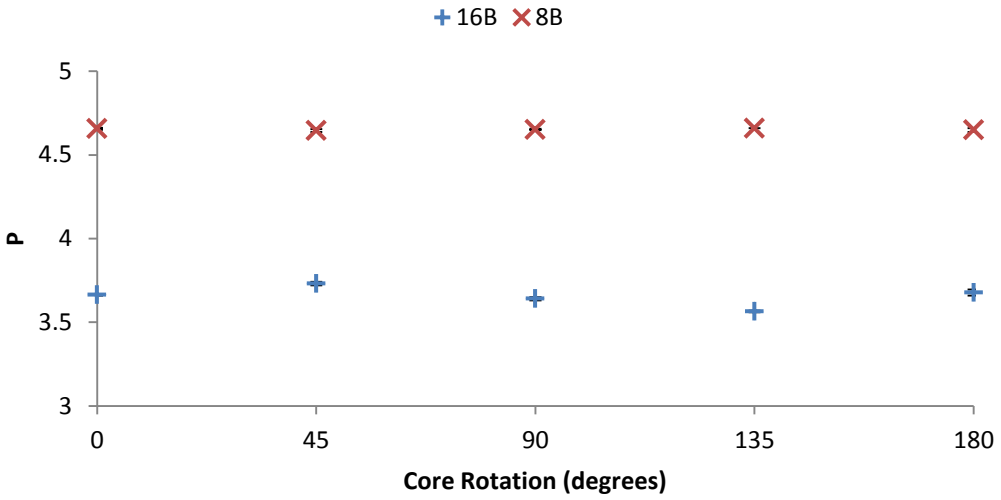

Figure 4-16 – Variation in P values for two SKN cores due to rotation

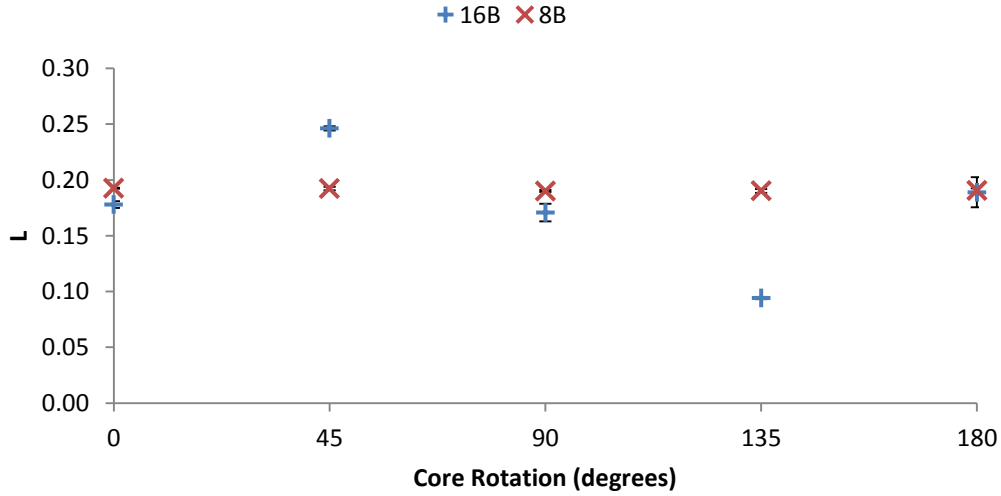

Figure 4-17 – Variation in L values for two SKN cores due to rotation

Table 4-8 – Physical dimensions of cores 8B and 16B

Core	*Diameter (mm)*	*Length (mm)*	*Volume (mm^3)*
8B	12.05	18.61	2121
16B	11.60	16.93	1789

4.3.4 Conclusion

A rectangular waveguide cavity was designed and manufactured with a 2.29 GHz TE_{101} resonance and a Q-factor of approx. 8500. Cylindrical samples were cut large size fraction SKN particles and calculated have a volumes comparable to -16.0 +13.2 mm particles. A series of cavity perturbation measurements were made while axially rotating core samples laying perpendicular to the electric field in 45° increments. While not explicitly calculating the dielectric properties of cores, *P* and *L* values (which differ from dielectric properties by constants of proportionality) were used to study the relative changes in core properties as a function of rotation. These measurements show that the loss factor, and consequently loss tangent, of SKN cores can vary significantly (up to approx. 83.6%) upon rotation through 180°. As the cores are cylindrical and their shape does not vary with rotation, this apparent dielectric anisotropy must be due an intrinsic property of the cores, such as mineral structuring. Finding is further supported by the sinusoidal nature of the rotational variations with a period of 180° which is consistent with elongated inclusions. A consequence of this finding is that whole particles, while also influenced factors such as geometric shape and field distribution, are likely to exhibit different heating rates depending on their orientation to an applied microwave field.

4.4 MLA Imaging of SKN Solid Sections

The heterogeneity and structuring of sulphides can be qualitatively examined in anomalous samples using the solid halves set aside during sample processing in the previous chapter (see Section 3.2.4 of Chapter 3). Solid halves of three anomalous SKN samples were mounted in resin blocks and imaged using an automated scanning electron microscope (MLA) with an Energy Dispersive X-Ray Spectroscopy (EDS) module. The face made by the diamond saw was used for the imaging and represents a cross-section of the particle. The aim of this imaging was simply to observe the presence of structuring in the sulphide minerals of the anomalously heating samples. Detailed mineral compositions can be found in the appendix (see Section 8.5.3 of the Appendix). In these images, the gangue mineral grouping includes: amphibole, biotite, chlorite, feldspar, garnet, olivine, pyroxene, quartz and talc. Furthermore, the titaniferous mineral grouping includes: rutile, ilmenite and titanite.

Figure 4-18, Figure 4-19 and Figure 4-20 show a high degree of sulphide heterogeneity in the anomalous SKN samples. This is particularly evident in Particles A and C which shows significant amounts pyrite in a band on the particle edge (Figure 4-18) and a discrete zone within the particle (Figure 4-20). Additionally, only a small proportion of the sulphides are copper bearing in these two particles. Particle B has approx. equal amounts chalcopyrite and pyrite disseminated throughout the particle, however the sulphides are zoned. Pyrite has mineralized predominantly on the left hand side of the particle section while chalcopyrite occurs on the right hand side. The heterogeneity of these particles supports the hypothesis that the differences between the microwave heating response and the dielectric properties of the powdered subsections could be explained as sampling error.

There are two pyrite bands in Particle A; a primary band of which along the upper edge of the particle and a smaller band which traverses the particle at roughly 60 degrees to the first band. These structures, either linear or planar in a 3-dimensional particle, form the basis for dielectric anisotropy. Additionally, Particle B may exhibit a degree of dielectric anisotropy which results from the different dielectric properties of sulphides on either side of the particle. Consequently, the imaging qualitatively shows a basis for both dielectric anisotropy and sampling error in the anomalous particles. However, skarn ores, such as the SKN ore are highly variable and since only anomalous samples were imaged, further imaging is required to compare the structuring of sulphides in normal and anomalous samples.

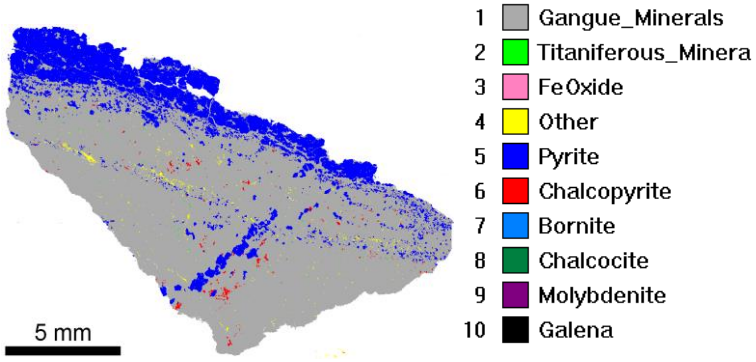

Figure 4-18 – MLA Image: Particle A

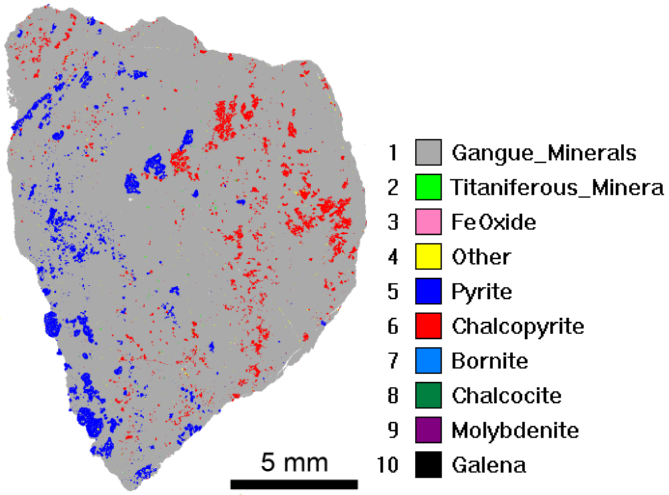

Figure 4-19 – MLA Image: Particle B

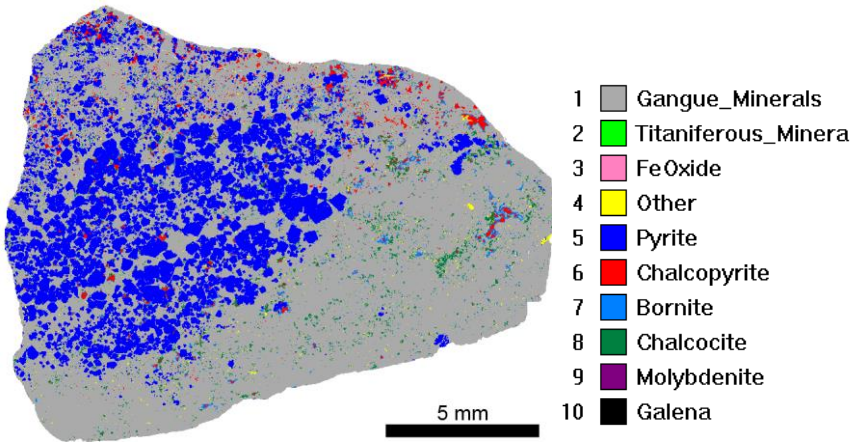

Figure 4-20 – MLA Image: Particle C

4.5 Conclusions

Three different effects were posed as explanations to the anomalous heating behaviour shown in Chapter 3: magnetic interactions, bulk dielectric anisotropy and heterogeneity which lead to unrepresentative powder samples. Three different measurement techniques were used to investigate these effects. A series of measurements investigating the RF permeability of powdered samples were conducted using a Magnasat. Analysis of these measurements found no relationship between permeability and the characterized microwave heating of the original particles. Additionally, the

permeability of anomalously heating samples was indistinguishable from the other ore samples. This finding indicates that interaction with the magnetic field component in a cavity does not explain the anomalously hot specimens. As permeability measurements were performed on powders it is feasible that mineral structures may enhance interaction with the magnetic field; however, this also simultaneously increases coupling to electric field. The effect of mineral structures on permeability could potentially be investigated further by using a higher order mode of the rectangular waveguide cavity in which a magnetic field maximum exists at the centre.

Dielectric anisotropy was investigated using a rectangular waveguide cavity with a TE_{101} resonance at 2.29 GHz and a Q-factor of approx. 8500. Measurements of SKN cores rotated in 45° increments demonstrated that the *P* and *L* values can vary significantly. Since the core shape does not vary with rotation, the changes in cavity properties with rotation are consistent with dielectric anisotropy resulting from internal mineral structures. MLA imaging of anomalous SKN samples was used to qualitatively investigate sulphide heterogeneity. The images obtained show distinct sulphide mineral structures and consequently supports the possibilities of both dielectric anisotropy and sampling error as explanations for the anomalous behaviour.

The investigations in this chapter lead to two overall conclusions. For the copper ore investigated, magnetic field interactions do not play a significant role in microwave heating. And, that mineral structuring likely contributes to microwave heating and merits further investigation. Any models of microwave/IR sorting will need some mechanism to account for the uncertainty in microwave heating introduced as a result of mineral structuring. It is evident that a parameter describing the magnitude of mineral structuring is required – as ores have different levels of structuring and range from highly disseminated to highly veined – but is a topic for future work.

5 Ore Composition and Mixture Modelling

5.1 Introduction

In Chapter 3 the heating rate and dielectric properties of ore samples were quantified and in Chapter 4 the variation in these properties were investigated in terms of magnetism and internal mineral structuring. This chapter addresses the relationship, identified in Chapters 2 and 3, between the dielectric properties of a specimen and the dielectric properties and relative abundances of the minerals (modal mineralogy) from which it is made. Additionally, the chemical composition of minerals can have a large effect on their dielectric properties (See Section 2.4 of the Literature Review) and varies both between and within deposits.

A key component in understanding the dielectric properties of an ore is knowledge of the dielectric properties of the minerals in the deposit from which it is sourced. This requires knowledge of both the minerals present and their abundances (i.e. the modal mineralogy) which can be measured using automated scanning electron microscopy. The chemistry of mineral species can be further investigated with an electron microprobe. The dielectric properties of samples measured in Chapter 3 (see Section 3.3.4.1) can then be matched to modal mineralogy data to form a system of linear equations based on a mixture equation (see Section 2.5 of the Literature Review). When the system of equations is solved, it results in values for the dielectric properties of each mineral species. The quality of these results can be assessed by comparison with the dielectric properties of pure minerals both measured previously in Chapter 3 (see Section 3.3.4.4), and reported in scholarly literature.

The small number of samples of each ore, and the particle selection process (see Section 3.2.3) mean that the sorting performance of the four ores studied cannot be directly assessed. However, it may be possible to predict how the ores will behave in a MW/IR sorting process via Monte Carlo simulations. These simulations are accomplished using the best fit dielectric properties of the gangue minerals in combination with models for the particle-by particle distribution of valuable

copper sulphide minerals. The microwave heating of gangue-sulphide mixtures are then calculated to reach an ideal, simulated sorting performance. More realistic sorting performances are then estimated using an empirical model for particle heating variability. This model is based on particle heating statistics measured in Chapter 3 as part of MW/IR characterization and accounts for all factors that may influence microwave heating such as: particle shape, mineral texture and E-field distribution in the cavity.

5.2 Quantification of Mineral Abundance and Chemistry

There are a number of techniques available to quantify mineral abundances, including automated scanning electron microscopy (MLA) and X-ray Diffraction (XRD). Additionally, there are a number of different techniques which can be used to analyse chemical compositions of minerals including electron probe microanalysis (EPMA) and X-ray fluorescence (XRF). Two techniques were selected to analyse ore samples:

- MLA for modal mineralogy
- EPMA for mineral chemistry

Both of these techniques use focussed electron beams to stimulate X-ray radiation from a small volume at the sample surface, called the interaction volume. Atoms within the interaction volume are struck by electrons from the electron bean and occasionally excite an atomic electron to a higher energy level. For the atomic electrons to return to the ground state the excess energy is emitted as an x-ray photon. These are called characteristic x-rays and have wavelengths defined by atomic energy level structures which are unique to each element. The MLA then detects the characteristic X-rays using an energy dispersive X-ray spectrometer (EDS), while the EPMA uses a wavelength dispersive x-ray spectrometer (WDS). The EDS detectors rapidly produce spectra but lack the spectral resolution of WDS measurements. For this reason EDS measurements are used to rapidly determine the major elements and then refer to libraries of spectra to assign a mineral classification. WDS detectors are single-channel detectors that move between characteristic x-ray element peaks

and measure count rates. From the counting statistics at an element peak, the quantity of that element in the interaction volume can be determined. A benefit of selecting these two analysis techniques is that the samples, mounted in 30mm resin blocks with carbon coatings, can be used in both machines.

5.2.1 MLA Measurement of Mineral Abundance

The MLA measurement technique was chosen to generate the modal mineralogy for each powdered sample. Twenty-eight powdered samples were chosen to represent a cross-section of both the different ores and microwave heating behaviours. These samples included the three of the high-heating and low-heating anomalous samples, along with the most magnetic sample and random selections of cold, medium and hot groups from each ore to total seven samples from each ore. Figure 5-1 only contains data for the samples selected for MLA analysis and demonstrates that the selected particles represent a cross-section of heating behaviours observed in Chapter 3 (see Section 3.3.4.1).

The chosen ore powder samples were submitted to the JKMRC MLA facility for mounting in resin blocks and measurement. These measurements involved the X-ray modal analysis (XMOD) acquisition routine which generates a modal mineralogy by collecting EDS spectra in a grid on the sample surface. A library of reference spectra is then used to determine the mineral at each grid point. Averaged results of the XMOD measurements for each ore type can be found in Table 5-1, while data for each sample can be found in the Appendix (See Section 8.6.1)

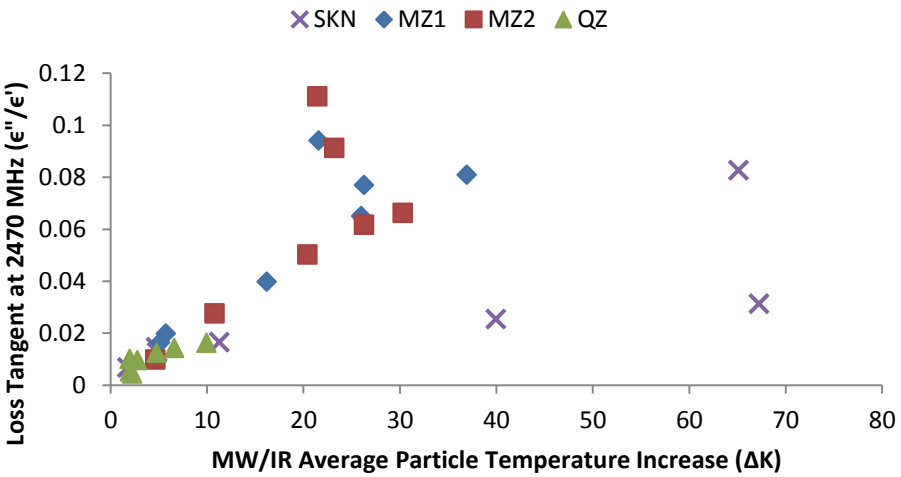

Figure 5-1 – The loss tangent and whole particle microwave heating of samples selected for MLA analysis

Table 5-1 – Averaged modal mineralogy data for each ore type

Sample	*QZ*	*SKN*	*MZ1*	*MZ1*
Sulphides				
Arsenopyrite	0.00	0.01	0.00	0.00
Bornite	0.15	0.30	0.84	0.15
Chalcocite	0.00	0.10	0.02	0.01
Chalcopyrite	0.28	1.44	0.28	0.08
Covellite	0.00	0.28	0.00	0.00
Galena	0.00	0.01	0.00	0.00
Molybdenite	0.07	0.00	0.03	0.13
Pyrite	0.04	6.60	0.05	0.03
Tetrahedrite	0.00	0.04	0.00	0.00
Gangue				
Amphibole	0.01	2.38	0.33	4.69

Apatite	0.14	0.23	1.00	0.76
Biotite	8.26	0.09	29.12	20.89
Calcite	0.07	8.73	0.11	0.62
Chlorite	0.32	0.30	0.27	1.70
Garnet	0.01	28.46	0.02	0.24
Muscovite	0.45	0.04	3.27	1.53
Olivine	0.04	0.21	0.01	0.03
Alkali Feldspar	9.00	0.36	39.13	19.39
Plagioclase Feldspar	0.03	0.01	3.20	11.18
Pyroxene	0.22	20.41	5.15	7.96
Quartz	80.58	29.39	16.77	29.94
Talc	0.11	0.33	0.01	0.03
Other				
Iron Oxide	0.02	0.01	0.01	0.12
Rutile_Ilm_Titanite	0.09	0.06	0.21	0.44
Other	0.09	0.19	0.16	0.10
Total	*100.00*	*100.00*	*100.00*	*100.00*

From the QZ samples analysed, sulphides in this ore are limited to chalcopyrite (0.28 wt. %), bornite (0.15 wt. %), molybdenite (0.07 wt. %) and pyrite (0.04 wt. %). Most QZ samples are almost entirely quartz with small amounts of biotite and alkali feldspar. This agrees with the results of MW/IR characterization which showed QZ had the lowest heating rates of all ores (see Section 3.2.2 of Chapter 3). However, one sample significantly deviated from this composition, containing 60.98 wt. % alkali feldspar and 22.65 wt. % biotite. Since there are only seven sets of modal mineralogy from each ore type, this significantly shifts the average composition (see Section 8.6.1, Table 8-20 of the Appendix).

The SKN ore has a highly variable composition and is rich in minerals that are uncommon in the other ore types such as calcite, garnet and pyroxene (see Section 8.6.1, Table 8-21 of the Appendix). During MW/IR characterisation, particles in this ore had the highest and lowest average microwave heating across all four ores types. The SKN samples show a high degree of sulphide mineralization; one sample contained 24.35 weight percent of pyrite. On averaging, pyrite is the most common sulphide (6.60 wt. %) in the SKN samples, followed by chalcopyrite (1.44 wt. %). Additionally, SKN samples contained smaller amounts of bornite (0.30 wt. %) and covellite (0.28 wt. %) and chalcocite (0.10%). The modal mineralogy data indicates that, like quartz, pyroxene and garnet do not significantly contribute to microwave heating since a particle containing 55.85 wt. % garnet and 41.95 % pyroxene heated an average of 1.73°C in MW/IR characterization.

On averaging, the MZ1 samples are more highly mineralized than the MZ2 samples; containing 1.22 and 0.39 weight percent average total sulphides respectively. Bornite appears to be the primary sulphide in the MZ1 and MZ2 samples tested with 0.85 and 0.15 average weight percent respectively. Furthermore, MZ1 samples contain chalcopyrite (0.28 wt. %) while a MZ2 sample contained molybdenite (0.73 wt. %). Unlike the SKN and QZ samples, feldspars are common in both MZ samples (MZ1: 42.33 wt. %, MZ2: 30.57 wt. %), as are biotites (MZ1: 29.12 wt. %, MZ2: 20.89 wt. %). There is, however, a considerable degree of variation, for instance an MZ2 sample contained 98.71 weight percent of quartz.

Additionally, the averaged modal mineralogy, while only on a small sample set, allows the rock types of the ores to be estimated according to Streckeisen (1976). The summed volume percentages of quartz (Q), alkali feldspar (A), plagioclase feldspar (P), feldspathoids (F) and mafic (M) minerals can be found in Table 5-2. Since none of the mafic mineral percentages exceed 90% the remaining minerals are normalized (see Section 8.6.3, Table 8-25 of the Appendix). Using the gangue mineral percentages, the rock types are then identified using the QAPF Diagram (see Section 8.6.3, Figure 8-32 of the Appendix). This is a qualitative method for classifying intrusive igneous rock types and not strictly valid for the SKN sample which as a skarn ore is metamorphic. Misclassification of rock types using the QAPF diagram in four orese studied can arise from misclassification of quartz,

alkali feldspar, plagioclase by the MLA. However, feldspathoid minerals are not encountered in silica rich deposits such as the one these ores originated from and misclassification of quartz, alkali feldspar and plagioclase as a mafic mineral means they do not contribute to the normalised percentages used in rock classification. Small sample numbers with a high degree of gangue heterogeneity between ore particles will also distort rock-type classification.

Table 5-2 – Mineral compositions of ores (Volume %)

	QZ	*SKN*	*MZ1*	*MZ2*
Quartz (Q)	81.35	32.68	17.44	30.66
Alkali Feldspars (A)	9.39	0.48	41.62	20.54
Plagioclase (P)	0.03	0.01	3.35	11.73
Feldspathoids (F)	0.00	0.00	0.00	0.00
Mafic Minerals (M)	9.23	66.83	62.42	37.08

Table 5-3 – Rock classification of ores

Ore	*Rock Classification*
QZ	Quartz-rich granitoid
SKN	Quartzolite
MZ1	Alkali-feldspar granite
MZ2	Granite

5.2.2 Electron Microprobe Analyses of Mineral Chemistry

The electron microprobe analysis was selected to investigate the chemical composition of mineral species within each ore. Measurements were performed on a Cameca SX50 microprobe (see Figure 5-2) in two stages, for gangue and sulphide minerals, as different sets of elements were measured and required different instrument calibrations. Additionally, different electron beam energies were

used for gangue and sulphide measurements (see Table 5-4). The size of the electron-sample interaction volume on a sample surface is a function of the mean atomic number of that region and the electron energy. For this reason, gangue minerals were measured using lower energy electrons than sulphides in order to achieve interaction volumes of comparable size. Three samples were selected from each ore that had MLA modal mineralogy data. Samples were selected to represent all of the minerals that could be found in that ore type. Additionally, analyses were performed on the solid half samples used in Chapter 4 (see Section 4.4) to verify mineral classification in the SKN sample. A table of the elements analysed in the gangue and sulphide measurements can be found in the Appendix along with the detection limit for each element (see Section 8.6.4).

For both gangue and sulphide measurements, target mineral grains were located using a combination of back-scatter electron (BSE) images and reflected light optical images. When measurements produced unusually low elemental total, the WDS detectors were driven to the peak positions of elements not in the acquisition routines and the count rates were monitored. After measurement, gangue mineral data was manually classified using the Formula1 program to calculate the structural formulae of minerals and is part of the SAMx XMAS software suite. Sulphide measurements did not require classification and were exported to a spread-sheet in weight and atomic percentages.

Table 5-4 – Electron microprobe beam parameters

	Accelerating Voltage	*Beam Current*
Gangue	15 kV	25 nA
Sulphide	25 kV	25 nA

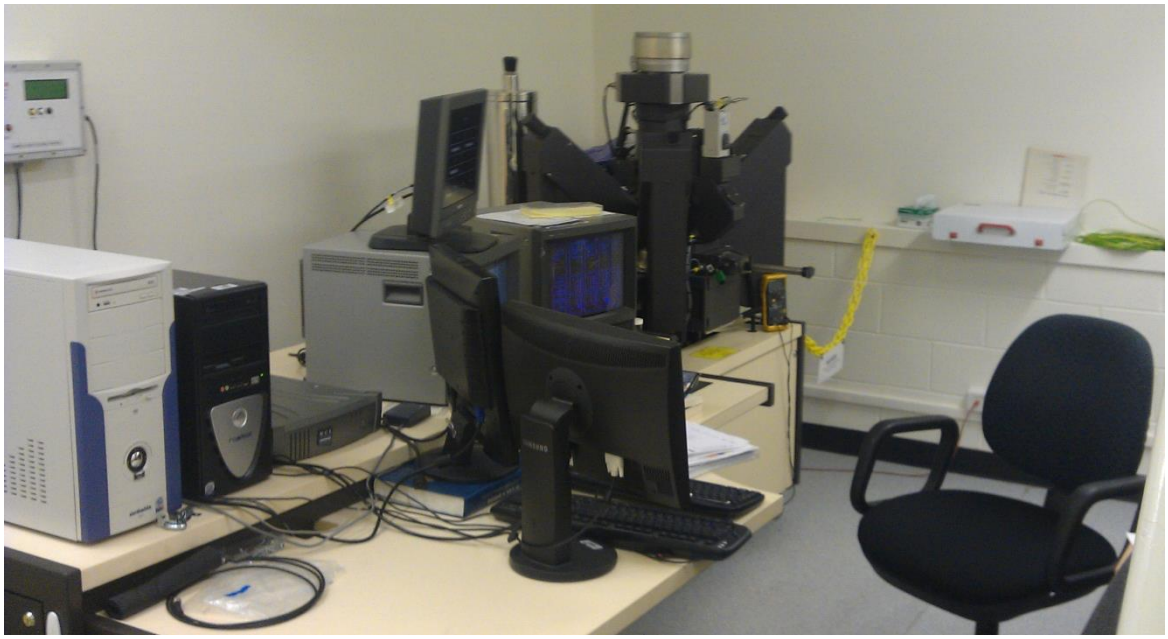

Figure 5-2 – The Cameca SX50 Electron Microprobe

5.2.2.1 Sulphides Minerals

Measurements of sulphide grains were assessed and then classified into a mineral species based on their atomic percentage data. With the exclusion of thirteen molybdenite measurements, all other measurements (159) were copper-iron-sulphides. The results of these measurements can be found in Figure 5-3, which is a ternary diagram displaying the Cu-Fe-S atomic percentage data from all ores. This figure shows that grains of pyrite and chalcopyrite measured have well defined Cu-Fe-S compositions, while some variation evident in the chemistry of other sulphide minerals. The 'Other' grouping includes less common minerals such as Yarrowite (Cu_9S_8), and an unidentified copper-iron-sulphide with a chemical formula of approx. $Cu_{6.8}Fe_{2.2}S_7$.

When comparing the minerals to their ideal atomic proportions and accounting for the minor elements –selenium and tellurium also substitute for sulphur – the sulphides in all ores are iron deficient. Tables of EPMA data for bornite, chalcopyrite, pyrite and molybdenite can be found in the Appendix (see Section 8.6.5). The bornite (Cu_5FeS_4) measurements indicate that MZ1, MZ2 and QZ have excess sulphur although the bornite in SKN is sulphur deficient. Additionally the QZ and

SKN have excess copper while MZ1 and MZ2 are copper deficient. Similarly, the chalcopyrite ($CuFeS_2$) samples of MZ2 and SKN are sulphur deficient and MZ2 and QZ have excess copper.

Despite being iron deficient, minor element substitutions in the pyrite samples of SKN indicate a metal excess – only one pyrite grain was detected in the QZ samples and none in the monzonite ores. The effect chemistry has on the dielectric properties of each grain is uncertain. An excess of sulphur in metal sulphides indicates an increase in acceptor defects and p-type conduction. Conversely, a metal excess indicates an increase in donor defects and n-type conduction. Uncertainty in the effect of chemistry can be found in the work of Kobayashi and Hiroshi (1988) At low frequencies, Fe^{2+} replacing Zn^{2+} in the sphalerite increases the dielectric constant proportionally from 7.4 in a 0.69 wt. % iron sample to 80.4 in a 13.38 wt. % iron sample (Kobayashi & Hiroshi 1988). Although these investigations also indicated that the presence of copper, potentially as chalcopyrite inclusions, tended to decrease the dielectric properties (Kobayashi & Hiroshi 1988). Additionally, the defects caused by the minor and trace elements depend on the sites that they substitute into.

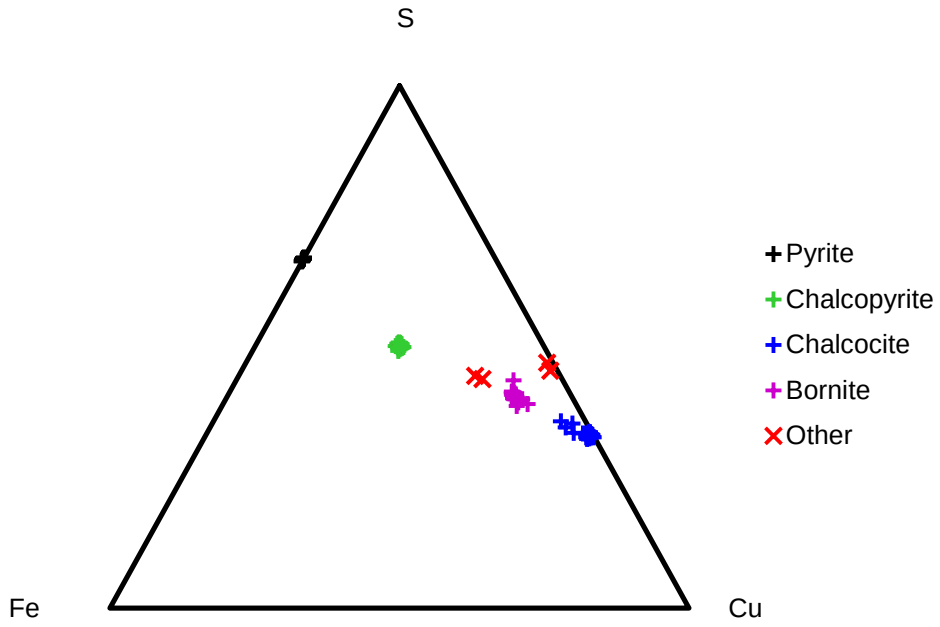

Figure 5-3 – Chemical composition of sulphides from combined ore data (Atomic %)

5.2.2.2 Feldspar

Feldspar grains were located in all four ores. EPMA measurements indicate that the dominant type is alkali-feldspar; rich in orthoclase component (Or), $KAlSi_3O_8$, and with small amounts of albite component (Ab), $NaAlSi_3O_8$. Additionally, grains of plagioclase feldspar identified in the MZ1 and MZ2 ores, these grains were predominantly albite component and anorthite component (An), $CaAl_2Si_2O_8$. Additionally, small amounts of Barium were detected (approx. 0.58 wt. % BaO). Average elemental analyses of alkali and plagioclase feldspars by ore can be found in the Appendix (see Section 8.6.5, Table 8-33 and Table 8-34).

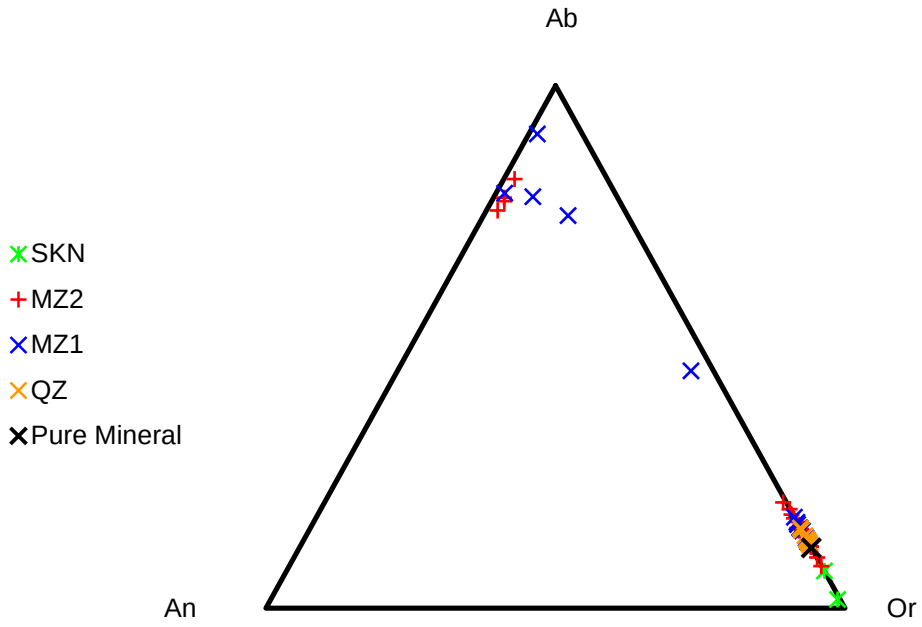

Figure 5-4 – End-member composition of feldspars in ore samples (mol%)

5.2.2.3 Pyroxene and Amphibole

Pyroxenes were only detected in SKN, while amphiboles were only detected in the MZ2 and SKN samples. Neither pyroxenes nor amphiboles were found in MZ1 or QZ. The pyroxenes in SKN are primarily an even mixture of Wollastonite (Wo), $Ca_2Si_2O_6$, and Enstatite (En), $Mg_2Si_2O_6$,

commonly known as diopside (see Figure 5-5). Additionally a measurement of almost pure wollastonite was obtained. In these pyroxene measurements there is an average of approx. 0.3% sodium cations substituting for the calcium or magnesium cations suggesting only very small amounts of Jadeite ($NaAlSi_2O_6$) or Aegirine ($NaFe^{3+}Si_2O_6$) are present. Calcic amphiboles were identified in the MZ2 (5 grains) and SKN (2 grains) ore samples. The number of silicon atoms per unit cell (MZ2: 7.57, and SKN: 7.78) indicate the amphiboles are classed as tremolite ($Ca_2Mg, Fe^{2+})_5Si_8O_{22}(OH, F)_2$) but are close to the bounds of hornblende ($(Na, K)_{0-1}Ca_2(Mg, Fe^{2+}, Fe^{3+}, Al)_5Si_{6-7.5}Al_{2-0.5}O_{22}(OH)_2$). Elemental analyses of pyroxene and amphibole grains can be found in the Appendix (see Section 8.6.5, Table 8-35 and Table 8-36).

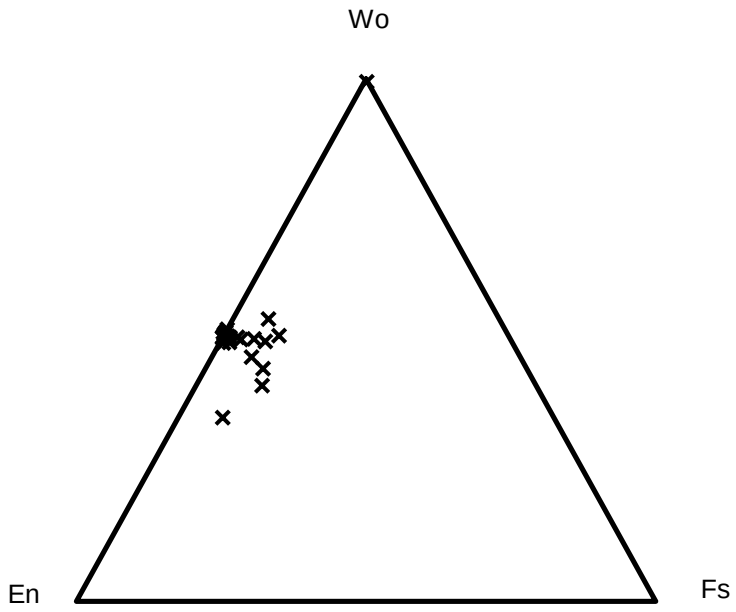

Figure 5-5 – End-member composition of pyroxenes in the SKN sample

5.2.2.4 Phyllosilicates

The phyllosilicate group covers a large number of different minerals, including the mica group, talc, chlorite, serpentine and clays. Of the phyllosilicates in MLA classifications, biotite (49

measurements total, QZ, SKN, MZ1, MZ2) and talc (2 measurements, MZ1 only) were detected, while muscovite and chlorite were not.

MLA mapping of the solid SKN halves displayed in Chapter 4 (see Section 4.4) identified olivine, which is unusual in a metamorphic ore such as SKN (Deer, Howie & Zussman 1992). BSE imaging indicates that the 'olivine' grains do not possess a well-defined structure and their electron microprobe analyses show low total weight percentages (see Table 5-5). As oxygen and hydrogen are not detectable, this is indicates a high degree of hydration which is characteristic of clay minerals such as chlorites, serpentines, or kaolinite which have been measured to contain 11.8, 14.0 and 13.8 wt. % water respectively (Deer, Howie & Zussman 1992). Measurements of other hydrous minerals show lower degrees of hydration, for instance amphiboles and micas contain approx. 1.8 and 4.3 wt. % water respectively (Deer, Howie & Zussman 1992). EPMA data indicates that the 'olivine' grains are likely to be greenalite ($(Fe^{2+},Fe^{3+})_{2-3}Si_2O_5OH_4$), a mineral in the kaolinite-serpentine group (Deer, Howie & Zussman 1963). EPMA analyses in SKN and MZ1 powdered samples also revealed minerals with low weight percent totals (see Table 5-5); likely belonging to smectite and a pyrophillite in SKN and MZ1 respectively.

Electron microprobe analysis identified biotite minerals in the QZ, MZ1 and MZ2 ores, none were detected in SKN. The end-member compositions of the biotites can be determined by plotting the aluminium ions per unit cell versus the magnesium number, which is the proportion of magnesium in the tri-octahedral sites (see Figure 5-6) (Deer, Howie & Zussman 1992). Additionally, the number of titanium ions per unit cell was added to the aluminium ions to account for substitutions. In each corner of Figure 5-6 are the end-members: Annite ($K_2Fe_6[Si_6Al_6O_{20}](OH)_4$), Phlogopite ($K_2Mg_6[Si_6Al_2O_{20}](OH)_4$), Siderophyllite ($K_2Fe_4Al_2[Si_4Al_4O_{20}](OH)_4$), and in the top right hand corner $K_2Mg_4Al_2[Si_4Al_4O_{20}](OH)_4$, which does not have a name (Deer, Howie & Zussman 1963). Figure 5-6 demonstrates that, while there is some variation in both the iron-magnesium ratio and the aluminium number, the micas detected in QZ, MZ1 and MZ2 are predominantly phlogopitic.

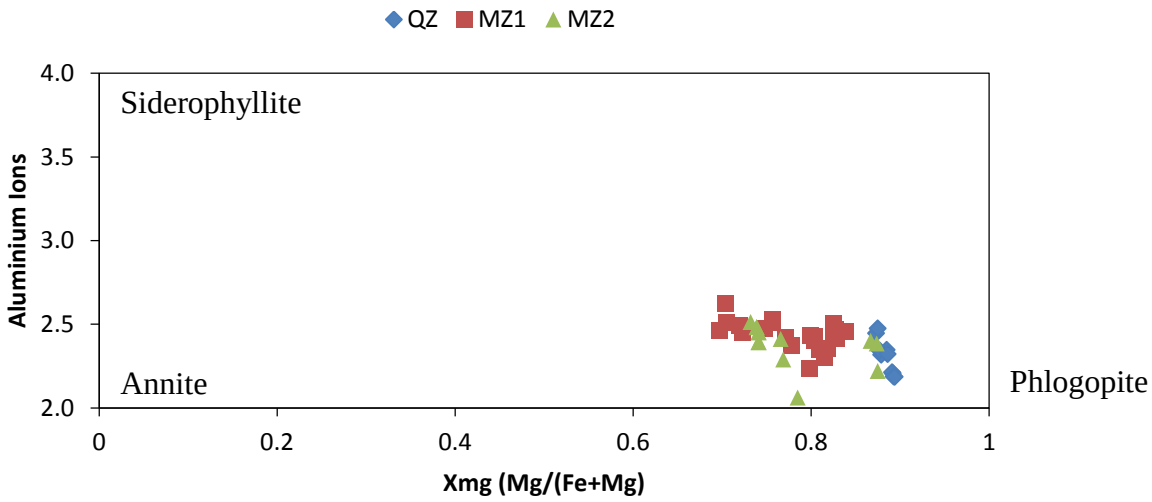

Figure 5-6 – End-member compositions of biotite in ore samples

Table 5-5 – Average elemental analyses of clays (wt. %). Analysis of greenalite from Deer, Howie and Zussman (1963)

	'Olivine' (SKN)	*SKN*	*MZ1*	*Greenalite*
SiO_2	27.25	45.11	57.93	34.7
Al_2O_3	1.43	3.30	17.83	0.90
Fe_2O_3	57.29	13.21	1.34	
FeO				47.3
MnO	0.77	0.07	0.02	0.15
MgO	2.48	18.72	5.24	4.98
CaO	1.26	0.98	0.51	
Na_2O	0.02	0.02	0.03	
K_2O	0.06	0.03	0.19	
Sum Ox%	90.55	85.26	83.07	88.03

5.2.2.5 Garnet

The garnet group is split into two series of end member minerals all of which form solid solutions: the pyralspite series consisting of pyrope, almandine and spessartine; and the ugrandite series consisting of uvarovite, andradite and grossular. Garnets were only observed in the SKN sample and were predominantly andradite with some grossular (see Table 5-6). To contrast, the pure garnet sample used for dielectric measurements in Chapter 3 (see Section 3.3.4.4) is a mixture of almandine and pyrope with only a small amount of andradite.

Table 5-6 – Average Composition of garnets in SKN and reference mineral samples (mol %)

		SKN		*Reference Mineral Samples*	
Mineral	*Formula*	*Mol. %*	*St. Dev.*	*Mol. %*	*St. Dev.*
Pyrope	$Mg_3Al_2Si_3O_{12}$	0.57	0.42	37.44	6.20
Almandine	$Fe^{2+}{}_3Al_2Si_3O_{12}$	0.65	0.67	55.43	5.25
Spessartine	$Mn_3Al_2Si_3O_{12}$	0.23	0.12	0.99	0.40
Andradite	$Ca_3(Fe^{3+}, Ti)_2Si_3O_{12}$	84.31	12.74	4.95	1.43
Uvarovite	$Ca_3Cr_2Si_3O_{12}$	0.04	0.04	0.06	0.06
Grossular	$Ca_3Al_2Si_3O_{12}$	14.22	12.66	1.14	1.16

5.2.2.6 Other Minerals

A range of minor minerals were observed in each of the ores when analysing gangue minerals with the electron microprobe (see Table 5-7).

Table 5-7 – Miscellaneous minerals observed in EPMA investigation

Mineral	*General Formula*	*Number Observed*	*Occurred In:*
Apatite	$Ca_5(PO_4)_3(F,Cl,OH)$	13	MZ1, MZ2, QZ, SKN
Calcite	$CaCO_3$	3	SKN
Epidote	$Ca_2Al_2(Fe^{3+};Al)(SiO_4)(Si_2O_7)O(OH)$	3	MZ1
Ilmenite	$(FeTiO_3)$	1	MZ2
Magnetite	$Fe^{2+}Fe^{3+}{}_2O_4$	1	MZ2
Monazite	$(Ce, La, Pr, Nd, Th, Y)PO_4$	1	MZ2
Rutile	TiO_2	6	MZ1, MZ2
Titanite	$CaTi(SiO_4)$	1	MZ2
Zircon	$ZrSiO_4$	1	MZ1

5.2.3 Conclusions

The MLA was used to determine the modal mineralogy of powdered ore samples and from this data the rock-types were classified according to Streckeisen (1976). These measurements highlighted the different proportions of gangue and sulphide mineral present in each of the ores. EPMA measurements were then used to determine the chemistry of minerals within a subset of the powdered samples used for MLA. These measurements allowed specific mineral end-member compositions to be determined within the modal mineralogy groupings.

5.3 Calculation of Dielectric Properties from Mixtures

In Chapter 3, the dielectric properties of a number of different ore mixtures was measured in a resonant cavity (see Section 3.3.4.1), and in this chapter (see Section 5.2.1), the modal mineralogy data of those mixtures was obtained. These data can then be written as a system of linear equations in the form of a n-component version of the Landau-Lifschitz-Looyenga (LLL) mixture equation (see Equation (5.1) and (5.2)). The LLL mixture equation was identified by Nelson (2005) as providing the best estimates of solid dielectric properties from powdered and granular mixtures. Furthermore, the LLL mixture equation was used in Chapter 3 (see Section 3.3.2) to calculate the dielectric properties that are used in these calculations.

Equation (5.2) represents the linear LLL dielectric mixing equation of a single n-component mixture. Multiple LLL equations can expressed in matrix form using Equation (5.3), which when expanded appears as Equation (5.4) – in this equation the elements, v_f in the vector **A** are volume fractions. The matrix form of the system of equations can then be solved using the mldivide function in MATLAB; which applies a least squares solution to solve over-determined systems. The least squares algorithm finds a solution by minimizing the length of Equation (5.5). In these calculations the permittivity and loss factor are solved independently.

$$\epsilon_M^{1/3} = \sum_{i=1}^{n} \frac{v_i}{v_t} \epsilon_i^{1/3} \tag{5.1}$$

$$\epsilon_M^{1/3} = \frac{v_1}{v_t}\epsilon_1^{1/3} + \frac{v_2}{v_t}\epsilon_2^{1/3} \cdots + \frac{v_n}{v_t}\epsilon_n^{1/3} \tag{5.2}$$

$$\mathbf{Ax = b} \tag{5.3}$$

$$\begin{bmatrix} v_{f1,1} & \cdots & v_{f1,n} \\ \vdots & \ddots & \vdots \\ v_{fm,1} & \cdots & v_{fm,n} \end{bmatrix} \begin{bmatrix} \epsilon_1^{1/3} \\ \vdots \\ \epsilon_n^{1/3} \end{bmatrix} = \begin{bmatrix} \epsilon_{M1}^{1/3} \\ \vdots \\ \epsilon_{Mm}^{1/3} \end{bmatrix} \tag{5.4}$$

$$\|\mathbf{Ax - b}\| \tag{5.5}$$

5.3.1 Trial with Quartz-Pyrite Mixtures

The dielectric calculation method described above was tested using the 2470 MHz quartz-pyrite mixture data obtained in the resonant cavity error characterization experiments of Chapter 3 (see Section 3.3.3). The mineral mass percentages of each of the three quartz-pyrite mixtures were converted to volume percentages and the cube root of both permittivity and loss factor calculated. Equation (5.6) demonstrates the form of the system of equations used to calculate permittivity and displays data averaged for each of the three quartz-pyrite mixtures. However, all 54 of the error characterisation data points were used in the full matrix solution.

The resulting best fit dielectric properties for pyrite and quartz can be found in Table 5-8 along with dielectric properties from pure mineral powder samples measured previously (see Section 3.3.4.4 of Chapter 3). Furthermore, duplicate least squares regression and error analysis were performed using Minitab, reports of the fitting can be found in the Appendix (see Section 8.7.1). The standard errors of these calculations demonstrate a reasonable degree of confidence in the results. Additionally, the results indicate reasonable level of agreement between measured and calculated values.

$$\begin{bmatrix} 0.1184 & 0.8816 \\ 0.0555 & 0.9445 \\ 0.0284 & 0.9716 \end{bmatrix} \begin{bmatrix} \epsilon_{pyrite}^{1/3} \\ \epsilon_{quartz}^{1/3} \end{bmatrix} = \begin{bmatrix} 1.8538 \\ 1.7919 \\ 1.7697 \end{bmatrix} \tag{5.6}$$

Table 5-8 – Measured and best fit dielectric properties of Pyrite and Quartz

	Measured		*Best Fit*			
Mineral	ϵ'	ϵ''	ϵ'	$SE_{\epsilon'}$	ϵ''	$SE_{\epsilon''}$
Quartz	4.63	0.02	5.28	0.106	0.03	0.004
Pyrite	26.38	5.94	19.36	3.041	6.94	2.218

5.3.2 Application to Ore Data

This method for least squares regression of dielectric properties was then applied to ore data. This involved the dielectric properties of powdered ore samples from Chapter 3 (see Section 3.3.4.1) and the modal mineralogy data produced from MLA XMOD analyses (see Section 8.6.1 of the Appendix). The MLA modal mineralogy reports include 25 mineral groupings – if mineral mixtures were controllable and a full factorial design experiment used (with 3 levels of each mineral) to determine dielectric properties this would result in 3^{25} different measurements. This is considerably more than the 28 points of data collected and for this reason a good solution for the dielectric properties all mineral groupings is not anticipated.

Since the modal mineralogy data were reported in mass percent these were converted to volume percent using density values (see Section 8.6.2 of the Appendix). Regression utilising the full mineralogy data set produces a poor solution with very large negative and positive dielectric property values – results can be found in the Appendix (see Section 8.7.2). The very low abundances of some mineral species cause them to have a high degree of leverage in the solution. Consequently a simpler, more condensed modal mineralogy is required. When regressions are constrained to positive coefficients the solutions produce very large numbers and zeros instead. Investigating the data using regression with positive constrained coefficients follows a similar path of data simplification as reported in this section.

To simplify the modal mineralogy data, minerals with very low total volume or similar physical properties are grouped (see Table 5-9). Simply removing minerals would require the data to be renormalized which could significantly affect the apparent volumes of other minerals. All sulphides were merged into a single group. Pyroxene and Amphibole were merged due to their chemically and physically similar nature. A phyllosilicate group includes biotite, chlorite, muscovite, olivine and talc. Olivine is not a sheet silicate but was included in the phyllosilicate group as it was found to be misreported clays (see Section 5.2.2.4). The other grouping contains apatite, calcite, titaniferous minerals and iron oxide, as well as miscellaneous minerals including monazite and zircon.

A solution with a separate Plagioclase group was obtained (see Section 8.7.3 of the Appendix) but produced unusually large dielectric properties for this mineral. Mixtures with significant quantities of plagioclase were then excluded from the system and the plagioclase in the remaining mixtures was added to the 'Other' group. This approach was taken for two reasons: there was a low total volume of plagioclase in the sample set; and samples with significant volumes of plagioclase always feature large volumes of phyllosilicates. Consequently, the relationship between plagioclase and the phyllosilicate grouping confuses the regression solution. Table 5-10 displays the dielectric properties of minerals solved without a plagioclase group using dielectric property data of samples at both 2470 and 912 MHz. Identical least squares solutions were obtained using Minitab, however, this software also produced estimates of error, the results of which can be found in Table 5-11 below. Full regression reports can be found in the Appendix (see Section 8.7.4).

The phyllosilicates possess a much larger calculated loss tangent than other gangue mineral groups. However, there real component of permittivity calculated lies between the values reported by Church, Webb and Salsman (1988) and Nelson, Lindroth and Blake (1989) for muscovite and phlogopite/biotite. Indeed, comparison of the dielectric properties reported in Church, Webb and Salsman (1988) and Nelson, Lindroth and Blake (1989) shows the former to be systematically lower. The large loss factor is potentially reasonable considering this grouping also contains clay minerals with high degrees of hydration.

The best fit dielectric properties of the sulphide mineral group are much higher than was measured for individual sulphides in the Chapter 3 (see Section 3.3.4.4). However, there is considerable variation in the dielectric properties of sulphide minerals reported in scholarly literature, which can extend to much large values (see Section 2.4 of the Literature Review). When the extent of the spread is considered, the best fit dielectric properties are reasonable. The dielectric properties calculated for the pyrobole group are also reasonable given they lie close to the values reported by Nelson, Lindroth and Blake (1989) – amphibole (richterite) $\epsilon' = 7.37$ $\epsilon'' = 0.026$, and pyroxene (diopside) $\epsilon' = 7.18$ $\epsilon'' = 0.17$. The best fit dielectric properties of quartz are close to values measured using the C1 cavity in Chapter 3 (see Section 3.3.4.4) although they are slightly higher than the values reported by Church, Webb and Salsman (1988) at 1 GHz ($\epsilon' = 3.89$). The calculated dielectric properties of the garnet group are comparable to those of quartz. Dielectric property measurements of garnet minerals in Chapter 3 produced much larger values ($\epsilon' = 10.64$ $\epsilon'' = 0.017$), however EMPA measurements revealed they possess very different chemical compositions (Section 5.2.2.5). Lastly, the calculated alkali feldspar properties are likely reasonable given they lie between those reported for orthoclase by (Church, Webb & Salsman 1988) and for labradorite by (Nelson, Lindroth & Blake 1989).

P-values show that all of the mineral groupings are statistically significant in calculations of permittivity (see Table 5-11). However, large P-values are encountered in the calculation of loss factors of ‘pyrobole’, ‘garnet’ and ‘other’ at these frequencies. These large P-values are reflected in the standard errors of mineral groups in the regression. While regressions of permittivity show all mineral groupings are statistically significant, the relative standard errors of each mineral, bar quartz, are greater than 10%. The relative standard error in loss factors is much higher and starts at 40% for quartz.

Low volume fractions of mineral groups may be a reason for the lack of confidence in solved dielectric properties. Figure 5-7 plots the relative standard error of mineral groups against their total volume fraction and clearly indicates that minerals with larger volume percentages have lower relative standard errors. One solution to this may be to split samples, and all further measurements and calculations, in two by using a technique such as density separation. Furthermore these regressions were performed on data from four different ores; differences in the chemistry of

minerals between the ores may increase the degree of error in the solution, particularly in 'phyllosilicates' and 'other'. Application of this technique to larger samples sets of individual ores will simultaneously reduce the complexity of the mixtures and reduce the error due to mineral chemistry.

Table 5-9 – Mineral groupings

Group	*Component Minerals*
Sulphides	Chalcopyrite, Bornite, Chalcocite, Pyrite, Molybdenite, Covellite, Tetrahedrite, Arsenopyrite, and Galena
Pyrobole	Pyroxene, Amphibole
Phyllosilicates	Biotite, Muscovite, Chlorite, Olivine, Talc
Other	Apatite, Calcite, Iron Oxide, Plagioclase Rutile_Ilmenite_Titanite, and Other

Table 5-10 – Best fit dielectric properties for mineral groups at 2470 and 912 MHz

		2470 MHz			*912 MHz*		
Mineral	*Total Vol%*	ϵ'	ϵ''	ϵ''/ϵ'	ϵ'	ϵ''	ϵ''/ϵ'
Sulphides	2.14%	49.81	33.78	0.678	54.81	49.05	0.895
Quartz	45.83%	4.61	0.04	0.008	4.47	0.05	0.011
Alkali Feldspar	17.16%	5.40	0.09	0.017	5.21	0.12	0.023
Pyrobole	8.93%	7.42	0.03	0.004	6.85	0.01	0.002
Phyllosilicates	14.07%	7.68	1.13	0.147	7.96	1.67	0.210
Garnet	7.35%	4.38	0.08	0.018	4.45	0.12	0.027
Other	4.52%	11.86	0.12	0.010	10.57	0.06	0.005

Table 5-11 – Probability and Standard Errors of best fit dielectric properties for mineral groups at 2470 and 912 MHz

		2470 MHz				*912 MHz*			
Mineral	*Total Vol%*	$P_{\epsilon'}$	$SE_{\epsilon'}$	$P_{\epsilon''}$	$SE_{\epsilon''}$	$P_{\epsilon'}$	$SE_{\epsilon'}$	$P_{\epsilon''}$	$SE_{\epsilon''}$
Sulphides	2.14%	0.002	39.55	0.015	37.35	0.001	42.96	0.019	56.21
Quartz	45.83%	0.000	0.29	0.000	0.01	0.000	0.29	0.000	0.02
Alkali Feldspar	17.16%	0.000	0.83	0.001	0.07	0.000	0.82	0.002	0.09
Pyrobole	8.93%	0.000	4.75	**0.566**	0.14	0.000	4.59	**0.695**	0.10
Phyllosilicates	14.07%	0.000	1.67	0.000	0.57	0.000	1.75	0.000	0.87
Garnet	7.35%	0.000	2.94	**0.354**	0.24	0.000	3.03	**0.360**	0.39
Other	4.52%	0.000	7.26	**0.397**	0.42	0.000	6.85	**0.571**	0.30

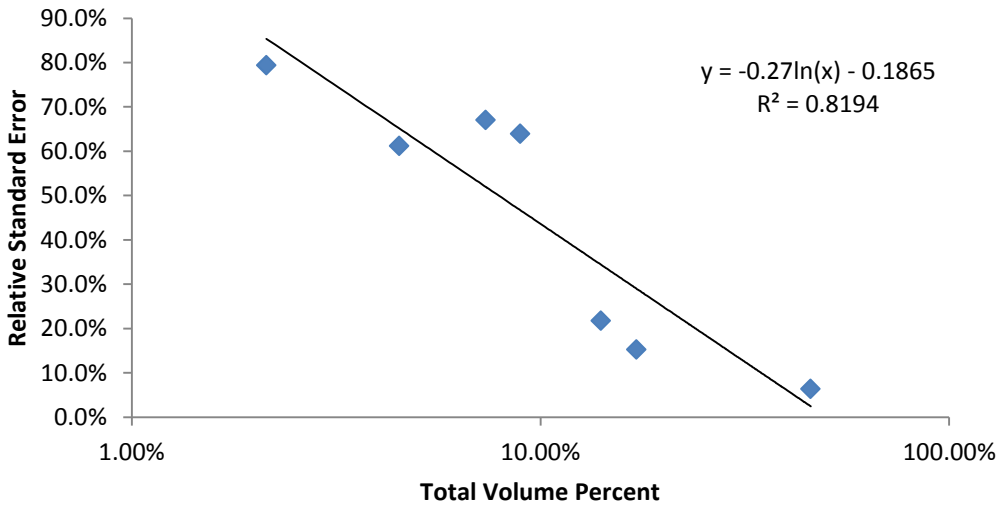

Figure 5-7 – The effect of volume concentration on the relative standard deviation of regressed permittivity values at 2470 MHz

5.3.3 Conclusions

The dielectric properties of discrete mineral groups across four different ores have been approximated from modal mineralogy and dielectric properties data of mixtures. This was accomplished in MATLAB by least squares solution of over-determined systems of linear equations. Minerals with low total volume were found to have a large leverage on the solution and were either grouped with similar minerals or moved to 'other' while mixtures very rich in that mineral were removed from the data set. The permittivities of mineral groups calculated in this manner are reasonable when compared with values measured previously (see Section 3.3.4.4 of Chapter 3) and those found in scholarly literature. However, error analysis in Minitab, despite low P-values, shows large standard errors.

5.4 Modelling Sorter Performance from Dielectric Properties

With the dielectric properties of specific valuable and gangue minerals measured and an existing body of literature on the specific heat capacity and density of minerals it becomes possible to model how arbitrary mixtures of these minerals might heat in electromagnetic fields. This simulated heating information can then be used to gain insight into the sorting behaviour of a hypothetical ore through the Monte Carlo simulations. The simulation code was written using MATLAB and copies of the functions used can be found in the Appendix (see Section 8.8.1). To accomplish these simulations a number of distinct steps are required, these include:

- Randomly generating a vector of simulated ore particle mixtures using copper grade distributions which form the basis for simulated particles.
- Calculating the dielectric properties, density and specific heat capacity of each simulated particle mixture using known values of minerals and a dielectric mixing equation.
- Applying microwave heating formulae to calculate the ideal temperature rise of each hypothetical particle mixture.
- Introducing an uncertainty into calculated ideal heating values.
- And finally, calculating the grade recovery curves of the simulated system.

To do this, a number of assumptions are made. As the model deals with random mixtures of chalcopyrite and gangue, large differences in the dielectric properties of simulated particles will arise. To accommodate these differences in dielectric properties a number of assumptions are made to simplify the model. Both spatially varying fields and different geometry particles greatly add to the complexity of the simulations. To address these effects would require numerical solutions for each particle and involve information on both the cavity and particle geometry. These effects are removed by assuming that there is no spatial variation of field within the particles and that the field intensity can be expressed as a scalar number. A consequence of this is that for a given field intensity the total power dissipated in a particle should be systematically over-estimated because the penetration depth is no longer considered.

Another assumption is that heating is only due to the dielectric properties of mixtures. While the dielectric properties of minerals have been characterized at microwave frequencies (see Section 3.3.4.4 of Chapter 3), the magnetic properties are not well known. Therefore heating due to interaction with the magnetic field is not considered. Furthermore, the mixture equations are assumed to completely homogenise the minerals within the particles and no internal structuring is considered. While particle shape, texture, heterogeneity and magnetic properties are not addressed explicitly, the introduction of a randomized uncertainty model does indirectly account for them.

5.4.1 The Particle-to-Particle Distribution of Valuable Phases

Variation of concentration of valuable minerals between particles is central to sorting as a pre-concentration technique. If a feed cannot be economically processed and there is little variation in the grade of particles then there is no case for either sorting or processing. A Monte Carlo simulation of a microwave/IR sorting therefore needs to model the distribution of valuable phase concentrations. In the case of a porphyry copper deposit valuable phase is primarily chalcopyrite. In ores deposits there are many reasons for grade variability between particles ranging from the genesis of the ore body, to the mining techniques used (e.g. the blasting energy).

While the MLA data in the previous section of this chapter could provide a proxy for a copper assay and consequently provide information on the distribution of copper in particles, not enough samples were analysed. For the purposes of recovery modelling, it is assumed that the mass of copper bearing minerals, on a particle-by-particle basis, falls into one of three types of distributions: Normal, Log-Normal, and Bi-Modal (two normal distributions, one offset from the other). The normal distribution represents the simplest case and the bi-modal distribution provides a 'best-case' for sorting as it has a large set of mostly barren particles and a small set of considerably richer particles. However, a Log-normal distribution of particle grades is the most likely case, having been observed in copper, gold and uranium deposits (Krige 1966; Razumovsky 1940). Histograms of these three distributions can be found in Figure 5-8; the parameters used to generate the distributions in Figure 5-8 are can be found in Table 5-12. The parameters of the distributions have been arranged such that they average of 0.33% copper per unit mass at large sample sizes. The value of 0.33% copper grade (or approx. 1% chalcopyrite) was chosen to represent ores close to but above a typical economic cut-off grade of approx. 0.3%.

The mass fraction of the valuable mineral phase, in this case chalcopyrite, is then calculated using the generated mass fractions of copper and supplied atomic weight ratios. Stoichiometric chalcopyrite ($CuFeS_2$) is approx. 34.63% copper. Once the quantity of the valuable phase has been determined, the remainder is considered to be gangue matrix. It must be noted that in this implementation only binary mixtures of 'valuable' and 'gangue' phase are dealt with. These phases contain mineral components in fixed ratios and the properties of each mixture are calculated before simulation using the mineralmixer function (see Section 8.8.1.1 of the Appendix for code) which is described further in the next section.

Table 5-12 – Parameters for generating Cu grade distributions

Distribution	*q*	*M*	*s*	*Mean Cu Fraction* (Sample Size: $1x10^6$)
Normal	1	0	4.1×10^{-3}	3.3×10^{-3}
Bi-Modal	0.75	0	1.2×10^{-3}	3.3×10^{-3}
	0.25	1.05×10^{-2}	2.5×10^{-3}	
Log-Normal	1	3.3×10^{-3}	4×10^{-6}	3.3×10^{-3}

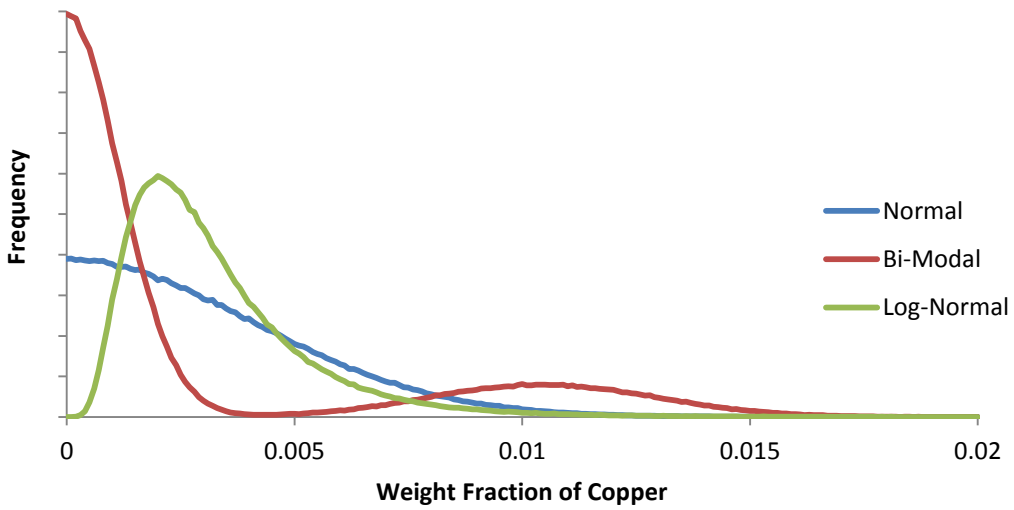

Figure 5-8 – A Histogram of the outputs of the different Cu Fraction Distribution functions (sample size $1x10^6$)

5.4.2 Generation of Physical Properties

The second stage of modelling calculates the physical properties of each simulated particle from the proportion of the gangue and valuable mineral phases and the properties of the individual phases. The physical properties calculated for the mixture include: the density, ρ_{mix}, specific heat capacity, C_{pmix} and relative permittivity, ϵ_{mix}. The dielectric properties of each simulant particle are calculated using the Landau Lifschitz Looyenga (LLL) dielectric mixing equation (5.7), discussed

in the Literature Review (see Section 2.5) while density and specific heat are calculated by linear combination.

Although the modelling function, RecoveryModeller2X (see Section 8.8.1.3 of the Appendix for code) only deals with binary mixtures of gangue and valuable phases the physical properties of more complex gangue and valuable mineral mixtures can be pre-calculated using the mineralmixer function (see Section 8.8.1.1 of the Appendix for code). This function calculates the physical properties of a mixture from an arbitrary number input of phases using Equations (5.9) and (5.10) as well as a reformulated LLL mixture equation (5.8). Physical properties of complex gangue and valuable mixtures are pre-calculated using mineralmixer and then returned to the RecoveryModeller2X function for simulation. For simplicity, the simulation assumes that the mixture is solid (i.e. no porosity and associated volume fraction of air or water) and homogeneous.

$$\epsilon_{mix}^{1/3} = v_1\epsilon_1^{1/3} + v_2\epsilon_2^{1/3} \tag{5.7}$$

$$\varepsilon_{mix}^{1/3} = \sum_{i=1}^{n} \frac{v_i}{v_T}\varepsilon_i^{1/3} \tag{5.8}$$

$$\rho_{mix} = \sum_{i=1}^{n} \frac{v_i\rho_i}{v_T} \tag{5.9}$$

$$C_{pmix} = \frac{\sum_{i=1}^{n} \rho_i v_i C_{pi}}{\rho_{mix} v_{mix}} \tag{5.10}$$

Two different multiphase gangue matrices were calculated as mixtures of quartz, potassium feldspar (K-feldspar) and phyllosilicate. The simulated ores consist of chalcopyrite in A) a quartz-rich granitoid type matrix similar to QZ, and B) an alkali feldspar granite matrix similar to MZ1 (see Table 5-14 for the calculated properties of the gangue matrices). To generate these gangue matrices, the dielectric property data for quartz measured in Chapter 3 (see Section 3.3.4.4) was used along with those calculated for K-feldspar and phyllosilicate above (see Section 5.3.2). Data on mineral

density and specific heat were obtained from Waples and Waples (2004). As the mineralogy obtained from the MLA analysis only distinguished broader groups of these minerals, the densities and specific heats for K-feldspar and phyllosilicates were averaged Na-K-feldspar and Mica groups in Waples and Waples (2004) respectively. The values used in the modelling for the physical properties can be found in Table 5-13.

Table 5-13 – Mineral Properties for Recovery Modelling (2470 MHz)

Mineral	ϵ'	ϵ''	*Density g/cm^3*	*Specific Heat J/(gK)*
Chalcopyrite	22.36	1.65	4.4	534
Quartz	4.36	0.001	2.8	740
K-Feldspar	5.42	0.11	2.6	715
Phyllosilicate	7.86	0.79	2.9	770

Table 5-14 – Properties of simulated gangue mixtures at 2470 MHz

	A	*B*
Quartz	85%	18%
K-Feldspar	15%	42%
Phyllosilicate	0%	40%
ϵ'	4.51	6.10
ϵ''	0.02	0.32
Density g/cm^3	2.77	2.76
Specific Heat J/(gK)	736.5	742.7

5.4.3 Internal Electric Field and Dielectric Heating

The power dissipated per unit volume in a medium, Equation (5.11), is first introduced in the literature review (see Section 2.2.2). To simulate recovery it is necessary to compare the heating of many different particles with different dielectric properties. A heating model based on Equation (5.11) would use a fixed internal field; however this implies a variable external field since each mixture will have different dielectric properties. To achieve the same field conditions for all mixtures it is necessary to approximate the internal electric field from a fixed external field, considered to be in a vacuum ($\epsilon_{vac} = 1$). To do this, the electric field in a dielectric is calculated using the following relationships:

- Applied electric field parallel to the material interface (Equation (5.12))
- Applied electric field normal to the material interface (Equation (5.13)
- A sphere in a uniform field (Equation (5.14))

$$P_d = 2\pi f \varepsilon_0 \varepsilon_r'' E^2 \tag{5.11}$$

$$E_{||vac} = E_{||mix} \tag{5.12}$$

$$\varepsilon'_{vac} E_{\perp vac} = \varepsilon'_{mix} E_{\perp mix} \tag{5.13}$$

$$E_{mix} = \frac{3\epsilon'_{vac} E_{vac}}{2\epsilon'_{vac} + \epsilon'_{mix}} \tag{5.14}$$

Applying these relationships to Equation (5.11) yields equations for power dissipation (5.15), (5.16) and (5.17) which correspond to internal electric fields described by Equations (5.12), (5.13) and (5.14) respectively. The change in mixture temperature, ΔT, for each of these power dissipation models is then reached using Equation (5.18)

$$P_{d1} = 2\pi f \epsilon_0 \epsilon''_{mix} \left| E_{\|vac} \right|^2 \tag{5.15}$$

$$P_{d2} = \frac{2\pi f \varepsilon_0 \varepsilon''_{mix} \left| E_{\perp vac} \right|^2}{\varepsilon'^{\,2}_{mix}} \tag{5.16}$$

$$P_{d3} = \frac{18\pi f \epsilon_0 \epsilon''_{mix} \left| E_{vac} \right|^2}{\left(2 + \epsilon'_{mix}\right)^2} \tag{5.17}$$

$$\Delta T = \frac{P_d t}{\rho_{mix} C_{pmix}} \tag{5.18}$$

The heating rates predicted by these different forms of the dielectric heating equation, with the addition of the power law heating discussed in Chapter 3 (see Section 3.3.4.1), can be found in Figure 5-9. The results in Figure 5-9 were generated from a binary mixture of quartz and chalcopyrite with the dievolmod function (see Section 8.8.1.2 of the Appendix for code). Heating is calculated based on an applied electric field of 60kV/m (approx. 2% dielectric breakdown voltage of air), this corresponds to the maximum electric field intensity in a WR340 waveguide delivered by a 2.45 GHz system delivering approx. 6.3kW. It can be seen in Figure 5-9 that the heating rates predicted are substantially different and that the inverse relationship with ϵ'^2_r in the modified form creates a peak heating rate at approximately 53.8% chalcopyrite.

This modelling of microwave heating assumes that the electric field is constant within each sample and the skin depth is not considered. However, the internal electric field is governed ratio of the internal and external dielectric properties and the orientation of the interface with the external field. The internal electric field of a sample should lie between $E_\perp$ and $E_\|$. Therefore these two models of internal electric field, when used in the heating calculations, should result in the maximum and minimum expected heating in empirical situations. Rock particles have complex and irregular geometries but if they are approximated as spheres, the E_{sphere} calculation of internal electric field can be used; as anticipated, microwave heating calculated using this model lies between $E_\perp$ and $E_\|$. The power law model, unlike the other three models, is empirical and specific to the 1200 Watt

2.45 GHz domestic system. This model consequently produces lower heating rates than either of the other models for low volume fractions of chalcopyrite.

The microwave heating data presented in Chapter 3 of this thesis was based on experiments using a single size fraction (-22.4 mm + 19.0 mm). As no relationship between particle size and microwave heating has been established this modelling cannot consider any effect of particle size might have on sorter performance. Furthermore the equations describing power dissipation are in terms of unit volumes and, while the heat transfer equation is normally in terms of mass, substituting with density and volume removes any volume dependence. Therefore differences in microwave heating that arise from differences in particle size cannot be addressed without the introduction of further terms into these equations.

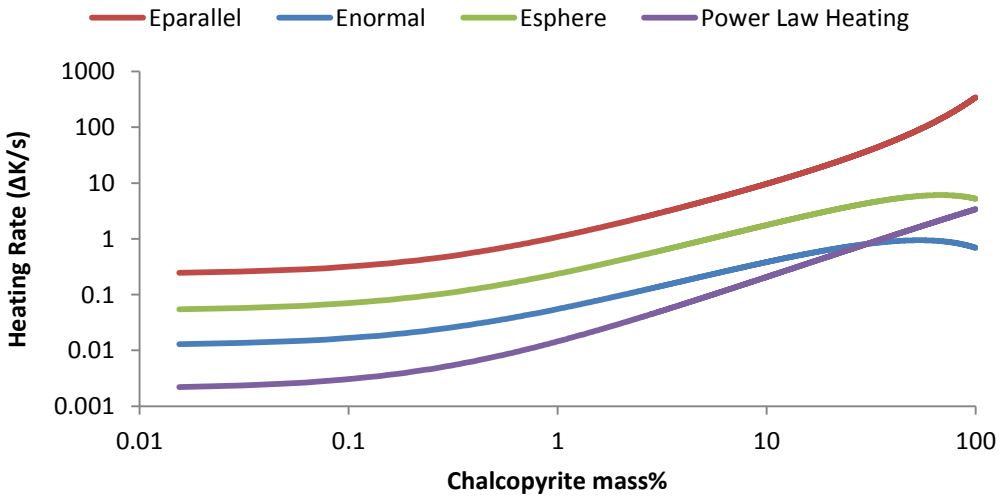

Figure 5-9 – The heating rates produce by the different dielectric heating models

When the heating models are implemented in the recovery modelling code and used in combination with the ore concentration distributions results the ore heating behaviour can be observed. The cumulative distribution function (CDF) in Figure 5-10 shows the heating behaviours of the different grade distribution models for 1 x 10^4 simulated quartz-chalcopyrite mixtures using the $E_{\perp}$ heating model (Equation (5.16)). Similar CDF graphs for the other heating models can be found in the

Appendix (see Section 8.8.2). The maximum chalcopyrite mass percentages generated by the grade distribution functions are not large (see Table 5-15). The CDFs produced (Figure 5-10 and Section 8.8.2; Figure 8-33, Figure 8-34 and Figure 8-35) have very similar shapes and is the result of highly linear behaviour in all heating models between 0 and 5% chalcopyrite. Results of linear regression of the heating models in the 0 to 5% chalcopyrite range can be found in the Appendix (see Section 8.8.2, Table 8-40).

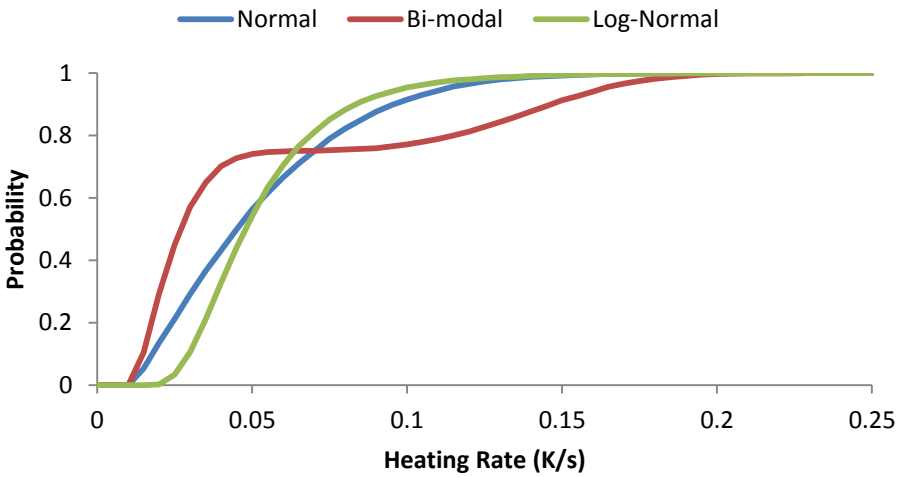

Figure 5-10 – Cumulative Distribution Function of Particle Heating ($E_{\perp}$)

Table 5-15 – Largest Mass% Chalcopyrite observed in the CDF data sets (e.g. Figure 5-10)

Grade Distribution Function	*Chalcopyrite (mass%)*
Normal	4.83
Bi-Modal	5.80
Log-Normal	6.80

The recovery curves below result when the ideal heating models are applied to the two gangue mixtures (see Figure 5-11, Figure 5-12 and Figure 5-13) – uncertainty in microwave heating is introduced in the following section. Grade recovery curves are a useful way of visualizing the

potential benefits of sorting (see Figure 5-11), in these graphs the black line, called 'Splitter', demonstrates what would be expected of a purely random selection of particles. This method of sorting results in equal proportions of copper reporting to the product and waste streams. For non-random, temperature based sorting process the mixtures are rearranged by temperature in descending order. As a consequence of this sorting the Cumulative Mass Recovery axis shows the percent of the feed that reports to the product stream. When a data set ordered in this manner deviates from the 'Splitter' line non-random grade selection may be achieved based on temperature. The further the deviation from the splitter performance, the greater the potential for sorting. Simulation predicts that for the Bi-modal distribution in Figure 5-11, the hottest 20% of the total mass contains close to 70% of copper.

The heating models produce identical grade recovery curves for Gangue A (see Section 8.8.3; Figure 8-36, Figure 8-37, Figure 8-38 of the Appendix). However, there is disagreement between the models for Gangue B. The grade recovery curves predicted by the $E_{\parallel}$ and Power Law models are consistent with those produced for Gangue A (See Figure 5-13 and Section 8.8.3, Figure 8-39 of the Appendix). However, the curves predicted by $E_{\perp}$ and E_{sphere} are inverted (see Figure 5-12, Figure 5-13 and Section 8.8.3, Figure 8-40 of the Appendix) which indicates that the gangue matrix may heat more than the chalcopyrite. This suggests that there is still a potential for sorting because the copper rich particles will be the coldest after microwave heating although this is a questionable result given the disagreement between the heating models.

Inverted grade-recovery curves are counter-intuitive given that the dielectric properties of chalcopyrite are greater than those of the gangue matrix. However, heating is power deposited divided by the product of density and specific heat (see Equation (5.18). The product of density and specific heat for chalcopyrite is greater than that for Gangue B. In situation where models predict of vary small changes of power deposition the increase in the size of the denominator of Equation (5.18) mean that it is feasible that there is a decrease in heating. This effect does not appear in modelling with Gangue A because it is a very poor absorber and has greater changes in power deposition with chalcopyrite.

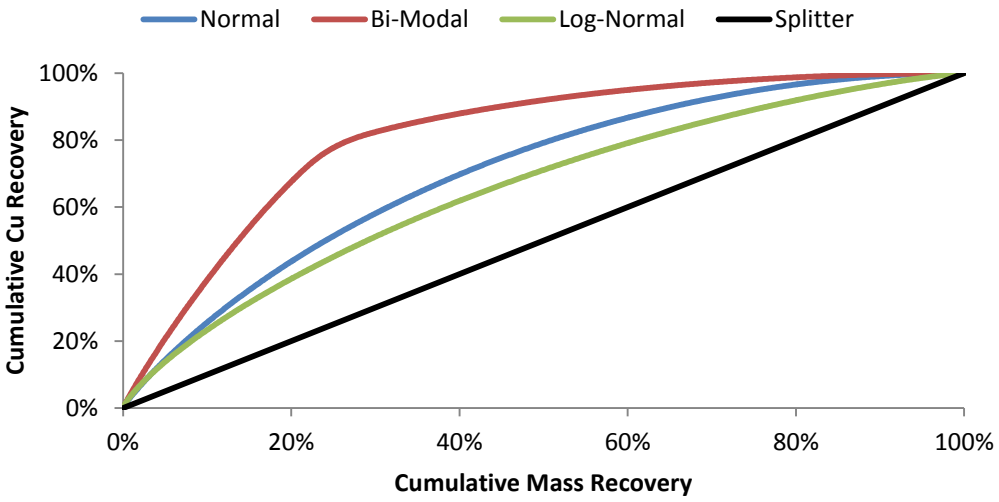

Figure 5-11 – Ideal Grade Recovery Curve, Gangue A ($E_{\perp}$)

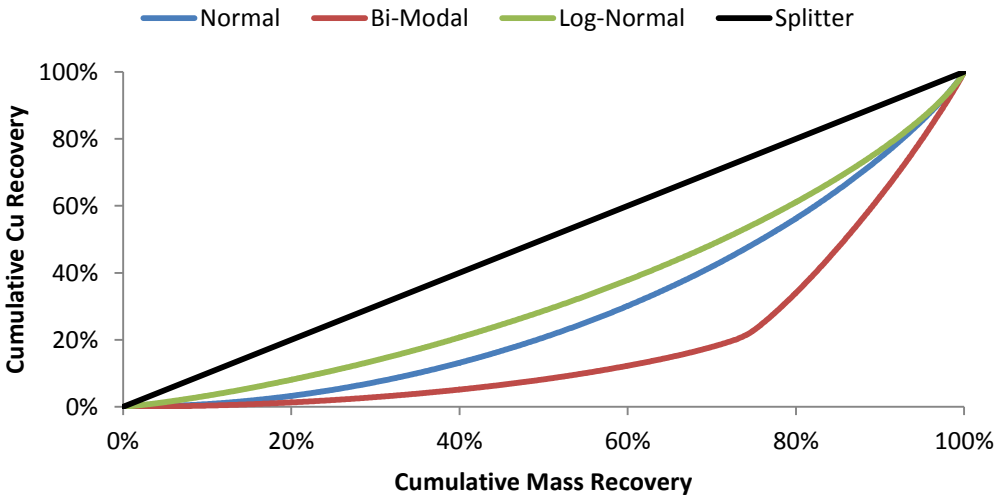

Figure 5-12 – Ideal Grade Recovery Curve, Gangue B ($E_{\perp}$)

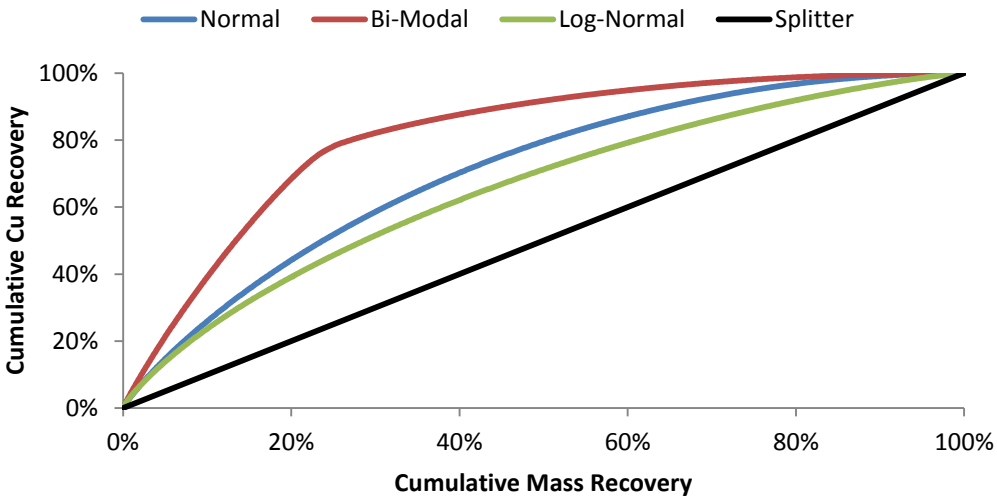

Figure 5-13 – Ideal Grade Recovery Curve, Gangue B (Power Law)

5.4.4 Modelling Uncertainty in Microwave Heating

In a perfect system, particles would report to either the 'product' or 'reject' streams based their grade alone. Systems which determine particle grade through indirect measurement techniques have numerous sources of uncertainty. This uncertainty means that particles report to the wrong streams, as either false negatives or false positives, and thereby reduce the quantity of valuable minerals recovered.

There are numerous sources of uncertainty in the measured temperature change of particles due to microwave heating. Sources of uncertainty include intrinsic properties, such as: geochemical variation affecting the dielectric properties, density and specific heat; porosity; and moisture content. Extrinsic effects that influence the measured particle temperatures include: emissivity (which changes the apparent temperature measured by the IR camera); the electric field mode structure of the cavity, particle shape and orientation within the field, and potentially even strongly absorbing particles nearby when exposed to the microwave field which may distort the local field intensity. Veins of highly conductive materials may further contribute to variation due to particle orientation within the field.

These effects can be modelled together, empirically, using the heating characterization data from Chapter 3 (see Section 3.2.2.1). The heating characterization involved heating sets of particles repeatedly in a domestic microwave oven and the variability can then be examined via the distribution in Relative Standard Deviations (RSDs), which are the standard deviation in temperature changes divided by the mean temperature changes for each particle and are consequently dimensionless. Cumulative Distribution Functions (CDFs) of the RSDs in particle temperature change are displayed in Figure 5-14 below. From this figure, SKN and MZ2 are noticeably different to other three monzonite ores (MZ1, MZ3 and MZ4) as well as the quartzite ore, QZ.

When SKN and MZ2 are excluded, the RSD data for the remaining ore samples is merged and then fitted with a normal distribution (see Figure 5-16) using the statistics toolbox in MATLAB. The details of this fitting can be found in Table 5-16. This normal distribution is then used as the basis for a model of variability in particle temperature increases as a result of microwave heating. A random number is generated according to fitted normal distribution (Table 5-16) for a simulated particle as an RSD; this value then converted to a standard deviation using the ideal value for temperature change calculated previously. The final temperature change (in Kelvins) for a simulated particle is generated using a second, normally distributed, random number. This second random number occurs within a distribution defined by a mean of the initially calculated temperature change and the generated standard deviation. This doubly random technique is valid because the RSD is weakly correlated (correlation coefficient: 0.25) to temperature rise, which is shown in Figure 5-15.

Table 5-16 – Parameters of Fitted Normal Distribution

	Estimate	Std. Err.
Mean	0.1554	0.0045
Standard Deviation	0.0515	0.0032

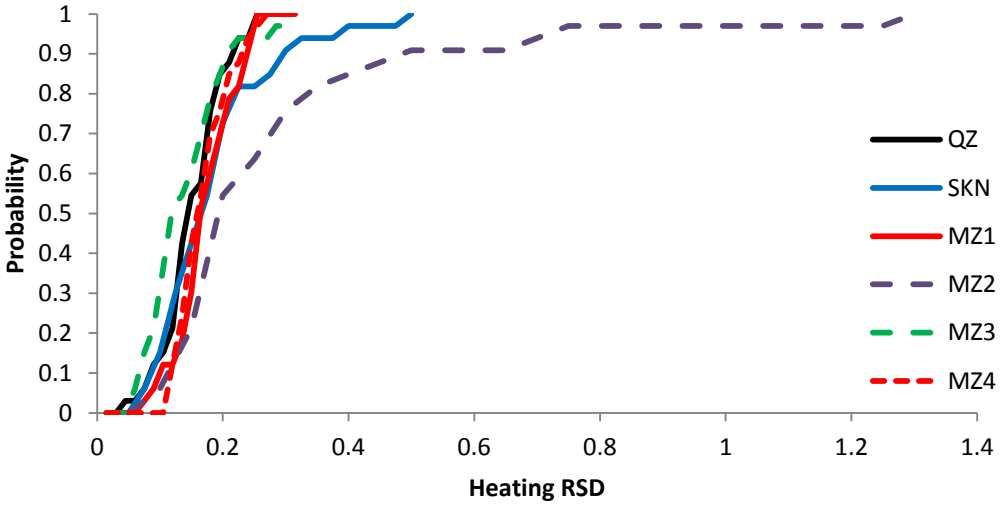

Figure 5-14 – CDFs of Particle Temperature Change RSDs

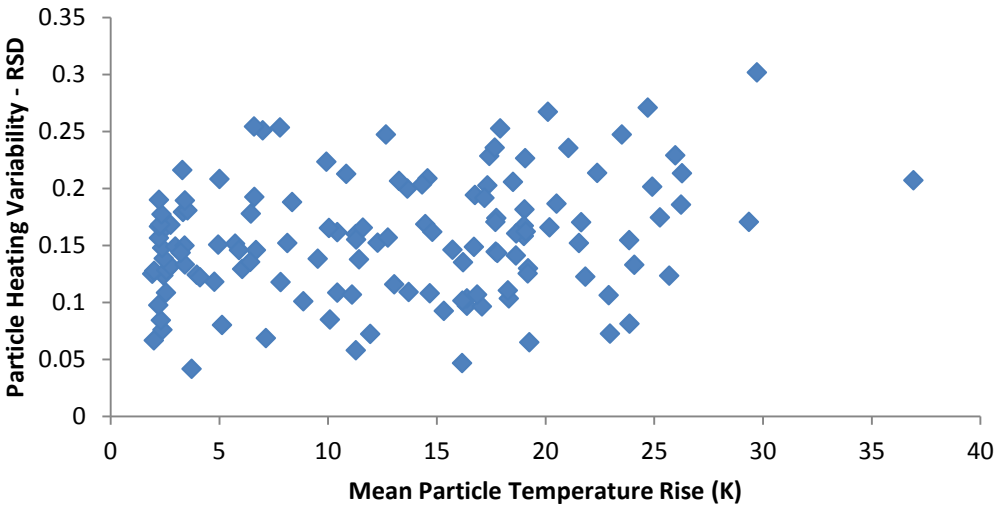

Figure 5-15 – Correlation of Heating RSD and Temperature Change (Correlation coefficient: 0.25).

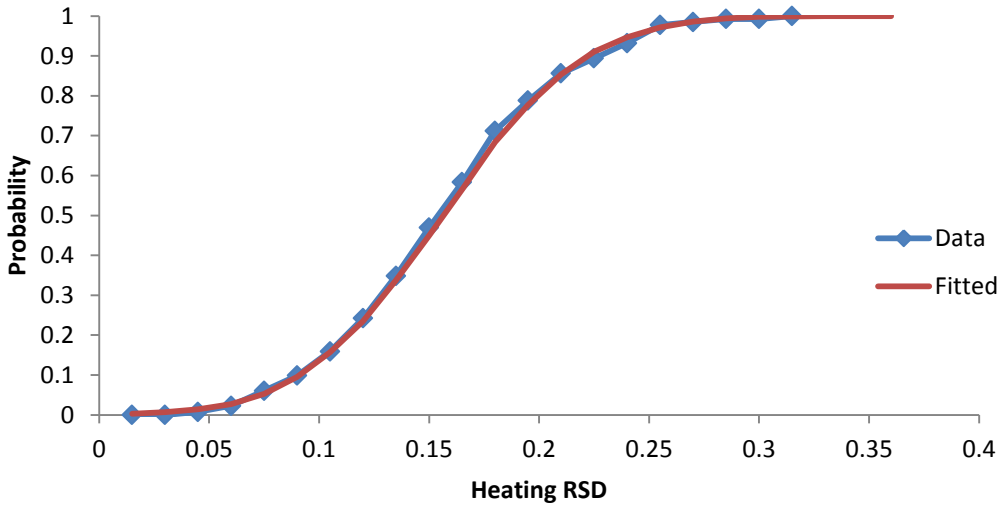

Figure 5-16 – CDF of Merged Monzonite & QZ Heating RSD data and a fitted normal distribution.

The heating uncertainty model is then applied to the simulated gangue mixtures. For Gangue A, the inclusion of the heating uncertainty model depresses the recovery curves of all three grade distributions, bringing them closer to the performance expected of a splitter Figure 5-17. While not matching the ideal case, MW/IR sorting of Gangue A still offers potential to upgrade the ore. The grade recovery curves of Gangue B collapse to the splitter line (see Figure 5-18) which indicates behaviour indistinguishable from random selection. The simulation clearly demonstrates that, at the current level of uncertainty in heating, Gangue B matrix is not suitable for microwave/IR sorting. The other heating models produce identical grade recovery curves to those displayed below for both Gangue A and Gangue B (see Section 8.8.4 of the Appendix).

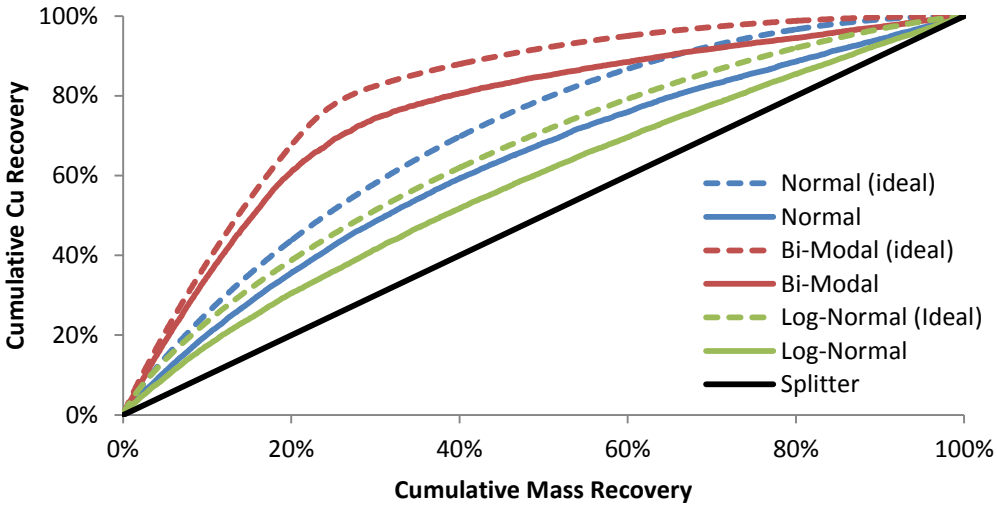

Figure 5-17 – Grade Recovery Curves Gangue A ($E_{\perp}$)

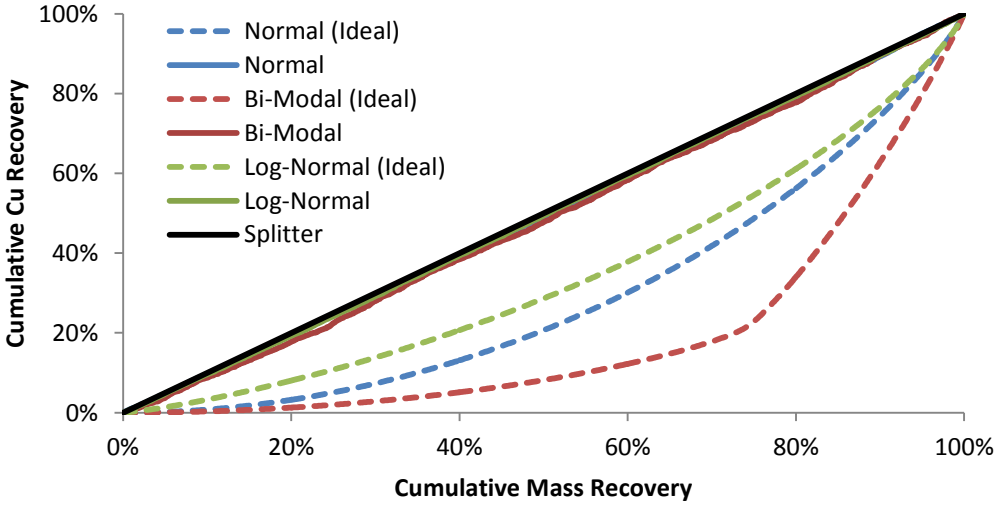

Figure 5-18 – Grade Recovery Curves Gangue B ($E_{\perp}$)

Figure 5-19 and Figure 5-20 show the grade recovery curves for smaller mixture sets (sample size = 50), averaged (n = 10) and with 95% confidence intervals (CIs). These graphs predict the range of recoveries that might be observed in small-scale feasibility studies. From these graphs it is evident that there is considerable uncertainty in grade recovery curves for small numbers of particles. The grade recovery curves for Gangue B, on average, behave as predicted in the large sample curves.

However, in Gangue A the log-normal copper distribution falls to the splitter line although the normal and bi-modal distributions remain similar to their large sample performance. Additionally, the lower 95% CI for both the normal and bi-modal distributions in Gangue A show that small-scale studies will show potential for beneficiation. Grade recovery curves produced by the other heating models for both gangue mixtures show similar behaviour (see Section 8.8.5 of the Appendix). When this modelling is performed using the CRI mixing equation (see Section 2.5 of the literature review) no beneficial sorting performance resulted in either gangue mixture for any heating model. This result is unsurprising given the CRI model is known to be less accurate than the LLL (Nelson, 2005).

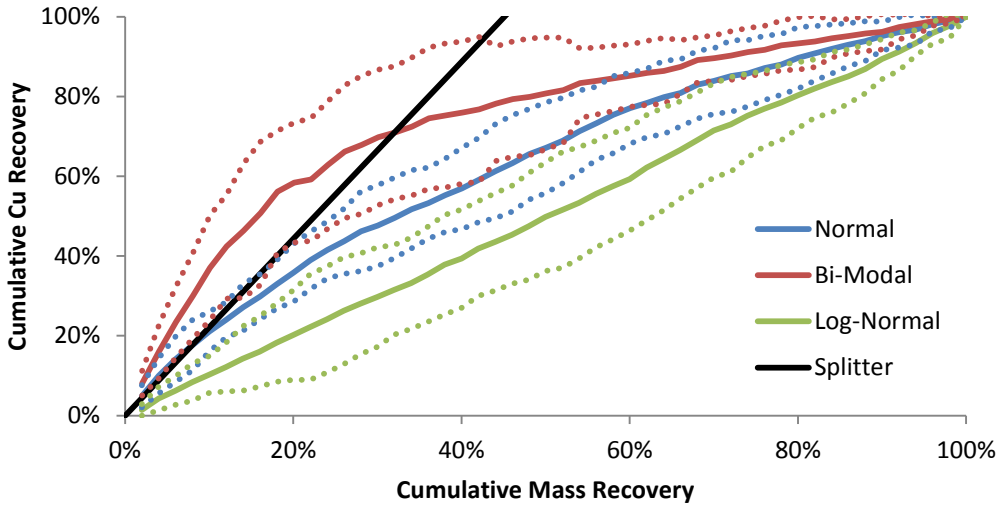

Figure 5-19 – Grade recovery curves of Gangue A with 95% CI (Dotted) ($E_{\perp}$, 50 particle set, 10 repeats)

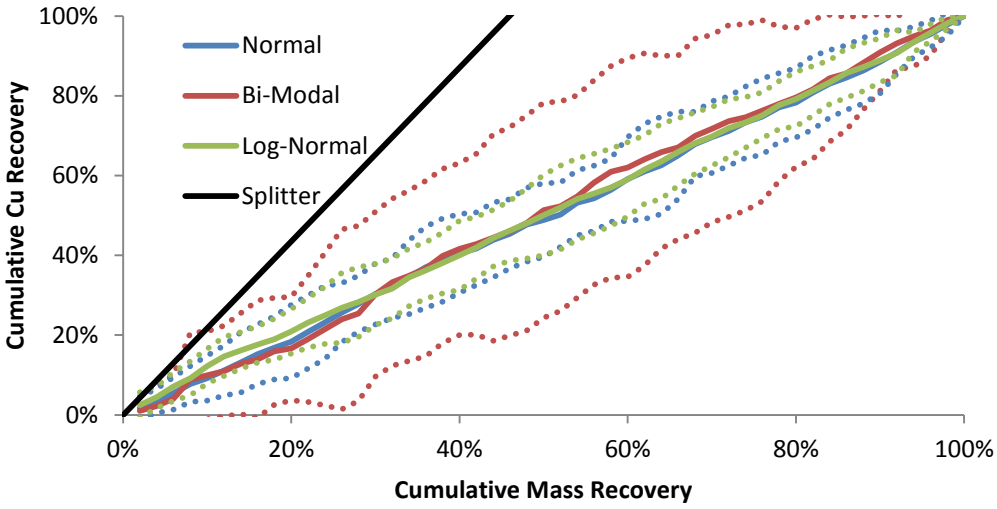

Figure 5-20 – Grade recovery curves of Gangue B with 95% CI (Dotted) ($E_{\perp}$, 50 particle set, 10 repeats)

5.4.5 Conclusions

MW/IR simulations were conducted using a custom MATLAB program to generate sets of mineral mixtures and then calculate the microwave heating those mixtures would experience, an empirical model of heating uncertainty was also included. Three hypothetical particle grade distributions were implemented, normal, bi-modal and log normal, each with an average of 0.33% copper weight. Grade recovery simulations were accomplished using gangue mixtures similar to the QZ and MZ1 ores; a quartz-rich granitoid and alkali-feldspar granite. Four different models for microwave heating were implemented based on three different calculations for electric field in the mixtures and the power law empirically found in Chapter 3 (see Section 3.3.4.1). The uncertainty model implemented was based on the distribution of relative standard deviations also found in Chapter 3 (see Section 3.2.2).

These simulations demonstrate an approach to understanding grade recovery results in sorting operations (large particle numbers) and in feasibility studies (small particle numbers) and how the gangue matrix of an ore may influence sorting.

Simulation results show that the assumption underpinning MW/IR sorting – that particles rich in valuable mineral phases, such as chalcopyrite, experience more heating (higher average surface temperatures as measured by infrared thermography) when exposed to microwave fields – **does not necessarily hold true and can depend on the properties of the gangue matrix alone**. The ideal grade recovery curves for the quartz-rich granitoid mixture demonstrated that preferential selecting hotter particles could produce an increased grade product stream. However, grade recovery curves for the alkali-feldspar granite mixture disagreed on the heating. Two of the four heating models suggested that selecting the coldest particles could improve the grade of the product stream.

When the heating uncertainty model was included in simulations, grade recovery curves for Gangue A were depressed and for Gangue B collapsed to random selection. These results demonstrate that sorting could produce an improved product grade for Gangue A but it would not match the ideal case due to uncertainty in the microwave heating of particles. Similarly the variability in heating of Gangue B mixtures meant that simulations of MW/IR based sorting performed no better than selecting particles at random. The heating uncertainty model is empirically determined from the results of a batch domestic oven procedure and accounts for all factors (other than the dielectric properties of the homogeneous mineral mixture) that may affect heating, such as particle size & shape, texture, magnetic permeability or field distribution within the cavity. The disparity between ideal and simulated MW/IR sorting performance is the result of temperature being an imperfect metric for the metal grade of particle. Industrial scale devices offer the potential for more even field distributions and therefor lower variability in heating which results in better sorting performance. Modelling sorting performance in an industrial system requires understanding heating uncertainty in that system.

When grade recovery curves were obtained from simulations of 50 mixtures, the heating variability of the log-normal copper distribution in Gangue A reduced to random selection. These simulations highlight the importance of finding methods to reduce the uncertainty in the microwave heating of particles. Improvement in the certainty of microwave heating and consequent temperature measurement will be reflected in improved grade recovery curves and sorting.

5.5 Conclusions

This Chapter drew on the dielectric property measurements of Chapter 3 in an attempt to understand the mineralogical compositions and underlying mineral chemistry of ores and how these properties relate to both dielectric properties and microwave heating. This was extended to the regression of mineral dielectric properties, the modelling of microwave heating and consequently the potential sorting outcomes of simulated ores.

The modal mineralogy of samples were analysed using the MLA XMOD technique. These data show each ore contains different and varying combinations of minerals. Averaging the modal mineralogy data for each ore allowed the rock type classified according to Streckeisen (1976). Electron microprobe analyses were then used to measure the chemical compositions of major mineral species in each ore. The dielectric properties of major mineral groups were estimated via least squares solution in MATLAB. This environment allowed the use of over determined systems of equations which were based on the LLL dielectric mixing equation. Results of this solution compared well with values measured in Chapter 3 and values reported in scholarly literature.

Simulations of MW/IR sorting performance were demonstrated using code developed in MATLAB. This code incorporated models for copper grade distribution, microwave heating, and heating uncertainty. The microwave heating and heating uncertainty models drew on the results of Chapter 3 and the mineral dielectric property measurements presented in this chapter. Mineral structuring was identified as an important consideration in Chapter 4; however, an explicit model for its affect was not developed. Heating uncertainty was instead based on an empirical model using the microwave heating data of Chapter 3 and implicitly accounts for mineral structuring. Simulations indicated that MW/IR sorting could be beneficial when applied to a gangue matrix similar to that of the QZ ore. Furthermore, simulations indicated MW/IR sorting would be indistinguishable from random selection when applied to a gangue matrix similar to that of the MZ1 ore. This finding indicates that properties of the gangue matrix can negate the assumption that microwave heating is only due to the high dielectric property valuable phases.

6 Conclusions and Future Work

A methodology has been proposed for assessing the suitability of copper sulphide ores for sorting in Microwave/Infrared (MW/IR) based systems. This began with measurements of microwave heating and dielectric properties of ore mixtures followed by calculation of mineral dielectric properties and Monte Carlo simulation of MW/IR based sorting. Additional investigations were undertaken to understand the reasons for specific unusual relationships between microwave heating and dielectric property data. In this thesis a series of research questions were addressed:

- Do the dielectric properties of powdered samples correlate with the MW/IR heating of particles?
- Can the interaction between samples and the magnetic component of an applied microwave field, or mineral structures within solid particles, be used to explain the observed apparent anomalies between microwave heating and dielectric properties in some particles?
- Can the dielectric properties of mineral species can be calculated from the dielectric properties of mixtures and modal mineralogy data?
- And finally, do simulations of microwave heating predict different sorting outcomes for different gangue matrices?

6.1 Microwave Heating and Dielectric Properties of Ores

In Chapter 3, the microwave heating of particles from six different ores were characterized using infrared thermography. Three distinct behaviours were observed in the ore MW/IR heating profiles (see Section 3.2.2, Figure 3-2 of Chapter 3). The quartzite ore, QZ, experienced very little heating. Monzonite ores, MZ1, MZ2, MZ3 and MZ4, all produced similar heating behaviours and were on average approx. five times hotter than the QZ ore. The skarn ore, SKN, produced a very pronounced heating profile; the coldest fraction heated similarly to QZ, while the hottest particles were significantly hotter than in any other ores

tested – the largest temperature increase in the SKN ore was 67 K while the next largest temperature increase in a different ore (MZ1) was 37 K.

Whilst analysing the thermal data from the MW/IR characterization experiments it was found that particles in each of the ore types displayed different degrees of temperature variation on the particle surface. This was assessed by plotting the profiles for relative standard deviation of IR pixel temperatures on the particle surfaces against cumulative mass. These different surface variations could potentially lead to an online method for identifying the petrologies of individual particles in a mixed set. Further investigation is needed to verify this.

Dielectric properties measurements were performed on powder and core subsets of the ore samples, along with a small set of minerals, using a resonant cavity perturbation technique at The University of Nottingham. Additionally, a 3 x 3 x 3 factorial design experiment was conducted using quartz-pyrite mixtures to characterise the uncertainty in cavity perturbation measurements. It was found that, with these mixtures the cavity data had a standard errors of 0.381 for ϵ' and 0.018 for ϵ''. Analysis of dielectric data for ore samples revealed that the loss tangent and modified loss tangent produced good fits (R^2 = 89% and 88% respectively) to describe temperatures achieved by particles in MW/IR characterization but only when specific samples were excluded. However, a log-log relationship between loss tangent and the MW/IR temperatures was found to describe the MW/IR temperatures of the entire measurement set (R^2 = 79%). In this thesis, MW/IR characterization was performed on a representative sample set while dielectric measurements focussed on a specific subset. To improve the quality of the fitting, and usefulness in predicting MW/IR behaviour, dielectric measurements could be extended to the entire sample set of the ores.

The loss tangents of powder samples at 912 MHz were found to be approx. 35% larger than at 2470 MHz. However, calculations predicted that despite the larger dielectric values, the lower frequency of 915 MHz radiation would result in a net drop in microwave heating since power dissipation is proportional to frequency. In future investigations, performing MW/IR

characterizations using a 915 MHz system would confirm this reduction in heating and the relationship between heating and loss tangent as well as better reflecting industrial scale operations.

Dielectric properties measured for most pure mineral samples were supported by values found in literature. The measurements confirm that sulphides have much higher permittivity and loss factor than gangue mineral and are good targets for selective heating. However, dielectric measurements at elevated temperatures show that, despite stable real components of permittivity, the loss factor and loss tangent of chalcopyrite and pyrite drop considerably between room temperature and about 200°C. This indicates that a MW/IR sorting process targeting copper has optimal selective heating below 100°C. While electron microprobe analyses were performed on selected grains within the mineral samples in Chapter 5, rigorous quantification of the phase purity, using techniques such as MLA or XRD, would contribute to the quality of the data.

6.2 Properties influencing microwave heating

Chapter 4 was an investigation into the potential reasons for anomalous heating identified in Chapter 3. While a decent fit could be achieved using log-log system, the relationship between loss tangent and MW/IR temperature did not produce a good fit without the exclusion of the anomalous particles. Three different effects were put forward to explain this anomalous relationship: magnetic interactions; dielectric anisotropy & depolarization resulting from mineral textures; and heterogeneity which, due to halving particles to retain solid sections, lead to unrepresentative powder samples.

A series of measurements investigating the RF magnetic permeability of powdered samples was conducted using a Magnasat. Analysis of these measurements found no relationship between radiofrequency magnetic permeability in the powder samples and microwave heating of the original particles. Additionally, the permeability of anomalously heating

samples was indistinguishable from the other ore samples. This finding indicates that interaction with the magnetic field component in a cavity does not explain the anomalously hot specimens. Future work on this effect could include the measurement of magnetic permeability using microwave frequency techniques such as resonant cavity perturbation.

Dielectric anisotropy & depolarisation was investigated using a rectangular waveguide cavity with a TE_{101} resonance at 2.29 GHz and a Q-factor of approx. 8500. Measurements of SKN cores rotated in 45° increments demonstrated that the centre frequency and bandwidth of the resonance can vary significantly. Since the shape of the core does not vary with rotation, the changes in cavity properties with rotation are consistent with bulk dielectric anisotropy resulting from internal mineral structures. Further investigation of mineral structures and their effect on the dielectric properties of cores is warranted. Several different approaches could be used including: the use of different core sizes to determine the apparent size of inclusions; X-ray tomography of cores to directly observe sulphide structuring; measurement of different ore types to observe differences between ores; and measurements on synthetic cores to measure the effect of internal structures in a controlled manner.

Finally, MLA GXMAP imaging was performed on the solid halves of three anomalous SKN samples. This imaging was used to qualitatively investigate sulphide heterogeneity. The images obtained showed distinct sulphide structuring in each of the samples and consequently supports both dielectric anisotropy & depolarization and sampling error resulting from heterogeneity as explanations for the anomalous behaviour. In a MW/IR based sorting system, structuring of sulphide minerals may generate both false negatives and false positives depending on the orientation of sulphide structures with respect to the applied fields.

6.3 Dielectric properties of minerals

Chapter 5 returned to the dielectric data collected in Chapter 3 with the goal of investigating the relationship between the dielectric properties of ores and their component minerals. To do

this, the modal mineralogy of ore powder samples was measured using the MLA XMOD technique. These measurements demonstrated that each sample contains different and varying combinations of minerals. The rock types of the ores were then classified from the averaged modal mineralogy data. An electron microprobe was then used to measure the elemental compositions of mineral grains in each ore and thereby ascertain the end-member compositions of minerals. The microprobe was also used to check MLA classification of minerals in the solid halves imaged in Chapter 4.

The dielectric properties of broad mineral groupings were then calculated from dielectric and modal mineralogy data of ore mixtures. This was accomplished by arranging the data as a system of linear equations based on the LLL dielectric mixing equation. The system was solved using a least squares method in MATLAB. Results of these solutions compared well with values of pure minerals measured in Chapter 3 and values reported in scholarly literature. It was also found that minerals with small volume fractions in only a handful of mixtures could have a large degree of leverage and lead to a poor solution. This naturally leads to future work measuring the dielectric properties and modal mineralogy of an expanded set of powder samples. Furthermore, a second round dielectric properties and modal mineralogy measurements could be performed after density separation to achieve larger volume fractions of higher density minerals.

Future work in this area could be the extension of a database written in Microsoft Access as part of this thesis and forms a library of ore mixture and dielectric properties. This allows the data of numerous samples and ores to be stored, accessed and manipulated centrally. Improvements to the database could improve the interface with MATLAB for calculating mineral properties from mixtures and also for MW/IR sorting simulations. The database design identified a number of attributes that are distributed in multiple tables and includes:

- Physical properties of ore samples including mass, density, volume and specific heat

- Dielectric permittivity and loss factors at 2470 MHz and 912 MHz along with measurement details.
- Sample identification numbers, names and details on the origin of the sample.
- Modal mineralogy of samples, and details of the measurement technique used.
- Mineral Properties such as density, specific heat and dielectric properties sourced from scholarly literature.

The elemental composition data of grains from EPMA measurements are more difficult to include but could appear as average end-members compositions and be reported in the mineral groups using SQL queries. When populated, a database could lead to more detailed investigations of mineral dielectric properties using the calculation technique outlined above and result in a more complete understanding of the relationship between geochemistry and mineral properties.

6.4 Recovery Modelling

In the second half of Chapter 5, an approach to assessing MW/IR sorting performance was demonstrated using Monte Carlo simulations which drew from the work presented earlier in the thesis. To arrive at grade recovery curves the simulations modelled: particle-by-particle copper grade distributions, microwave heating, and heating uncertainty of homogenized gangue matrices. Four models for microwave heating were used including a qualitative and empirical power law model drawn from dielectric measurement results of Chapter 3. A model for uncertainty in microwave heating was developed based on the microwave-infrared measurements presented in Chapter 3 and implicitly dealt with effects such as mineral structuring. Simulations indicated that MW/IR sorting would likely be beneficial when applied to a gangue matrix similar to QZ ore but would be indistinguishable from random selection when applied to a gangue matrix similar to MZ1 ore. This finding shows that a lossy gangue matrix can experience enough microwave heating to mask the effect of high dielectric property valuable phases. For a sorting process to be effective on the MZ-type ore it must have some other method for gangue recognition.

The modelling of heating and uncertainty was based on empirical data of small data sets but for this simulation technique to be used in assessing the suitability of an ore for MW/IR sorting, the results need to be verified using larger sample sets. Refinements to the simulations could include:

- Extending the code to model combinations of different gangue matrices within an ore due to petrology or blending.
- Functions to the frequency dependence of mineral dielectric properties so that the optimum applied field can be applied for sorting.
- Temperature cut-points, along with false-positive and false negative rates of a simulated sorting system, which would allow the assessment of multiple stage sorting.

Additionally, simulations would be enhanced by investigation into particle-by-particle grade distributions, methods for decreasing heating variability & characterizing industrial scale applicators, and particle size distributions. Furthermore, these simulations are not necessarily limited to chalcopyrite ores. With different physical property data, the simulations can be used to assess the potential for MW/IR sorting of ores with any valuable mineral species.

6.5 Conclusions

In this thesis a methodology for assessing the suitability of an ore for MW/IR sorting has been demonstrated. This methodology began in Chapter 3 with the microwave heating and thermal imaging of a small set of ore particles, particles of interest were then processed and their dielectric properties measured using the C1 cavity at the University of Nottingham. Modal mineralogy measurements in Chapter 5, combined with the ore dielectric property data, allowed the regression of dielectric properties for mineral groupings. The methodology concluded with the sorting simulations in Chapter 5. Chapter 4 followed a digression from

the characterization methodology in which the mechanisms behind anomalous heating were further investigated. As part of the development of this methodology it was found that microwave heating is not necessarily driven by the quantity of valuable minerals in a particle and that heating due to gangue minerals, particularly sheet silicates, e.g. clays, can render an ore unsuitable for MW/IR based sorting as applied at present. In the development of the characterisation methodology, five original contributions to knowledge were identified:

- The combination of mineralogical measurements with dielectric property and microwave heating measurements to characterise the sorting potential of ores.
- Identification of the relative standard deviation of temperatures on particle surfaces in microwave IR analysis as a potential means of identifying the petrology of individual particles.
- The calculation of dielectric properties from complex mixtures by way of solutions of a system of mixture equations containing modal mineralogy and dielectric property data.
- A methodology for evaluating the potential of ores for microwave sorting based primarily on the dielectric properties of minerals.
- Microwave frequency dielectric property data for ores and minerals which support existing measurements.

6.6 Future Work

In the course of this thesis seven topics have been identified that merit further investigation. These topics would either extend the body of knowledge or refine techniques used in this thesis and include:

- The use of particle surface variations as a method for determining the petrology of particles
- MW/IR characterisation at 915 MHz and potentially also at radio frequencies
- Measurements of the magnetic properties of minerals at microwave frequencies

- Development of the resonant cavity texture measurement technique and the characterisation of synthetic samples as well as other ores.
- Development of the least squares calculation of mineral dielectric properties as well as extended modal mineralogy data sets to increase confidence in current solutions.
- Validation of the Monte Carlo recovery modelling technique.

7 References

Adams, F, de Jong, M & Hutcheon, R 1992, 'Sample shape correction factors for cavity perturbation measurements', *Journal of Microwave Power and Electromagnetic Energy*, vol. 27, no. 3, pp. 131-5.

Al-Harahsheh, M & Kingman, SW 2004, 'Microwave-assisted leaching - a review', *Hydrometallurgy*, vol. 73, no. 3-4, pp. 189-203.

Arai, M, Binner, JGP & Cross, TE 1995, 'Use of mixture equations for estimating theoretical complex permittivities for measurements on porous or powder ceramic specimens', *Japanese Journal of Applied Physics*, vol. 34, pp. 6463-7.

ASTM 2001, *Standard Test Methods for Complex Permittivity (Dielectric Constant) of Solid Electrical Insulating Materials at Microwave Frequencies and Temperatures to 1650°C*, ASTM International.

---- 2008, *Standard Test Method for Measuring Relative Complex Permittivity and Relative Magnetic Permeability of Solid Materials at Microwave Frequencies*, ASTM International.

Ayres, RU, Ayres, L & Råde, I 2003, *The Life Cycle of Copper, Its Co-Products and Byproducts*, Kluwer Academic.

Baker-Jarvis, J, Vanzura, EJ & Kissick, WA 1990, 'Improved technique for determining complex permittivity with the transmission/reflection method', *Microwave Theory and Techniques, IEEE Transactions on*, vol. 38, no. 8, pp. 1096-103.

Bamber, AS 2008, 'Integrated Mining, Pre-Concentration and Waste Disposal Systems for the Increased Sustainability of Hard Rock Metal Mining', PhD thesis, University of British Columbia, Vancouver.

Beroual, A, Brosseau, C & Boudida, A 2000, 'Permittivity of lossy heterostructures: effect of shape anisotropy', *Journal of Phyics D: Applied Physics*, vol. 33, pp. 1969-74.

Bethe, HA & Schwinger, J 1943, *Perturbation Theory for Cavities*, Cornell University.

Bradshaw, S, Louw, W, van der Merwe, C, Reader, H, Kingman, SW, Celuch, M & Kijewska, W 2007, 'Techno-Economic Considerations in the Commercial Microwave Processing of Mineral Ores', *Journal of Microwave Power & Electromagnetic Energy*, vol. 40, no. 4, pp. 228-40.

Brosseau, C & Beroual, A 1999, 'Dielectric properties of periodic heterostructures: A computational electrostatics approach', *The European Physical Journal: Applied Physics*, vol. 6, pp. 23-31.

Burdette, EC, Cain, FL & Seals, J 1980, 'In Vivo Probe Measurement Technique for Determining Dielectric Properties at VHF through Microwave Frequencies', *Microwave Theory and Techniques, IEEE Transactions on*, vol. 28, no. 4, pp. 414-27.

Can, NM & Bayraktar, I 2007, 'Effect of microwave treatment on the flotation and magnetic separation properties of pyrite, chalcopyrite, galena and sphalerite', *Minerals & Metallurgical Processing*, vol. 24, no. 3, pp. 185-92.

Carmona, F & El Amarti, A 1987, 'Anisotropic electrical conductivity in heterogeneous solids with cylindrical conducting inclusions', *Physical Review B*, vol. 35, no. 7, pp. 3284-90.

Carter, RG 2001, 'Accuracy of microwave cavity perturbation measurements', *IEEE Transactions on Microwave Theory and Techniques*, vol. 49, no. 5, pp. 918-23.

Casimir, HBG 1951, 'On the Theory of Electromagnetic Waves in Resonant Cavities', *Philips Research Reports*, vol. 6, no. 3, pp. 162-82.

Cavanough, G 2003, 'Measurement of Magnetic Susceptibility in Titanium Minerals Processing', University of Queensland.

Cavanough, G & Holtham, PN 2000, 'On-line measurement of magnetic susceptibility for titanium minerals processing', *AusIMM Proceedings*, vol. 305, no. 1, pp. 29-34.

Chen, L, Ong, CK & Tan, BTG 1996, 'A resonant cavity for high-accuracy measurement of microwave dielectric properties', *Measurement Science and Technology*, vol. 7, pp. 1255–9.

Chen, LF, Ong, CK, Neo, CP, Varadan, VV & Varadan, VK 2004, *Microwave Electronics: Measurement and Materials Characterisation*, Wiley, West Sussex.

Chen, TT, Dutrizac, JE, Haque, KE, Wyslouzil, W & Kashyap, S 1984, 'The Relative Transparency of Minerals to Microwave Radiation', *Canadian Metallurgical Quarterly*, vol. 23, no. 3, pp. 349-51.

Cheng, DK 1989, *Field and Wave Electromagnetics*, 2 edn, Addison-Wesley, Sydney.

Church, RH, Webb, WE & Salsman, JB 1988, *Dielectric properties of low-loss minerals*, US Bureau of Mines.

Clarke, RN, Gregory, AP, Cannell, D, Patrick, M, Wylie, S, Youngs, I & Hill, G 2003, *A Guide to the Characterisation of Dielectric Materials at RF and Microwave Frequencies*, 0904457389, National Physical Laboratory, London.

Clarke, RN & Rosenburg, CB 1982, 'Fabry-Perot and open resonators at microwave and millimetre wave frequencies, 2-300 GHz', *Journal of Physics E: Scientific Instruments*, vol. 15, pp. 9-24.

Clauset, A, Shalizi, C & Newman, M 2009, 'Power-Law Distributions in Empirical Data', *SIAM Review*, vol. 51, no. 4, pp. 661-703.

Crine, JP, Friedmann, A, Wertheimer, MR & Yelon, A 1977, 'The relationship between chemical composition and electrical conductivity of some North American micas', *Canadian Journal of Physics*, vol. 55, no. 3, pp. 270-5.

Cutmore, NG & Eberhardt, JE 2002, 'The Future of Ore Sorting in Sustainable Processing', paper presented to Green Processing 2002 - Proceedings: International Conference on the Sustainable Processing of Minerals, May 29, 2002 - May 31, 2002, Cairns, QLD., Australia.

Cutmore, NG, Liu, Y & Middleton, AG 1997, 'Ore Characterisation and Sorting', *Minerals Engineering*, vol. 10, no. 4, pp. 421-6.

Davidson, AT & Yoffe, AD 1965, 'Dielectric breakdown in thin mica crystals', *Nature*, vol. 206, no. 4990, pp. 1247-&.

---- 1968, 'Hopping Electrical Conduction and Thermal Breakdown in Natural and Synthetic Mica', *Physica Status Solidi*, vol. 30, no. 2, pp. 741-&.

Deer, WA, Howie, RA & Zussman, J 1963, *Rock Forming Minerals. Volume 3, Sheet Silicates*, Wiley.

Deer, WA, Howie, RA & Zussman, J 1992, *An introduction to the rock-forming minerals*, Longman Scientific & Technical.

Djordjevic, N 2009, *Method of Determining the Presence of a Mineral Within a Material*, US Patent 2009/0314086 A1.

Djordjevic, N & Adair, BJ 2010, *Method and Apparatus for the Characterization of Geological Materials*, US Patent 2001/0207018 A1.

Donovan, S, Klein, O, Dressel, M, Holczer, K & Grüner, G 1993, 'Microwave cavity perturbation technique: Part 2: Experimental Scheme', *International Journal of Infrared and Millimeter Waves*, vol. 14, no. 12, pp. 2459-87.

Dressel, M, Klein, O, Donovan, S & Grüner, G 1993, 'Microwave cavity perturbation technique: Part 3: Applications', *International Journal of Infrared and Millimeter Waves*, vol. 14, no. 12, pp. 2489-517.

Fannin, PC, Relihan, T & Charles, SW 1995, 'Investigation of ferromagnetic resonance in magnetic fluids by means of the short-circuited coaxial line technique', *Journal of Physics D: Applied Physics*, vol. 28, no. 10, p. 2003.

Feely, KC & Christensen, PR 1999, 'Quantitative compositional analysis using thermal emission spectroscopy: Application to igneous and metamorphic rocks', *Journal of Geophysical Research: Planets*, vol. 104, no. E10, pp. 24195-210.

Fitzgibbon, KE & Veasey, TJ 1990, 'Thermally assisted liberation - a review', *Minerals Engineering*, vol. 3, no. 1–2, pp. 181-5.

Ford, JD & Pei, DCT 1967, 'High Temperature Chemical Processing Via Microwave Absorption', *The Journal of Microwave Power*, vol. 2, no. 2.

Grant, JP, Clarke, RN, Symm, GT & Spyrou, NM 1989, 'A critical study of the open-ended coaxial line sensor technique for RF and microwave complex permittivity measurements', *Journal of Physics E: Scientific Instruments*, vol. 22, no. 9, p. 757.

Greffe, JL & Grosse, C 1992, 'Static Permittivity of Emulsions', in A Priou (ed.), *Dielectric Properties of Heterogeneous Materials*, Elsevier, New York.

Haque, KE 1999, 'Microwave energy for mineral treatment processes--a brief review', *International Journal of Mineral Processing*, vol. 57, no. 1, pp. 1-24.

Hatton, BD & Pickles, CA 1994, 'Microwave treatment of ferrous slags', paper presented to Proceedings of the 77th Steelmaking Conference, March 20, 1994 - March 23, 1994, Chicago, IL, USA.

Hodsman, GF, Eichholz, G & Millership, R 1949, 'Magnetic Dispersion at Microwave Frequencies', *Proceedings of the Physical Society. Section B*, vol. 62, no. 6, p. 377.

Holderfield, SP & Salsman, JB 1992, 'Observed trends in the dielectric properties of minerals at elevated temperatures', paper presented to Materials Research Society Symposium, San Francisco, 27 April - 1 May.

Husk, DE & Seehra, MS 1978, 'Dielectric constant of Iron Pyrite (FeS2)', *Solid State Communications*, vol. 27, pp. 1147-8.

Hutcheon, R, de Jong, M & Adams, F 1992, 'A System for rapid measurements of RF and Microwave properties up to 1400C', *Journal of Microwave Power & Electromagnetic Energy*, vol. 27, no. 2, pp. 87-92.

Jenkinson, DE, Gough, PB, King, HG & Daykin, KW 1974, 'Coal Sorting by X-Ray Transmission', no. Compendex, pp. 1023-41.

Jones, RG 1976, 'The measurement of dielectric anisotropy using a microwave open resonator', *Journal of Phyics D: Applied Physics*, vol. 9, pp. 819-27.

Jones, SB & Friedman, SP 2000, 'Particle shape effects on the effective permittivity of anisotropic or isotropic media consisting of aligned or randomly oriented ellipsoidal particles', *Water Resources Research*, vol. 36, no. 10, pp. 2821-33.

Jonscher, AK 1996, *Universal relaxation law: a sequel to Dielectric relaxation in solids*, Chelsea Dielectrics Press.

Ketcham, RA & Carlson, WD 2001, 'Acquisition, optimization and interpretation of X-ray computed tomographic imagery: applications to the geosciences', *Computers & Geosciences*, vol. 27, pp. 381-400.

Kidd, DG & Wyatt, NPG 1982, 'Radiometric sorting of ore', paper presented to Proceedings, 12th Congress of the Council of Mining and Metallurgical Institutions., Johannesburg, S Afr.

Kingman, SW, Jackson, K, Bradshaw, SM, Rowson, NA & Greenwood, R 2004, 'An investigation into the influence of microwave treatment on mineral ore comminution', *Powder Technology*, vol. 146, no. 3, pp. 176-84.

Kingman, SW, Jackson, K, Cumbane, A, Bradshaw, SM, Rowson, NA & Greenwood, R 2004, 'Recent developments in microwave-assisted comminution', *International Journal of Mineral Processing*, vol. 74, pp. 71-83.

Kingman, SW, Vorster, W & Rowson, NA 2000, 'The influence of mineralogy on microwave assisted grinding', *Minerals Engineering*, vol. 13, no. 3, pp. 313-27.

Kinsey, JL 1977, 'Laser-induced fluorescence', in *Annual review of physical chemistry, vol.28, 1977*, Annual Reviews Inc, Palo Alto, CA, USA, pp. 349-72.

Kittel, C 1946, 'Theory of the Dispersion of Magnetic Permeability in Ferromagnetic Materials at Microwave Frequencies', *Physical Review*, vol. 70, no. 5-6, pp. 281-90.

Klein, O, Donovan, S, Dressel, M & Grüner, G 1993, 'Microwave cavity perturbation technique: Part 1: Principles', *International Journal of Infrared and Millimeter Waves*, vol. 14, no. 12, pp. 2423-57.

Kobayashi, M & Hiroshi, K 1988, 'Measurements of Dielectric Properties for Particulate Sphalerite Samples and Zinc Concentrates', *Metallurgical Transaction B*, vol. 19B.

Krige, DG 1966, 'A study of gold and uranium distribution patterns in the Klerksdorp gold field', *Geoexploration*, vol. 4, no. 1, pp. 43-53.

Kruesi, PR & Frahm, VH 1980, *Process for the recovery of nickel, cobalt and manganese from their oxides and silicates*, Cato Research Corporation, 4311520.

Krupka, J, Gregory, AP, Rochard, OC, Clarke, RN, Riddle, B & Baker-Jarvis, J 2001, 'Uncertainty of complex permittivity measurements by split-post dielectric resonator technique', *Journal of the European Ceramic Society*, vol. 21, no. 15, pp. 2673-6.

Landau, LD & Lifschitz, EM 1984, *Electrodynamics of Continuous Media*, Pergamon, Oxford.

Lovás, M, Kovácová, M, Dimitrakis, G, Cuvanová, S, Znamenácková, I & Jakabský, S 2010, 'Modeling of microwave heating of andesite and minerals', *International Journal of Heat and Mass Transfer*, vol. 53, no. 17-18, pp. 3387-93.

Mercer, SR, Downing, BJ, Salter, JD & Nordin, L 1988, 'Microwave discrimination techniques for rock sorting', paper presented to Second Joint Symposium on Antennas and Propagation and Microwave Theory and Techniques, 17-19 Aug. 1988, Marshalltown, South Africa.

Meredith, R 1998, *Engineer's Handbook of Industrial Microwave Heating*, vol. 25, 25 vols., IEE Power Series, The Institution of Electrical Engineers, Exeter.

Metaxas, AC 1996, *Foundations of Electroheat*, John Wiley & Sons, Brisbane.

Meunier, M, Currie, JF, Wertheimer, MR & Yelon, A 1983, 'Electrical conduction in biotite micas', *Journal of Applied Physics*, vol. 54, no. 2, pp. 898-905.

Michaux, S 2005, 'Analysis of Fines Generation in Blasting', PhD thesis, University of Queensland, Brisbane.

Morrison, RD 2010, *Rock Analysis Apparatus and Method*, US Patent 2010/0204825 A1.

Mudd, GM 2010, 'The Environmental sustainability of mining in Australia: key mega-trends and looming constraints', *Resources Policy*, vol. 35, no. 2, pp. 98-115.

Music, S, Popović, S & Ristić, M 1992, 'Thermal decomposition of pyrite', *Journal of Radioanalytical and Nuclear Chemistry*, vol. 162, no. 2, pp. 217-26.

Nelson, SO 2001, 'Measurement and calculation of powdered mixture permittivities', *Instrumentation and Measurement, IEEE Transactions on*, vol. 50, no. 5, pp. 1066-70.

---- 2005, 'Density-Permittivity Relationships for Powdered and Granular Materials', *IEEE Transactions on Instrumentation and Measurement*, vol. 54, no. 5, pp. 2033-40.

Nelson, SO & Kraszewski, AW 1998, 'Sensing pulverized material mixture proportions by resonant cavity measurements', *IEEE Transactions on Instrumentation and Measurement*, vol. 47, no. 5, pp. 1201-4.

Nelson, SO, Lindroth, DP & Blake, RL 1989, 'Dielectric properties of selected minerals at 1 to 22 GHz', *Geophysics*, vol. 54, no. 10, pp. 1344-9.

Nelson, SO & You, T-S 1990, 'Relationships between microwave permittivities of solid and pulverised plastics', *Journal of Phyics D: Applied Physics*, vol. 23, no. 3, pp. 346-53.

Orumwense, AO & Negeri, T 2004, 'Impact of microwave irradiation on the processing of a sulfide ore', *Minerals & Metallurgical Processing*, vol. 21, no. 1, pp. 44-.

Osepchuk, JM 1984, 'A history of microwave heating applications', *IEEE Transactions on Microwave Theory and Techniques*, vol. MTT-32, no. 9, pp. 1200-24.

Parkash, A, Vaid, JK & Mansingh, A 1979, 'Measurement of dielectric parameters at microwave frequencies by cavity-perturbation technique', *IEEE Transactions on Microwave Theory and Techniques*, vol. MTT-27, no. 9, pp. 791-5.

Pipiskova, A & Lukac, P 1970, 'Electric field distribution in a cylindrical TM010 microwave cavity with end holes and a glass tube', *Journal of Phyics D: Applied Physics*, vol. 3, p. 1381.

Pridmore, DF & Shuey, RT 1976, 'The Electrical Resistivity of Galena, Pyrite, and Chalcopyrite', *American Mineralogist*, vol. 61, no. 3-4, pp. 248-59.

Priou, A (ed.) 1992, *Dielectric Properties of Heterogeneous Materials*, vol. 6, Progress in Electromagnetics Research, Elsevier, New York.

Razumovsky, NK 1940, 'Distribution of Metal values in Ore Deposits', *Comptes rendus (Doklady) de l'Académie des sciences de l'URSS*, vol. 9.

Rizmanoski, V 2011, 'The effect of microwave pretreatment on impact breakage of copper ore', *Minerals Engineering*, vol. 24, no. 14, pp. 1609-18.

Roberts, S & von Hippel, A 1946, 'New method for measuring dielectric constant and loss in range of centimeter waves', *Journal of Applied Physics*, vol. 17, no. 7, pp. 610-6.

Rusak, DA, Castle, BC, Smith, BW & Winefordner, JD 1997, 'Fundamentals and Applications of Laser-Induced Breakdown Spectroscopy', *Critical Reviews in Analytical Chemistry*, vol. 27, no. 4, pp. 257-90.

Rüscher, CH & Gall, S 1995, 'On the Polaron-Mechanism in Iron-Bearing Trioctahedral Phyllosilicates - an Investigation of the Electrical and Optical Properties', *Physics and Chemistry of Minerals*, vol. 22, no. 7, pp. 468-78.

---- 1997, 'Dielectric properties of iron-bearing trioctahedral phyllosilicates', *Physics and Chemistry of Minerals*, vol. 24, no. 5, pp. 365-73.

Sahyoun, C, Kingman, SW & Rowson, NA 2003, 'The effect of heat treatment on Chalcopyrite', *Physical Separation in Science and Engineering*, vol. 12, no. 1, pp. 23-30.

Sahyoun, C, Rowson, NA, Kingman, SW, Groves, L & Bradshaw, SM 2005, 'The influence of microwave pretreatment on copper flotation', *Journal of The South African Institute of Mining and Metallurgy*, vol. 105, no. 1, pp. 7-13.

Salsman, JB 1991, 'Measurement of dielectric properties in the frequency range of 300 MHz to 3 GHz as a function of temperature and density', paper presented to Microwaves:Theory & Applications in Materials Processing.Proc.Symp, Cincinnati, 29 Apr.-3 May 1991.

Salsman, JB & Holderfield, SP 1994, *Technique for Measuring the Dielectric Properties of Minerals at Microwave Heating Frequencies Using an Open-Ended Coaxial Line*, United States.

Salsman, JB, Williamson, RL, Tolley, WK & Rice, DA 1996, 'Short-pulse microwave treatment of disseminated sulfide ores', *Minerals Engineering*, vol. 9, no. 1, pp. 43-54.

Salter, JD, Nordin, L & Downing, BJ 1989, 'Kimberlite-gabbro sorting by use of microwave attenuation: development from the laboratory to a 100 t/h pilot plant', paper presented to Proc. Mat. Min. Inst. Japan & IMM Symp. Today's Technology for the Mining & Metallurgical Industries, Kyoto.

Salter, JD & Wyatt, NPG 1991, 'Sorting in the Minerals Industry - Past, Present and Future', *Minerals Engineering*, vol. 4, no. 7-11, pp. 779-96.

Shuey, RT 1975, *Semiconducting Ore Minerals*, Developments in Economic Geology, Elsevier Scientific Publishing Company, Amsterdam.

Sihvola, AH & Lindell, IV 1992, 'Effective Permeability of Mixtures', in A Priou (ed.), *PIER6: Dielectric Properties of Heterogeneous Materials*, Elsevier, New York, vol. 6, pp. 153-80.

Sivamohan, R & Forssberg, E 1991, 'Electronic sorting and other preconcentration methods', *Minerals Engineering*, vol. 4, no. 7–11, pp. 797-814.

Slight, DL 1966, 'Some X-ray absorption and scatter properties of potatoes and stones', *Journal of Agricultural Engineering Research*, vol. 11, no. 3, pp. 148-51.

Spencer, EG, LeCraw, RC & Reggia, F 1956, 'Measurement of microwave dielectric constants and tensor permeabilities of ferrite spheres', *Proceedings of the Institute of Radio Engineers*, vol. 44, no. 6, pp. 790-800.

Standish, N & Pramusanto 1991, 'Reduction of microwave irradiated iron ore particles in CO', *ISIJ International*, vol. 31, no. 1, pp. 11-6.

Streckeisen, A 1976, 'To each plutonic rock its proper name', *Earth-Science Reviews*, vol. 12, no. 1, pp. 1-33.

Tinga, WR 1992, 'Mixture Laws and Microwave-Material Interactions', in A Priou (ed.), *PIER6: Dielectric Properties of Heterogeneous Materials*, Elsevier, New York, vol. 6.

Tolland, HG & Strens, RGJ 1972, 'Electrical conduction in physical and chemical mixtures. Application to planetary mantles', *Physics of the Earth and Planetary Interiors*, vol. 5, pp. 380-6.

van Weert, G & Kondos, P 2007, 'Infrared recognition of high sulphide and carbonaceous rocks after microwave heating', paper presented to 39th annual meeting of the Canadian Mineral Processors, Ottowa, 2007.

van Weert, G, Kondos, P & Gluck, E 2009, 'Upgrading Molybdenite Ores between Mine and Mill Using Microwave/Infrared (MW/IR) Sorting Technology', paper presented to 41st Annual Meeting of the Canadian Mineral Processors, Ottowa, Ontario, Canada.

Vanzura, EJ, Baker-Jarvis, JR, Grosvenor, JH & Janezic, MD 1994, 'Intercomparison of permittivity measurements using the transmission/reflection method in 7-mm coaxial transmission lines', *Microwave Theory and Techniques, IEEE Transactions on*, vol. 42, no. 11, pp. 2063-70.

Venkatesh, MS & Raghavan, GSV 2005, 'An overview of dielectric properties measuring techniques', *Canadian Biosystems Engineering / Le Genie des biosystems au Canada*, vol. 47, pp. 7.15-7.30.

Vorster, W, Rowson, NA & Kingman, SW 2001, 'The effect of microwave radiation upon the processing of Neves Corvo copper ore', *International Journal of Mineral Processing*, vol. 63, no. 1, pp. 29-44.

Waldron, RA 1956, 'Theory of the measurement of the elements of the permeability tensor of a ferrite by means of a resonant cavity', *Proceedings of the Institution of Electrical Engineers*, pp. 307-15.

---- 1960, 'Perturbation theory of resonant cavities', in Institution of Electrical Engineers (IEE), London, England, vol. 107, pp. 272-4.

Walkiewicz, JW, Clark, AE & McGill, SL 1991, 'Microwave-Assisted Grinding', *IEEE Transactions on Industry Applications*, vol. 27, no. 2, pp. 239-43.

Walkiewicz, JW, Kazonich, G & McGill, SL 1988, 'Microwave heating characteristics of selected minerals and compounds', *Minerals & Metallurgical Processing*, vol. 5, no. 1, pp. 39-42.

Wang, JR & Schmugge, TJ 1980, 'An Empirical Model for the Complex Dielectric Permittivity of Soils as a Function of Water Content', *Geoscience and Remote Sensing, IEEE Transactions on*, vol. GE-18, no. 4, pp. 288-95.

Waples, DW & Waples, JS 2004, 'A Review and Evaluation of Specific Heat Capacities of Rocks, Minerals, and Subsurface Fluids. Part 1: Minerals and Nonporous Rocks.', *Natural Resources Research*, vol. 13, no. 2, pp. 97-122.

Williamson, RL, Salsman, JB & Tolley, WK 1994, 'Modeling the thermomechanical response of ore materials during microwave processing', paper presented to Microwave Processing of Materials IV, San Francisco, California.

Wotruba, H & Riedel, F 2006, 'Sensor-based Sorting of Metalliferous Ores - an Overview', paper presented to Sensorgestüetzte Sortierung 2006, Aachen.

Xia, DK & Pickles, CA 2000, 'Microwave caustic leaching of electric arc furnace dust', *Minerals Engineering*, vol. 13, no. 1, pp. 79-94.

Xiao, J 1985, 'The effects of mineral composition and structure on dielectric constants', *Kuang Wu Xue Bao = Acta Mineralogica Sinica*, vol. 5, no. 4, pp. 331-7.

---- 1990, 'Dielectric properties of minerals and their applications in microwave remote sensing', *Chinese Journal of Geochemistry (English Edition)*, vol. 9, no. 2, pp. 169-77.

Young, KF & Frederikse, HPR 1973, 'Compilation of the static dielectric constant of inorganic solids', *Journal of Physical and Chemical Reference Data*, vol. 2, no. 2, pp. 313-409.

8 Appendix

8.1 Dielectric Property Measurement

Table 8-1 – A generalized comparison of microwave dielectric measurement systems after (Venkatesh & Raghavan 2005)

	Slotted Line reflection	*Guided wave transmission*	*Free-space transmission*	*Filled cavity resonance*	*Partially filled cavity resonance*	*Probe reflection*
Frequency	Broadband	Banded	Banded	Single	Single	Broadband
Measured parameter	ε	ε and μ	ε and μ	ε and μ	ε and μ	ε
Temperature Control	Difficult	Difficult	Very easy	Very easy	Very easy	Easy
Accuracy:						
Low Loss	Very low	Moderate	Moderate	Very high	High	Low
High Loss	Low	Moderate	Moderate	N/A	Low	High
Samples:						
Preparation	Easy	Difficult	Easy	V difficult	V difficult	Easy
Size	Moderate	Moderate	Large	Large	Very small	Small
Suitable for:						
Solids	✓	✓	×	✓	✓	✓
Semi-solids	✓	×	×	✓	×	✓
Liquids	×	×	×	✓	×	✓
Large Sheets	×	×	✓	×	×	×
Non-destructive	×	×	✓	×	×	✓

8.1.1 ASTM D2520 resonant cavity calculations

Table 8-2 – Legend of ASTM D2520 symbols

f_c	Resonant frequency of the empty cavity (Hz)
f_s	Resonant frequency of the cavity with specimen (Hz)
Q_c	Quality factor of the empty cavity
Q_s	Quality factor of the cavity with specimen
V_c	Volume of the cavity (m^3)
V_s	Volume of the sample (m^3)
P	$\frac{V_c(f_c - f_s)}{2V_s f_s} + 1$
L	$\frac{V_c}{4V_s}\left(\frac{1}{Q_s} - \frac{1}{Q_c}\right)$

Table 8-3 – ASTM D2520-01 Formulas for calculating the dielectric properties of different geometry samples in a rectangular waveguide cavity (ASTM 2001)

Specimen	*Volume*	*Optimum Dimension*	*Permittivity*	*Loss Factor*
Vertical Rod or Bar	$\pi r^2 h$	$A \ll wd$	P	L
Horizontal Rod or Bar	$\pi r^2 w$	$r \ll h$	$\frac{P}{2-P}$	$\frac{2L}{(2-P)^2}$
Sheet	wdb	$b \ll h$	$\frac{1}{5-4P}$	$\frac{4L}{(5-4P)^2}$
Sphere	$\frac{4}{3}\pi r^3$	$r \ll w$ $r \ll d$ $r \ll h$	$\frac{1+2P}{4-P}$	$\frac{9L}{(4-P)^2}$

8.2 Dielectric Properties

Table 8-4 – Microwave heating results of selected minerals (Chen, TT et al. 1984)

Mineral	*Heating response*	*Products*
Calcite	Transparent	No change
Almandine	Transparent	No change
Potassium Feldspar	Transparent	No change
Quartz	Transparent	No change
Hematite	Heats readily; arcing at high temperature	No change
Magnetite	Heats readily	No change
Pitchblende	Heats readily	Some fused to UO_2, U_3O_8, ThO2 and Fe-Al-CaSiO2 glass; some unchanged
Bornite	Heats readily	Some changed to bornite-chalcopyrite-digenite; some unchanged
Chalcopyrite	Heats readily; emission of sulphur fumes	Sulphur fumes and two Cu-Fe-Sulphides or Pyrite and a Cu-Fe-Sulphide
Pyrite	Heats readily; emission of sulphur fumes	Pyrrhotite and Sulphur fumes
Sphalerite (high Fe; Zn 58.9, Fe 7.4, S 33.7)	Difficult to heat when cold	Converted to wurtzite
Sphalerite (low Fe; Zn 67.1, Fe 0.2, S 32.7)	Does not heat	No change

Table 8-5 – Dielectric Properties of selected minerals after Young and Frederikse (1973)

Compound	ϵ'	*Frequency (Hz)*
Calcium Carbonate	8.3	10^8
Haematite	12	$10^5 – 10^7$
Magnetite	20	$10^5 – 10^7$
Mica (Muscovite)	5.4	$10^2 – 3x10^9$
Magnesium Oxide (Periclase)	9.65	10^2 - 10^8
Spinel $(MgO)_xAl_2O_3$	8.6	--
Titanium Dioxide (Rutile)	114	$10^4 – 10^6$
Sphalerite	8.35	10^4

Table 8-6 – Dielectric properties of minerals at 915 MHz (Holderfield & Salsman 1992)

Grouping	*Mineral*	ε'	
Tetragonal	Chalcopyrite	77.5	Sulphide
Hexagonal	Niccolite	88.0	Sulphide
Trigonal	Siderite	1.6	Carbonate
	Smithsonite	1.1	Carbonate
Orthorhombic	Marcasite	24.0	Sulphide
	Barite	5.6	Sulphate
	Goethite	4.5	Oxide
Isometric	Smaltite	5.6	Sulphide
	Chalcocite	235.0	Sulphide
	Bornite	103.5	Sulphide
	Cobaltite	30.8	Sulphide
	Galena	103.5	Sulphide
Monoclinic	Arsenopyrite	49.3	Sulphide
	Azurite	0.8	Carbonate

Table 8-7 – Heating rates of minerals exposed to 1kW at 2.45GHz after Walkiewicz et al (1988)

Mineral	*Heating Rate (K/s)*	*Mineral*	*Heating Rate (K/s)*
Albite	0.16	Molybdenite	0.46
Arizonite	0.48	Orpiment	0.34
Chalcocite	1.78	Orthoclase	0.16
Chalcopyrite	15.33	Pyrite	2.52
Chromite	0.37	Pyrrhotite	8.44
Cinnabar	0.28	Quartz	0.19
Galena	2.28	Sphalerite	0.21
Hematite	0.43	Tetrahedrite	0.36
Magnetite	7.62	Zircon	0.12
Marble	0.29		

Table 8-8 – Dielectric Property Ranges of Mineral Groups (Xiao 1990)

	$f \leq 10^6$ *Hz*		*f = 9370 MHz*			
Mineral Group	ϵ'		ϵ'		ϵ''	
	Min.	*Max.*	*Min.*	*Max.*	*Min.*	*Max.*
Sulphides	6.00	450	4.44	600	0.02	900
Oxides	4.50	173	4.17	150	0.02	4.04
Hydrides	4.39	12.3	5.37	18.0	0.02	0.110
Silicates	4.30	25.4	3.58	24.8	0.02	0.901
Complex Oxides	4.90	26.8	3.84	44.0	0.02	0.368

Table 8-9 – Dielectric Property Ranges of Some Rock-Types Xiao 1990)

Rock Type	ϵ'			ϵ''		
	Min.	*Max.*	*Avg.*	*Min.*	*Max.*	*Avg.*
Ultrabasic & Basic	3.76	7.99	5.65	0.024	0.534	0.142
Intermediate	3.58	7.46	5.27	0.020	0.387	0.109
Acidic	3.45	5.97	4.64	0.020	0.322	0.050
Alkaline	3.96	5.08	4.46	0.020	0.141	0.103
Shale & Mudstone	3.90	6.92	5.38	0.058	0.452	0.253
Sandstone	3.94	7.01	5.22	0.020	0.328	0.109
Limestone	6.02	8.53	6.91	0.020	0.148	0.032
Gneiss	4.30	5.89	5.50	0.020	0.185	0.073
Skarn	5.68	8.62	7.18	0.023	0.488	0.117
Marble	5.22	8.15	6.52	0.020	0.163	0.041
Slate	4.34	5.92	5.39	0.026	0.286	0.111

Table 8-10 – Low frequency dielectric properties of minerals with structural water (Xiao 1990)

Mineral	ϵ'
Gibbsite	8.4
Brucite	8.6
Datolite	7.2 – 7.5
Chrysocolla	13.1
Afwillite	9.2
Halloysite	7.9
Epsomite	5.46
Chalcanthite	6.50
Goslarite	6.20
Vivianite	6.07 – 7.70

Colemanite	12.5 – 13.5
Ulexite	5.8
Kernite	5.3
Annabergite	5.5 – 6.6

Table 8-11 – Dielectric Properties and Specific Gravities of Minerals after Xiao (1990)

Mineral	*Specific Gravity*	ϵ' *(*f < 10^6 *MHz)*	ϵ' *(*f = *9370 MHz)*
Sodalite	2.30	8.1	5.59
Kaolinite	2.65	9.4 – 13.7	11.24
Quartz	2.65	4.5 – 5.2	4.17 – 4.53
Andalusite	3.15	5.4 – 11.0	11.83
Realgar	3.56	6.0 – 7.0	6.58
Anatase	3.90	4.2 – 5	42.6
Siderite	3.96	8.0 – 9.3	9.97
Chalcopyrite	4.20	> 81	99.9
Stibnite	4.60	11.2 – 49	49.0
Greenockite	4.95	9.35	18.8
Proustite	5.60	16.5	22.4
Chalcocite	5.70	> 81	3.30
Bismuthinite	6.78	18.2 – 45.2	62.8
Vanadinite	6.88	--	31.2
Wolframite	7.5	12.0 – 14.0	18.8
Galena	7.5	205	71.8
Cinnabar	8.1	10.9 – 20.0	16.8

8.3 Microwave Characterization Data

8.3.1 Mass Data

Table 8-12 – Particle mass statistics of ore samples and P-value results of 2-Sample T-Tests comparing the mass of 16 and 17 particles

Ore	*JK ID*	*Avg. (g)*	*Std. Dev.*	*P-value*
QZ	JK2429-1	14.171	4.700	0.604
SKN	JK2176	17.252	4.598	0.518
MZ2	JK2490-1	14.117	4.006	0.544
MZ1	JK2373-6	14.881	4.618	0.578
MZ3	JK2373-2	15.875	4.412	0.535
MZ4	JK2373-4	15.340	5.262	0.615

Table 8-13 – Particle volume statistics of ore samples and P-value results of 2-Sample T-Tests comparing the volume of 16 and 17 particles

Ore	*Avg. (cm^3)*	*St. Dev.*	*P-value*
QZ	5.770	2.132	0.614
SKN	5.980	2.034	0.613
MZ2	5.336	1.291	0.744
MZ1	5.265	1.606	0.572

8.3.2 Ore Microwave/IR Temperature Profiles

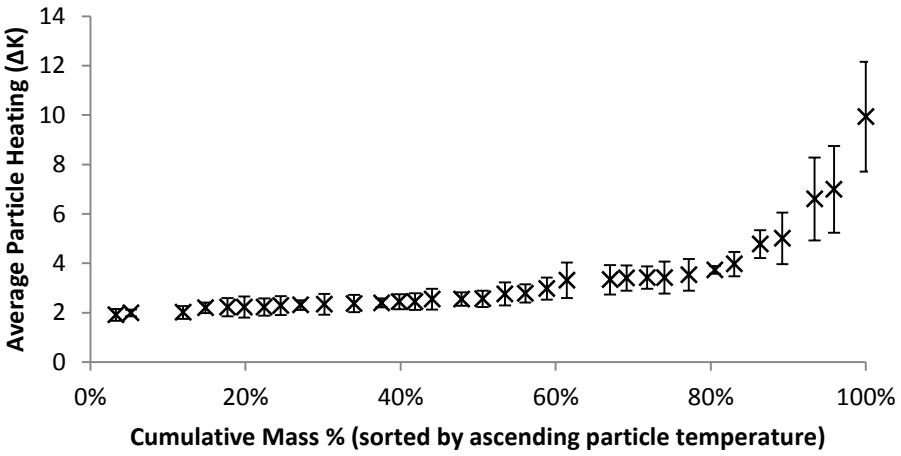

Figure 8-1 – MW/IR heating profile (QZ)

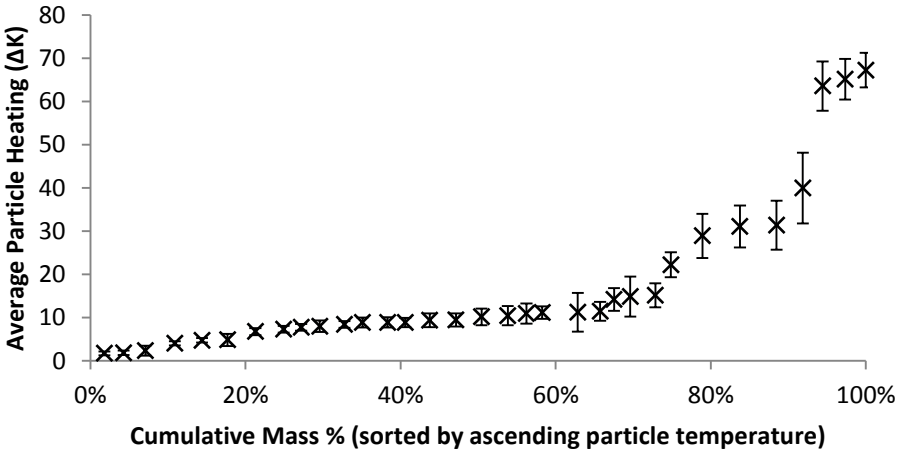

Figure 8-2 – MW/IR Heating Profile (SKN)

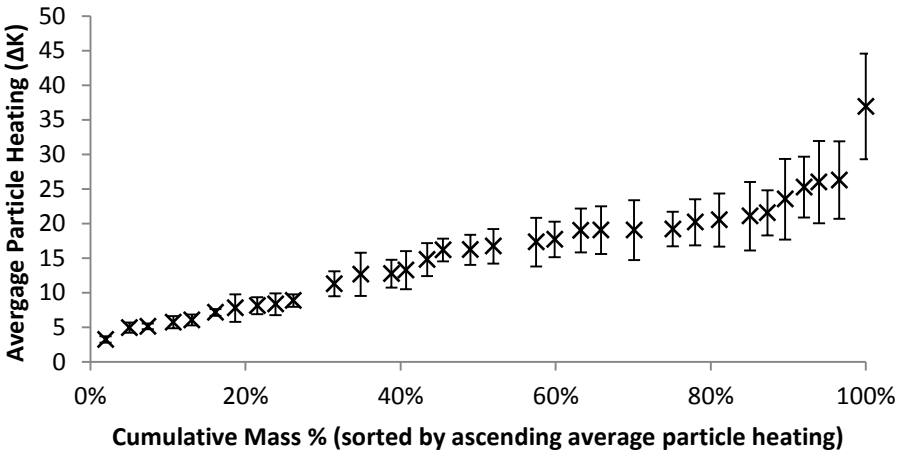

Figure 8-3 – MW/IR Heating Profile (MZ1)

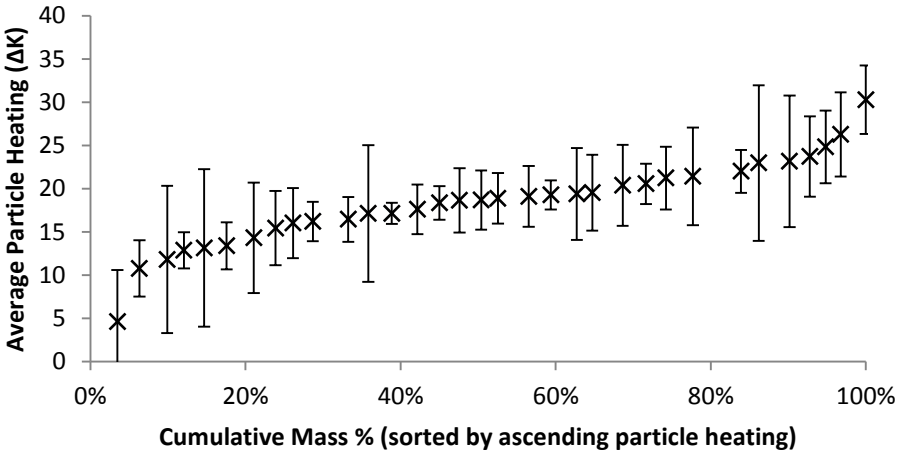

Figure 8-4 – MW/IR Heating Profile (MZ2)

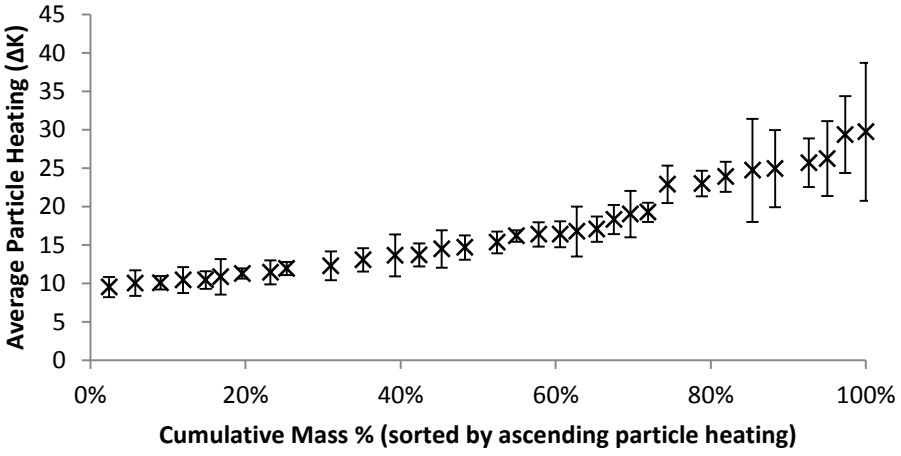

Figure 8-5 - MW/IR Heating Profile (MZ3)

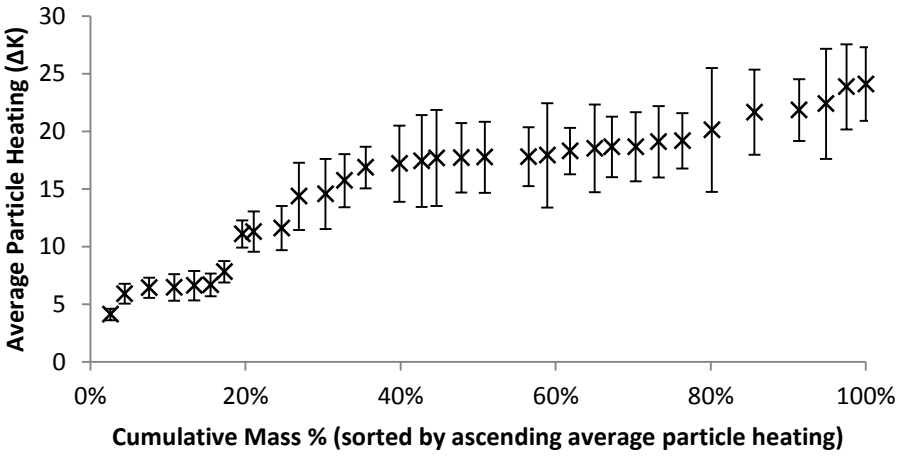

Figure 8-6 – MW/IR Heating Profile (MZ4)

8.3.3 Correlation of Temperature and Surface Variation

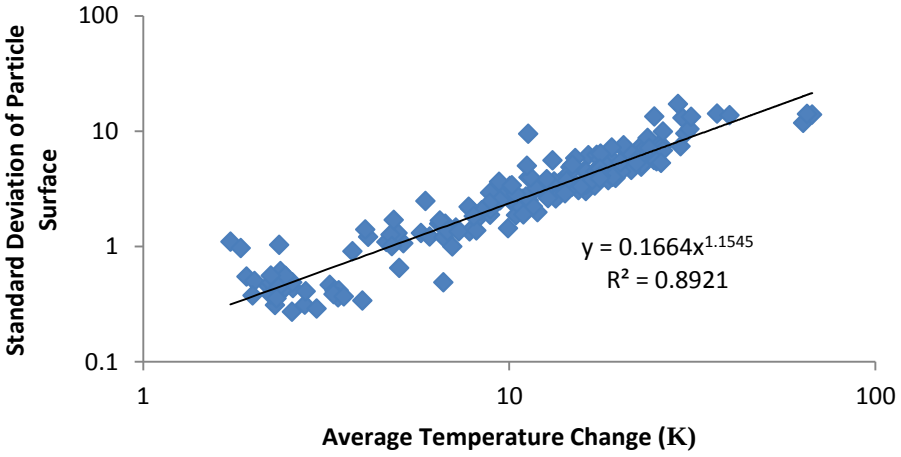

Figure 8-7 – The correlation between average temperature change and the variation in surface pixel temperatures (all ores combined)

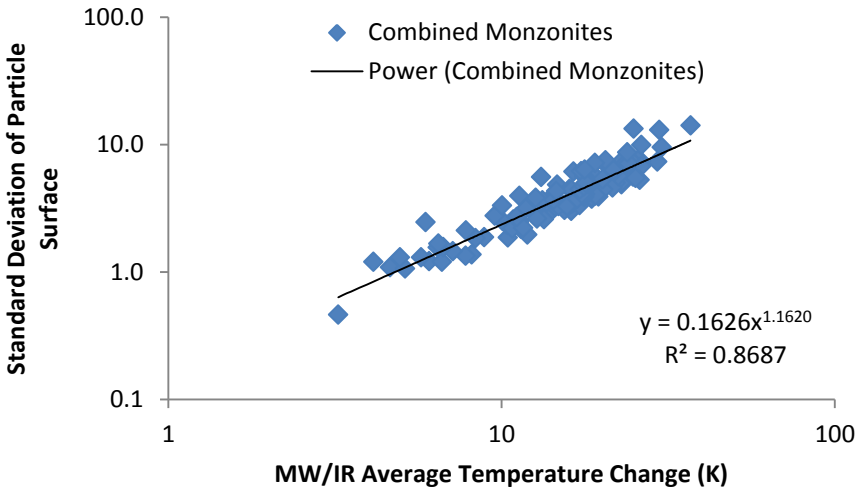

Figure 8-8 – The correlation between average temperature change and the variation in surface pixel temperatures (Combined monzonites)

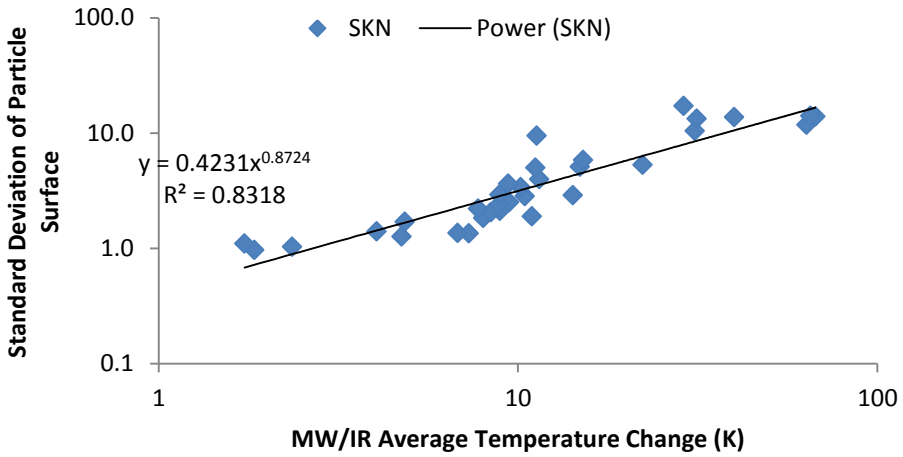

Figure 8-9 – The correlation between average temperature change and the variation in surface pixel temperatures (SKN)

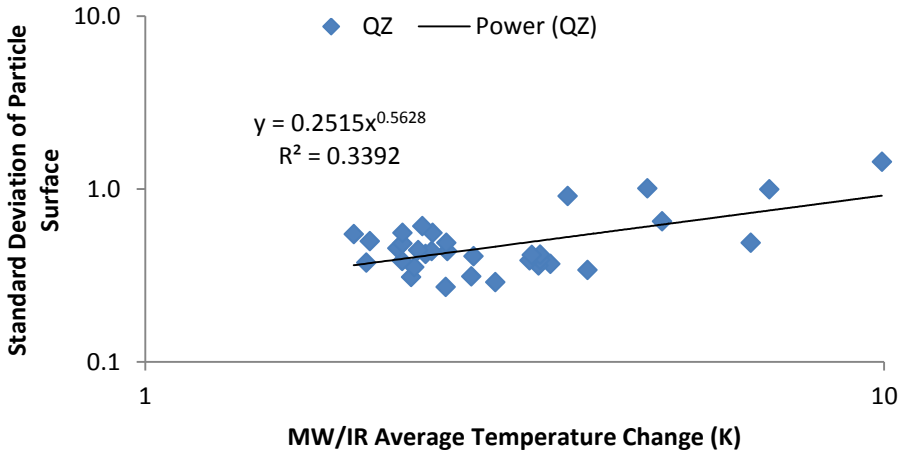

Figure 8-10 – The correlation between average temperature change and the variation in surface pixel temperatures (QZ)

8.3.4 Cylindrical Cavity TM_{0n0} Mode Details

Table 8-14 – Values for Bessel functions of TM_{0n0} modes

TM Mode	*ka* ($J_0(ka)=0$)	$J_1(ka)$
010	2.405	0.519
020	5.520	-0.340
030	8.654	0.271
040	11.792	-0.232
050	14.931	0.207

8.3.5 Error Characterization

Table 8-15 –Density of Quartz and Pyrite calculated from mass and volume of cores

	Density (kg/m^3)
Quartz	2843
Pyrite	5283

$$\rho_{mixture} = \frac{m_1 + m_2}{\frac{m_1}{\rho_1} + \frac{m_2}{\rho_2}} \qquad (1.1)$$

Table 8-16 – Factorial characterization experiment: Mixture properties

	Quartz (g)	*Quartz (mass%)*	*Pyrite (g)*	*Pyrite (mass%)*	*Theoretical Solid Density (kg/m^2)*
Mixture 1	1.015	20	4.068	80	3132
Mixture 2	0.491	10	4.494	90	2978
Mixture 3	0.258	5	4.757	95	2912

8.3.5.1 Statistical Analysis of the Factorial Experiment

Data analysis performed using the Minitab 16 Statistical Software Suite. Analyses were performed using Permittivity and Loss Factor results after application of mixture equations to correct for density. An analysis was also performed using sample density data.

8.3.5.1.1 Permittivity

Analysis of Variance using Adjusted SS for Tests

Source	DF	Seq SS	Adj SS	Adj MS	F	P
Taps	2	1.5511	1.5511	0.7755	5.33	0.011
Mass	2	0.9835	0.9835	0.4917	3.38	0.049
Mixture	2	6.6996	6.6996	3.3498	23.04	0.000
Taps*Mass	4	0.2376	0.2376	0.0594	0.41	0.801
Taps*Mixture	4	0.1886	0.1886	0.0471	0.32	0.859
Mass*Mixture	4	1.2917	1.2917	0.3229	2.22	0.093
Taps*Mass*Mixture	8	0.6982	0.6982	0.0873	0.60	0.769
Error	27	3.9256	3.9256	0.1454		
Total	53	15.5758				

S = 0.381303 R-Sq = 74.80% R-Sq(adj) = 50.53%

Term	Coef	SE Coef	T	P
Constant	5.89817	0.05189	113.67	0.000
Taps				
45	-0.19564	0.07338	-2.67	0.013
90	-0.02209	0.07338	-0.30	0.766
Mass				
0.05	-0.01399	0.07338	-0.19	0.850
0.10	-0.15784	0.07338	-2.15	0.041
Mixture				
0.05	-0.34540	0.07338	-4.71	0.000
0.10	-0.13814	0.07338	-1.88	0.071
Taps*Mass				
45 0.05	-0.0089	0.1038	-0.09	0.932
45 0.10	-0.1076	0.1038	-1.04	0.309
90 0.05	-0.0047	0.1038	-0.05	0.964

90	0.10		0.0392	0.1038	0.38	0.709
Taps*Mixture						
45	0.05		0.0234	0.1038	0.23	0.823
45	0.10		0.0591	0.1038	0.57	0.574
90	0.05		-0.0678	0.1038	-0.65	0.519
90	0.10		0.0364	0.1038	0.35	0.729
Mass*Mixture						
0.05	0.05		0.2003	0.1038	1.93	0.064
0.05	0.10		-0.2195	0.1038	-2.11	0.044
0.10	0.05		-0.0794	0.1038	-0.77	0.451
0.10	0.10		0.2417	0.1038	2.33	0.028
Taps*Mass*Mixture						
45	0.05	0.05	-0.0557	0.1468	-0.38	0.707
45	0.05	0.10	0.2010	0.1468	1.37	0.182
45	0.10	0.05	0.1411	0.1468	0.96	0.345
45	0.10	0.10	-0.1686	0.1468	-1.15	0.261
90	0.05	0.05	0.1564	0.1468	1.07	0.296
90	0.05	0.10	-0.1543	0.1468	-1.05	0.302
90	0.10	0.05	-0.0787	0.1468	-0.54	0.596
90	0.10	0.10	0.0030	0.1468	0.02	0.984

Re-Analysis of Variance for Permittivity excluding Taps, using Adjusted SS for Tests

Source	DF	Seq SS	Adj SS	Adj MS	F	P
Mass	2	0.9835	0.9835	0.4917	3.35	0.044
Mixture	2	6.6996	6.6996	3.3498	22.84	0.000
Mass*Mixture	4	1.2917	1.2917	0.3229	2.20	0.084
Error	45	6.6011	6.6011	0.1467		
Total	53	15.5758				

S = 0.383002 R-Sq = 57.62% R-Sq(adj) = 50.09%

Term	Coef	SE Coef	T	P
Constant	5.89817	0.05212	113.17	0.000
Mass				
0.05	-0.01399	0.07371	-0.19	0.850
0.10	-0.15784	0.07371	-2.14	0.038
Mixture				
0.05	-0.34540	0.07371	-4.69	0.000
0.10	-0.13814	0.07371	-1.87	0.067
Mass*Mixture				
0.05 0.05	0.2003	0.1042	1.92	0.061
0.05 0.10	-0.2195	0.1042	-2.11	0.041
0.10 0.05	-0.0794	0.1042	-0.76	0.450
0.10 0.10	0.2417	0.1042	2.32	0.025

8.3.5.1.2 Loss Factor

Analysis of Variance using Adjusted SS for Tests

Source	DF	Seq SS	Adj SS	Adj MS	F	P
Taps	2	0.0007629	0.0007629	0.0003814	1.15	0.330
Mass	2	0.0070599	0.0070599	0.0035300	10.69	0.000
Mixture	2	0.0527584	0.0527584	0.0263792	79.87	0.000
Taps*Mass	4	0.0064242	0.0064242	0.0016061	4.86	0.004
Taps*Mixture	4	0.0013692	0.0013692	0.0003423	1.04	0.407
Mass*Mixture	4	0.0016267	0.0016267	0.0004067	1.23	0.321
Taps*Mass*Mixture	8	0.0037696	0.0037696	0.0004712	1.43	0.231
Error	27	0.0089170	0.0089170	0.0003303		
Total	53	0.0826879				

S = 0.0181731 R-Sq = 89.22% R-Sq(adj) = 78.83%

Term			Coef	SE Coef	T	P
Constant			0.075148	0.002473	30.39	0.000
Taps						
45			-0.003966	0.003497	-1.13	0.267
90			0.005048	0.003497	1.44	0.160
Mass						
0.05			-0.013429	0.003497	-3.84	0.001
0.10			-0.001086	0.003497	-0.31	0.759
Mixture						
0.05			-0.032473	0.003497	-9.28	0.000
0.10			-0.009737	0.003497	-2.78	0.010
Taps*Mass						
45	0.05		-0.003424	0.004946	-0.69	0.495
45	0.10		-0.002287	0.004946	-0.46	0.647
90	0.05		0.019214	0.004946	3.88	0.001
90	0.10		-0.003209	0.004946	-0.65	0.522
Taps*Mixture						
45	0.05		-0.000570	0.004946	-0.12	0.909
45	0.10		-0.008041	0.004946	-1.63	0.116
90	0.05		0.001436	0.004946	0.29	0.774
90	0.10		0.001477	0.004946	0.30	0.768
Mass*Mixture						
0.05	0.05		0.004469	0.004946	0.90	0.374
0.05	0.10		0.000605	0.004946	0.12	0.904
0.10	0.05		0.004758	0.004946	0.96	0.345
0.10	0.10		-0.000080	0.004946	-0.02	0.987
Taps*Mass*Mixture						
45	0.05	0.05	-0.000608	0.006995	-0.09	0.931
45	0.05	0.10	-0.013402	0.006995	-1.92	0.066
45	0.10	0.05	0.007037	0.006995	1.01	0.323
45	0.10	0.10	0.010254	0.006995	1.47	0.154
90	0.05	0.05	0.004730	0.006995	0.68	0.505

90	0.05	0.10	-0.003636	0.006995	-0.52	0.607
90	0.10	0.05	-0.004470	0.006995	-0.64	0.528
90	0.10	0.10	-0.003170	0.006995	-0.45	0.654

Re-Analysis of Variance for Loss Factor excluding Taps, using Adjusted SS for Tests

Source	DF	Seq SS	Adj SS	Adj MS	F	P
Mass	2	0.0070599	0.0070599	0.0035300	7.48	0.002
Mixture	2	0.0527584	0.0527584	0.0263792	55.88	0.000
Mass*Mixture	4	0.0016267	0.0016267	0.0004067	0.86	0.494
Error	45	0.0212429	0.0212429	0.0004721		
Total	53	0.0826879				

S = 0.0217271 R-Sq = 74.31% R-Sq(adj) = 69.74%

Term	Coef	SE Coef	T	P
Constant	0.075148	0.002957	25.42	0.000
Mass				
0.05	-0.013429	0.004181	-3.21	0.002
0.10	-0.001086	0.004181	-0.26	0.796
Mixture				
0.05	-0.032473	0.004181	-7.77	0.000
0.10	-0.009737	0.004181	-2.33	0.024
Mass*Mixture				
0.05 0.05	0.004469	0.005913	0.76	0.454
0.05 0.10	0.000605	0.005913	0.10	0.919
0.10 0.05	0.004758	0.005913	0.80	0.425
0.10 0.10	-0.000080	0.005913	-0.01	0.989

8.3.5.1.3 Volume

Analysis of Variance for Volume, using Adjusted SS for Tests

Source	DF	Seq SS	Adj SS	Adj MS	F	P
Taps	2	13.50	13.50	6.75	0.14	0.866
Mass	2	21649.86	21649.86	10824.93	231.77	0.000
Mixture	2	44.55	44.55	22.28	0.48	0.626
Taps*Mass	4	324.26	324.26	81.06	1.74	0.171
Taps*Mixture	4	411.68	411.68	102.92	2.20	0.095
Mass*Mixture	4	444.76	444.76	111.19	2.38	0.077
Taps*Mass*Mixture	8	495.61	495.61	61.95	1.33	0.273
Error	27	1261.03	1261.03	46.70		
Total	53	24645.26				

S = 6.83410 R-Sq = 94.88% R-Sq(adj) = 89.96%

Term	Coef	SE Coef	T	P
Constant	51.7404	0.9300	55.63	0.000
Taps				
45	0.323	1.315	0.25	0.808
90	-0.706	1.315	-0.54	0.596
Mass				
0.05	-25.282	1.315	-19.22	0.000
0.10	1.595	1.315	1.21	0.236
Mixture				
0.05	0.399	1.315	0.30	0.764
0.10	0.858	1.315	0.65	0.520
Taps*Mass				
45 0.05	0.570	1.860	0.31	0.762
45 0.10	-2.396	1.860	-1.29	0.209
90 0.05	1.633	1.860	0.88	0.388

90	0.10		2.928	1.860	1.57	0.127
Taps*Mixture						
45	0.05		4.781	1.860	2.57	0.016
45	0.10		-1.135	1.860	-0.61	0.547
90	0.05		-2.939	1.860	-1.58	0.126
90	0.10		-0.858	1.860	-0.46	0.648
Mass*Mixture						
0.05	0.05		1.325	1.860	0.71	0.482
0.05	0.10		-0.649	1.860	-0.35	0.730
0.10	0.05		-5.445	1.860	-2.93	0.007
0.10	0.10		2.092	1.860	1.12	0.271
Taps*Mass*Mixture						
45	0.05	0.05	-1.390	2.630	-0.53	0.602
45	0.05	0.10	-1.751	2.630	-0.67	0.511
45	0.10	0.05	1.530	2.630	0.58	0.566
45	0.10	0.10	4.541	2.630	1.73	0.096
90	0.05	0.05	1.819	2.630	0.69	0.495
90	0.05	0.10	0.194	2.630	0.07	0.942
90	0.10	0.05	-1.811	2.630	-0.69	0.497
90	0.10	0.10	1.918	2.630	0.73	0.472

8.3.5.1.4 Density

Analysis of Variance for Density, using Adjusted SS for Tests

Source	DF	Seq SS	Adj SS	Adj MS	F	P
Taps	2	4050	4050	2025	0.02	0.979
Mass	2	113862	113862	56931	0.60	0.558
Mixture	2	58012	58012	29006	0.30	0.741
Taps*Mass	4	354709	354709	88677	0.93	0.462
Taps*Mixture	4	809949	809949	202487	2.12	0.106
Mass*Mixture	4	489958	489958	122490	1.28	0.302

Taps*Mass*Mixture	8	608438	608438	76055	0.80	0.611
Error	27	2579901	2579901	95552		
Total	53	5018879				

S = 309.115 R-Sq = 48.60% R-Sq(adj) = 0.00%

Term		Coef	SE Coef	T	P
Constant		1976.73	42.07	46.99	0.000
Taps					
45		-11.04	59.49	-0.19	0.854
90		10.12	59.49	0.17	0.866
Mass					
0.05		-3.10	59.49	-0.05	0.959
0.10		-54.63	59.49	-0.92	0.367
Mixture					
0.05		-30.69	59.49	-0.52	0.610
0.10		-14.73	59.49	-0.25	0.806
Taps*Mass					
45	0.05	-20.36	84.13	-0.24	0.811
45	0.10	80.18	84.13	0.95	0.349
90	0.05	-68.75	84.13	-0.82	0.421
90	0.10	-79.36	84.13	-0.94	0.354
Taps*Mixture					
45	0.05	-184.84	84.13	-2.20	0.037
45	0.10	24.34	84.13	0.29	0.775
90	0.05	101.93	84.13	1.21	0.236
90	0.10	87.88	84.13	1.04	0.305
Mass*Mixture					
0.05	0.05	-92.79	84.13	-1.10	0.280
0.05	0.10	20.56	84.13	0.24	0.809
0.10	0.05	187.82	84.13	2.23	0.034
0.10	0.10	-72.60	84.13	-0.86	0.396

Taps*Mass*Mixture

45	0.05	0.05	-11.8	119.0	-0.10	0.922
45	0.05	0.10	105.4	119.0	0.89	0.383
45	0.10	0.05	-90.1	119.0	-0.76	0.455
45	0.10	0.10	-131.9	119.0	-1.11	0.278
90	0.05	0.05	-51.6	119.0	-0.43	0.668
90	0.05	0.10	20.9	119.0	0.18	0.862
90	0.10	0.05	111.7	119.0	0.94	0.356
90	0.10	0.10	-93.0	119.0	-0.78	0.441

8.3.6 Dielectric Property Measurement

8.3.6.1 Ore Powders

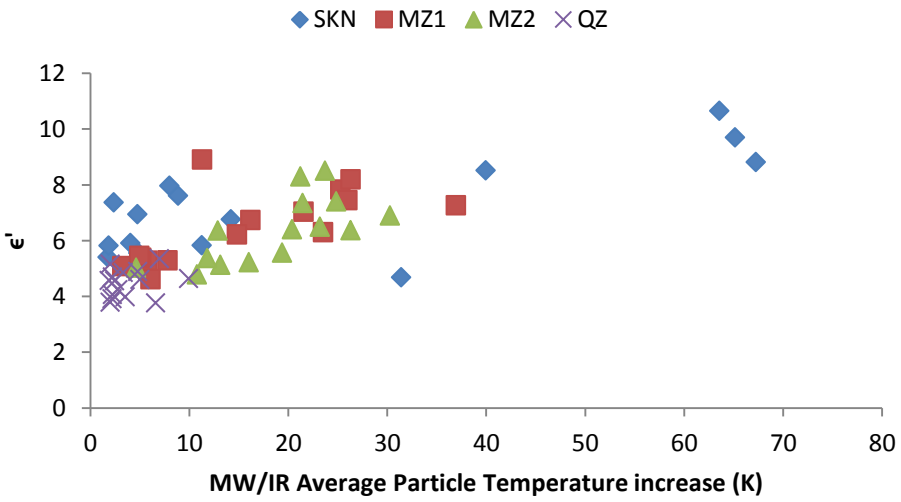

Figure 8-11 – ϵ' of ore powders at 912 MHz

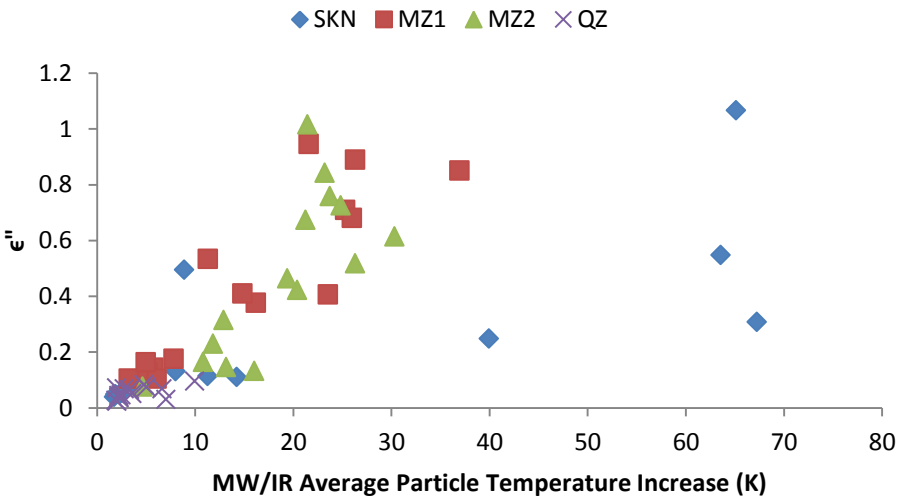

Figure 8-12 – ϵ'' of ore powders at 912 MHz

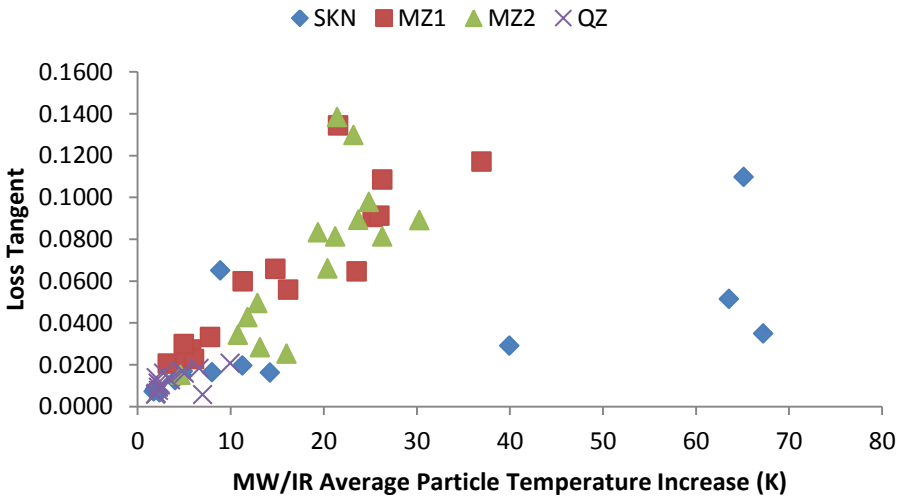

Figure 8-13 – Loss tangent of ore powders at 912 MHz

8.3.6.2 Regression analysis

8.3.6.2.1 Regression Analysis 1: Loss Tangent versus Temperature

The regression equation is

losf = 0.0159 + 0.00116 fult

Predictor	Coef	SE Coef	T	P
Constant	0.015942	0.003967	4.02	0.000
fult	0.0011588	0.0001869	6.20	0.000

S = 0.0217068 R-Sq = 40.7% R-Sq(adj) = 39.6%

Analysis of Variance

Source	DF	SS	MS	F	P
Regression	1	0.018108	0.018108	38.43	0.000
Residual Error	56	0.026386	0.000471		
Total	57	0.044494			

Unusual Observations

Obs	fult	losf	Fit	SE Fit	Residual	St Resid
1	67.2	0.03137	0.09385	0.01021	-0.06247	-3.26RX
2	65.1	0.08264	0.09141	0.00984	-0.00877	-0.45 X
3	63.5	0.05020	0.08958	0.00955	-0.03937	-2.02RX
5	23.2	0.09133	0.04280	0.00326	0.04853	2.26R
6	21.5	0.09413	0.04091	0.00312	0.05322	2.48R
7	21.4	0.11108	0.04078	0.00311	0.07030	3.27R

R denotes an observation with a large standardized residual.

X denotes an observation whose X value gives it large leverage.

8.3.6.2.2 Regression Analysis 2: Loss Tangent versus Temperature (Fit excludes unusual observations identified in Regression 1)

```
The regression equation is
partan = 0.00531 + 0.00199 parT

Predictor       Coef    SE Coef      T      P
Constant    0.005314   0.002541   2.09  0.042
parT       0.0019858  0.0001683  11.80  0.000

S = 0.0119866   R-Sq = 73.6%   R-Sq(adj) = 73.1%

Analysis of Variance
Source          DF        SS        MS       F      P
Regression       1  0.020013  0.020013  139.29  0.000
Residual Error  50  0.007184  0.000144
Total           51  0.027197

Unusual Observations
Obs  parT   partan      Fit   SE Fit  Residual  St Resid
  1  39.9  0.02540  0.08462  0.00508  -0.05922     -5.45RX
  2  36.9  0.08094  0.07865  0.00460   0.00230      0.21 X
 24   8.9  0.04735  0.02293  0.00172   0.02442      2.06R

R denotes an observation with a large standardized residual.
X denotes an observation whose X value gives it large leverage.
```

8.3.6.2.3 Regression Analysis 3: Loss Tangent versus Temperature (Fit excludes Obs 1 of Regression 2)

```
The regression equation is
lost = 0.00207 + 0.00239 T
```

```
Predictor       Coef    SE Coef      T      P
Constant    0.002071   0.001678   1.23  0.223
T          0.0023912  0.0001183  20.22  0.000

S = 0.00770706   R-Sq = 89.3%   R-Sq(adj) = 89.1%

Analysis of Variance
Source          DF        SS        MS       F      P
Regression       1  0.024279  0.024279  408.75  0.000
Residual Error  49  0.002911  0.000059
Total           50  0.027190

Unusual Observations
Obs     T     lost      Fit   SE Fit  Residual  St Resid
  1  36.9  0.08094  0.09038  0.00327  -0.00943     -1.35 X
 14  16.0  0.01995  0.04035  0.00124  -0.02041     -2.68R
 23   8.9  0.04735  0.02328  0.00110   0.02406      3.15R

R denotes an observation with a large standardized residual.
X denotes an observation whose X value gives it large leverage.
```

8.3.6.2.4 Regression Analysis 1: Modified Loss Tangent (MLT) versus Temperature

```
The regression equation is
MLT = 0.00280 + 0.000155 Temp

Predictor        Coef     SE Coef     T      P
Constant    0.0028006   0.0005381  5.20  0.000
Temp       0.00015465  0.00002536  6.10  0.000

S = 0.00294437   R-Sq = 39.9%   R-Sq(adj) = 38.8%
```

Analysis of Variance

Source	DF	SS	MS	F	P
Regression	1	0.00032250	0.00032250	37.20	0.000
Residual Error	56	0.00048548	0.00000867		
Total	57	0.00080798			

Unusual Observations

Obs	Temp	MLT	Fit	SE Fit	Residual	St Resid
1	63.5	0.007485	0.012628	0.001296	-0.005142	-1.95 X
3	67.2	0.004411	0.013198	0.001385	-0.008787	-3.38RX
4	65.1	0.011994	0.012872	0.001334	-0.000877	-0.33 X
5	21.4	0.015816	0.006115	0.000422	0.009701	3.33R
6	23.2	0.013984	0.006385	0.000442	0.007599	2.61R
7	21.5	0.013519	0.006133	0.000423	0.007386	2.53R

R denotes an observation with a large standardized residual.

X denotes an observation whose X value gives it large leverage.

8.3.6.2.5 Regression Analysis 2: MLT versus Temperature (Fit excludes the unusual observations identified in Regression 1)

The regression equation is

MLT2 = 0.00139 + 0.000262 t2

52 cases used, 4 cases contain missing values

Predictor	Coef	SE Coef	T	P
Constant	0.0013854	0.0003207	4.32	0.000
t2	0.00026190	0.00002123	12.34	0.000

S = 0.00151260 R-Sq = 75.3% R-Sq(adj) = 74.8%

```
Analysis of Variance
Source           DF          SS          MS       F      P
Regression        1  0.00034812  0.00034812  152.15  0.000
Residual Error   50  0.00011440  0.00000229
Total            51  0.00046252

Unusual Observations
Obs    t2      MLT2       Fit    SE Fit   Residual  St Resid
  1  39.9  0.004882  0.011845  0.000641  -0.006962     -5.08RX
  2  36.9  0.011211  0.011057  0.000581   0.000153      0.11 X
  3  19.4  0.011041  0.006461  0.000269   0.004580      3.08R

R denotes an observation with a large standardized residual.
X denotes an observation whose X value gives it large leverage.
```

8.3.6.2.6 Regression Analysis 3: MLT versus Temperature (Fit excludes Obs 1 of Regression 2)

```
The regression equation is
MLT3 = 0.00100 + 0.000310 t3

Predictor        Coef     SE Coef      T      P
Constant    0.0010040   0.0002314   4.34  0.000
t3         0.00030957  0.00001631  18.98  0.000

S = 0.00106258   R-Sq = 88.0%   R-Sq(adj) = 87.8%

Analysis of Variance
Source           DF          SS          MS       F      P
Regression        1  0.00040694  0.00040694  360.41  0.000
Residual Error   49  0.00005533  0.00000113
```

```
Total           50   0.00046226

Unusual Observations
Obs     t3      MLT3       Fit     SE Fit    Residual  St Resid
  1   36.9  0.011211  0.012436  0.000450  -0.001225     -1.27 X
  2   19.4  0.011041  0.007003  0.000204   0.004038      3.87R
 14    8.9  0.006109  0.003750  0.000152   0.002359      2.24R
 23   16.0  0.003722  0.005960  0.000171  -0.002238     -2.13R

R denotes an observation with a large standardized residual.
X denotes an observation whose X value gives it large leverage.
```

8.3.6.3 Log-Log Analysis

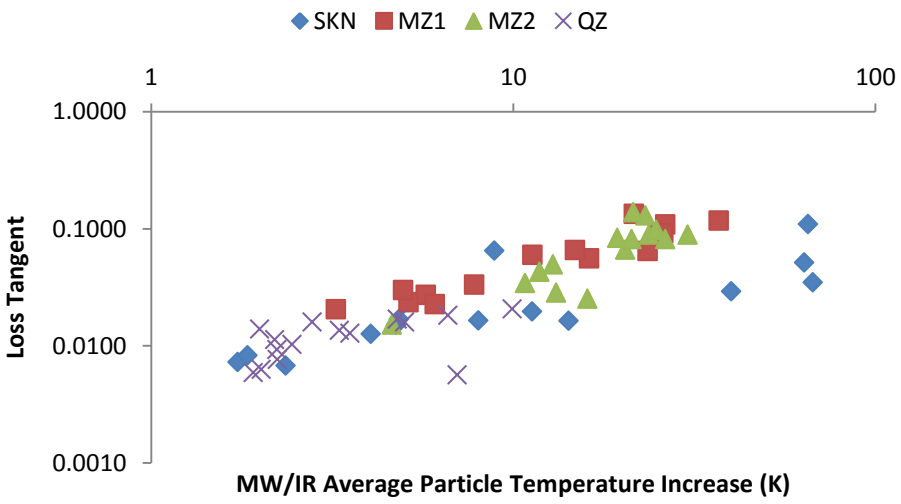

Figure 8-14 – Log-Log plot of loss tangent (912 MHz) of ore powders and particle temperature change due to microwave exposure (2.45 GHz)

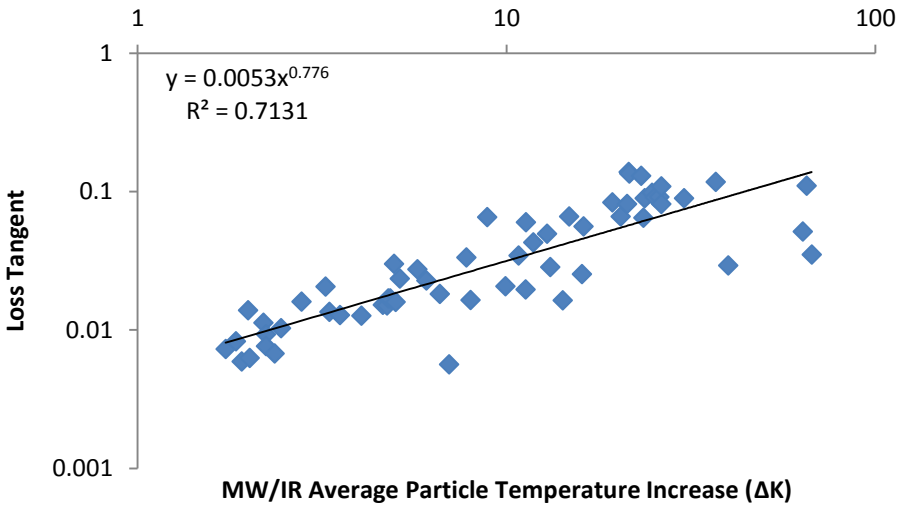

Figure 8-15 – Loss tangent data for all ore powders combined at 912 MHz

8.3.6.4 Ore Cores

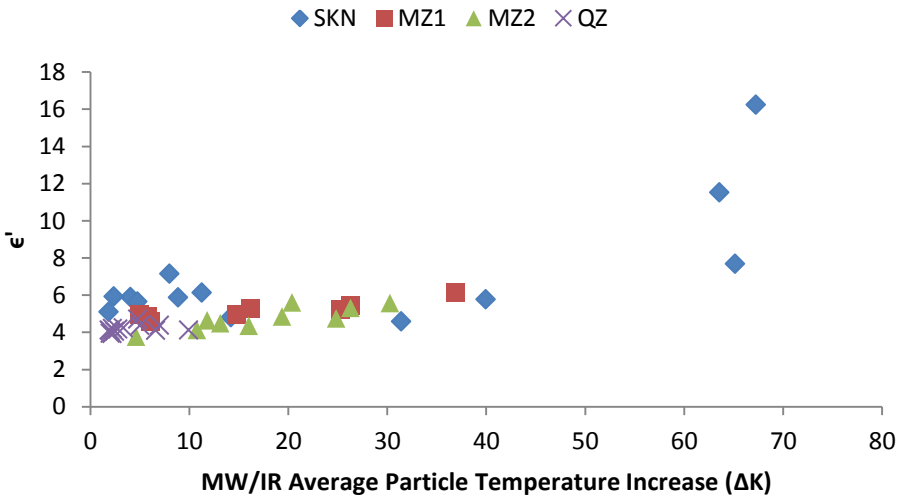

Figure 8-16 – ϵ' of cores samples at 2470 MHz

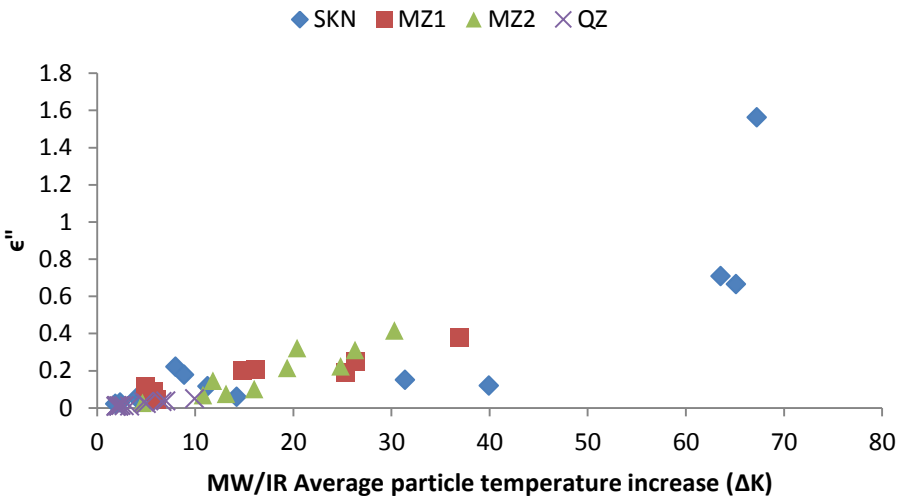

Figure 8-17 – ϵ'' of cores samples at 2470 MHz

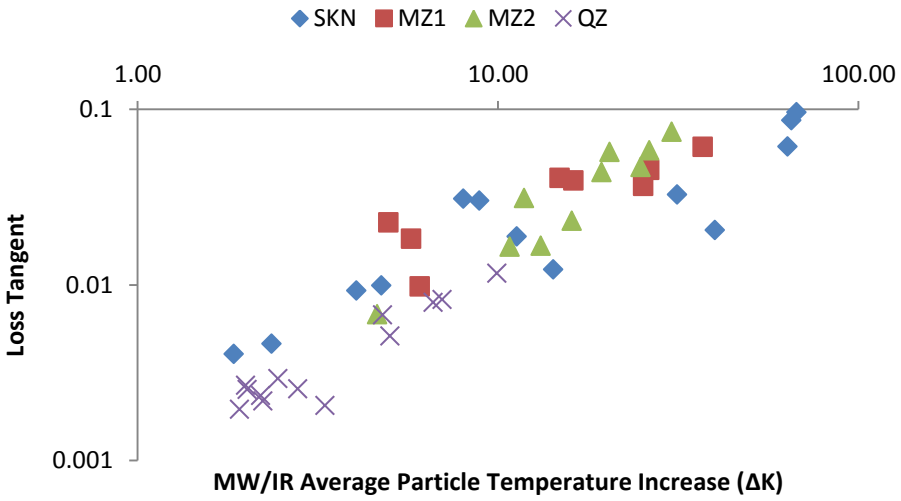

Figure 8-18 – Log-Log plot of loss tangent v. Average MW/IR temperature increase for cores at 2470 MHz

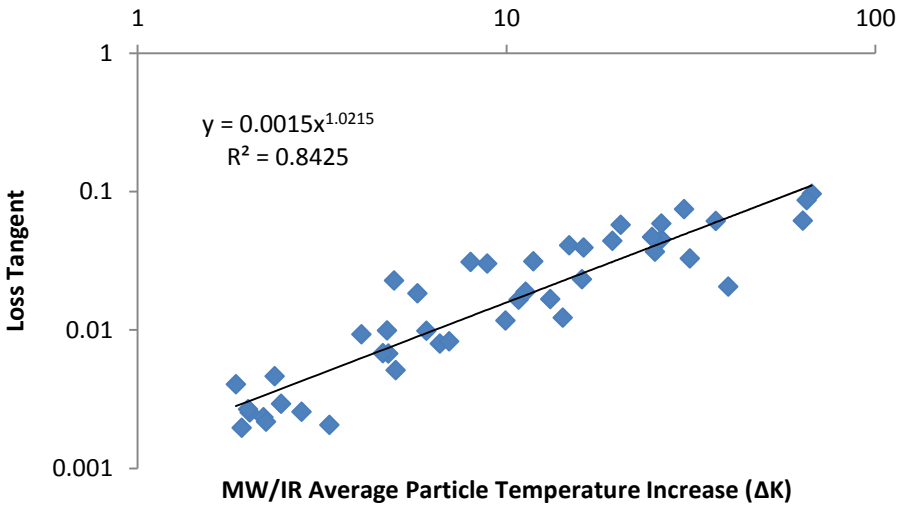

Figure 8-19 – Loss tangent data for all ore cores combined at 2470 MHz

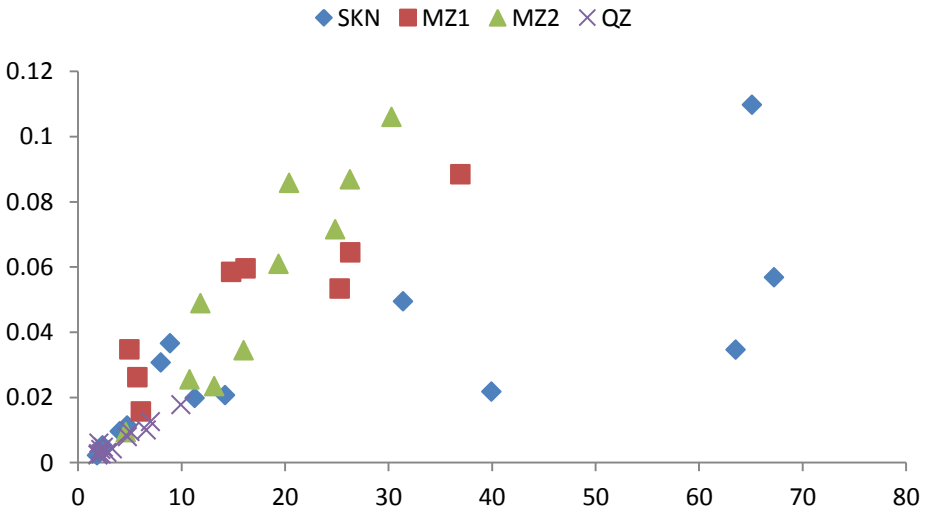

Figure 8-20 – Loss Tangent of cores at 912 MHz

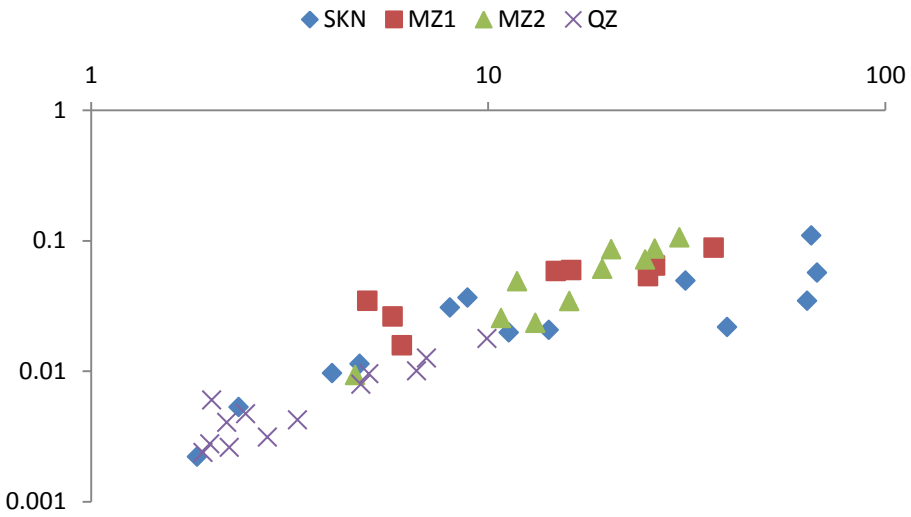

Figure 8-21 – Log-Log Plot of Loss Tangent and Average MW/IR Temperature Increase for Cores at 912 MHz

8.3.6.5 Comparison of Ore Powder and Core Measurements

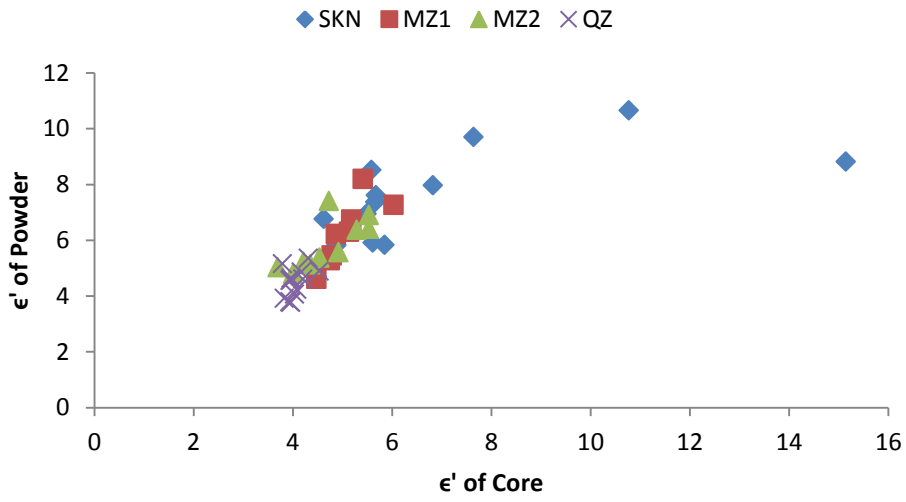

Figure 8-22 –The correlation of core and powder ϵ' at 912 MHz

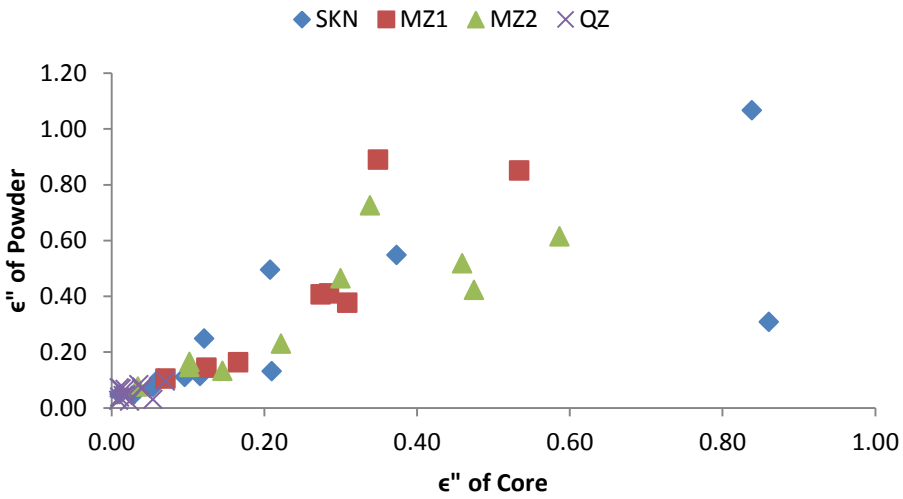

Figure 8-23 –The correlation of core and powder ϵ'' at 912 MHz

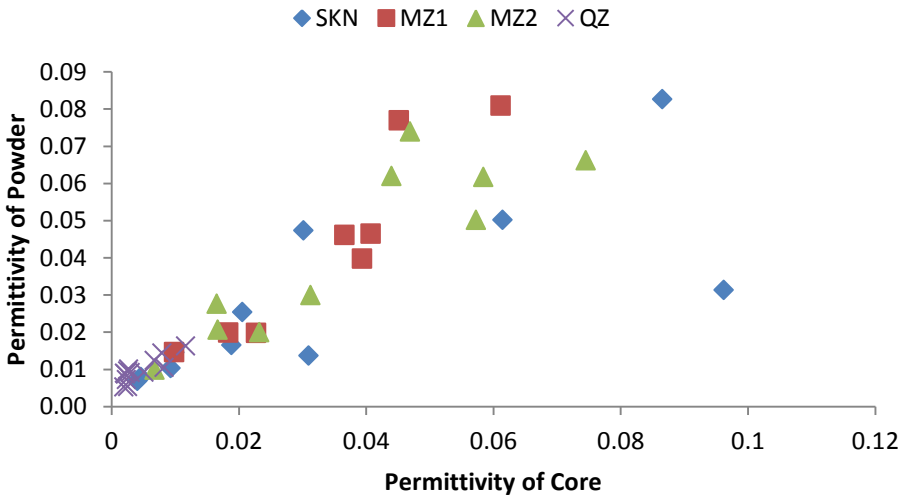

Figure 8-24 – The correlation of core and powder loss tangent at 912 MHz

8.3.6.6 Frequency Relationship

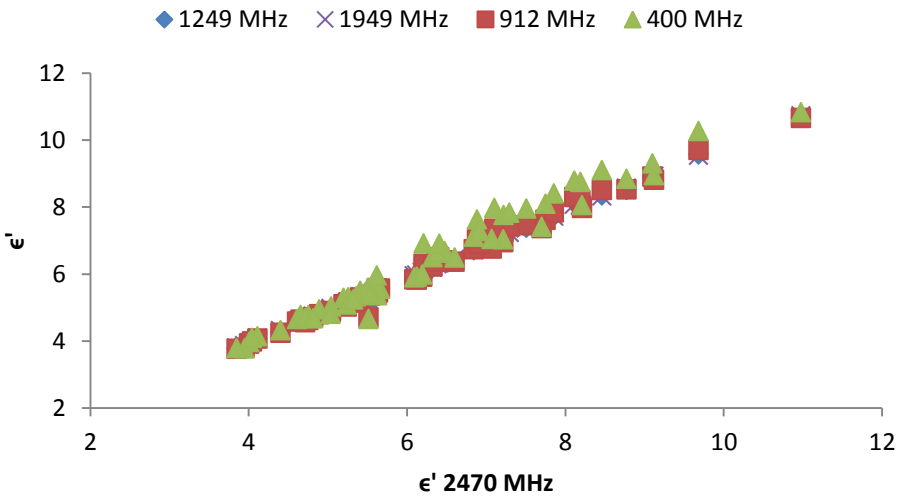

Figure 8-25 –Correlation of 2470 MHz ϵ' measurements with measurements at other frequencies using combined ore data

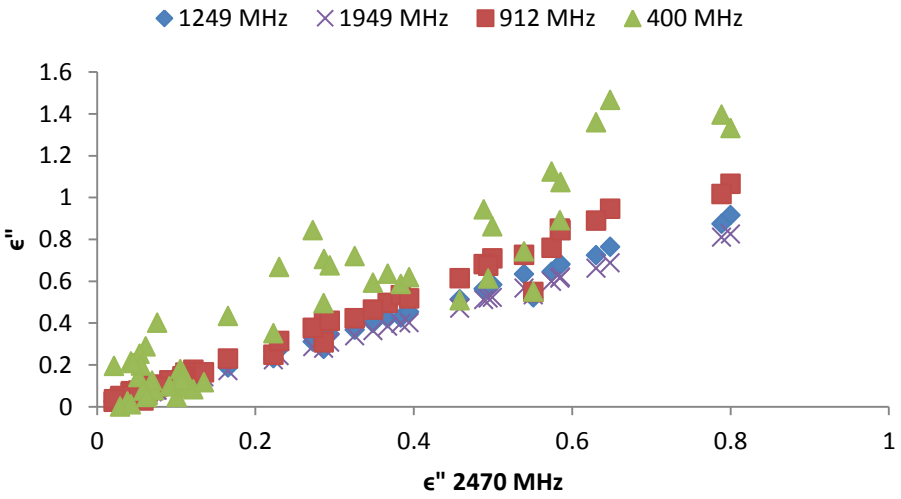

Figure 8-26 – Correlation of 2470 MHz ϵ'' measurements with measurements at other frequencies using combined ore data

8.3.6.7 Mineral Dielectric Properties

Table 8-17 – Measured dielectric properties of mineral powder specimens at 912 MHz

Mineral	ϵ'	ϵ''	$\tan\delta$

Chalcopyrite	21.81	1.51	0.0692
Pyrite	26.38	5.94	0.2252
Molybdenite	15.42	2.18	0.1411
Mica	8.17	0.089	0.0109
Feldspar	4.60	0.018	0.0040
Garnet	10.64	0.017	0.0016
Quartz	4.63	0.018	0.0039

Table 8-18 – Measured dielectric properties of mineral core specimens at 912 MHz

Mineral	ϵ'	ϵ''	$\tan\delta$
Quartz	4.19	0.0032	0.0008
Feldspar	4.98	0.0408	0.0082
Pyrite	12.72	0.6856	0.0539
Chalcopyrite	11.14	0.1411	0.0127

8.3.6.8 Mineral Thermal Effects

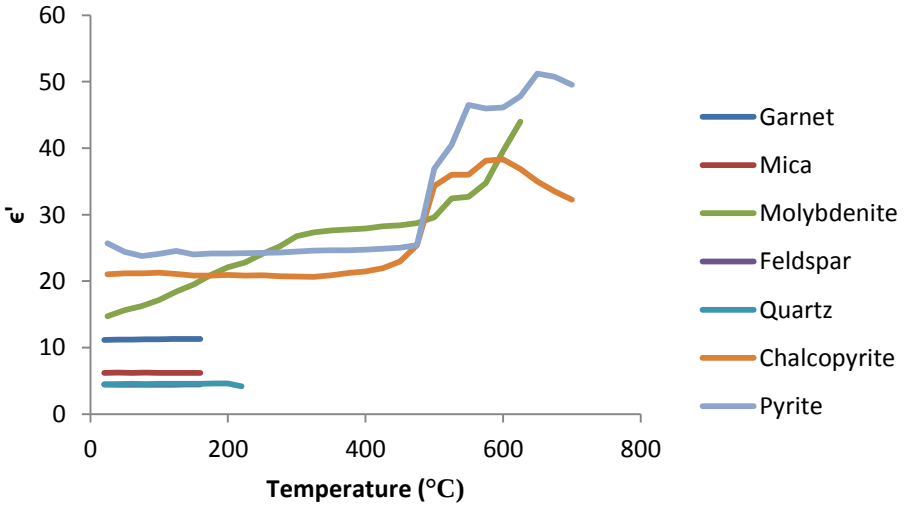

Figure 8-27 – Evolution of ϵ' with temperature for minerals at 912 MHz

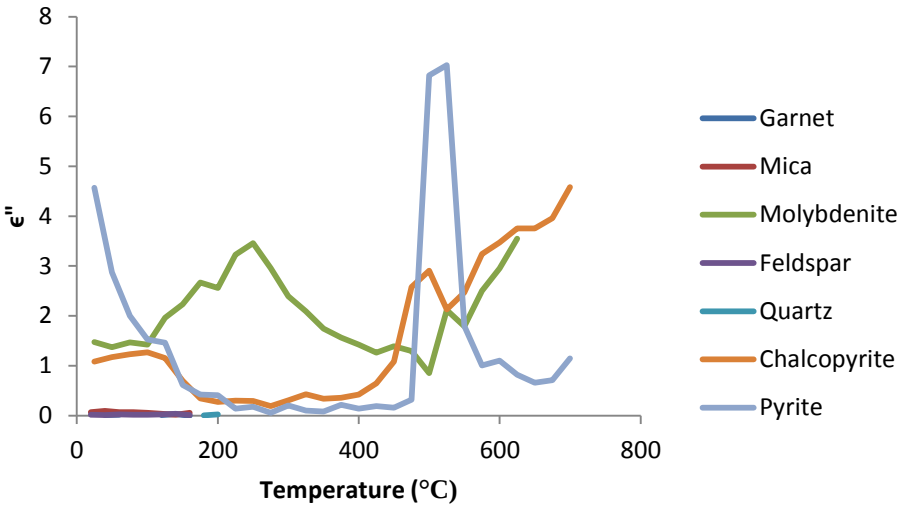

Figure 8-28 – Evolution of ϵ'' with temperature for minerals at 912 MHz

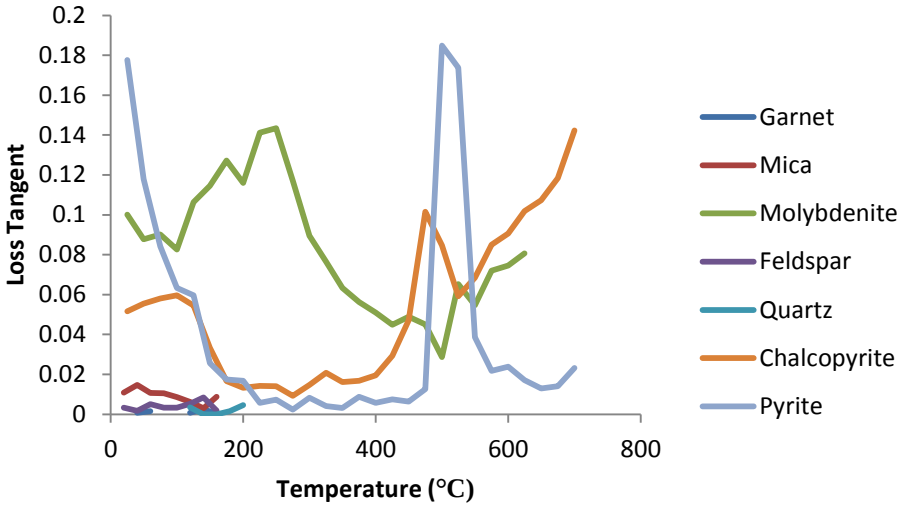

Figure 8-29 – Evolution of loss tangent with temperature for minrals at 912 MHz

8.4 Magnetic Characterization

8.4.1 Relationships Between Frequency and Permeability

8.4.1.1 General Regression Analysis: QZ versus frequency

Regression Equation

QZ = 1.00239 + 5.76957e-008 f_a - 4.54446e-012 f_a*f_a

Coefficients

Term	Coef	SE Coef	T	P
Constant	1.00239	0.0000367	27348.7	0.000
f_a	0.00000	0.0000000	3.3	0.006
f_a*f_a	-0.00000	0.0000000	-3.8	0.002

Summary of Model

S = 0.0000743649 R-Sq = 60.70% R-Sq(adj) = 54.15%

PRESS = 9.696263E-08 R-Sq(pred) = 42.57%

Analysis of Variance

Source	DF	Seq SS	Adj SS	Adj MS	F	P
Regression	2	0.0000001	0.0000001	0.0000001	9.2660	0.0036860
f_a	1	0.0000000	0.0000001	0.0000001	11.1787	0.0058505
f_a*f_a	1	0.0000001	0.0000001	0.0000001	14.7152	0.0023695
Error	12	0.0000001	0.0000001	0.0000000		
Total	14	0.0000002				

8.4.1.2 General Regression Analysis: MZ2 versus frequency

Regression Equation

LGM = 1.01338 - 1.04196e-007 f_b + 2.71219e-012 f_b*f_b

Coefficients

Term	Coef	SE Coef	T	P
Constant	1.01338	0.0001295	7824.95	0.000

```
f_b       -0.00000  0.0000001    -1.73  0.109
f_b*f_b    0.00000  0.0000000     0.66  0.521

Summary of Model
S = 0.000262435       R-Sq = 69.17%        R-Sq(adj) = 64.03%
PRESS = 1.248170E-06  R-Sq(pred) = 53.44%

Analysis of Variance
Source          DF     Seq SS     Adj SS     Adj MS        F         P
Regression       2  0.0000019  0.0000019  0.0000009  13.4602  0.000859
  f_b            1  0.0000018  0.0000002  0.0000002   3.0031  0.108699
  f_b*f_b        1  0.0000000  0.0000000  0.0000000   0.4376  0.520767
Error           12  0.0000008  0.0000008  0.0000001
  Lack-of-Fit   11  0.0000008  0.0000008  0.0000001  21.7657  0.165800
  Pure Error     1  0.0000000  0.0000000  0.0000000
Total           14  0.0000027
```

8.4.1.3 General Regression Analysis: MZ1 versus frequency

```
Regression Equation
HRD  =  1.00072 - 2.11836e-009 f_c - 2.73178e-014 f_c*f_c

Coefficients
Term          Coef    SE Coef        T      P
Constant   1.00072  0.0000216  46384.3  0.000
f_c       -0.00000  0.0000000     -0.2  0.836
f_c*f_c   -0.00000  0.0000000     -0.0  0.969

Summary of Model
S = 0.0000438247      R-Sq = 10.49%         R-Sq(adj) = -4.43%
PRESS = 3.601562E-08  R-Sq(pred) = -39.88%
```

Analysis of Variance

Source	DF	Seq SS	Adj SS	Adj MS	F	P
Regression	2	0.0000000	0.0000000	0.0000000	0.70310	0.514342
f_c	1	0.0000000	0.0000000	0.0000000	0.04451	0.836454
f_c*f_c	1	0.0000000	0.0000000	0.0000000	0.00159	0.968843
Error	12	0.0000000	0.0000000	0.0000000		
Lack-of-Fit	10	0.0000000	0.0000000	0.0000000	2.23065	0.349054
Pure Error	2	0.0000000	0.0000000	0.0000000		
Total	14	0.0000000				

8.4.1.4 General Regression Analysis: SKN versus frequency

```
Regression Equation

LRO  =  1.00068 + 4.30129e-008 f_d - 2.13792e-012 f_d*f_d


Coefficients

Term          Coef    SE Coef        T      P
Constant   1.00068  0.0000592  16913.8  0.000
f_d        0.00000  0.0000000      1.6  0.143
f_d*f_d   -0.00000  0.0000000     -1.1  0.275

Summary of Model

S = 0.000120218       R-Sq = 32.65%         R-Sq(adj) = 21.43%
PRESS = 2.964068E-07  R-Sq(pred) = -15.11%

Analysis of Variance

Source      DF     Seq SS     Adj SS     Adj MS        F         P
Regression   2  0.0000001  0.0000001  0.0000000  2.90887  0.093319
  f_d        1  0.0000001  0.0000000  0.0000000  2.46179  0.142625
  f_d*f_d    1  0.0000000  0.0000000  0.0000000  1.31017  0.274681
Error       12  0.0000002  0.0000002  0.0000000
Total       14  0.0000003
```

8.4.2 The Relationship between Permeability and MW/IR Characterization

8.4.2.1 General Regression Analysis: Permeability of MZ1 versus MW/IR Characterization Temperature

```
Regression Equation


UA  =  1.00152 - 4.91746e-005 TA + 1.17254e-006 TA*TA
```

Coefficients

Term	Coef	SE Coef	T	P
Constant	1.00152	0.0003789	2643.49	0.000
TA	-0.00005	0.0000509	-0.97	0.353
TA*TA	0.00000	0.0000014	0.85	0.410

Summary of Model

S = 0.000497689 R-Sq = 8.00% R-Sq(adj) = -7.33%

PRESS = 4.203006E-06 R-Sq(pred) = -30.09%

Analysis of Variance

Source	DF	Seq SS	Adj SS	Adj MS	F	P
Regression	2	0.0000003	0.0000003	0.0000001	0.521967	0.606228
TA	1	0.0000001	0.0000002	0.0000002	0.934956	0.352662
TA*TA	1	0.0000002	0.0000002	0.0000002	0.727210	0.410487
Error	12	0.0000030	0.0000030	0.0000002		
Total	14	0.0000032				

8.4.2.2 General Regression Analysis: Permeability of SKN versus MW/IR Characterization Temperature

Regression Equation

UB = 1.00161 - 1.70028e-005 TB + 8.09509e-008 TB*TB

Coefficients

Term	Coef	SE Coef	T	P
Constant	1.00161	0.0003712	2698.52	0.000
TB	-0.00002	0.0000412	-0.41	0.687
TB*TB	0.00000	0.0000006	0.14	0.895

Summary of Model

S = 0.000782851 R-Sq = 13.72% R-Sq(adj) = -0.66%

PRESS = 9.961595E-06 R-Sq(pred) = -16.87%

Analysis of Variance

Source	DF	Seq SS	Adj SS	Adj MS	F	P
Regression	2	0.0000012	0.0000012	0.0000006	0.954237	0.412487
TB	1	0.0000012	0.0000001	0.0000001	0.170046	0.687342
TB*TB	1	0.0000000	0.0000000	0.0000000	0.018332	0.894544
Error	12	0.0000074	0.0000074	0.0000006		
Total	14	0.0000085				

8.4.2.3 General Regression Analysis: Permeability of QZ versus MW/IR Characterization Temperature

Regression Equation

UC = 1.0041 - 0.000524129 TC + 3.87917e-005 TC*TC

Coefficients

Term	Coef	SE Coef	T	P
Constant	1.00410	0.0011715	857.115	0.000
TC	-0.00052	0.0005402	-0.970	0.351
TC*TC	0.00004	0.0000490	0.791	0.444

Summary of Model

S = 0.00102621 R-Sq = 10.95% R-Sq(adj) = -3.89%

PRESS = 0.0000336196 R-Sq(pred) = -136.90%

Analysis of Variance

Source	DF	Seq SS	Adj SS	Adj MS	F	P
Regression	2	0.0000016	0.0000016	0.0000008	0.73780	0.498652

TC	1	0.0000009	0.0000010	0.0000010	0.94145	0.351057
TC*TC	1	0.0000007	0.0000007	0.0000007	0.62595	0.444200
Error	12	0.0000126	0.0000126	0.0000011		
Lack-of-Fit	11	0.0000118	0.0000118	0.0000011	1.29029	0.602505
Pure Error	1	0.0000008	0.0000008	0.0000008		
Total	14	0.0000142				

8.4.2.4 General Regression Analysis: Permeability of MZ2 versus MW/IR Characterization Temperature

Regression Equation

UD = 1.00652 - 0.00089141 TD + 3.00262e-005 TD*TD

Coefficients

Term	Coef	SE Coef	T	P
Constant	1.00652	0.0029413	342.207	0.000
TD	-0.00089	0.0003497	-2.549	0.026
TD*TD	0.00003	0.0000097	3.088	0.009

Summary of Model

S = 0.00189605 R-Sq = 54.86% R-Sq(adj) = 47.34%

PRESS = 0.000155455 R-Sq(pred) = -62.65%

Analysis of Variance

Source	DF	Seq SS	Adj SS	Adj MS	F	P
Regression	2	0.0000524	0.0000524	0.0000262	7.29305	0.0084559
TD	1	0.0000182	0.0000234	0.0000234	6.49849	0.0255025
TD*TD	1	0.0000343	0.0000343	0.0000343	9.53371	0.0094029
Error	12	0.0000431	0.0000431	0.0000036		
Total	14	0.0000956				

8.5 Texture Measurement

8.5.1 MATLAB Code: Waveguide Cavity Resonant Frequency and Q-Factor Calculator

This function was used to find the centre frequency and Q-factor of a resonance using frequency and log magnitude S_{21} data recorded from a network analyser. It first smooths the data using a 5 point rolling average and then removes the first and last two data points from the array (the rolling average creates a discontinuity at these points). The S_{21} maximum is located and the corresponding frequency point is taken to be the centre frequency. The resonance full-width half-maximum (or 3-dB points) are located by interpolation. The 3 dB points are then used to calculate the bandwidth of the peak and consequently the Q-factor of the resonance.

```
function Output = myrqfinder(Z)
%function to find the resonant frequency and Q of log-mag data

X=Z(:,1);
Y=Z(:,2);

xsize=size(X);
ysize=size(Y);

%basic smoothing
span=5;
window=ones(span,1)/span;
Ya=convn(Y,window,'same');

%chop the ends off
Yb=Ya(ceil(span/2):ysize(1)-ceil(span/2));
Xb=X(ceil(span/2):xsize(1)-ceil(span/2));
```

```
[ymax ii] =max(Yb);

%chop into upper and lower halves
Yl=Yb(1:ii);
Yu=Yb(ii:end);
Xl=Xb(1:ii);
Xu=Xb(ii:end);

%interpolate
fl=interp1(Yl,Xl,ymax-3);
fu=interp1(Yu,Xu,ymax-3);

BW=fu-fl;
Q=Xb(ii)/BW;

Output=[Xb(ii),BW,Q];

return
```

8.5.2 Core Rotation Data

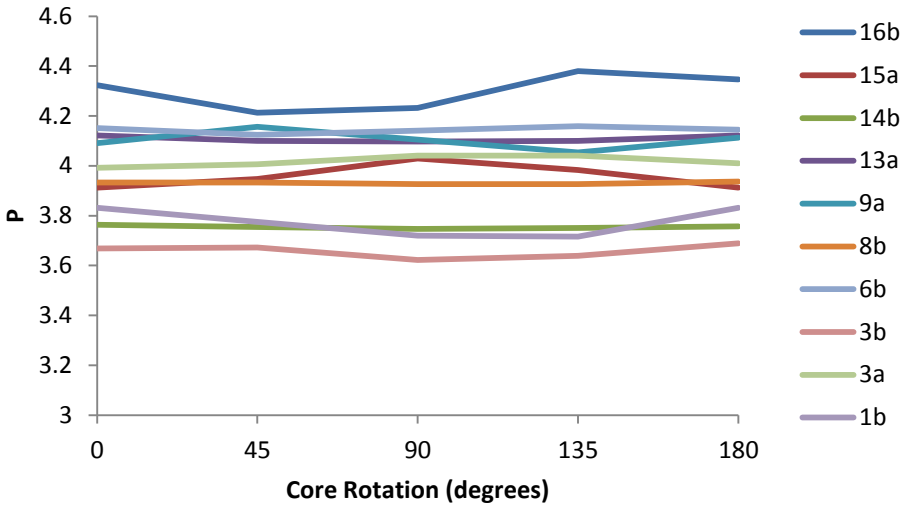

Figure 8-30 – Changes in P values as cores are rotated

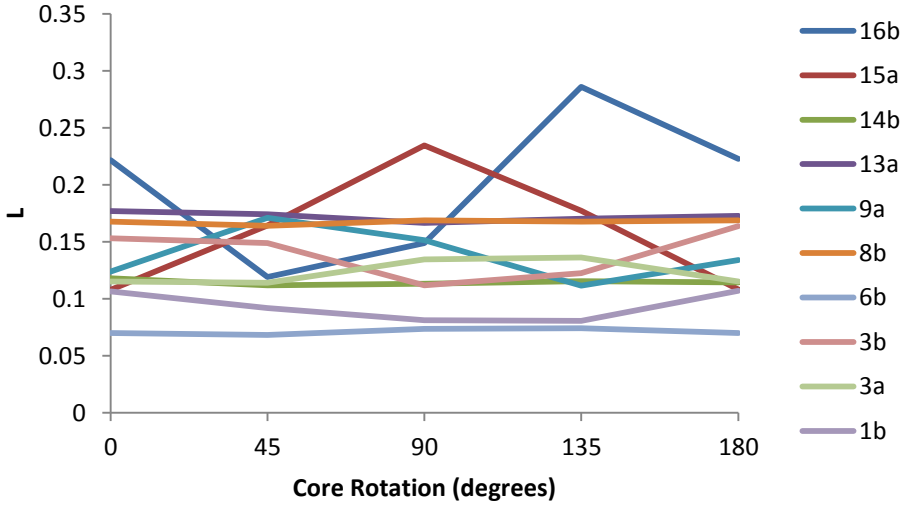

Figure 8-31 – Changes in L values as cores are rotated

8.5.3 MLA Data

Table 8-19 – Weight Percent Data for MLA Analysed Solid Sections (GXMap)

Particle:	*A*	*B*	*C*
Sulphides			
Pyrite	20.43	4.33	25.48
Arsenopyrite	0.02	0.00	0.00
Chalcopyrite	0.57	4.17	2.09
Bornite	0.00	0.01	1.84
Chalcocite	0.00	0.01	2.51
Tennantite	0.00	0.00	0.04
Molybdenite	0.00	0.01	0.00
Galena	0.00	0.00	0.00
Total	*21.02*	*8.53*	*31.96*
Gangue Minerals			
Feldspar	2.80	0.02	1.99
Quartz	22.49	67.34	7.96
Olivine	0.29	0.04	10.46
Pyroxene	1.89	0.96	2.09
Amphibole	33.01	7.48	26.01
Biotite	1.30	0.01	5.23
Garnet	10.59	1.27	0.72
Chlorite	2.47	0.25	2.34
Talc	0.00	0.00	0.01
Calcite	2.68	13.65	9.93
Apatite	0.37	0.19	0.35
Total	*77.89*	*91.21*	*67.09*

Titaniferous Minerals			
Rutile	0.00	0.00	0.00
Ilmenite	0.00	0.00	0.00
Titanite	0.18	0.05	0.10
Total	*0.18*	*0.05*	*0.10*
Iron Oxide	0.01	0.00	0.01
Other	0.91	0.21	0.83

8.6 Modal Mineralogy Data

8.6.1 Powder XMOD DATA

Table 8-20 – MLA XMOD Summary for selected QZ samples (wt%)

Sample	*10-1*	*1-2*	*4-2*	*7-2*	*9-2*	*2-3*	*9-3*	*Avg*
Sulphides								
Arsenopyrite	0.00	0.00	0.00	0.00	0.00	0.00	0.00	*0.00*
Bornite	0.02	0.00	0.03	0.00	0.16	0.87	0.00	*0.15*
Chalcocite	0.00	0.00	0.00	0.00	0.00	0.01	0.00	*0.00*
Chalcopyrite	0.10	0.04	0.20	0.00	0.44	1.15	0.06	*0.28*
Covellite	0.00	0.00	0.00	0.00	0.00	0.00	0.00	*0.00*
Galena	0.00	0.00	0.00	0.00	0.00	0.00	0.00	*0.00*
Molybdentite	0.00	0.09	0.20	0.00	0.13	0.00	0.09	*0.07*
Pyrite	0.00	0.01	0.04	0.15	0.01	0.08	0.02	*0.04*
Tetrahedrite	0.00	0.00	0.00	0.00	0.00	0.00	0.00	*0.00*

Gangue								
Amphibole	0.00	0.00	0.00	0.00	0.02	0.03	0.00	*0.01*
Apatite	0.01	0.00	0.04	0.00	0.74	0.18	0.00	*0.14*
Biotite	1.82	11.71	3.42	0.01	22.65	12.24	5.97	*8.26*
Calcite	0.02	0.02	0.16	0.07	0.04	0.03	0.12	*0.07*
Chlorite	0.01	0.02	0.03	0.00	0.06	2.11	0.02	*0.32*
Garnet	0.00	0.00	0.01	0.00	0.01	0.06	0.00	*0.01*
Muscovite	0.18	0.02	0.15	0.13	2.64	0.00	0.01	*0.45*
Olivine	0.09	0.02	0.11	0.00	0.00	0.04	0.02	*0.04*
Alkali Feldspar	0.23	0.05	1.60	0.04	60.91	0.04	0.13	*9.00*
Plagioclase Feldspar	0.01	0.02	0.02	0.12	0.02	0.03	0.02	*0.03*
Pyroxene	0.05	0.13	0.15	0.69	0.10	0.31	0.10	*0.22*
Quartz	97.45	87.51	93.65	98.70	11.40	82.09	93.26	*80.58*
Talc	0.00	0.09	0.01	0.00	0.01	0.60	0.07	*0.11*
Other								
Iron Oxide	0.01	0.03	0.06	0.01	0.02	0.01	0.02	0.02
Rutile_Ilm_Titanite	0.00	0.00	0.04	0.01	0.58	0.00	0.00	0.09
Other	0.01	0.23	0.06	0.08	0.06	0.11	0.06	0.09
Total	*100.0*	*100.0*	*100.0*	*100.0*	*100.0*	*100.0*	*100.0*	

Table 8-21 – MLA XMOD Summary for selected SKN samples (wt%)

Sample	*6-1*	*11-1*	*3-2*	*9-2*	*10-2*	*9-3*	*11-3*	*Avg*
Sulphides								
Arsenopyrite	0.01	0.00	0.00	0.01	0.00	0.00	0.04	0.01
Bornite	1.93	0.00	0.01	0.07	0.09	0.00	0.01	0.30
Chalcocite	0.52	0.00	0.00	0.07	0.14	0.00	0.00	0.10

Chalcopyrite	3.64	0.02	1.49	3.12	1.05	0.32	0.41	1.44
Covellite	1.68	0.00	0.00	0.03	0.28	0.00	0.00	0.28
Galena	0.01	0.00	0.00	0.00	0.05	0.00	0.00	0.01
Molybdentite	0.00	0.00	0.00	0.01	0.02	0.00	0.00	0.00
Pyrite	11.18	0.00	0.08	9.56	0.87	0.16	24.35	6.60
Tetrahedrite	0.21	0.00	0.00	0.00	0.04	0.00	0.00	0.04
Gangue								
Amphibole	3.08	0.05	0.24	0.80	0.68	3.74	8.08	2.38
Apatite	0.33	0.13	0.14	0.21	0.36	0.04	0.43	0.23
Biotite	0.29	0.00	0.00	0.02	0.00	0.00	0.31	0.09
Calcite	9.72	0.31	16.17	7.53	25.88	0.15	1.35	8.73
Chlorite	0.63	0.00	0.03	0.17	0.06	0.02	1.21	0.30
Garnet	12.02	55.34	55.85	7.43	45.39	0.04	23.12	28.46
Muscovite	0.13	0.00	0.00	0.00	0.01	0.01	0.15	0.04
Olivine	1.44	0.00	0.00	0.01	0.01	0.02	0.02	0.21
Alkali Feldspar	1.18	0.00	0.01	0.02	0.00	0.05	1.28	0.36
Plagioclase Feldspar	0.02	0.00	0.00	0.02	0.00	0.02	0.00	0.01
Pyroxene	34.47	41.95	13.29	13.16	7.03	3.05	29.94	20.41
Quartz	16.37	2.18	12.50	57.28	17.68	91.92	7.81	29.39
Talc	0.05	0.00	0.17	0.35	0.03	0.39	1.32	0.33
Other								
Iron Oxide	0.03	0.01	0.00	0.00	0.00	0.03	0.00	0.01
Rutile_Ilm_Titanite	0.10	0.00	0.00	0.11	0.01	0.01	0.17	0.06
Other	0.96	0.00	0.00	0.01	0.33	0.02	0.00	0.19
Total	*100.0*	*100.0*	*100.0*	*100.0*	*100.0*	*100.0*	*100.0*	

Table 8-22 – MLA XMOD Summary for selected MZ1samples (wt%)

Sample	*10-3*	*11-3*	*3-12*	*6-12*	*8-12*	*4-35*	*11-35*	*Avg*
Sulphides								
Arsenopyrite	0.00	0.00	0.00	0.00	0.00	0.00	0.00	0.00
Bornite	0.35	0.00	0.50	0.00	1.24	1.38	2.38	0.84
Chalcocite	0.02	0.00	0.01	0.00	0.01	0.07	0.02	0.02
Chalcopyrite	0.61	0.16	0.19	0.20	0.29	0.28	0.26	0.28
Covellite	0.00	0.00	0.00	0.00	0.00	0.00	0.00	0.00
Galena	0.01	0.00	0.00	0.00	0.02	0.00	0.00	0.00
Molybdentite	0.13	0.00	0.00	0.08	0.01	0.00	0.00	0.03
Pyrite	0.03	0.02	0.03	0.15	0.05	0.01	0.03	0.05
Tetrahedrite	0.00	0.00	0.00	0.00	0.00	0.00	0.01	0.00
Gangue								
Amphibole	0.03	0.19	0.23	0.01	0.70	0.86	0.32	0.33
Apatite	1.83	0.89	1.19	0.34	0.88	1.20	0.69	1.00
Biotite	23.33	31.72	41.98	12.06	31.74	29.38	33.61	29.12
Calcite	0.11	0.09	0.05	0.04	0.13	0.10	0.25	0.11
Chlorite	0.03	0.05	0.23	0.01	0.22	1.20	0.17	0.27
Garnet	0.01	0.02	0.00	0.00	0.07	0.04	0.01	0.02
Muscovite	1.87	3.39	2.68	3.15	5.00	2.97	3.86	3.27
Olivine	0.01	0.00	0.00	0.02	0.01	0.02	0.00	0.01
Alkali Feldspar	63.96	45.46	26.19	44.91	36.15	21.64	35.60	39.13
Plagioclase Feldspar	0.10	1.35	1.62	0.15	1.95	14.13	3.07	3.20
Pyroxene	0.11	1.88	7.92	0.61	7.15	12.88	5.51	5.15
Quartz	6.96	14.12	17.05	37.62	14.15	13.53	13.94	16.77
Talc	0.00	0.01	0.01	0.00	0.00	0.01	0.02	0.01

Other								
Iron Oxide	0.01	0.01	0.00	0.02	0.01	0.02	0.00	0.01
Rutile_Ilm_Titanite	0.41	0.15	0.06	0.29	0.16	0.21	0.20	0.21
Other	0.11	0.49	0.03	0.35	0.05	0.06	0.04	0.16
Total	*100.0*	*100.0*	*100.0*	*100.0*	*100.0*	*100.0*	*100.0*	

Table 8-23 – MLA XMOD Summary for selected MZ2 samples (wt%)

Sample	*4-1*	*5-2*	*1-3*	*3-3*	*4-3*	*6-3*	*7-3*	*Avg*
Sulphides								
Arsenopyrite	0.00	0.00	0.00	0.00	0.00	0.00	0.00	0.00
Bornite	0.00	0.01	0.00	0.51	0.37	0.10	0.07	0.15
Chalcocite	0.00	0.00	0.00	0.03	0.01	0.00	0.00	0.01
Chalcopyrite	0.02	0.11	0.03	0.23	0.08	0.04	0.02	0.08
Covellite	0.00	0.00	0.00	0.01	0.00	0.00	0.00	0.00
Galena	0.00	0.00	0.00	0.00	0.00	0.00	0.00	0.00
Molybdentite	0.00	0.73	0.01	0.01	0.13	0.00	0.00	0.13
Pyrite	0.01	0.04	0.05	0.01	0.02	0.02	0.04	0.03
Tetrahedrite	0.00	0.00	0.00	0.00	0.00	0.00	0.00	0.00
Gangue								
Amphibole	6.54	0.01	0.00	0.59	0.12	23.51	2.05	4.69
Apatite	0.59	0.37	0.01	0.82	0.81	1.30	1.44	0.76
Biotite	64.73	2.96	0.01	25.71	25.73	7.70	19.41	20.89
Calcite	1.28	0.06	0.48	0.33	0.04	2.00	0.13	0.62
Chlorite	5.11	0.01	0.00	0.73	0.15	5.00	0.90	1.70
Garnet	0.23	0.01	0.02	0.12	0.02	1.25	0.05	0.24
Muscovite	0.24	2.61	0.01	2.00	1.79	0.47	3.59	1.53

Olivine	0.00	0.01	0.06	0.01	0.01	0.04	0.06	0.03
Alkali Feldspar	3.55	52.36	0.42	13.46	30.00	2.41	33.51	19.39
Plagioclase Feldspar	3.05	0.46	0.01	22.14	13.92	24.93	13.72	11.18
Pyroxene	4.19	1.57	0.12	10.25	14.70	13.08	11.78	7.96
Quartz	10.02	38.45	98.71	22.64	11.79	16.03	11.94	29.94
Talc	0.06	0.00	0.00	0.03	0.00	0.08	0.01	0.03
Other								
Iron Oxide	0.00	0.00	0.02	0.02	0.02	0.38	0.43	0.12
Rutile_Ilm_Titanite	0.37	0.21	0.02	0.11	0.28	1.61	0.46	0.44
Other	0.01	0.01	0.01	0.23	0.00	0.05	0.37	0.10
Total	*100.0*	*100.0*	*100.0*	*100.0*	*100.0*	*100.0*	*100.0*	

8.6.2 Mineral Densities

Table 8-24 – Densities of MLA reported minerals (from mindat.org database)

Mineral	*Density g/cm^3*
Sulphides	
Arsenopyrite	6.2
Bornite	5.1
Chalcocite	5.8
Chalcopyrite	4.2
Covellite	4.6
Galena	7.6
Molybdentite	5.0
Pyrite	5.0
Tetrahedrite	5.0

Gangue & Other	
Amphibole	3.0
Apatite	3.2
Biotite	3.0
Calcite	2.7
Chlorite	2.6
Garnet	4.0
Muscovite	2.8
Olivine	3.3
Orthoclase	2.6
Plagioclase	2.7
Pyroxene	3.2
Quartz	2.7
Talc	2.8
Iron Oxide	5.2
Rutile_Ilm_Titanite	4.2
Other	2.7

8.6.3 Rock Classification

Table 8-25 – Normalized volume percentages of QAPF mineral for the different ores

	QZ	*SKN*	*MZ1*	*MZ2*
Quartz (Q)	89.6%	98.5%	27.9%	48.7%
Alkali Feldspars (A)	10.3%	1.4%	66.7%	32.6%
Plagioclase (P)	0.0%	0.0%	5.4%	18.6%

Feldspathoids (F)	0.0%	0.0%	0.0%	0.0%

From Streckeisen (1976):

"1a, quartzolite (silexite); 1b, quartz-rich granitoids; 2, alkali-feldspar granite; 3, granite; 4, granodiorite; 5, tonalite, 6, quartz alkali-feldspar syenite; 7*, quartz syenite; 8*, quartz monzonite; 9*, quartz monzodiorite/quartz monzogabbro; 10*, quartz diorite/quartz gabbro/quartz anorthosite; 6, alkali-feldspar syenite; 7, syenite; 8, monzonite; 9, monzodiorite/monzogabbro; 10, diorite/gabbro/anorthosite; 6', foid-bearing alkali-feldspar syenite; 7', foid-bearing syenite; 8', foid-bearing monzonite; 9', foid-bearing monzodiorite/monzogabbro; 10', foid-bearing diorite/gabbro; 11, foid syenite; 12, fold monzosyenite (syn. foid plagisyenite); 13, foid monzodiorite/foid monzogabbro (essexite = nepheline monzodiorite/monzogabbro); 14, foid diorite/foid gabbro (theralite = nepheline gabbro, teschenite = analcime gabbro); 15, foidolites"*

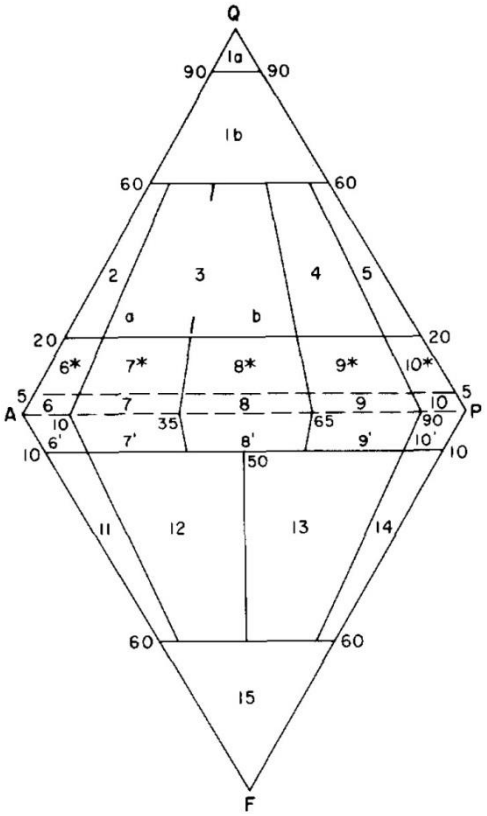

Figure 8-32 – The general classification of plutonic rocks according their mineral content in volume%. (Streckeisen 1976)

8.6.4 Detection limits for EPMA measurements

Table 8-26 – Detection limits for gangue measurements (Provided by Dr D. Steele)

Element	*Detection Limit (wt. %)*
F	0.020
Na	0.010
Mg	0.011
Al	0.009
Si	0.012
P	0.022
S	0.009
Cl	0.013
K	0.013
Ca	0.022
Ti	0.029
Cr	0.018
Mn	0.009
Fe	0.031
Ba	0.009

Table 8-27 – Detection limits for sulphide measurements (Provided by Dr D. Steele)

Element	*Detection Limit (wt. %)*
S	0.024

Mn	0.018
Fe	0.032
Cu	0.035
Zn	0.034
As	0.006
Se	0.005
Mo	0.054
Ag	0.016
Cd	0.019
Sb	0.023
Te	0.020
Au	0.082
Hg	0.049
Pb	0.068
Bi	0.067

Table 8-28 – Ideal atomic percentages for major sulphide minerals

A%	*Bornite*	*Chalcopyrite*	*Pyrite*	*Molybdenite*
Cu	50	25		
Fe	10	25	33.33	
S	40	50	66.67	66.67
Mo				33.33

8.6.5 EPMA Results

Table 8-29 – Elemental analysis of average bornite by ore (A. %)

	MZ1	*MZ2*	*QZ*	*SKN*
Samples:	(40)	(1)	(3)	(4)
Cu	49.36	49.54	50.32	51.35
Fe	9.86	9.94	9.54	9.32
S	40.60	40.39	40.01	39.15
Mo	0.05	0.05	0.06	0.08
Mn	0.00	0.01	0.00	0.01
Zn	0.01	0.00	0.00	0.03
As	0.00	0.00	0.00	0.01
Ag	0.02	0.01	0.01	0.01
Cd	0.00	0.00	0.00	0.01
Sb	0.01	0.00	0.01	0.02
Au	0.01	0.02	0.01	0.00
Hg	0.01	0.00	0.01	0.00
Pb	0.02	0.01	0.00	0.01
Bi	0.03	0.01	0.00	0.00
Se	0.01	0.02	0.01	0.00
Te	0.00	0.00	0.00	0.00

Table 8-30 – Elemental analysis of average chalcopyrite by ore (A. %)

	MZ1	*MZ2*	*QZ*	*SKN*
Samples:	(8)	(2)	(6)	(28)
Cu	24.77	25.14	25.12	24.89
Fe	24.76	24.96	24.53	24.97

S	50.30	49.72	50.20	49.96
Mo	0.06	0.04	0.04	0.07
Mn	0.00	0.00	0.00	0.00
Zn	0.01	0.03	0.01	0.02
As	0.04	0.04	0.04	0.04
Ag	0.00	0.00	0.00	0.00
Cd	0.00	0.00	0.01	0.00
Sb	0.01	0.01	0.01	0.01
Au	0.01	0.02	0.01	0.00
Hg	0.01	0.01	0.01	0.01
Pb	0.03	0.01	0.02	0.02
Bi	0.01	0.00	0.01	0.01
Se	0.00	0.00	0.01	0.00
Te	0.00	0.01	0.00	0.00

Table 8-31 – Elemental analysis of average pyrite by ore (A. %)

	MZ1	*MZ2*	*QZ*	*SKN*
Samples:	(0)	(0)	(1)	(30)
Cu			0.00	0.01
Fe			33.18	33.24
S			66.61	66.57
Mo			0.06	0.04
Mn			0.00	0.00
Zn			0.02	0.01
As			0.06	0.05
Ag			0.00	0.00
Cd			0.00	0.00

Sb		0.01	0.01
Au		0.03	0.01
Hg		0.01	0.01
Pb		0.01	0.02
Bi		0.00	0.01
Se		0.00	0.01
Te		0.00	0.00

Table 8-32 – Elemental analysis of average molybdenite by ore (A. %)

	MZ1	*MZ2*	*QZ*	*SKN*
Samples:	(4)	(2)	(2)	(5)
Cu	0.03	0.01	0.05	0.03
Fe	0.03	0.02	0.01	0.03
S	66.67	66.48	66.39	66.85
Mo	33.18	33.41	33.43	32.99
Mn	0.01	0.01	0.00	0.01
Zn	0.02	0.01	0.02	0.01
As	0.00	0.00	0.00	0.00
Ag	0.00	0.00	0.00	0.00
Cd	0.01	0.01	0.00	0.01
Sb	0.02	0.01	0.01	0.02
Au	0.00	0.00	0.05	0.01
Hg	0.01	0.02	0.01	0.02
Pb	0.00	0.00	0.00	0.00
Bi	0.00	0.00	0.00	0.00
Se	0.02	0.02	0.03	0.02
Te	0.00	0.00	0.00	0.00

Table 8-33 – Average oxide analyses of alkali feldspars by ore (wt. %)

	MZ1	*MZ2*	*QZ*	*SKN*
SiO_2	64.033	63.731	65.146	64.090
TiO_2	0.004	0.004	0.024	0.000
Al_2O_3	18.243	17.774	18.054	17.605
Fe_2O_3	0.089	0.074	0.056	0.600
MgO	0.007	0.006	0.016	0.475
CaO	0.250	0.027	0.005	0.045
BaO	0.766	0.684	0.592	0.170
Na_2O	2.474	1.602	1.470	0.480
K_2O	12.768	14.229	14.639	15.965
Sum Ox%	98.636	98.130	100.003	99.450

Table 8-34 – Average oxide analyses of plagioclase feldspars by ore (wt. %)

	MZ1	*MZ2*
SiO_2	64.847	63.553
TiO_2	0.003	0.008
Al_2O_3	21.167	22.135
Fe_2O_3	0.197	0.223
MgO	0.023	0.000
CaO	2.817	4.000
BaO	0.000	0.040
Na_2O	9.360	8.990
K_2O	0.567	0.353
Sum Ox%	98.973	99.308

Table 8-35 – Average oxide analyses of pyroxene in SKN (wt. %)

SiO_2	53.629
TiO_2	0.138
Al_2O_3	0.884
Cr_2O_3	0.019
Fe_2O_3(c)	1.256
FeO(c)	1.774
MnO	0.134
MgO	16.683
CaO	25.233
Na_2O	0.085
K_2O	0.003
Sum Ox%	99.844

Table 8-36 – Average oxide analyses of amphiboles by ore (wt. %)

	MZ2	*SKN*
SiO_2	53.102	53.880
TiO_2	0.212	0.020
Al_2O_3	2.656	0.670
Cr_2O_3	0.016	0.010
$Fe2O_3$(c)	3.488	0.000
FeO(c)	6.768	6.860
MnO	0.108	0.445
MgO	17.740	14.640
CaO	12.344	20.590
Na_2O	0.726	0.285

K_2O	0.148	0.065
F	0.244	0.150
Cl	0.056	0.030
H_2O(c)	1.976	1.995
O=F	0.100	0.065
O=Cl	0.012	0.005
Sum Ox%	99.696	99.710

Table 8-37 – Average oxide analyses of biotite by ore (wt. %)

	QZ	*MZ1*	*MZ2*
SiO2	40.971	39.186	39.250
TiO2	2.056	2.611	2.335
Al2O3	12.300	12.126	12.090
Cr2O3	0.113	0.086	0.082
FeO	5.455	10.317	10.135
MnO	0.028	0.041	0.027
MgO	23.431	19.444	19.942
CaO	0.020	0.031	0.098
Na2O	0.113	0.113	0.112
K2O	10.303	9.747	9.423
BaO	0.145	0.219	0.118
F	1.887	1.500	1.295
Cl	0.052	0.122	0.110
H2O(c)	3.267	3.290	3.391
O=F	0.796	0.634	0.544
O=Cl	0.012	0.026	0.025
Sum Ox%	99.336	98.178	97.835

8.7 Calculation of Dielectric Properties

The following Minitab regressions report coefficients in terms of the cube root of the dielectric properties which is due to the form of the LLL mixing equations.

8.7.1 Regression of Dielectric Properties from Quartz-Pyrite Test Mixtures

8.7.1.1 General Regression Analysis: Permittivity (2470 MHz) versus Q (quartz) and P (pyrite)

```
Regression Equation

A2470  =  1.74152 Q + 2.68522 P

Coefficients

Term     Coef    SE Coef         T      P
Q     1.74152  0.011636   149.660  0.000
P     2.68522  0.140600    19.098  0.000

Summary of Model

S = 0.0417325      R-Sq = 99.95%        R-Sq(adj) = 99.95%
PRESS = 0.0982506  R-Sq(pred) = 99.94%

Analysis of Variance

Source         DF   Seq SS   Adj SS   Adj MS        F         P
Regression      2  176.030  176.030  88.0152  50537.0  0.000000
  Q             1  175.395   39.009  39.0087  22398.2  0.000000
```

```
  P             1    0.635    0.635   0.6352    364.7  0.000000
Error          52    0.091    0.091   0.0017
  Lack-of-Fit   1    0.000    0.000   0.0001      0.1  0.802671
  Pure Error   51    0.090    0.090   0.0018
Total          54  176.121
```

```
Fits and Diagnostics for Unusual Observations
```

```
Obs    A2470      Fit     SE Fit  Residual  St Resid
  3  1.94724  1.85323  0.0095483  0.094003   2.31389  R
 42  1.89634  1.76828  0.0081780  0.128061   3.12930  R
```

```
R denotes an observation with a large standardized residual.
```

8.7.1.2 General Regression Analysis: Loss Factor (2470 MHz) versus Q (quartz) and P (pyrite)

```
Regression Equation
```

```
B2470  =  0.297408 Q + 1.90736 P
```

```
Coefficients
```

```
Term     Coef   SE Coef        T      P
Q     0.29741  0.016819  17.6831  0.000
P     1.90736  0.203216   9.3859  0.000
```

```
Summary of Model
```

```
S = 0.0603179     R-Sq = 97.96%        R-Sq(adj) = 97.88%
PRESS = 0.202907  R-Sq(pred) = 97.82%
```

```
Analysis of Variance

Source          DF   Seq SS   Adj SS   Adj MS        F         P
Regression       2  9.09804  9.09804  4.54902  1250.33  0.000000
  Q              1  8.77753  1.13765  1.13765   312.69  0.000000
  P              1  0.32051  0.32051  0.32051    88.09  0.000000
Error           52  0.18919  0.18919  0.00364
  Lack-of-Fit    1  0.00161  0.00161  0.00161     0.44  0.511621
  Pure Error    51  0.18758  0.18758  0.00368
Total           54  9.28722

Fits and Diagnostics for Unusual Observations

Obs     B2470       Fit     SE Fit   Residual  St Resid
 19  0.180606  0.386809  0.0086069  -0.206203  -3.45395  R
 40  0.143256  0.343064  0.0118200  -0.199809  -3.37809  R
 42  0.210061  0.343064  0.0118200  -0.133003  -2.24864  R

R denotes an observation with a large standardized residual.
```

8.7.2 Least Squares Regression in MATLAB of the Full Modal Mineralogy Dataset

Table 8-38 – Best fit dielectric properties of minerals at 2470 MHz using the full modal mineralogy data set

Mineral	*Total Vol%*	ϵ'	ϵ''	ϵ''/ϵ'
Bornite	0.21%	1475.25	-178.40	-0.121
Chalcocite	0.02%	-11708.75	-669617485.68	57189.513
Covellite	0.05%	-6734901.21	-6535850.10	0.970
Chalcopyrite	0.38%	-19317.74	11541.86	-0.597
Tetrahedrite	0.01%	-792413190.60	16997213898.01	-21.450
Molybdentite	0.03%	-7715.52	2626.07	-0.340

Galena	0.00%	14865043.54	-2492595867.13	-167.682
Pyrite	1.13%	85415.01	-26509.87	-0.310
Arsenopyrite	0.00%	-36500834615272.30	11265657689193.20	-0.309
Quartz	40.53%	3.80	0.04	0.011
Orthoclase	18.01%	6.90	0.00	0.000
Plagioclase	3.78%	8.60	-0.02	-0.002
Olivine	0.07%	10812277.09	1803.94	0.000
Pyroxene	8.39%	4.78	90.26	18.880
Amphibole	1.86%	73.12	0.95	0.013
Biotite	13.65%	7.83	0.00	0.000
Chlorite	0.73%	-0.34	128.17	-381.433
Muscovite	1.31%	83.21	1193.47	14.343
Talc	0.13%	40977.07	-7448.30	-0.182
Garnet	6.07%	6.54	-53.36	-8.162
Iron Oxide	0.02%	-13118.21	-6272363.12	478.142
Rutile_Ilm_Titanite	0.14%	-44836.03	-4715.55	0.105
Calcite	2.86%	54.04	249.99	4.626
Apatite	0.48%	12.45	26547.60	2131.537
Other	0.15%	-141.81	298.34	-2.104

8.7.3 Least Squares Regression of a Reduced Mineralogy Set that includes Plagioclase

Table 8-39 – Best fit dielectric properties of minerals at 2470 MHz using a reduced modal mineralogy data set which includes plagioclase

Mineral	*Total Vol%*	ϵ'	ϵ''
Sulphides	1.83%	54.20	20.84
Quartz	40.53%	4.61	0.04
Orthoclase	18.01%	5.42	0.11

Plagioclase	3.78%	8.66	5.34
Pyrobole	10.24%	6.92	0.15
Pyllosilicates	15.90%	7.86	0.79
Garnet	6.07%	4.80	0.02
Other	3.64%	10.65	0.24

8.7.4 Least Squares Regression of a Reduced Mineralogy Set using Minitab at 2470 and 912 MHz

8.7.4.1 General Regression Analysis: Permittivity (2470 MHz) versus Sulphides, Quartz, Orthoclase, Pyrobole, Phyllosilicates, Garnet and Other.

```
Regression Equation

X2470  =  3.67944 Sulphides + 1.66463 Quartz + 1.75443 Orthoclase + 1.9505
          Pyrobole + 1.9727 Pyllosilicates + 1.63674 Garnet + 2.28047 Other

Coefficients

Term              Coef   SE Coef        T      P
Sulphides       3.67944  0.973462   3.7797  0.002
Quartz          1.66463  0.035260  47.2099  0.000
Orthoclase      1.75443  0.089362  19.6329  0.000
Pyrobole        1.95050  0.415803   4.6909  0.000
Pyllosilicates  1.97270  0.143172  13.7786  0.000
Garnet          1.63674  0.365711   4.4755  0.000
Other           2.28047  0.465354   4.9005  0.000

Summary of Model

S = 0.0945502     R-Sq = 99.81%        R-Sq(adj) = 99.73%
```

PRESS = 0.418205 R-Sq(pred) = 99.45%

Analysis of Variance

Source	DF	Seq SS	Adj SS	Adj MS	F	P
Regression	7	76.4072	76.4072	10.9153	1220.99	0.0000000
Sulphides	1	17.8944	0.1277	0.1277	14.29	0.0016414
Quartz	1	33.4109	19.9247	19.9247	2228.77	0.0000000
Orthoclase	1	14.3583	3.4458	3.4458	385.45	0.0000000
Pyrobole	1	6.2302	0.1967	0.1967	22.00	0.0002454
Pyllosilicates	1	2.0662	1.6972	1.6972	189.85	0.0000000
Garnet	1	2.2325	0.1791	0.1791	20.03	0.0003824
Other	1	0.2147	0.2147	0.2147	24.01	0.0001600
Error	16	0.1430	0.1430	0.0089		
Total	23	76.5503				

Fits and Diagnostics for Unusual Observations

Obs	X2470	Fit	SE Fit	Residual	St Resid	
2	1.77830	1.78985	0.0905162	-0.0115504	-0.422726	X

X denotes an observation whose X value gives it large leverage.

8.7.4.2 General Regression Analysis: Loss Factor (2470 MHz) versus Sulphides, Quartz, Orthoclase, Pyrobole, Phyllosilicates, Garnet and Other

Regression Equation

Y2470 = 3.23275 Sulphides + 0.327613 Quartz + 0.447494 Orthoclase + 0.298591 Pyrobole + 1.04026 Pyllosilicates + 0.426797 Garnet + 0.495237 Other

Coefficients

Term	Coef	SE Coef	T	P
Sulphides	3.23275	1.19128	2.71368	0.015
Quartz	0.32761	0.04315	7.59243	0.000
Orthoclase	0.44749	0.10936	4.09207	0.001
Pyrobole	0.29859	0.50884	0.58681	0.566
Pyllosilicates	1.04026	0.17521	5.93732	0.000
Garnet	0.42680	0.44754	0.95365	0.354
Other	0.49524	0.56948	0.86963	0.397

Summary of Model

S = 0.115706 R-Sq = 96.99% R-Sq(adj) = 95.67%

PRESS = 0.734441 R-Sq(pred) = 89.68%

Analysis of Variance

Source	DF	Seq SS	Adj SS	Adj MS	F	P
Regression	7	6.90373	6.90373	0.986248	73.6668	0.000000
Sulphides	1	2.25323	0.09859	0.098589	7.3640	0.015336
Quartz	1	1.77143	0.77175	0.771748	57.6450	0.000001
Orthoclase	1	1.71350	0.22418	0.224181	16.7450	0.000851
Pyrobole	1	0.39594	0.00461	0.004610	0.3443	0.565522
Pyllosilicates	1	0.63105	0.47195	0.471949	35.2518	0.000021
Garnet	1	0.12846	0.01218	0.012176	0.9094	0.354447
Other	1	0.01012	0.01012	0.010125	0.7563	0.397360
Error	16	0.21421	0.21421	0.013388		
Total	23	7.11794				

Fits and Diagnostics for Unusual Observations

Obs	Y2470	Fit	SE Fit	Residual	St Resid

```
  2  0.337612  0.364144  0.110770  -0.026532  -0.79349     X
 14  0.687679  0.831968  0.093875  -0.144288  -2.13314  R

R denotes an observation with a large standardized residual.
X denotes an observation whose X value gives it large leverage.
```

8.7.4.3 General Regression Analysis: Permittivity (912 MHz) versus Sulphides, Quartz, Orthoclase, Pyrobole, Phyllosilicates, Garnet and Other

```
Regression Equation

X912  =  3.7986 Sulphides + 1.64759 Quartz + 1.7339 Orthoclase + 1.8992
         Pyrobole + 1.99646 Pyllosilicates + 1.6452 Garnet + 2.19453 Other

Coefficients

Term               Coef   SE Coef        T      P
Sulphides       3.79860  0.992432   3.8276  0.001
Quartz          1.64759  0.035947  45.8335  0.000
Orthoclase      1.73390  0.091103  19.0323  0.000
Pyrobole        1.89920  0.423906   4.4802  0.000
Pyllosilicates  1.99646  0.145962  13.6779  0.000
Garnet          1.64520  0.372838   4.4126  0.000
Other           2.19453  0.474422   4.6257  0.000

Summary of Model

S = 0.0963928     R-Sq = 99.80%        R-Sq(adj) = 99.72%
PRESS = 0.433697  R-Sq(pred) = 99.43%

Analysis of Variance
```

Source	DF	Seq SS	Adj SS	Adj MS	F	P
Regression	7	75.3148	75.3148	10.7593	1157.96	0.0000000
Sulphides	1	17.6970	0.1361	0.1361	14.65	0.0014839
Quartz	1	32.8113	19.5189	19.5189	2100.71	0.0000000
Orthoclase	1	14.2267	3.3657	3.3657	362.23	0.0000000
Pyrobole	1	6.1073	0.1865	0.1865	20.07	0.0003787
Pyllosilicates	1	2.1093	1.7383	1.7383	187.09	0.0000000
Garnet	1	2.1644	0.1809	0.1809	19.47	0.0004357
Other	1	0.1988	0.1988	0.1988	21.40	0.0002805
Error	16	0.1487	0.1487	0.0093		
Total	23	75.4635				

Fits and Diagnostics for Unusual Observations

Obs	X912	Fit	SE Fit	Residual	St Resid	
2	1.75578	1.76880	0.0922801	-0.0130229	-0.467508	X

X denotes an observation whose X value gives it large leverage.

8.7.4.4 General Regression Analysis: Loss Factor (912 MHz) versus Sulphides, Quartz, Orthoclase, Pyrobole, Phyllosilicates, Garnet and Other

Regression Equation

Y912 = 3.6604 Sulphides + 0.36105 Quartz + 0.490338 Orthoclase + 0.238641 Pyrobole + 1.18693 Phyllosilicates + 0.495151 Garnet + 0.386512 Other

Coefficients

Term	Coef	SE Coef	T	P
Sulphides	3.66040	1.39834	2.61768	0.019
Quartz	0.36105	0.05065	7.12833	0.000

Orthoclase	0.49034	0.12836	3.81989	0.002
Pyrobole	0.23864	0.59729	0.39954	0.695
Pyllosilicates	1.18693	0.20566	5.77127	0.000
Garnet	0.49515	0.52533	0.94255	0.360
Other	0.38651	0.66846	0.57821	0.571

Summary of Model

S = 0.135818 R-Sq = 96.54% R-Sq(adj) = 95.02%

PRESS = 1.08262 R-Sq(pred) = 87.30%

Analysis of Variance

Source	DF	Seq SS	Adj SS	Adj MS	F	P
Regression	7	8.22723	8.22723	1.17532	63.7150	0.000000
Sulphides	1	2.58587	0.12640	0.12640	6.8522	0.018658
Quartz	1	2.15036	0.93732	0.93732	50.8131	0.000002
Orthoclase	1	2.12097	0.26916	0.26916	14.5915	0.001508
Pyrobole	1	0.42846	0.00294	0.00294	0.1596	0.694777
Pyllosilicates	1	0.80809	0.61441	0.61441	33.3076	0.000029
Garnet	1	0.12732	0.01639	0.01639	0.8884	0.359925
Other	1	0.00617	0.00617	0.00617	0.3343	0.571172
Error	16	0.29514	0.29514	0.01845		
Total	23	8.52237				

Fits and Diagnostics for Unusual Observations

Obs	Y912	Fit	SE Fit	Residual	St Resid	
2	0.339726	0.369885	0.130023	-0.030158	-0.76838	X
14	0.750437	0.926840	0.110193	-0.176403	-2.22175	R

R denotes an observation with a large standardized residual.

```
X denotes an observation whose X value gives it large leverage.
```

8.8 Simulated Sorting

8.8.1 Matlab Functions

8.8.1.1 Mineralmixer

```
function minmixture = mineralmixer(minmatrix)

%this function takes an preformed array, minmatrix, and creates an
%effective mixture properties matrix. minmatrix is a n-by-5 array with
%column values [vol%, perm, loss, density, cp].

%check validity of input vol%
unitycheck=sum(minmatrix(:,1));

if unitycheck ~= 1;
    error('volume fractions do not add to one');
end

%calculate density
density=sum(minmatrix(:,1).*minmatrix(:,4));

%calculate specific heat
cp=sum(minmatrix(:,1).*minmatrix(:,4).*minmatrix(:,5))/density;

%calculate dielectric properties
%merge perm and loss into a complex vector, then cuberoot
dielectric=(minmatrix(:,2)+1i*minmatrix(:,3)).^(1/3);
```

```
%multiply dielectric by volumefraction

dielectric=minmatrix(:,1).*dielectric;


%sum and cube for complex answer

dielectricanswer=sum(dielectric)^3;


%split out the real and imaginary components

perm=real(dielectricanswer);

loss=imag(dielectricanswer);


%assemble output

minmixture=[perm,loss,density,cp];


return
```

8.8.1.2 Dievolmod

```
function [TDIFF, MineralVolume, MassPercent, TMIX] = dievolmod(mindata, ganguedata, heatingtime)


%this function has two inputs arrays, mindata and ganguedata. each contains the dielectric properties, density and specific heat. in the following form: x = [permittivity, loss, density, specific heat]

%this function calculates based on an array of valuable mineral volume percents.


%break into managable bits

Emin = mindata(1)+1i*mindata(2);

egan = ganguedata(1)+1i*ganguedata(2);

regan = ganguedata(1);

legan = ganguedata(2);

rhomin = mindata(3);

rhogan = ganguedata(3);

cpmin = mindata(4);
```

```
cpgan = ganguedata(4);


%Assumed calculation parameters

efreespace = 8.85418782e-12; %permittivity of freespace

appliedEfield = 60e3; %V/m

appliedfreq = 2.45e9; %2.45GHz


compositeconstant=2*pi()*appliedfreq*efreespace*heatingtime*appliedEfield^2;


% create a array of heating mineral volume percentages. This way always Vtotal
== 1, and Vgangue = 1- MineralVolume

MineralVolume = 0:0.0001:1;

MineralVolume = MineralVolume.';


% generate the effective mixture density

MixtureDensity = MineralVolume.*rhomin + (1-MineralVolume).*rhogan;


% generate the effective specific heat

MixtureCP             =             ((rhomin.*MineralVolume.*cpmin)+(rhogan.*(1-
MineralVolume).*cpgan))./MixtureDensity;


% generate the effective permittivity array using the LLL equation

emix = (MineralVolume.*emin.^(1/3)+(1-MineralVolume).*egan.^(1/3)).^3;

remix =real(emix);

lemix = imag(emix);

losstangent = lemix./remix;


%% Evalulate the heating of the mixture array


%powder disipation

Pmix1 = compositeconstant.*(lemix./remix.^2);

Pmix2 = compositeconstant.*(lemix);

Pmix3 = 9*compositeconstant.*(lemix./(2+remix).^2);
```

```
%heating rates

Tmix1 = Pmix1./(MixtureCP.*MixtureDensity);

Tmix2 = Pmix2./(MixtureCP.*MixtureDensity);

Tmix3 = Pmix3./(MixtureCP.*MixtureDensity);

Tmix4 = (heatingtime.*(losstangent./0.0041).^1.2830)./12;


% Compare the heating of the mixture to the heating of pure gangue.

Tdiff1 = (Tmix1-Tmix1(1));

Tdiff2 = (Tmix2-Tmix2(1));

Tdiff3 = (Tmix3-Tmix3(1));

Tdiff4 = (Tmix4-Tmix4(1));


%mass percent rescaling

MassPercent  =  (rhomin.*MineralVolume)./(((rhomin.*MineralVolume))+(rhogan.*(1-
MineralVolume))).*100;


TDIFF = [Tdiff1,Tdiff2,Tdiff3,Tdiff4];

TMIX = [Tmix1,Tmix2,Tmix3,Tmix4];

return
```

8.8.1.3 Recoverymodeller2x

```
function  [OutputA,  OutputB,  OutputC]=RecoveryModeller2X(DistType,  GANGUEMIX,
MINERALMIX, ELEMENTAL, SampleSize)


%This is a re-write of the recoverymodeller function. It is now designed to be

%more generic (ie less hard-coded variables). There is a degree of hard

%coding, however.


%DistType is the distribution selection variable 1,2,3


%Fudgefactor is the relative standard deviation temperature fuge factor
```

```
%GANGUEMIX is the gangue mixture properties data
%form: [permittivity,lossfactor,density,specific heat]
%example: quartz= [4.36,0.001,2843.05,740.00];

%MINERALMIX is the valuable mineral mixture properties data
%form: [permittivity,lossfactor,density,specific heat]
%example:chalcopyrite=[22.36,1.65,4391.24,534];

%ELEMENTAL is the data matrix of valuable element mass percents of each
%species. The first row needs to be a zero (if its non-zero we have to deal
%with multidimensionality) the second row is the primary element. It is
%possible to extend this funtion later with additional valuable elements,
%however with the current calculations this be directly proportional to the
%primary element. Extensibility option: add an element value matrix to
%investigate the optimum value discrimination threshold.
%form: column for each valuable element. first row ganguemix and second row
mineralmix.
%example: ELEMENTAL=[0;0.3463] (copper)

%% Initialization of Data and Variables.

%set the SampleSize:SampleSize=100;

%Heating calculation Parameters
HeatingTime=12;             %seconds
efreespace= 8.85418782e-12; %permittivity of freespace
AppliedEfield=30e3;         %30ksV/m
Appliedfreq=2.45e9;         %2.45GHz

%create the complex dielectic property of quartz and cuberoot for later
qdp=(GANGUEMIX(1)+1i*GANGUEMIX(2))^(1/3);
```

```
%create the complex dielectic property of chalcopyrite and cuberoot for later
cdp=(MINERALMIX(1)+1i*MINERALMIX(2))^(1/3);

%Get the dimensions of the input data arrays
CheckGANGUGEMIX = size(GANGUEMIX);
CheckMINERLMIX = size(MINERALMIX);
CheckELEMENTAL = size(ELEMENTAL);

%Check that each of the input data arrays are the correct size
if CheckGANGUGEMIX(2) ~= 4;
    error('invalid input Gangue Mixture')
end

if CheckMINERLMIX(2) ~= 4;
    error('invalid input mineral mixture')
end

if CheckELEMENTAL(1) ~= 2;
    error('the element matrix is an invalid size')
end

%% Distribution selection and generation

%Generate the samples based on the selected distribution. This is currently
%generates a massfraction of valuable element. The generator functions,
%unimodaldister, bimodaldister, and lognormdister have their parameters
%hard-coded below.

%The current settings for all distrubtion generators produce an average
%element grade (fraction) of 0.0033 for large sample sizes.
```

```
%also please note that these function use ABS() on their outputs to get rid
%of negative values.

switch DistType
    case 1          %selected normal distribution
        q = 1;        %peak height
        m = 0.0;      %mean
        s = 0.0041;   %standard deviation
        %call the unimodal distribution function
        X=unimodaldister(SampleSize,q,m,s);

    case 2                    %selected bimodal normal distribution
        q = [.75 .25];        %relative heights of each peak
        m = [0.00 0.0105];    %mean
        s = [.0012 .0025];    %standard deviation
        %call the bimodaldister function to generate the ore
        X=bimodaldister(SampleSize,q,m,s);

    case 3            %selected a lognormal distribution
        m = 0.0033;     %mean (comes out very close to head grade)
        s = 4e-6;       %standard deviation
        %call the lognormal function to generate the ore
        X = lognormdister(SampleSize,m,s);

    otherwise
        %just 'cause
        error('invalid distribution selection')

end

HeadGrade=mean(X);
```

```
%% Apply Mixing Formulas etc.


Xmassfractionmineral=X./ELEMENTAL(2);            %Change to fraction of valuable
mineral species

Xmassfractiongangue=1-Xmassfractionmineral;     %calculate fraction gangue


%calculate the volume and then volume fraction of mineral and gangue

Vmineral=  Xmassfractionmineral./MINERALMIX(3);     %mineral  volume  (volume  =
massfraction of mineral / mineral density)

Vgangue=Xmassfractiongangue./GANGUEMIX(3);      %gangue volume

Vtotal=Vmineral+Vgangue;                            %total volume (sum component
volumes. for a set MASS we EXPECT volume to DECREASE as we increase the denser
fraction!)

Xvolumepercentmineral=Vmineral./Vtotal;         %Vol% mineral

Xvolumepercentgangue=1-Xvolumepercentmineral;   %Vol% gangue


%Calculate particle density

XmixDensity=1./Vtotal;


%Calculate mixture specific heat

XmixSpecificHeat=Xmassfractiongangue.*GANGUEMIX(4)+Xmassfractionmineral.*MINERAL
MIX(4);


%generate the dielectic properties of each particle

EXprop=(Xvolumepercentmineral.*cdp+Xvolumepercentgangue.*qdp).^3;

EXreal=real(EXprop); %break out the real part

EXimag=imag(EXprop); %break out the imaginary part


%calculate simulated particle grades

TotalMineral=sum(Xmassfractionmineral);

TotalGangue=sum(Xmassfractiongangue);


MassElementMineral=TotalMineral.*ELEMENTAL(2,:);
```

```
MassElementGangue=SampleSize.*ELEMENTAL(1,:);


%% Calculate Heating
%This section applies calulates the microwave heating each particle should
experience based on the dielectric properties.


%combine all the scalar variables together
compositeconstant=2*pi()*Appliedfreq*efreespace*HeatingTime*AppliedEfield^2;


%Divide EXimag by EXreal^2 (Again with the not doing './')
Ecombinant=zeros(SampleSize,1);
for ii=1:SampleSize;
    Ecombinant(ii)=EXimag(ii)/(EXreal(ii)).^2;
end


%calculate the power absorbed.
Pmix=compositeconstant.*Ecombinant;


%again no './' this calculates the change in temperature of the particle
Tmix=zeros(SampleSize,1);
for ii=1:SampleSize;
    Tmix(ii)=Pmix(ii)/(XmixSpecificHeat(ii).*XmixDensity(ii));
end


%% Apply Heating RSD Fudging
%At this point the microwave heating is the perfect case, real rocks never
%heat exactly the same twice. This function takes the perfect heating
%and randomly alters it based on empirical data.


HotRSD=abs(normrnd(0.1554,0.0515,SampleSize,1));
HotSD=Tmix.*HotRSD;
```

```
%third step: use the final temperature as the mean and the calculated SD
%together to find the new final temperature.
Tfudge=normrnd(Tmix,HotSD);

%% calculate recovery curves
%this section calculates mass recovery curves

%sort descending
Xsort=[X Tfudge XmixDensity];
Xsort2=sortrows(Xsort,-2);
Tfudge2=Xsort2(:,2);
Xmixdens2=Xsort2(:,3);
rec=cumsum(Xsort2(:,1));
recpercent=rec/rec(SampleSize);
massrec=cumsum(Xmixdens2);
massrecpercent=massrec/massrec(SampleSize);

%sort ascending
XsortB=[X Tfudge XmixDensity];
Xsort2B=sortrows(XsortB,2);
Tfudge2B=Xsort2B(:,2);
Xmixdens2B=Xsort2B(:,3);
recB=cumsum(Xsort2B(:,1));
recpercentB=recB/recB(SampleSize);
massrecB=cumsum(Xmixdens2B);
massrecpercentB=massrecB/massrecB(SampleSize);

%outplobD=[massrecpercent recpercent X,Tfudge2 Xmassmin,Xmassgan];
%outplobU=[massrecpercentB recpercentB X Tfudge2B Xmassmin Xmassgan];

plot(massrecpercent,recpercent,[0,1],[0,1]);
```

```
%% Set the Outputs And Testing

OutputA=massrecpercent;

OutputB=recpercent;

OutputC=X;

%OutputB=0;

%hist();

return
```

8.8.2 Ore Heating Behaviour

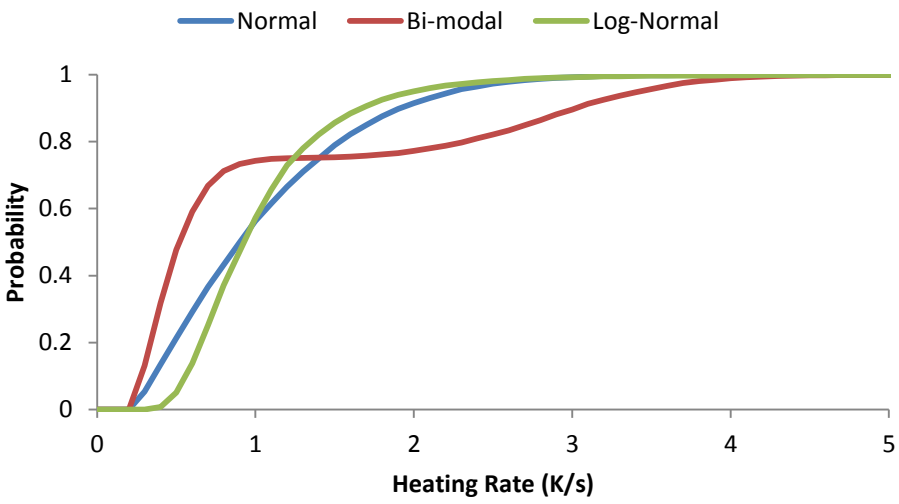

Figure 8-33 – Cumulative Distribution Function of Simulated Ore Heating Behaviour ($E_{\parallel}$)

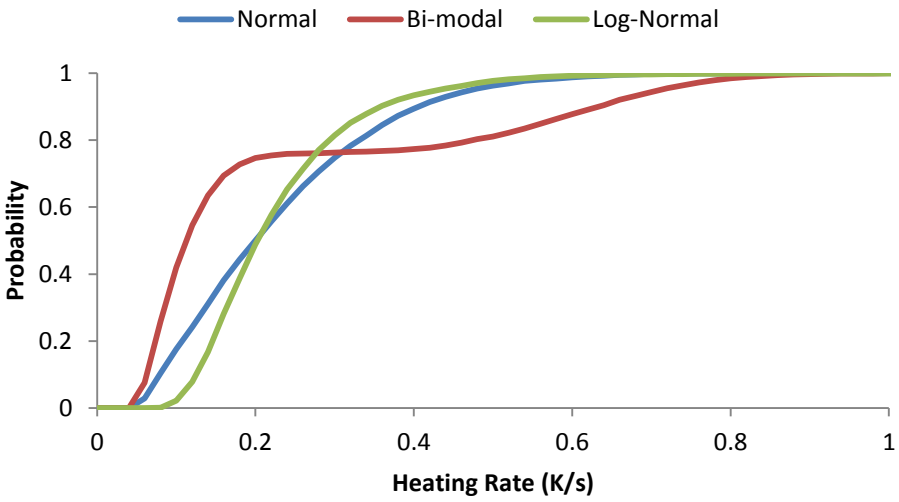

Figure 8-34 – Cumulative Distribution Function of Simulated Ore Heating Behaviour (E_{sphere})

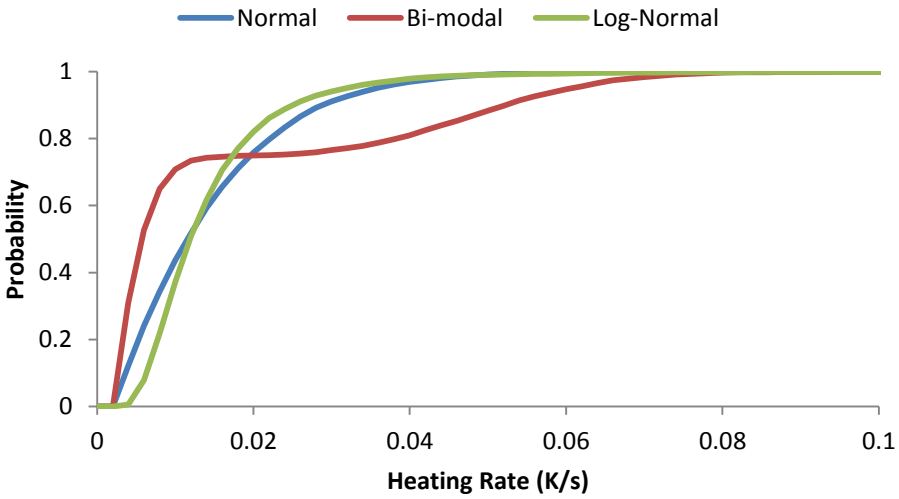

Figure 8-35 – Cumulative Distribution Function of Simulated Ore Heating Behaviour (Power law)

Table 8-40 –Regression of the heating rates predicted by heating models for 0 to 5 mass% Chalcopyrite mixtures

Heating Model	*Regression Equation*	R^2
$E_{\parallel}$	$0.8901x + 0.1889$	100%
$E_{\perp}$	$0.0403x + 0.0151$	100%

E_{sphere}	0.1786x + 0.0575	100%
Power Law	0.0176x - 0.0030	99.5%

8.8.3 Ideal Grade Recovery Curves

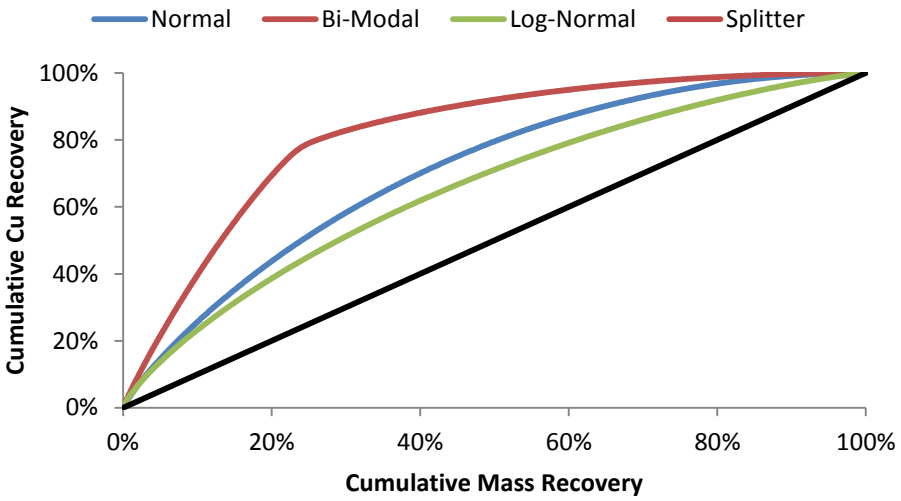

Figure 8-36 – Ideal Grade Recovery Curve Gangue A ($E_{||}$)

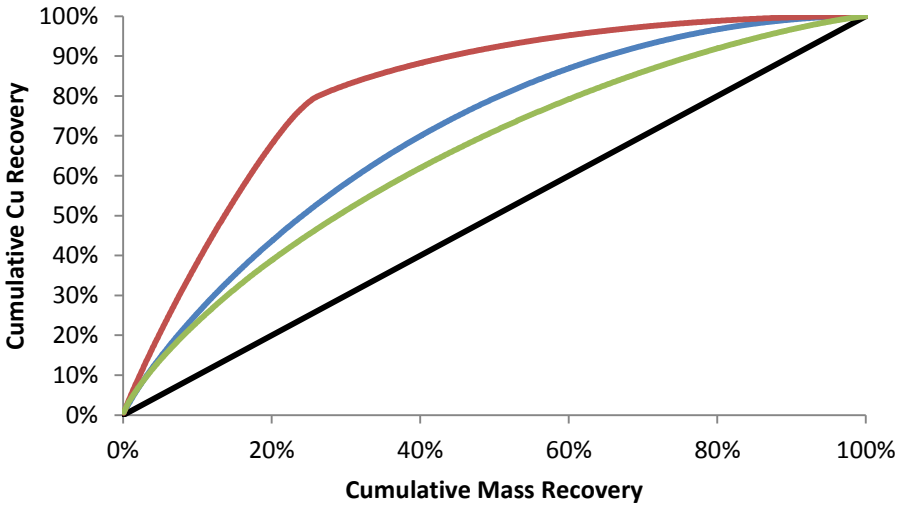

Figure 8-37 – Ideal Grade Recovery Curve Gangue A (E_{sphere})

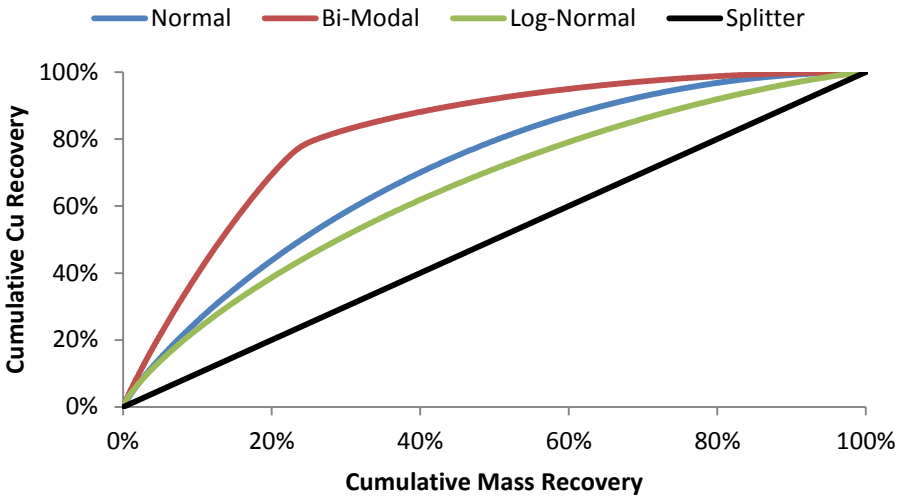

Figure 8-38 – Ideal Grade Recovery Curve Gangue A (Power Law)

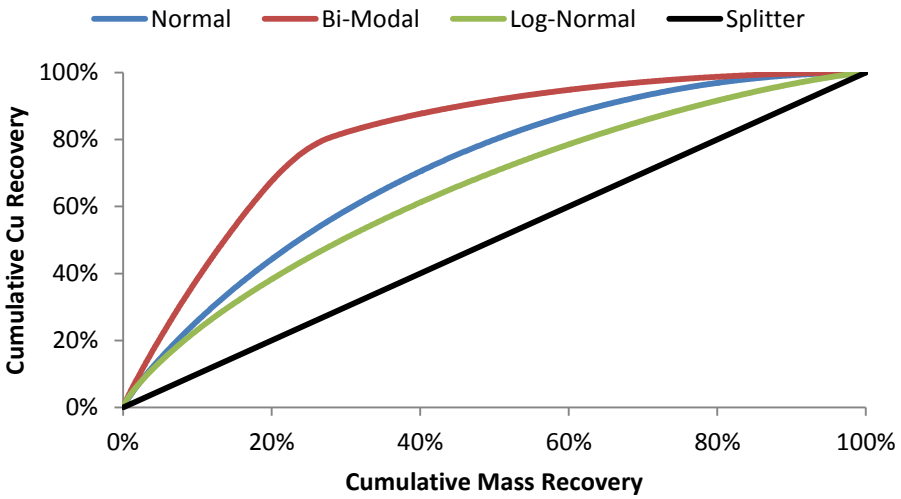

Figure 8-39 – Ideal Grade Recovery Curve Gangue B ($E_{||}$)

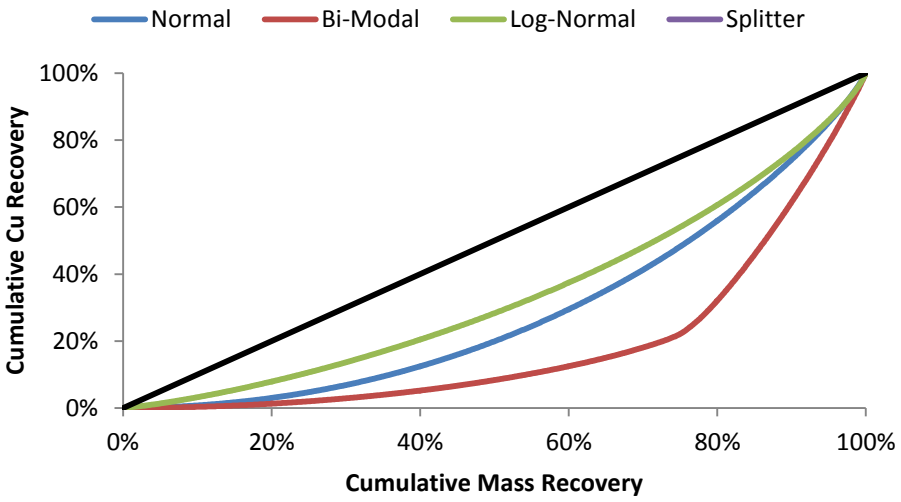

Figure 8-40 – Ideal Grade Recovery Curve Gangue B (E_{sphere})

8.8.4 Uncertain Heating Grade Recovery Curves

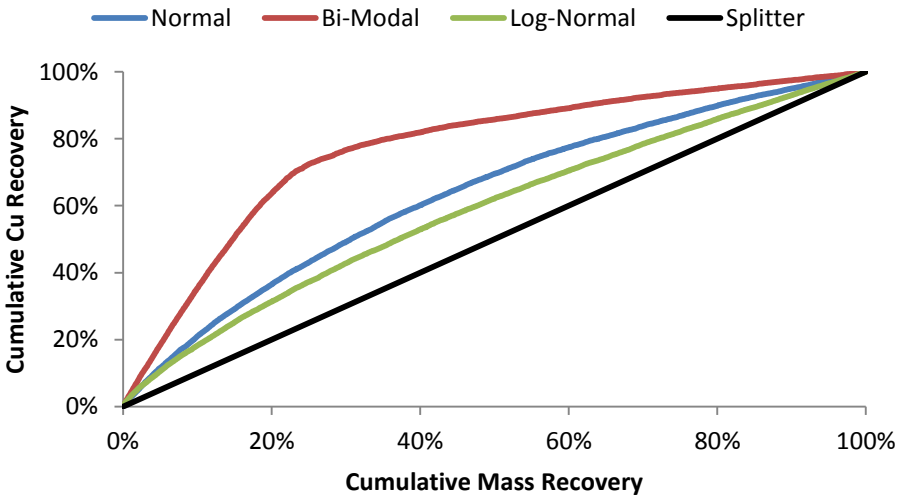

Figure 8-41 – Grade Recovery Curve Gangue A ($E_{||}$)

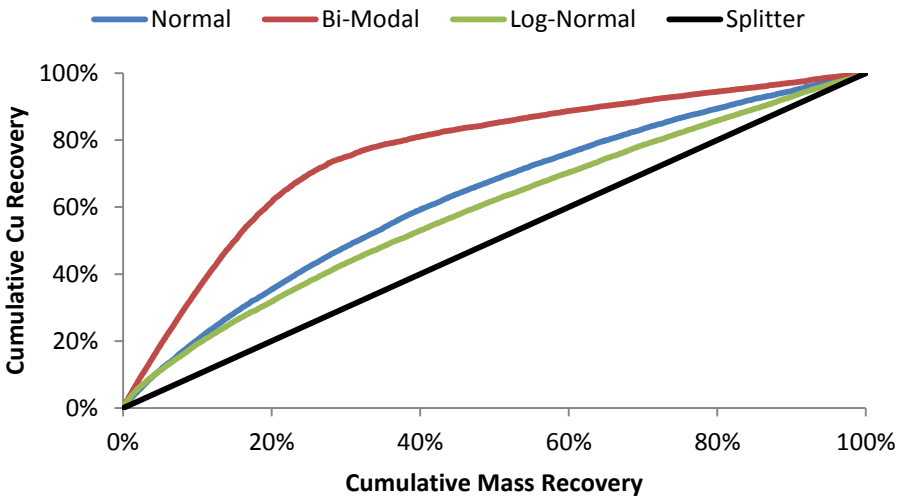

Figure 8-42 – Grade Recovery Curve Gangue A (E_{sphere})

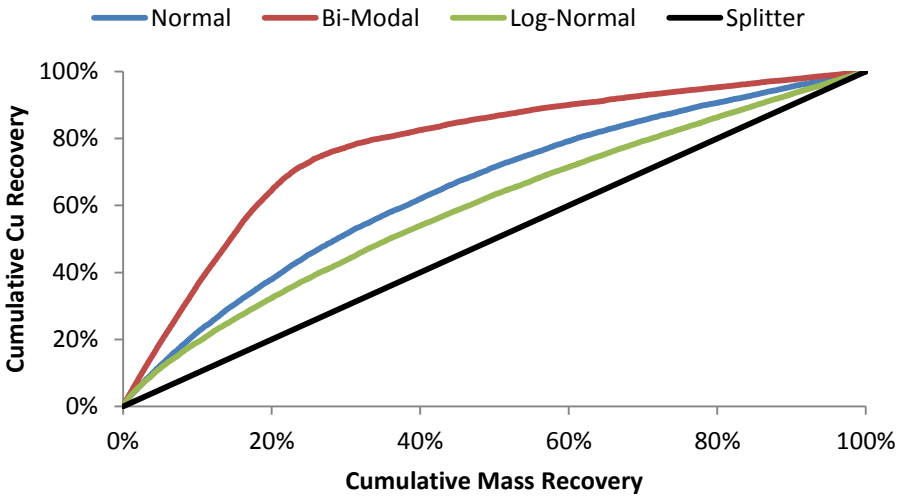

Figure 8-43 – Grade Recovery Curve Gangue A (Power Law)

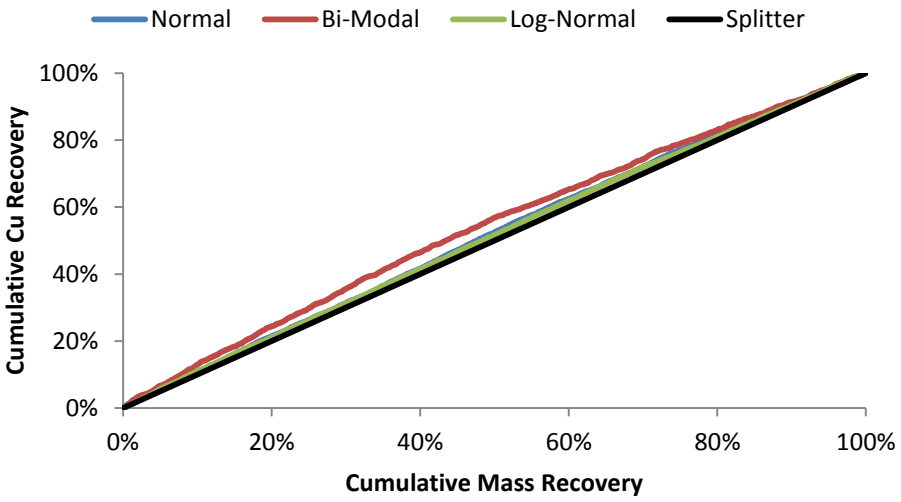

Figure 8-44 – Grade Recovery Curve Gangue B ($E_{\|}$)

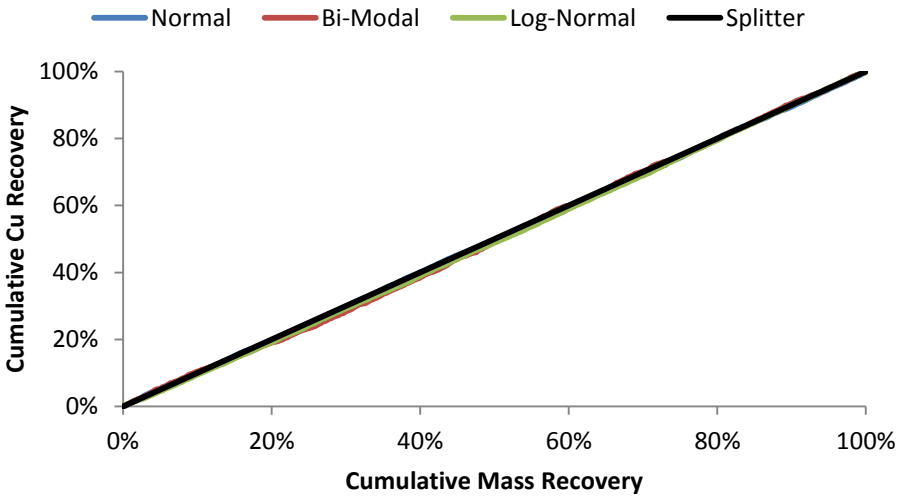

Figure 8-45 – Grade Recovery Curve Gangue B (E_{sphere})

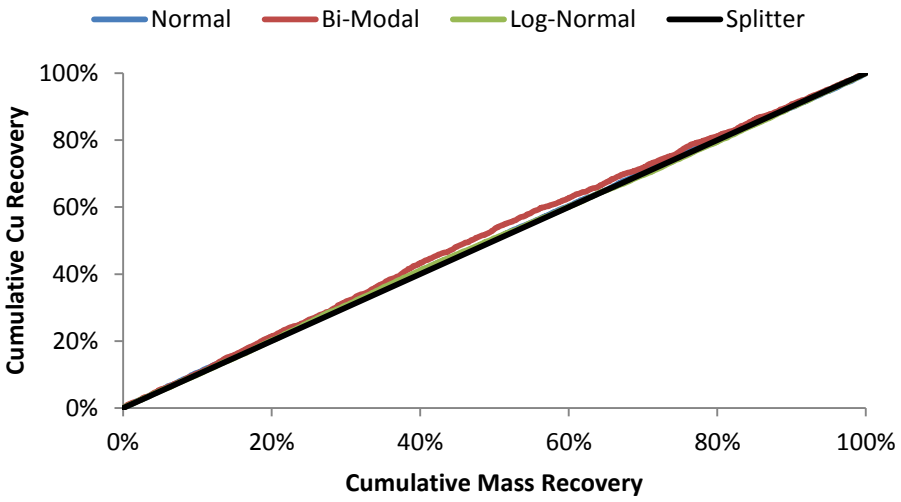

Figure 8-46 – Grade Recovery Curve Gangue B (Power Law)

8.8.5 Grade Recovery Curves for Small Sample Sizes

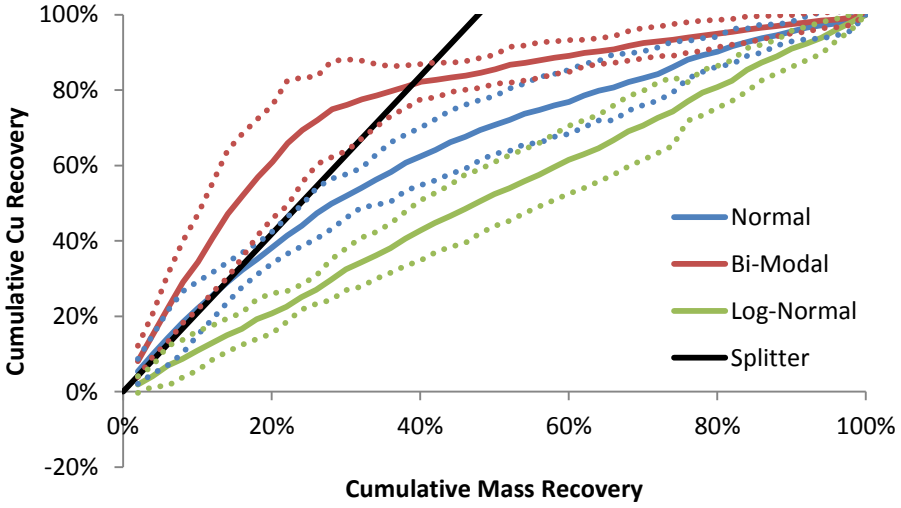

Figure 8-47 – Grade recovery curves of Gangue A with 95% CIs (Dotted) ($E_{\|}$, n = 10, sample size = 50)

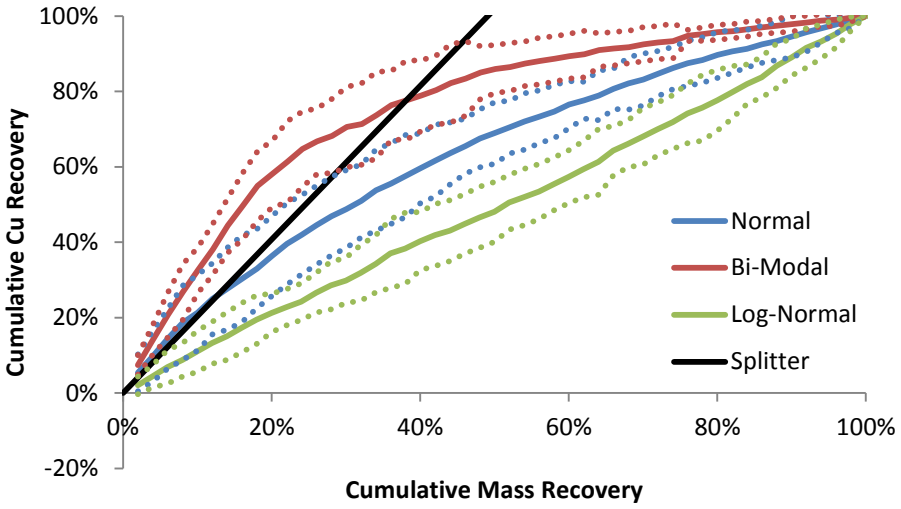

Figure 8-48 – Grade recovery curves of Gangue A with 95% CIs (Dotted) (E_{sphere} , n = 10, sample size = 50)

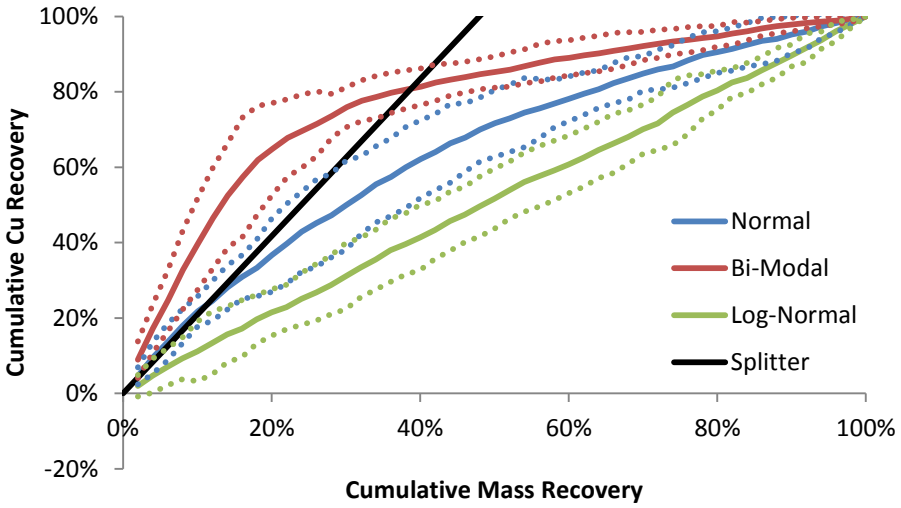

Figure 8-49 – Grade recovery curves of Gangue A with 95% CIs (Dotted) (Power Law, n = 10, sample size = 50)

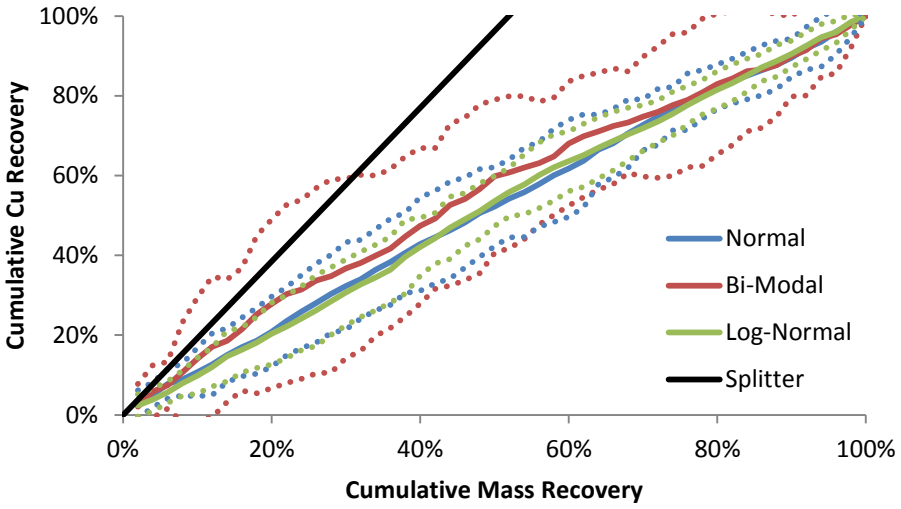

Figure 8-50 – Grade recovery curves of Gangue B with 95% CIs (Dotted) ($E_{||}$, n = 10, sample size = 50)

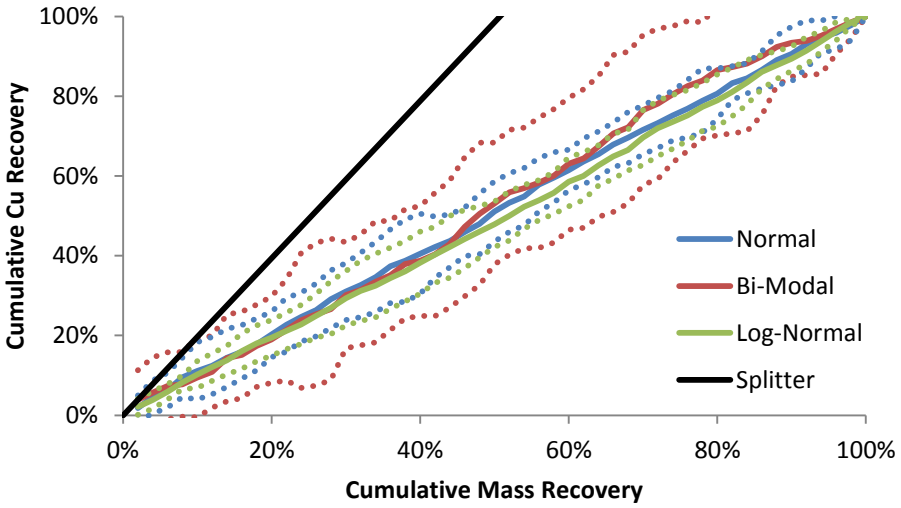

Figure 8-51 – Grade recovery curves of Gangue B with 95% CIs (Dotted) (E_{sphere} , n = 10, sample size = 50)

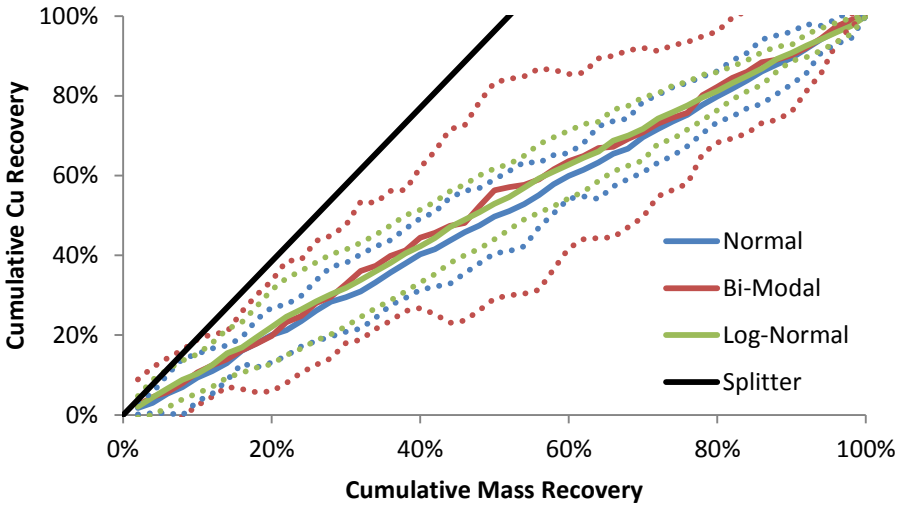

Figure 8-52 – Grade recovery curves of Gangue B with 95% CIs (Dotted) (Power Law, n = 10, sample size = 50)